ABSTRACT

MISHRA, KAUSHAL KISHOR. Phase Contrast Neutron Imaging using Single and Multiple Pinhole Apertures. (Under the direction of Dr. Ayman I. Hawari (Chair) and Dr. Sujit K. Ghosh (Co-chair).)

In the present work phase contrast neutron imaging at low/medium intensity neutron sources using single and multiple pinhole apertures has been investigated. Phase contrast techniques utilize the wave nature of neutrons (along with the particle nature used by conventional neutron imaging) to enhance the material edge contrast in the object image. The technique benefits from differences in the coherent scattering length densities of different materials in the sample. The performed investigation included multiple aspects related to the theoretical understanding, simulation techniques, experimental feasibility at the PULSTAR imaging facility, and image processing/reconstruction pertaining to these techniques.

The theoretical aspects include the physical understanding of phase contrast as well as multi-pinhole imaging. The theory for the image intensity variation for mixed phase-amplitude objects was developed. Presence of an additional interaction term, quantified by the scalar product of the gradient of real and imaginary parts of the transmission function of the object, was found in the neutron intensity expression. Further, a theoretical understanding of the image formation process using multi-pinhole masks was also developed. It was shown that the formed image of the object from a multiple pinhole aperture can be written as a convolution of the source mask image at the detector with the object image obtained through a single pinhole.

The theoretical work performed above was used to develop simulation and design methodologies. An image simulation technique was developed to simulate phase contrast images of specified objects using the phase-amplitude formulation. Demonstration of the technique was performed using various designed phantoms. The simulation technique can act as a tool for assessing the usefulness of phase contrast imaging as an edge enhancement method for a particular sample.

Performance of phase contrast neutron imaging requires a spatially coherent beam. Spatial coherence of the beam can be increased by increasing the L/d ratio and the average wavelength of the neutron beam. These methods of improving the spatial coherence lead to a significant reduction in the neutron intensity available to image the object, thereby favoring its implementation at high intensity neutron sources. However, in order to harness the potential of this technique, its usability needs to be expanded to low/medium intensity neutron sources that are more common worldwide. In the present work experimental demonstration of the technique was performed at the 1MWth PULSTAR reactor, which represents a medium intensity neutron source. This required meticulous design to maximize the spatial coherence of the beam while maintaining the neutron intensity at the image plane. Twelve inches of single crystal sapphire was used to filter out fast neutrons to lower the average energy of the neutron beam. A 500μm gadolinium foil with a 0.5mm diameter pinhole was used as the aperture following which, a 0.6^{o} beam divergence was provided using borated polyethylene discs with holes of increasing diameter.

In order to improve the SNR in the image multiple pinhole apertures were explored. Un-coded masks were considered for this purpose. A collimator with seven pinholes was designed to perform the imaging. Masks with greater number of pinholes were studied using simulations but could not be explored experimentally due to space restrictions at the facility. The image reconstruction of the raw data was performed using a least square de-convolution technique. Tikhonov regularization was investigated in this regard to make the convolution matrices well behaved wherever required. Also, various de-noising techniques like median filtering, Wiener filtering and soft thresholding using Symlets were explored to improve the reconstructed image. It was concluded that the choice of the de-noising techniques depends upon the properties desired in the reconstructed image like smoothness, blockiness etc.

Thus, in the present work two of the comparatively new neutron imaging modalities namely, Phase Contrast Neutron Imaging and Multi-Pinhole Neutron Imaging, were investigated in detail. The investigation established better understanding of these techniques and enhanced the potential for their usability in practical applications.

Phase Contrast Neutron Imaging using Single and Multiple Pinhole Apertures

by
Kaushal Kishor Mishra

A dissertation submitted to the Graduate Faculty of
North Carolina State University
in partial fulfillment of the
requirements for the degree of
Doctor of Philosophy

Nuclear Engineering
Statistics

Raleigh, North Carolina

2010

APPROVED BY:

_____	_____
Dr. Ayman I. Hawari	Dr. Sujit K. Ghosh
Committee Chair	Committee Co-chair
_____	_____
Dr. Bernard W. Wehring	Dr. Jason Osborne
_____	
Dr. Paul R. Huffman	

DEDICATION

This Dissertation is dedicated to my beloved parents and sisters.

BIOGRAPHY

Kaushal Kishor Mishra was born February 15th 1981, at Bokaro Steel City, Jharkhand India to Shri Ram Nath Mishra and Smt. Lalita Devi. Bokaro Steel City is a small place in south east of Jharkhand with an Integrated Steel Plant and a population of about one million.

In August 1999, the author began attending Indian Institute of Technology at Kanpur (IITK), India and obtained a Bachelor of Technology (B.Tech.) degree in Mechanical Engineering in May 2003. During his junior year the author came in contact with Dr. P. Munshi, a professor of nuclear engineering at IITK, and worked under him on beam hardening in computed X-ray tomography. This work made him interested in the field of Radiation Imaging.

In his senior year the author decided to continue his education by going for graduate studies in Nuclear Engineering. The author joined North Carolina State University (NCSU) as a graduate student in Nuclear Engineering in August 2003. He started in the field of Neutron Imaging under Dr. Ayman I. Hawari pursuing his interest in Radiation Imaging. The author earned his Master's degree in Nuclear Engineering in August 2005 by designing a thermal neutron imaging facility on the PULSTAR Reactor located in the university campus. During, this period he took a few courses in Statistics and got interested in it. So, he decided to continue further for a Doctorate in Nuclear Engineering with Statistics as his co-major.

During his Ph.D. the author worked on investigating phase contrast neutron imaging techniques. He also worked on the feasibility of performing these imaging exercises at his designed facility. Moreover, the facility was upgraded in terms of shielding and automation. The time the author spent here with all the diligent and knowledgeable people provided him with great experience and made him learn immense amount of technical and inter-personal skills. The author presents a part of this learning in here, which he thinks will be a purposeful contribution in furthering this field.

ACKNOWLEDGEMENTS

The author would like to extend his deepest gratitude to Dr. Ayman I. Hawari for his guidance throughout the course of this work. He appreciates the opportunity provided to him to work with so many diligent people. The trust and the confidence shown on him by Dr. Hawari regarding this project really mean a lot to him.

The author would like to express his gratitude to Dr. Sujit K. Ghosh who agreed to spend his time and effort in guiding the author in the statistical aspects of the project. His guidance really helped the author in various aspects throughout this work. The author would also like to acknowledge the help provided by Dr. Bibhuti B. Bhattacharya. Discussions with him provided a great deal of insight to the author in various aspects related to this work.

The author expresses his thanks to Dr. Paul R. Huffman, Dr. Bernard W. Wehring and Dr. Jason Osborne for their valuable inputs and advice all throughout this work. He wants to thank all of them to serve in his committee.

The author would like to thank Mr. Andrew Cook, Mr. Larry Broussard, Mr. Kerry Kincaid, Mr. Scott Lassell, Mr. Gerald Wicks, and Mr. Stephen Bilyj for their valuable assistance in developing the Neutron Imaging Facility and performing modifications in it from time to time. He also conveys his sincere thanks to all the student operators who assisted in the facility construction and operation.

Last but not the least, the author expresses his thanks to the faculty of the Department of Nuclear Engineering and to fellow colleagues and friends for making his stay at NCSU purposeful yet enjoyable. The author would also like to thank Ms. Hermine Kabbendjian, Ms. Wendy So and all other fellow students and staff for their valuable assistance and making his stay comfortable for all these years.

TABLE OF CONTENTS

LIST OF FIGURES ix

LIST OF TABLES xviii

CHAPTER 1 INTRODUCTION 1

1.1 Introduction to Neutron Imaging 1

1.1.1 History and Trends 2

1.1.2 Neutron vs. X-ray Imaging 3

1.1.3 Image Formation Process 7

1.1.4 Detection Systems for Neutron Imaging 9

1.1.5 Image Degradation Sources 14

1.1.6 Conventional Neutron Imaging 18

1.1.7 Advanced Neutron Imaging Techniques 20

1.2 Objective 28

CHAPTER 2 NEUTRON IMAGING AT THE PULSTAR: AN OVERVIEW 29

2.1 Introduction 29

2.2 The PULSTAR Reactor 29

2.3 Design of the Neutron Imaging Facility 32

2.3.1 Design Criteria and Constraints 32

2.3.2 Design Performance using Simulations 33

2.3.3 Design Verification using Simulations 39

2.3.4 Facility Construction 42

2.3.5 Safety and Control Systems 45
2.3.6 Detection Systems 47
2.3.7 Facility Characterization 55
CHAPTER 3 PRINCIPLES OF PHASE CONTRAST AND MULTI-PINHOLE NEUTRON IMAGING 60
3.1 Phase contrast Neutron Imaging 60
3.2 Background of Phase Contrast Neutron Imaging 61
3.3 Motivation 61
3.4 The Physics of Phase Contrast Imaging 63
3.4.1 Kirchhoff's Formulation 63
3.4.2 Fresnel Diffraction 65
3.4.3 Phase and Amplitude Objects 67
3.4.4 Non-Interferometric Phase Contrast 69
3.4.5 Multi-Component Systems 72
3.4.6 Neutron Transmission Function of Materials 73
3.4.7 Assumptions and Beam Requirements 79
3.5 Introduction to the Multi-pinhole Neutron Imaging 85
3.6 Image Formation using Multi-Pinhole Masks 88
CHAPTER 4 DESIGN AND TESTING OF PHASE CONTRAST AND MULTI-PINHOLE NEUTRON IMAGING SYSTEMS 92
4.1 Introduction 92
4.2 Design Considerations for Phase Contrast Imaging 92
4.3 Image Simulation Technique 94
4.4 Design Performance for PULSTAR 98

4.5 Phase Image Simulations 102
4.5.1 Simulation Results 105
4.6 Design Verification and Experimental Results 110
4.6.1 Design Verification 111
4.6.2 Performance of Neutron Phase Contrast Imaging Experiments 116
4.6.3 Routine Performance of Phase Contrast Neutron Imaging 128
4.7 Design Considerations for Multi-Pinhole Collimator 130
4.8 Experimental Results 139
CHAPTER 5 MULTI-PINHOLE IMAGE RECONSTRUCTION 146
5.1 Introduction 146
5.2 Image Reconstruction: An Inverse Problem 146
5.3 Coded Mask Image Reconstruction 150
5.4 Image Reconstruction for Un-coded Masks 151
5.5 Simulation Results and Discussion 153
5.5.1 Reconstruction of the System Point Spread Function 154
5.5.2 Reconstruction of Simulated Test Object 164
5.6 System PSF Estimation and Image Reconstruction: Simulated Results 164
5.7 System PSF Estimation and Image Reconstruction: Experimental Results 177
CHAPTER 6 CONCLUSION AND FUTURE WORK 184
6.1 Conclusion 184
6.2 Future Work 186
REFERENCES 189

APPENDICES 199

Appendix A. Fourier Transform of the Fresnel Propagator 200

Appendix B. Selected Properties of Fourier Transform 202

Appendix C. Conjugate Gradient Technique: A Brief Note 203

Appendix D. Image De-noising Techniques: A Brief Note 204

LIST OF FIGURES

Figure 1.1. A comparison between neutron and X-ray attenuation coefficients [5]. 3

Figure 1.2. Radiograph of a computer floppy disk (a) using neutrons depicting the polymeric low 'Z' components clearly, (b) using X-rays depicting metallic components clearly [6]. 4

Figure 1.3. Schematic depicting the image formation process in conventional neutron imaging. 8

Figure 1.4. A characteristic curve depicting important parameters associated with it [18]. 11

Figure 1.5. (a) Generic shape of a PSF. (b) The normalized intensity profile of the PSF taken through its center with the depicted full width at half maximum (FWHM). 16

Figure 1.6. Different functional forms that can be used to model LSF and PSF. 16

Figure 1.7. Neutron radiograph of a spark plug at (a) 0.69nm (0.457meV) (b) 0.32nm (2.125meV). (c) Division of the two radiographs reducing the contrast of the outer steel cover [25]. 21

Figure 1.8. Neutron Bragg scattering edges of face centered and body centered iron [27]. 21

Figure 1.9. (a) Attenuation contrast image of the object obtained using particle nature of the neutrons. (b) Phase contrast image of the same object obtained using both particle and wave nature of neutrons. 24

Figure 1.10. The schematic of polarized neutron imaging. The spin rotation of the neutrons depends on the magnetic field along the neutron path [36]. 25

Figure 2.1. A picture showing the PULSTAR reactor core with all the 6 beam tubes. 30

Figure 2.2. The relative neutron flux profile across the PULSTAR reactor core. 31

Figure 2.3. Layout of the imaging facility on BT #5. 32

Figure 2.4. MCNP model of the PULSTAR reactor core. 34

Figure 2.5. Normalized neutron energy spectrum at BT #5 entrance. 34

Figure 2.6. Normalized gamma energy spectrum at BT #5 entrance. 35

Figure 2.7. The calculated single crystal sapphire thermal neutron total cross-sections and comparison with experimental data. Hemex, Hemlux and Hemlite are three grades of sapphire mainly differing in the degree of crystal alignment and the photon transparency. 36

Figure 2.8. The calculated single crystal bismuth thermal neutron total cross-sections and comparison with experimental data. 37

Figure 2.9. The neutron energy spectrum ($d\phi/d(\ln(E))$) at the 6m image plane with 4 inch Bi and 6 inch sapphire filters using the generated thermal neutron scattering cross-sections. 38

Figure 2.10. The collimator model used in the MCNP simulation. The various components that are shown in the figure are: (1) air, (2) aluminum, (3) lead, (4) SWX-277 (concrete type material with 1.6% boron content), (5) bismuth filter, (7) boral, and (8) borated polyethylene. 38

Figure 2.11. MCNP simulated radiograph of BPI. The pixel resolution is 50μm. 39

Figure 2.12. Simulated PSFs for different imaging media. 41

Figure 2.13. (a) Six inches long single crystal sapphire filter. (b) Four inches long bismuth filter with large monocrystals. 44

Figure 2.14. Photograph of the beam shutter used to open/close imaging beam. 45

Figure 2.15. The imaging facility shielding enclosure and the control system. 46

Figure 2.16. A view of the computer screen showing the safety and control system. 47

Figure 2.17. A picture of different equipments associated with the film detection system. 48

Figure 2.18. Equipments for the image plate detection system. 49

Figure 2.19. Thompson tube detection system. 51

Figure 2.20. Equipments associated with the scintillation screen detection system. 52

Figure 2.21. Schematic of the neutron detection within a boron doped MCP structure [66]. 54

Figure 2.22. The micro-channel plate detection system. 54

Figure 2.23. Measured neutron beam profile at the image plane located at a distance of 6m from the aperture. The pixel size is 50μm. 55

Figure 2.24. (a) Scanned neutron radiograph of the ASTM BPI using film. (b) Neutron radiograph of the ASTM BPI using an IP. (c) Scanned neutron radiograph of the ASTM SI using a film. (d) Neutron radiograph of the ASTM SI using an IP. 57

Figure 2.25. Measured LSF using a radiography film. The data was fitted to a Lorentzian function and the FWHM was extracted from the fit result. 58

Figure 2.26. Measured LSF using digital image plates. The data was fitted to a Gaussian function and the FWHM was extracted from the fit results. 58

Figure 3.1. Diagram illustrating Kirchhoff's derivation of the amplitude at *P* due to a point source at *Q*. 64

Figure 3.2. Schematic for the small angle approximation of the Kirchhoff's formula. 66

Figure 3.3. The geometry and coordinate system for the Fresnel diffraction..... 67

Figure 3.4. Diagram illustrating the description of wave propagation through a multi-component system. 73

Figure 3.5. Schematic showing the interaction of neutron with atoms leading to the creation of mean optical potential [84]. 75

Figure 3.6. Diagram depicting the optical path difference between the neutron waves passing through the object and the vacuum..... 78

Figure 3.7. (a) Two monochromatic waves with a delay of τ. The coherence time τ_c is infinite since they are perfectly correlated with each other for all delays τ. (b) The amplitude of a wave whose phase drifts significantly in time τ_c as a function of time *t* (red) and a copy of the same wave delayed by $2\tau_c$ (green). At any particular time *t* the wave can interfere perfectly with its delayed copy. But, since half the time the red and green waves are in phase and half the time out of phase, when averaged over *t* any interference disappears at this delay [89]. 81

Figure 3.8. (a) A plane wave with an infinite coherence length. (b) A wave with varying wave-front and infinite coherence length. (c) A wave with varying wave-front and finite coherence length [89]. 82

Figure 3.9. Schematic depicting the increase in the coherence area A_c of a wave incident on a pinhole at a large distance from the pinhole [89]. The coherence length L_c remains unchanged. 84

Figure 3.10. Schematic of the multiple pinhole neutron source imaging. 85

Figure 3.11. A coded mask with pinhole pattern based on the URA scheme. 87

Figure 3.12. Ray diagram depicting the formation of overlapped images of the object on the detector by the multi-pinhole source..... 88

Figure 4.1. Simulated beam profile at the 6m image plane. 99

Figure 4.2. Neutron source energy spectrum plotted along with the sapphire and the bismuth thermal neutron cross-sections. 101

Figure 4.3. Neutron energy spectrum at the image plane using 3 inches of sapphire filter..... 101

Figure 4.4. MCNP design of the collimator. The material specifications are (1) Concrete (2) 5% Borated Polyethylene (3) Aluminum (4) Air (5) Sapphire Filter (6) Lead (7) SWX-277 (look in Chapter 2). 102

Figure 4.5. Geometry of (a) Phantom 1 (b) Phantom 2. Table 4.1 gives the material composition of the phantoms. 103

Figure 4.6. Phantom 1 Simulation Results: (a) Normal Attenuation Radiograph (1st term in Eq. (4.9)) (b) The pure phase image (2nd term in Eq. (4.9)) (c) The phase amplitude interaction image (3rd term in Eq. (4.9)) (d) The phase image with phase-amplitude interaction which is the difference of (b) and (c) as given by Eq. (4.9) (e) Phase contrast radiograph with pure phase approximation (1st and 2nd term in Eq. (4.9)) (f) Phase contrast radiograph with phase-amplitude interaction (all terms in Eq. (4.9)). The object to detector distance R = 80cm. The grayscale for all six images is the same. 106

Figure 4.7. An intensity profile taken across (a) slice '*a*-*a*' of Figure 4.6(e) and Figure 4.6(f) and (b) slice '*b*-*b*' of Figure 4.6(e) and Figure 4.6(f). The profiles compare the pure phase and the mixed phase-amplitude approximations. The circled regions show the edge overlap effect. 108

Figure 4.8. The shape of the pure phase term with odd symmetry about a material edge in a sample, the phase-amplitude interaction term with even symmetry about the edge in the sample and their difference which is asymmetric about the edge. 109

Figure 4.9. Phantom 2 simulation results: (a) Normal Attenuation Radiograph (b) Phase contrast radiograph with pure phase approximation (c) Phase contrast radiograph with phase-amplitude interaction. The object to detector distance R = 50cm. 110

Figure 4.10. Phantom 2 Simulation Results: (a) Phase image using pure phase approximation (b) Phase-amplitude interaction image (c) The phase image with phase-amplitude interaction which is the difference of (a) and (b) as given by Eq. 4.9. The object to detector distance R = 50cm. The images were normalized between zero and one. 110

Figure 4.11. The divergent section of the collimator with the lead discs. The gadolinium pinhole is shown in the blowup section. The diameter of the pinhole is 0.5mm. 112

Figure 4.12. Alignment of the gadolinium pinhole with the lead discs using laser. 113

Figure 4.13. Bare beam neutron image of the gadolinium pinhole taken using image plates. (a) The raw image as obtained by reading the image plate. (b) The image processed in the multi gauge software using the spike noise filter and the 9×9 median filter. The exposure time was 60 minutes at a 6m distance between pinhole and the detector. The size of the image plate is 20×25 cm^2. 114

Figure 4.14. The neutron energy spectrum at the 6m image plane using 12 inches of single crystal sapphire. 115

Figure 4.15. The sectional view of the final design of the pinhole collimator used for phase contrast neutron imaging. The material specifications are (1) aluminum tube (2) 5% borated polyethylene (3) lead (4) sapphire filter (5) SWX-277 (look in Chapter 2). 117

Figure 4.16. Geometry of imaging setup used to perform phase contrast neutron imaging. 118

Figure 4.17. Overlapped image of the bare beam taken at different distances from the source depicting rail misalignment. 118

Figure 4.18. Plot of beam center location against the distance on the rail (which has a fixed offset from the source). Position 0 indicates the misaligned position of the rail and Position 1 indicates the corrected position. 119

Figure 4.19. Photograph of Sample 1 (Stack of Aluminum Plates). 120

Figure 4.20. Image of the aluminum stack taken (a) at R = 8cm (b) at R = 200cm. The exposure time for both of them was 120 minutes at the 1MW reactor power. 121

Figure 4.21. A normalized intensity profile of the top edge of the aluminum with air for Sample 1 for both the radiographs shown in Figure 4.20. Image of the aluminum stack taken (a) at R = 8cm (b) at R = 200cm. The exposure time for both of them was 120 minutes at the 1MW reactor power. The intensity clearly indicates the phase contrast intensity variation at the aluminum edge. Both the shown profile has been averaged over 400 edges to reduce the fluctuation due to noise. 122

Figure 4.22. Photograph of the designed phantom with the different material marked (Sample 2). 123

Figure 4.23. Neutron radiograph (without post processing) of Sample 2 (designed phantom) for the object-to-detector distance (a) R = 3cm and (b) R = 250cm. 124

Figure 4.24. Neutron radiograph of Sample 2 (designed phantom) for the object-to-detector distance (a) R = 3cm and (b) R = 250cm. The image was de-noised using spike noise filter. 125

Figure 4.25. Neutron radiograph of Sample 2 (designed phantom) for the object-to-detector distance (a) R = 3cm and (b) R = 250cm. The image was de-noised using spike noise filter and 11×11 median filter. 126

Figure 4.26. Photograph of Sample 3. 128

Figure 4.27. Neutron radiograph of Sample 3 at (a) R = 2.5cm (b) R = 250cm and (c) R = 300cm. The image sizes are proportional to the magnification of the object at the image plane. The exposure time for each of the images was 45 minutes. 129

Figure 4.28. Photograph of (a) a Duracell battery (b) a BNC connector. 130

Figure 4.29. Neutron radiograph of a battery taken at (a) R = 2.5cm and (b) R = 250cm. The exposure times for both the radiographs were 45 minutes. 131

Figure 4.30. Neutron radiograph of a BNC connector taken at (a) R = 2.5cm and (b) R = 250cm. The exposure times for both the radiographs were 45 minutes. 132

Figure 4.31. The multiple pinhole geometries considered in the design of the mask. (a) A circular 9 hole geometry (Geometry 1) (b) A square 9 hole geometry (Geometry 2) (c) A circular 7 hole geometry (Geometry 3). All dimensions are in centimeters. 134

Figure 4.32. Schematic of the diverging conical section of the multi-pinhole collimator. 135

Figure 4.33. The common illumination area at the object plane for the pinholes arranged as shown in Fig. 4.31(a) (Geometry 1). All dimensions are in centimeters. 136

Figure 4.34. The common illumination area at the object plane for the pinholes arranged as shown in Fig. 4.31(b) (Geometry 2). All dimensions are in centimeters. 137

Figure 4.35. The common illumination area at the object plane for the pinholes arranged as shown in Fig. 4.31(c) (Geometry 3). All dimensions are in centimeters. 138

Figure 4.36. Schematic of the diverging beam cross-section at the image plane for Geometry 3 (shown in Figure 4.31(c)). All dimensions are in centimeters. 139

Figure 4.37. The multi-pinhole phase contrast neutron imaging collimator design. The materials as indicated in the figure are (1) aluminum (2) borated polyethylene (3) lead (4) sapphire filter (5) SWX-277. The gadolinium mask design with the pinhole pattern is also shown in the figure. 140

Figure 4.38. Photograph of the manufactured multi-pinhole collimator divergent section assembly. 141

Figure 4.39. Bare beam image taken on an image plate placed at the farthest image plane using the multi-pinhole collimator. The exposure time is 40 minutes at 1MW reactor power..... 142

Figure 4.40. Radiograph of an aluminum rod 2 inches in length 1cm in diameter taken using the multi-pinhole collimator. The object to image plane distance is 170cm. The exposure time was 120 minutes at the 1MW reactor power. 143

Figure 4.41. Normalized intensity profile along the edges (a) 'a-a' and (b) 'b-b' shown in Figure 4.40. 144

Figure 5.1. (a) The random multi-pinhole mask image at the image plane with 300 holes. (b) The raw image at the image plane with no noise obtained for a delta function. (c) The raw image at the image plane with no noise obtained for an inverted delta function. (d) The reconstructed delta function from Figure 5.1(b) using two-step least square de-convolution process ($\varepsilon = 2.81\times10^{-7} \pm 4.73\times10^{-24}$). (e) The reconstructed inverted delta function from Figure 5.1(c) using two-step least square de-convolution process ($\varepsilon = 3.84 \times 10^{-6} \pm 7.26 \times 10^{-22}$). All the images are in the grayscale with white being the maximum. 155

Figure 5.2. The raw image of the delta function with additive white noise (a) with 0.05 standard deviation (b) 0.2 standard deviation (c) 0.5 standard deviation and (d) 1.0 standard deviation. All the images have same grayscale. 157

Figure 5.3. The reconstructed delta function using two-step least square de-convolution technique from the noisy raw images shown in (a) Figure 5.2(a) (b) Figure 5.2(b) (c) Figure 5.2(c) and (d) Figure 5.2(d). The error values of the reconstructed images from (a) to (d) are 0.121 ± 0.003, 0.484 ± 0.015, 1.254 ± 0.029 and 2.508 ± 0.059 respectively..... 158

Figure 5.4. The reconstructed delta function using two-step regularized least square de-convolution technique at their respective optimum scale parameters from the noisy raw images shown in (a) Figure

5.2(a) (b) Figure 5.2(b) (c) Figure 5.2(c) and (d) Figure 5.2(d). Error values of the reconstructed images from (a) to (d) are 0.122 ± 0.004 ($\alpha_1 = 0$, $\alpha_2 = 0.06$), 0.400 ± 0.010 ($\alpha_1 = 0$, $\alpha_2 = 0.15$), 0.680 ± 0.012 ($\alpha_1 = 0.1$, $\alpha_2 = 0.9$) and 0.845 ± 0.011 ($\alpha_1 = 0.4$, $\alpha_2 = 1.4$) respectively. 160

Figure 5.5. The surface plots depicting the variation of the error with the change in the scale parameter α_1 and α_2 in the two-step regularized least square de-convolution of the images shown in (a) Figure 5.2(a) (b) Figure 5.2(b) (c) Figure 5.2(c) and (d) Figure 5.2(d). 161

Figure 5.6. The bar chart comparing the error values obtained in the reconstructed images using two step regularized de-convolution at optimum scale parameter values and different de-noising techniques 163

Figure 5.7. (a) Ideal image of the object. (b) Image of the pinhole mask at the image plane (c) The noisy raw image data at the image plane. 165

Figure 5.8. Reconstruction of the raw data shown in Figure 5.7(c) using (a) two-step least square de-convolution ($\varepsilon = 5.061 \pm 0.022$) (b) two-step regularized least square de-convolution ($\alpha_1 = 0.2$, $\alpha_2 = 1.7$, $\varepsilon = 1.666 \pm 0.003$) (c) two-step regularized de-convolution followed by adaptive Wiener filtering ($\alpha_1 = 0.1$, $\alpha_2 = 0.3$, $\varepsilon = 1.222 \pm 0.003$). 165

Figure 5.9. The MCNP model of the imaging system used to simulate the multi-pinhole images. The blow up of the Sections A is shown in Figure 5.10. 166

Figure 5.10. The collimator model used to perform simulation of system images. It can be compared with the designed collimator shown in Figure 4.37. The materials as indicated in the figure are (1) aluminum (2) borated polyethylene (3) lead (4) sapphire filter (5) SWX-277. 166

Figure 5.11. The simulated system PSF obtained using radiation transport calculations. The distance between the multi-pinhole mask and the object pinhole is 4m and the distance between the object and the image plane is 1m. The image plane grid resolution is 50μm. The image is normalized between 0 and 1. 168

Figure 5.12. The reconstruction of the image shown in Figure 5.11 using conjugate gradient iterative least square with no regularization. The pixel size is 50μm. The source mask image for the reconstruction was calculated using known parameters $b/a = 0.25$, $\gamma = 30^o$ and the source mask pinhole diameter of 0.5mm. 169

Figure 5.13. The reconstruction of the image shown in Figure 5.11 using conjugate gradient iterative least square with no regularization. The pixel size is 50μm. The source mask image for the reconstruction was calculated using estimated parameters $b/a = 0.243$, $\gamma = 29.99^o$ and the known source mask pinhole diameter of 0.5mm. 171

Figure 5.14. The simulated image of a black object with a central hole of 0.5mm diameter. The distance between the multi-pinhole mask and the object pinhole is 4m and the distance between the object and the

image plane is 1m. The image plane grid resolution is 50μm. The image is normalized between 0 and 1. 172

Figure 5.15. The reconstruction of the image shown in Figure 5.14 using conjugate gradient iterative least square with no regularization. The SPSF for the reconstruction was calculated using estimated values from Figure 5.11. The pixel size is 50μm. 173

Figure 5.16. The reconstruction of the image shown in Figure 5.14 using conjugate gradient iterative least square with no regularization. The SPSF for the reconstruction was calculated using Figure 5.14. The pixel size is 50 μm. 174

Figure 5.17. The reconstruction of the image shown in Figure 5.14 using conjugate gradient iterative least square with no regularization. The SPSF for the reconstruction was calculated using Figure 5.14 with the effect of the non-zero diameter of the source mask pinholes removed. The pixel size is 50μm. 175

Figure 5.18. The cadmium sample used to perform MCNP simulation. 176

Figure 5.19. The simulated image of 1mm thick cadmium square with a rectangular hole in it. The distance between the multi-pinhole mask and the object pinhole is 4m and the distance between the object and the image plane is 1m. The image is normalized between 0 and 1. (a) The image plane grid resolution is 50μm. (b) The image plane grid resolution is 50μm but every 4th row and column from Figure 5.19(a) is selected. 176

Figure 5.20. Reconstruction of the image shown in Figure 5.19(b) using conjugate gradient iterative least square with no regularization. The SPSF for the reconstruction was calculated using (a) ideal parameter values of $b/a = 0.25$, $\gamma = 30^o$, (b) parameters estimated using Figure 5.14 ($b/a = 0.249$, $\overline{\gamma} = 30.25^o$) (c) $b/a = 0.245$, $\gamma = 30^o$ (d) $b/a = 0.25$, $\overline{\gamma} = 31^o$ with the effect of the non-zero diameter of the source mask pinholes removed. 178

Figure 5.21. The system point spread function (SPSF) obtained using the multi-pinhole collimator. The distance between the pinhole and the detector was 130cm. The exposure time was 60 minutes at 1 MW reactor power. The image has been normalized between 0 and 1. 179

Figure 5.22. De-noised SPSF using (a) 7×7 Median filtering. (b) 7×7 Wiener filtering (c) soft thresholding of Symlet (of order 4) coefficients using a threshold of 0.3906. The SNR for these images are 21.98, 22.95, and 18.41 respectively. 180

Figure 5.23. Reconstruction of the image shown in Figure 5.22(b) using conjugate gradient iterative least square with no regularization. The SPSF for the reconstruction was calculated using parameter values of $b/a = 0.237$, $\gamma = 14.5^o$. 182

Figure 5.24. Raw image for the gadolinium foil with three pinholes after 7×7 Wiener filtering. 182

Figure 5.25. The reconstruction of the image shown in Figure 5.24 using the SPSF estimated using Figure 5.22(b). 182

Figure 5.26. The reconstructed image of the aluminum rod from the multi-pinhole image shown in Figure 4.40. 183

LIST OF TABLES

Table 1.1. Performance parameters of different neutron detection systems for imaging purposes under the condition at the radiography station NEUTRA at PSI [17]. 10

Table 2.1. Final parameters of the designed neutron imaging facility. 40

Table 2.2 Grades of single crystal sapphire [47]. 43

Table 2.3 Measured beam parameters according to ASTM (E-545) standard. The 3rd column has parameters calculated using an IP image even though it is not prescribed by the ASTM. 56

Table 3.1 The list of various facilities where phase contrast neutron imaging has been performed. 62

Table 4.1 The material composition of the phantoms used in the simulations. 104

Table 4.2 The coherent scattering length densities of materials in Sample 2. 127

CHAPTER 1

INTRODUCTION

Radiation imaging has been a well known technique for non-destructive testing (NDT) and non-invasive measurements (NIM) of materials. Almost all different kinds of radiations like photons, gamma rays, X-rays, electrons, neutrons, micro waves, radio waves etc. are used for obtaining multitude of information about an object non-destructively, by performing a transmission or reflection imaging of it. The use of these different kinds of radiation particles is associated with certain advantages and limitations. Therefore, depending upon the type of sample and the objective of imaging exercise, the suitability of the type of imaging can be decided. In the present case the focus is on imaging with neutrons. Specifically, non-interferometric phase contrast imaging was investigated in this work.

In the present Chapter an introduction to neutron imaging is being presented. This includes its usefulness as a radiation imaging technique, the process of image formation, the detection systems used, the different neutron imaging techniques and the process of image degradation. Finally, the purpose and motivation of the present work will be outlined in the last Section of this Chapter.

1.1 Introduction to Neutron Imaging

Neutron imaging is one of the radiation imaging techniques used for NDT/NIM of materials. Usually transmission imaging is performed using neutrons because neutrons (being neutral particles) can penetrate the object even when they are at thermal energies. Thus, in this case the image obtained by the transmitted neutron beam through the object represents the two dimensional variation of the neutron attenuation characteristics of the object averaged over the thickness of the object. Therefore, in neutron imaging the interior of the object is also depicted unlike the usual visible light imaging. Moreover, neutron attenuation characteristics being very

different than X-ray or gamma-ray attenuation characteristics for any object, results into an image formed that depicts different information about the object.

1.1.1 History and Trends

Radiography with neutrons began shortly after the discovery of neutrons in 1932 by James Chadwick. The initial experiments in neutron radiography were performed in Germany in the late 1930's by H. Kallmann and E. Khun [1]. In the years 1935 to 1938 H. Kallmann and Khun used Radium-Beryllium (Ra-Be) sources and a small neutron generator at the research laboratory of the I.G. Farben Aktiengesellschaft to develop methods of photographic detection of neutrons. The findings of the study by Kallmann and Khun got published several years after the work was finished and reported in several patents conclusively showing the potential of neutron radiography. However, the available neutron intensities were insufficient for practical industrial neutron radiography, and it was not until after the work of Fermi and co-workers on the thermal neutron reactor that, in 1955, the first neutron radiographs were taken using a reactor beam (8 MW BEPO reactor at Harwell) [2]. In 1960s and 70s the popularity of neutron radiography increased at other places with the help of people like J. P. Barton, Harold Watts, Dan Polanski, Harold Berger etc. It got further momentum with the formation of the Neutron Radiography Working Group (NRWG) in 1979 which lead to a coordinated effort and promulgation of knowledge in a systematic manner within the community [3]. In 1981, the First World Conference on Neutron Radiography was held in San Diego, California, USA. The formalization of this existing worldwide community of scientists into the International Society of Neutron Radiology (ISNR) started in 1992 [4].

In the last two decades the activities in this field has risen with the development of new digital detection systems like digital image plates, scintillation screens and charged coupled device (CCD) systems, micro channel plates (MCPs) etc. Further, many new high performance facilities have been constructed on high intensity neutron sources which has lead to increased research activities in this field. This resulted in the demonstration of multiple new imaging techniques like non-interferometric phase contrast imaging, energy selective neutron imaging, Bragg edge imaging etc. which are being developed further in order to make them applicable for practical NDT/NIM of materials.

1.1.2 Neutron vs. X-ray Imaging

Often neutron imaging is considered as being complimentary to X-ray or gamma-ray imaging. Figure 1.1 presents a comparison between neutron and X-ray attenuation for different elements [5]. From the figure it can be clearly observed that the neutron attenuation and hence its cross section does not follow a particular trend with the atomic number (Z) of the elements.

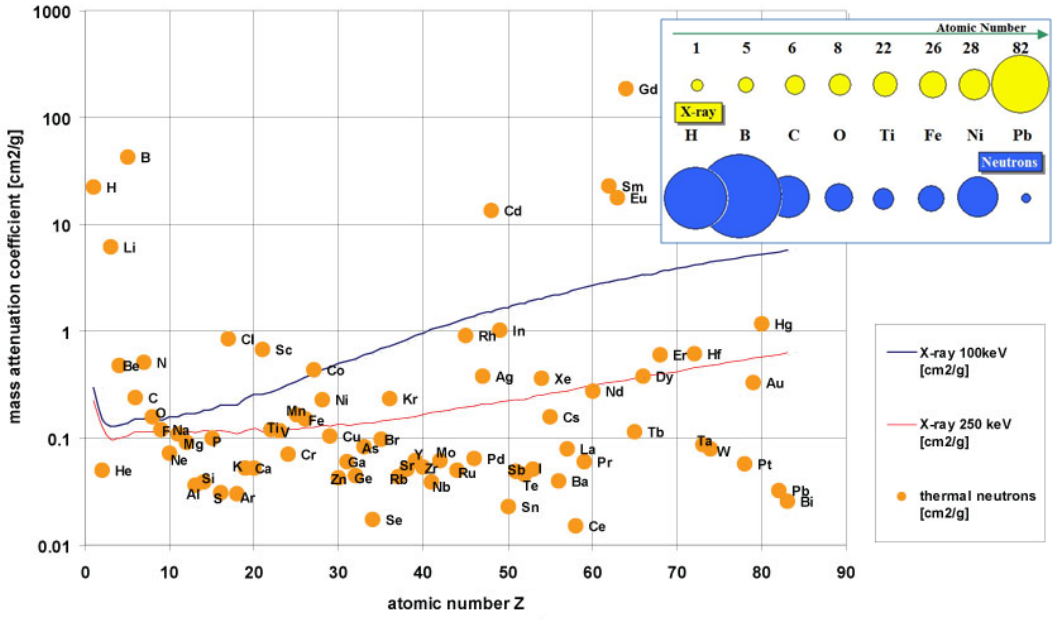

Figure 1.1. A comparison between neutron and X-ray attenuation coefficients [5].

Neutrons being neutral particles are not affected by the electromagnetic field of the electrons surrounding the nucleus of the atom. Instead they interact with the atomic nucleus of the material and therefore, the nuclear structure and energy levels play a role in deciding the amount and type of interaction. Due to this it is possible with neutrons to see light (low 'Z') materials in a specimen and also it is easier to distinguish high 'Z' materials even if the atomic number is not sufficiently different. Moreover, isotopic differentiation is also possible with neutron imaging. Examples of high neutron cross-section materials include hydrogen, boron, cadmium, gadolinium etc. while iron, aluminum, lead etc. have lower neutron cross-sections. Thus, the components in an object made up of low 'Z' materials especially hydrogenous

compounds like different kind of polymers, organic materials etc. can provide higher contrast in the neutron image. As an example, the neutron and X-ray radiograph of a computer floppy disk is shown in Figure 1.2 [6]. The neutron radiograph clearly depicts the polymeric components of the floppy disk where as X-ray provides more contrast for the metallic components. This is a good visual description indicating the complementary nature of the neutron and X-ray imaging. This complimentary nature can be utilized fruitfully in the NDT of various objects to a large degree.

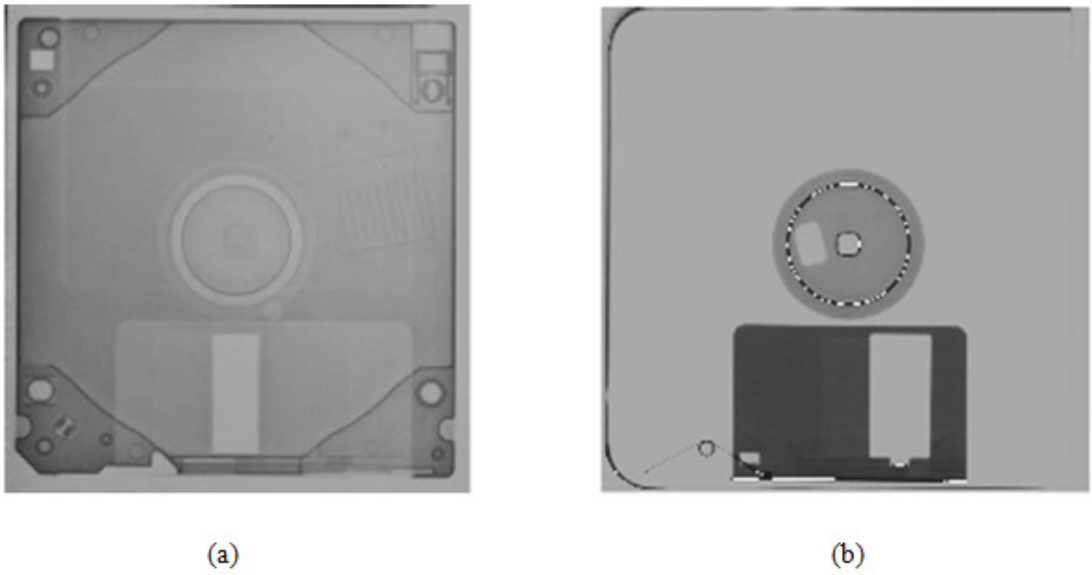

Figure 1.2. Radiograph of a computer floppy disk (a) using neutrons depicting the polymeric low 'Z' components clearly, (b) using X-rays depicting metallic components clearly [6].

Another advantage associated with neutron imaging is the ability to use contrast agents to increase the image contrast thereby making the NDT more reliable. Materials like boron and gadolinium have such a high neutron absorption cross-section for thermal and cold neutrons that even a thin layer of them (~10μm) is sufficient enough to attenuate the neutrons significantly producing sufficient contrast in the image. These materials can be used as contrasting agents to enhance the contrast of the edges formed by cracks, delaminations, voids etc. These kind of contrasting agents do not exist for X-ray or gamma ray imaging as their attenuation in the material increases gradually. Thus, with neutron imaging with the use of contrast agents it

becomes possible to locate the defects which may not become visible in the regular neutron or X-ray image.

But despite the advantages which neutron imaging offers over photons (γ- and X-rays) it also has some difficulties associated with it. The first difficulty associated with neutron imaging is the limited availability of high flux neutron sources for such applications. Also, often the neutron beam obtained from such sources is contaminated with gamma rays. In the case of photons the sources can be obtained or manufactured (X-rays) easily with required flux and are also not very expensive. In the case of neutrons the available sources can be divided into three types: [7]

- Reactor source
- Accelerator-based sources
- Radioactive sources

Cost wise, these sources (except radioactive sources which have the least neutron flux comparatively) are significantly more expensive than photon sources. Also, the physical size of these sources is much larger than the same flux or even a much higher flux gamma ray or X-ray source. Thus, portability of such sources is less.

Other problem associated with neutron source is "*thermalization*" of the neutron beam. Neutrons are mainly categorized based on their energy into five categories [7]:

- Cold Neutrons (below 0.01 eV)
- Thermal Neutrons (0.01 to 0.3 eV)
- Epithermal Neutrons (0.3 to 10,000 eV)
- Fast Neutrons (10 keV to 20 MeV)
- Relativistic Neutrons (> 20 MeV)

Neutron imaging is performed mainly in the thermal and cold region due to the large cross section for attenuation and detection in this energy range. Advantages of neutron imaging mentioned above are applicable for thermal and cold neutron beams. Therefore, fast neutrons generated from the source must be moderated (lowered in energy) by some means. Usually hydrogenous material (e.g., water) or graphite is used for this purpose. But this tends to increase the size of the sources and hence decrease their portability further.

The third difficulty associated with it arises from one of its advantages only, i.e. to be able to image hydrogen contain materials. Cold and thermal neutrons that are often used for performing imaging have very high scattering cross-section for hydrogen. Although this helps in detecting presence of hydrogen in the sample, it does not take a lot of it to saturate the image. Therefore, differentiation between different hydrogenous materials may not be possible even when the samples are reasonably thin. Moreover, other features of the sample may get overshadowed by the very high contrast produced by hydrogen in the sample. Similarly, some other materials like cadmium, boron, gadolinium etc., due to their high absorption cross section, can also be traced using neutrons if present in very small quantities but, their presence in somewhat larger quantities can easily stop the neutron from penetrating the sample leading to a loss of contrast available for other materials present in the object.

The fourth difficulty associated with neutron imaging is related with the detection technique. In the case of photons the image can be directly taken on a film. But neutrons will not form image directly on a film. Hence, some mechanism is required which converts the neutron signal into a detectable secondary radiation signal without adding much noise or without reducing the signal strength appreciably. For this purpose a converter screen (intensifying screen) is used which in principle absorbs the neutrons and emits photons or electrons to which the image recorder is sensitive. This extra process makes the detection efficiency of neutron less than the gamma rays for similar detectors and also adds to the image unsharpness. Further, it requires the beam to have high neutron-to-gamma (N/G) ratio as the gamma rays will also get detected on the detector with an equal or lesser efficiency depending upon the type of detector being used.

Another problem with neutron imaging is the radiation dose and shielding concerns

associated with the neutrons. The quality factor for neutrons is 20 times more than that of photons [8]. Therefore, neutrons are potentially more damaging to human tissue than photons. Moreover, the presence of sufficient number of fast neutrons in the neutron beam even after the process of thermalization and filtering can make the shielding problem more difficult to handle than photons. The thickness of the shielding can be as large as a three to four feet consisting of stacks of various neutron and photon attenuating materials. When there is a constraint on the available beam-line space then a good design of shielding fulfilling the dose requirements while taking as little a space as possible can be an elaborate problem.

But there are some applications where neutron imaging is the only feasible option for the NDT. One example is the inspection of radioactive materials, a problem which is becoming more prevalent in this nuclear age. The radioactivity of the inspection sample can present problems for conventional radiographic methods because the X-ray films are fogged by the radioactive decay radiation from the sample. For this a special neutron radiographic technique, called the transfer detection method can be used [7]. Additional types of applications become obvious when one appreciates that significant neutron-attenuation differences often occur between isotopes of the same element [9]. Useful neutron radiographic work in this area has included differentiation between Cd^{113} and other cadmium isotopes in an irradiated reactor control element [10] and between isotopes of uranium. Also, the difference between neutron cross-section of hydrogen and deuterium is used to establish the contrast matching concentration in biological analysis of tissues. There are various other applications like imaging of fuel cells, biological materials, reactor fuel rod cladding, plant tissues etc. where neutron imaging has been used to perform NDT/NIM of low 'Z' materials which do not produce enough contrast with X-rays [11]-[14].

1.1.3 Image Formation Process

Figure 1.3 depicts the schematic of the image formation process in conventional transmission neutron imaging. In the figure (η,ζ), (u,v) .and (x,y) are reference co-ordinate systems at the collimator, the object and the image plane respectively. The quantities, $\phi(\eta,\zeta)$ and $\phi_t(u,v)$ denote the neutron flux profile at the collimator plane and the object plane

respectively whereas $\psi_t(x,y)$ denotes the secondary radiation profile at the image plane induced by the neutrons on the converter material. Characteristics of the neutrons being emitted by the neutron source are modified in the collimator in order to meet the desired qualities in terms of its energy spectrum, directional properties and N/G ratio while maintaining sufficient neutron flux intensity at the image plane. These qualities of the neutron beam are achieved by proper design of different elements of the collimator like beam filters, aperture, divergence angle etc. Neutrons with these desired properties being emitted through the collimator get attenuated in the sample. The attenuated neutron beam falls on the convertor screen which emits secondary radiation proportional to the neutron intensity. This secondary radiation is capable of producing an image on the recorder which could be a photographic film in some practical applications.

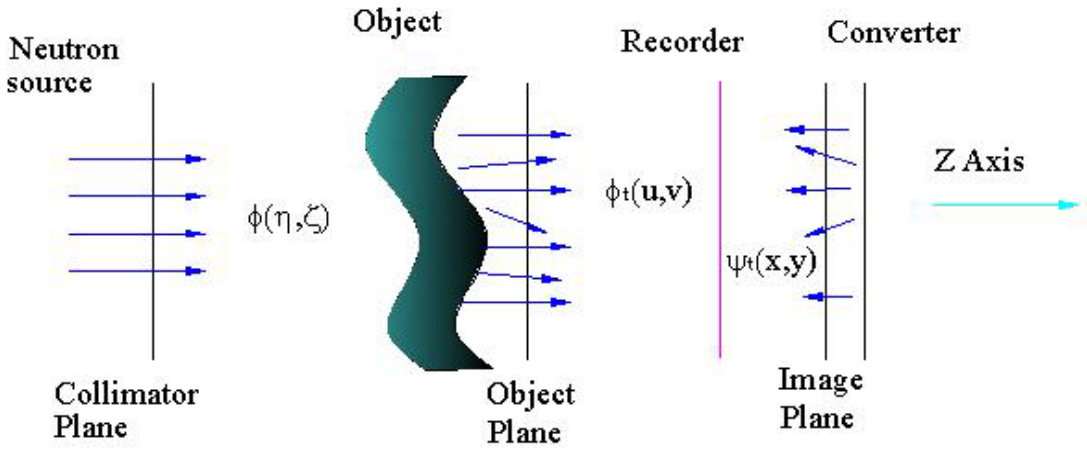

Figure 1.3. Schematic depicting the image formation process in conventional neutron imaging.

The whole image formation process can be illustrated by the sequence of physical transformations shown in Eq. (1.1). In the equation, $D(x,y)$ represents the optical density or the gray scale density distribution that develops on the recorder (photographic film or digital media) when it is exposed to the secondary radiation $\psi_t(x,y,t)$.

$$\phi(\eta,\zeta) \rightarrow \phi_t(u,v) \rightarrow \psi(x,y) \rightarrow D(x,y) \tag{1.1}$$

1.1.4 Detection Systems for Neutron Imaging

Various different kinds of detector systems (convertor + recorder system) are available with different characteristics to record the neutron image. Some of the available choices are photographic films with an intensifying screen, track etch detectors, digital image plates, scintillation screens with CCD, micro channel plates, silicon flat panel screens, Thompson tubes etc. Traditionally, photographic films with intensifying screens have been used as the detector for neutron imaging. There are three basic types of intensifying screens available to be used with films - granular or crystalline, glass, and foil, in order of increasing resolution and decreasing speed (sensitivity to neutrons (explained later in detail)). In the past, some of the exclusively used screens in these categories for practical work are NE 421- granular, NE 905- glass, Gadolinium (Gd) - foil, Dysprosium - foil [15]. Even currently, for routine NDT applications films with Gd intensifying screens are the choice for the recording media. American Society of Testing and Materials (ASTM) has defined standards for performing neutron imaging for only film detection system [16]. This is because, film still has higher spatial resolution than most of the other options available even though it is one of the oldest and simple to use detection methods. Moreover, film detectors can be made in large sizes to image large samples. Table 1.1 compares the performance characteristics of some of the available detection systems under the conditions at NEUTRA facility [17]. From the table it can be clearly observed that film has a spatial resolution range between ~20μm to ~50μm. The only other detector which compares with the film are the track etch foils made up of dielectrics like glass, mica, plastics etc. where, the tracks caused in them by the radiation damage are chemically etched in a preferential manner so that the tracks become visible. A collection of many tracks form the visual image of the object. The drawbacks associated with the film detection system are the small dynamic range, no time resolution and high gamma sensitivity. Other detection systems like digital image plates, scintillation screens etc. have been developed in the last two decades which perform better than the film system in terms of these characteristics.

The dynamic range of the detector is related to the characteristic curve of the detection system. A characteristic curve is the relationship between the exposure $E(x,y)$ and the optical

Table 1.1. Performance parameters of different neutron detection systems for imaging purposes under the condition at the radiography station NEUTRA at PSI [17].

Detector System	X-ray film and Transmission light scanner	Scintillator + CCD camera	Imaging Plates	Amorphous Silicon Flat Panel	CMOS pixel detector
Max. spatial resolution (μm)	20-50	100-500	25-100	127-750	200
Typical exposure time for suitable image	5 min.	10 sec.	20 sec.	1-10 sec.	0.1-50 sec.
Detector Area (typical)	18cm × 24cm	25cm × 25cm	20cm ×40cm	30cm × 40cm	3.5cm × 8cm
Number of pixels per line	4000	1000	6000	1750	400
Dynamic Range	10^2 (Non-linear)	10^5 (Linear)	10^5 (Linear)	10^3 (Non-linear)	10^5 (Linear)
Digital format	8 bit	16 bit	16 bit	12 bit	16 bit
Readout time	20 min.	2-100 sec.	5 min.	0.03-1 sec.	0.2 sec.

density $D(x,y)$, where, the exposure $E(x,y)$ of the recorder at an arbitrary point (x,y) on the image plane is defined as the integration of the secondary radiation flux $\psi_t(x,y,t)$ (considering ψ_t as time dependent) over exposure time τ_E. The characteristic curve shape depends upon the type of the recorder, the exposure time τ_E, the type of secondary radiation emitted by the converter and the development method (for films) or the readout method (for electronic sensors) of the recorder. A sample characteristic curve depicting all the important parameters associated with it is shown in Figure 1.4 [18]. The linearity in the characteristic curve over the wide range of the exposure is a highly desired feature in the recorder. The range of exposure over which the curve is linear is called the *latitude* of the recorder. The range of optical density variation which is produced in the *latitude* is called the *dynamic range* of the recorder. In the case of digital detection the dynamic range can also be specified by the number of gray levels which is used. The recorder should be used in this range to get the optical density

which is directly proportional to the amount of exposure or else the precise characteristic curve should be known. But in no situation it should be allowed to saturate, because after that optical density becomes constant and hence no differentiation can be achieved between different exposures of the recorder due to varying neutron attenuation in the different regions of the sample.

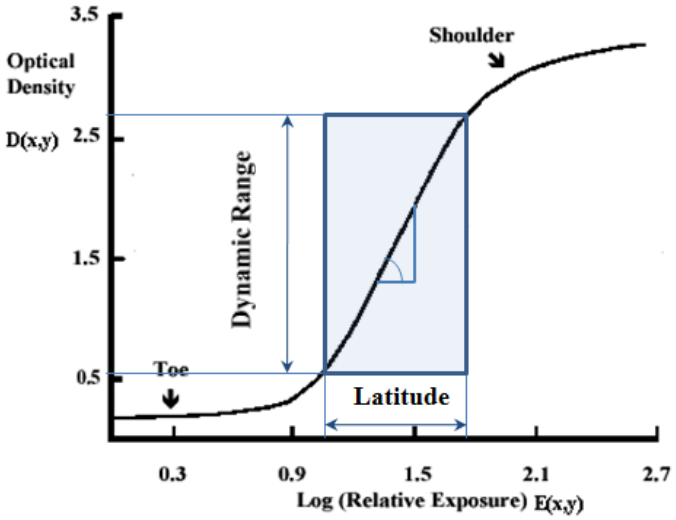

Figure 1.4. A characteristic curve depicting important parameters associated with it [18].

For most of the digital detection systems the dynamic range is larger than that of films. For digital image plates and scintillation screen with CCD system the dynamic range is more than 100 times larger than the film (refer to Table 1.1) [17]. Further, the linearity within this range is also greater for these detection systems than that of film. Thus, in the case of film the exposure time should be carefully selected in order to keep the film response within the dynamic range which is not much of a problem for the digital detection techniques.

The time resolution of the detection system is defined as the minimum time required by the detection system to generate a neutron image with acceptable optical density. This dictates the frequency of motion of a dynamic sample which can be captured by the detector unambiguously. The efficiency of the detection system is one of the important factors affecting

the time resolution of the detection system. The efficiency of the detection system is dictated by the conversion screen material, its thickness and the neutron energy spectrum. The screen efficiency $\varepsilon(E)$ can be defined by

$$\varepsilon(E) = \int_0^t \exp\{-\Sigma(E)x\}\Sigma(E)R(x)dx \tag{1.2}$$

where, t is the thickness of the screen, $\Sigma(E)$ is the energy dependent macroscopic neutron absorption cross-section of the screen material and $R(x)$ describes the attenuation of the secondary radiation in the screen material. If the neutron energy spectrum is known then the average efficiency ε_{avg} can be calculated as

$$\varepsilon_{avg} = \frac{\int_0^{E_{\max}} \varepsilon(E)\phi(E)dE}{\int_0^{E_{\max}} \phi(E)dE} \tag{1.3}$$

where, $\phi(E)$ is the neutron flux energy spectrum and $E_{\max}$ is the maximum neutron energy in the energy spectrum. It can be easily observed that to obtain the higher neutron conversion efficiency the conversion screen should have high macroscopic absorption cross-section with an optimum thickness to absorb most of the neutrons. The thickness is limited by the attenuation of the secondary radiation produced due to absorption of neutrons, which is not desirable. High efficiency is a key in decreasing the exposure time required by the detector thereby improving the time resolution.

Other important parameter affecting the time resolution is the sensitivity or the *speed* of the recorder to the secondary radiation. It is defined by the slope of the characteristics curve in the linear range (latitude). The higher the slope, the more the detector sensitivity is to the secondary radiation generated by the neutrons when they fall on the intensifying screen. The sensitivity affects the time resolution by defining the exposure time required to obtain required optical/gray scale density on the recorder. When the sensitivity is high the number of neutrons

required per pixel to obtain the desired gray scale density on the recorder is less. This helps in decreasing the exposure time for a fixed neutron flux and average efficiency. It also helps in performing neutron imaging with low neutron fluxes without making the exposure time too long. This makes high sensitivity detectors very desirable for performing some imaging exercises like real-time neutron imaging, phase contrast neutron imaging etc. But, the images obtained with the high sensitivity detectors tend to have more noise in them because the detector captures the random fluctuations in the neutron beam. Because of the high time resolution of the detector the random fluctuations get less time to average out over time. Therefore, usually as the detector speed increases the spatial resolution decreases.

Most of the neutron detectors used for neutron imaging are also sensitive to gamma rays. The sensitivity varies with the type of detector being used. The detection system consisting of high 'Z' elements like gadolinium (Z = 64), barium (Z = 56) etc. are more sensitive to gamma rays because of their higher interaction probabilities with the gamma rays. Photographic film with different intensifying screens possess different sensitivity to gamma rays. The gadolinium foil provides the worst γ-ray rejection among the four convertor screens mentioned before, namely – NE 421 granular, NE 905 glass, Gd - foil and dysprosium - foil [15]. The gamma rejection values for NE 421 granular (thickness 0.65mm), NE 905 glass (thickness 1.3mm), Gd foil (thickness 0.025mm) and dysprosium foil (thickness 0.1mm) as quoted by Hawkesworth [15] for a thermal neutron energy spectrum are 27, 6.6, 1.3 and infinity respectively. Here, the numbers indicate photons per neutron taken arbitrarily to be that which gives gamma ray induced density of 10% of the neutron induced density. The thicknesses mentioned are the thicknesses of the intensifying screens used in practical applications. NE421 and NE905 have much better gamma rejection than the Gd foil because of their lower effective 'Z' than the Gd. In the case of dysprosium, even if it has higher atomic number than gadolinium its gamma sensitivity is quoted as zero as it is used in the *transfer* radiography, where only the conversion screen is placed in the direct neutron beam and the recorder is exposed afterwards using the radioactive image formed on the conversion screen. The neutron sensitive digital image plates also have significant gamma sensitivity as they consist of Gd_2O_3 as the conversion material and BaFBr:Eu^{2+} as the storage phosphor. But, because of their higher time resolution less exposure time is required and therefore, the effect of the gamma noise on the image is much less than that

of the film detection system. They have higher time resolution because of less attenuation of the secondary radiation (which is conversion electrons) before being trapped in the storage phosphor. Moreover, they have lower spatial resolution which increases their speed by providing larger number of neutrons per pixel thereby reducing the exposure time. But, in high gamma content beam even the image plates will not perform satisfactorily. It has been studied that for Fuji's BAS-IP ND-2025 (which are often used image plates) a gamma dose rate of 1μS/h is equivalent to a neutron flux of about 1.2n/cm^2.sec [19]. To enhance the gamma rejection capability of the neutron IPs alternative conversion materials like Li^{6}F with storage phosphor like KCl:Eu^{2+} and KBr:Eu^{2+} have been proposed [19]. But, this leads to an increase in the thickness of the recording layer of the IPs and a decrease in their spatial resolution. Even with this tradeoff under unavoidable conditions of high gamma background the high gamma rejection capability may be a desirable characteristic.

This makes the ratio of neutron to gamma sensitivity an important property to be considered in selecting the detector type. If this ratio is not sufficiently high then care should be taken in the design of the collimator to maximize the N/G ratio thereby minimizing the gamma exposure of the detector while taking the images. That is why for the use of photographic film as the imaging medium the N/G ratio of the beam should be kept considerably large. For this reason N/G ratio is one of the parameters in defining the beam quality using ASTM standards. But, in some imaging modalities like pinhole imaging, phase contrast imaging where pinhole neutron sources are desired, maintaining a large N/G ratio can turn out to be challenging. In such circumstances detectors with high neutron to gamma sensitivity that are less affected by the gamma rays during their exposure like digital image plates can be used to perform imaging.

1.1.5 Image Degradation Sources

In the previous Sections the process of image formation and the detection system characteristics were presented. The spatial and time resolution characteristics of the different detection system were outlined in that context. A closely related concept to the process of image formation and the detection systems is the image degradation. This is also directly related to the resolution of the images obtained which can be different from the resolution of the

detection system. Also, it relates to the visual image quality of the obtained radiograph which is mostly degraded by the noise sources.

The image formed using the process of neutron imaging is degraded due to multiple sources of degradation involved in the formation process which are dependent on the system geometry during the imaging exercise, the object characteristics, and the detection system characteristics. The sources of degradation can be broadly classified into two categories namely: the Blurring Sources and the Noise Sources. The blurring sources contribute to the point spread function (PSF) of the system making its spread larger, thereby blurring the image that results into unsharp edges. The PSF of the imaging system is the image of a point object taken with the system. This is also sometimes referred to as the Impulse Response of the system. Usually, the measurement of the system PSF (independent of the object being imaged) is performed by imaging of a pinhole that is materialized using neutron absorbing materials like cadmium or gadolinium with a small hole in it. A typical intensity profile of such a radiograph is shown in Figure 1.5(a). To quantify the spatial resolution of the system the full width at the half maximum (FWHM) of the intensity profile going through the center of the PSF, as shown in Figure 1.5(b), is taken most of the time [20]. This indicates the resolution of the system for an ideal neutron absorbing object. For other kind of objects that scatter neutrons the resolution will be worse than this. Sometimes, instead of measuring the PSF, an edge spread function (ESF) is measured using a sharp edge, again made up of a neutron absorbing material. The profile of an edge spread function looks like an edge function with some spread. That curve is then differentiated in order to obtain the line spread function (LSF) profile that looks similar to the profile shown in Figure 1.5(b). FWHM can be calculated from the LSF can be also used to define system resolution. The LSF is basically a PSF integrated over a line. Therefore, the spatial resolution obtained from the FWHM measurement of the LSF is a little larger than the PSF FWHM ideally. But, since in experiments, pinholes used to measure PSF always have non-zero diameter so the difference between spatial resolutions obtained using PSF and LSF may not be significant enough to observe.

Sometimes curve fitting approach is followed in order to obtain an empirical function of the ESF and the LSF profile and from that FWHM is calculated. The ESF is usually modeled

by an inverse tangent function with additive and multiplicative parameters for scaling and shifting of the function. Different functional forms which can be used to model LSF/PSF are shown in Figure 1.6. Often either Lorentzian or a Gaussian function with scale and shift parameters are used as the exponential function is not smooth at the maximum [21]. Various different sources that contribute to the spread of PSF or the blurring are geometric, recorder, converter and the motion of the sample relative to the system.

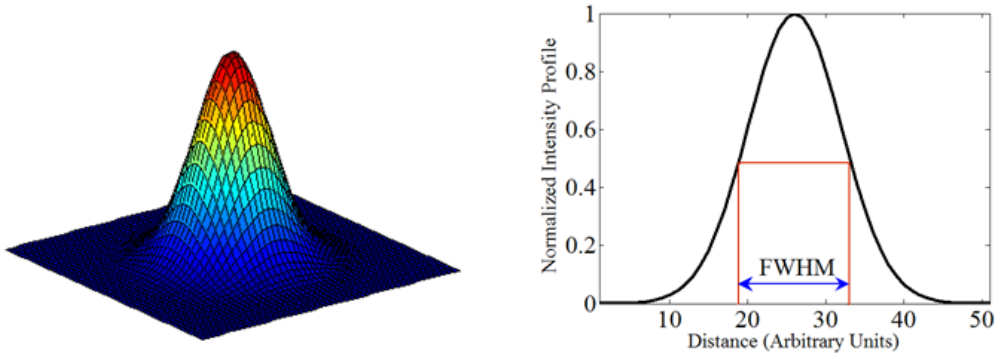

Figure 1.5. (a) Generic shape of a PSF. (b) The normalized intensity profile of the PSF taken through its center with the depicted full width at half maximum (FWHM).

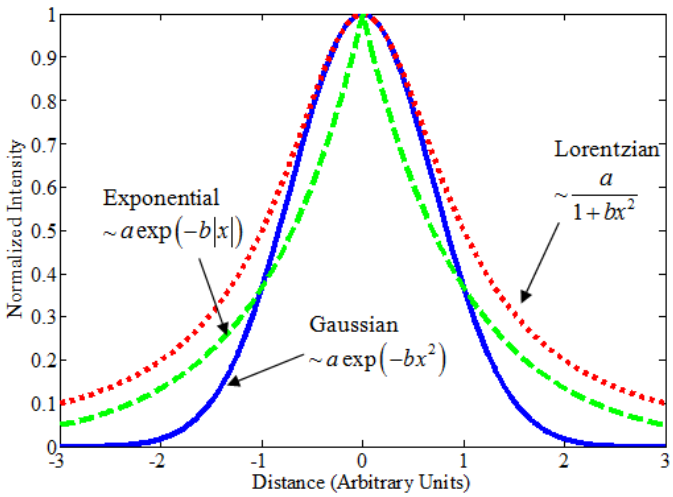

Figure 1.6. Different functional forms that can be used to model LSF and PSF.

The geometric blurring takes place due to the spread of the neutron source and depends upon the sample-to-detector distance R as well as the L/d ratio of the system where L is the source-to-sample distance and d is the effective diameter of the neutron aperture which decides the source size being observed by the object. The blur increases with increasing R and decreasing L/d .ratio. Therefore, lower beam divergence or larger L/d ratio is always desirable. Also, often the sample is either kept in contact with the film or very close to it in order to minimize the geometric unsharpness in the image. Still, for bigger samples the regions far from the image plane can have significantly greater geometric blurring than the regions close to the image plane. In such situation either the L/d ratio of the system should be increased or image post processing may be performed to de-blur those regions selectively. There are some techniques where sharp images are produced even when the distance R is large. The sharpness comes from very high L/d ratio in such systems and is also related to one of the alternative contrast enhancement mechanisms demonstrated using neutrons recently- the phase contrast mechanism.

Recorder and convertor unsharpness pertains to the detection system being used. For the film system it depends on the size of the silver halide particles, the distance between the convertor and the recorder and the thickness of the convertor. For digital image plates, along with these factors, the size of each pixel as well as the spread of the laser beam which reads the image plate also contributes to the unsharpness. Similarly, for scintillation screen and CCD systems the pixel size of the CCD as well as inaccuracy in the optics will be the additional factors contributing to the unsharpness of the image. The motion unsharpness is present only when there is a relative motion between the sample, the source and the detector. This can happen due to unnecessary vibrations present from some sources or due to motion of the sample in case of real-time imaging. To remove the unsharpness from the image various de-blurring techniques can be used. A few of these techniques will be discussed in detail in the later chapters.

The noise component of image degradation also has multiple sources. The two main sources of noise are the gammas present in the beam and the scattered neutrons. To reduce

these noises the design should be performed to maximize the N/G ratio and minimize the scattering of neutrons. To maximize the N/G ratio various gamma filters like lead, bismuth etc can be used. To minimize the scattering the shield walls could be made to absorb more neutrons and scatter less. Also, helium filled collimator can be used to reduce the scattering noise. Less scatter loss also leads to a gain in the neutron intensity at the image plane which helps in improving the signal to noise ratio (SNR). As a rule of thumb for thermal neutrons there is a 10% gain in the intensity per meter of helium compared to air [22]. The noise in the image is also related to the exposure time and the beam intensity per pixel of the detector. As the pixel size decreases, to obtain better spatial resolution, the neutrons available per pixel per unit time reduces, which leads to more statistical fluctuations. Similarly, when the exposure time is decreased, a higher standard deviation of the gray scale intensity is observed due to fluctuations in the beam. In these cases frame averaging is usually performed to reduce the fluctuations. Image de-noising methods can also be used to de-noise the images. Some of these techniques will be discussed in the later chapters.

Thus, the image data collected is a superposition of the ideal object image with the local point spread function and the noise. This, kind of image degradation happens in almost any kind of imaging. The difference lies in the sources of degradation and its mechanism whose understanding leads to its treatment thereby restoring the image. Plenty of work has been performed in the field of characterizing and restoring images obtained from radiation imaging or visual imaging. Some of the references that are relevant and are directly related to blurring mechanisms in radiation imaging are [20], [21], [23]-[25].

1.1.6 Conventional Neutron Imaging

The image formation explained in Section 1.1.3 is applicable to any transmission neutron imaging technique. But, the contrast formation in the image which plays a key role in the distinction of features present in the image depends on the kind of imaging being performed. Difference in the attenuation of the neutron beam passing through different materials in the sample forms the basis of the contrast obtained in the neutron images in most cases. This contrast mechanism is referred to as *attenuation contrast mechanism*. This has proved to be quite successful in providing contrast between different regions of the object that differ in

material composition and thickness. The use of contrast agents mentioned above to increase the attenuation at desired places like cracks, voids, etc. in the sample in order to obtain higher contrast at those locations in the image widened its scope further to a wide variety of NDT applications in different materials. This is the contrast mechanism that is used in the conventional neutron imaging. Such imaging exercise is usually performed using a time continuous thermal neutron beam having a distribution of energy. The object is placed close to the neutron detector and the obtained image is averaged over the neutron energy spectrum, the object thickness and the exposure time. Thus, conventional imaging does not impose stringent requirements on the neutron beam energy, timing and directional characteristics to perform the imaging which makes it simple to implement, standardize and use for different imaging applications. It has been used to perform practical neutron imaging for NDT purposes over many years and has turned out to be quite successful as an NDT technique with the use of contrast agents and transfer technique. It has been routinely used to perform NDT of turbine blades, nuclear fuel pins, honeycomb structures etc.

Even though it is quite useful, there are some limitations of the conventional imaging technique. If two materials have similar attenuation coefficients then the image produced using this technique will not have enough contrast to differentiate between the materials. Further, materials with low neutron cross sections (for thermal neutrons) like aluminum, silicon, calcium etc. may not produce enough contrast on the image unless they have sufficient thickness present in the sample. To enhance contrast in such situations alternative contrast mechanisms have been proposed and demonstrated in the last decade. Some of the imaging techniques utilizing these different contrast mechanisms are phase contrast imaging, energy selective neutron imaging, Bragg Edge imaging etc. To exploit these mechanisms in order to obtain better contrast in images requires some stringent requirements to be put on the neutron beam energy, timing and directional characteristics depending on the type of the contrast mechanism. Often in the process of achieving the required beam characteristics to perform such imaging exercises, the beam intensity is sacrificed to a large extent. It increases the exposure time in the same proportion or else reduces the signal-to-noise ratio (SNR) of the image (if exposure time is not increased proportionally because of some other constraints). In order to take advantage of the alternative contrast enhancement mechanisms without reducing the beam intensity to

unreasonably low levels other novel approaches have been proposed and demonstrated. These techniques necessarily require post processing of the collected raw image data in order to obtain the desired image and will be discussed in later chapters.

1.1.7 Advanced Neutron Imaging Techniques

As mentioned before, conventional neutron radiography uses attenuation contrast mechanism to generate contrast in the image. This may not provide enough contrast in the image for some objects. For an improvement in the contrast resolution alternative mechanism has to be utilized along with this. Some imaging techniques have been demonstrated which can generate more contrast in the images of such objects utilizing the attenuation contrast mechanism in a different way by specifically controlling the beam characteristics or by using a different contrast mechanism altogether. These techniques will be referred to as advanced neutron imaging techniques.

1.1.7.1 Energy Selective Neutron Imaging

Conventional neutron imaging works in the '*integrating mode*' in which the image captured is averaged over the full applied energy spectrum. In the last few years energy selective neutron imaging methods have been demonstrated using thermal and cold neutrons which offer higher contrast images for the sample if the energies of the neutrons are selected correctly. As an example Figure 1.7(a) and (b) show the neutron radiographs of a steel plug taken at two different wavelengths (0.69nm (0.457meV) and 0.32nm (2.125meV)) having almost same attenuation coefficient for steel. When these two images are divided (as shown in Figure 1.7(c)) then the outer steel cover is reduced in contrast making the internal features more clear [26].

In this case the contrast produced relies on the sudden change in the neutron scattering cross-section in the vicinity of the Bragg edges, thus providing enhanced contrast over a small energy range. Bragg edges appear in the cross-section of polycrystalline materials at different energies depending upon the lattice spacing of the materials. As an example Figure 1.8 depicts the Bragg edges of face centered cubic (FCC) and body centered cubic (BCC) iron [27]. The

coherent elastic scattering or the Bragg scattering results in the appearance of these Bragg edges. Bragg edges are most pronounced and best separated in the cold followed by the thermal neutron energy ranges. The lowest Bragg edge corresponding to the largest spacing lattice planes is called the Bragg cut-off. For many engineering type materials such as iron, copper, zirconium, aluminum etc. the Bragg cut off occurs at the thermal to cold neutron wavelength of about 0.4nm (1.4 meV) [27].

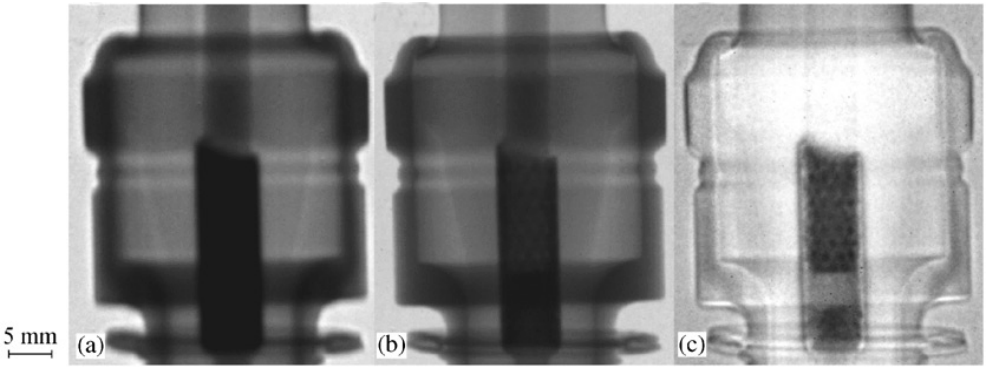

Figure 1.7. Neutron radiograph of a spark plug at (a) 0.69nm (0.457meV) (b) 0.32nm (2.125meV). (c) Division of the two radiographs reducing the contrast of the outer steel cover [25].

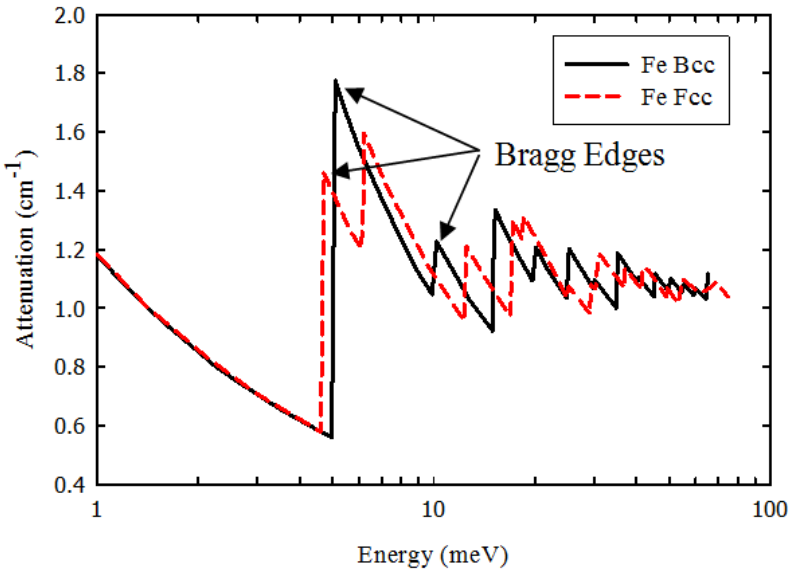

Figure 1.8. Neutron Bragg scattering edges of face centered and body centered iron [27].

It should be noted that energy selective neutron imaging does not offer any extra advantage for the neutron absorbing materials. But, often for practical thermal and cold neutron imaging, neutron absorption plays a minor role compared to the scattering except for materials like cadmium, boron, gadolinium etc. In transmission neutron imaging all neutrons that interact with the sample and do not reach to the detector, i.e. are removed from the primary beam are attributed to the total attenuation coefficient (macroscopic cross-section) given by $\Sigma_{tot} = \sum_{i=1}^{n} N_i \left(\sigma_{s_i} + \sigma_{a_i} \right)$, where N_i is the atomic number density and σ_i (s = scattering, a = absorption) is the microscopic cross-sections of the i^{th} isotope component. The absorption cross-section has generally a simple linear dependence in the cold and thermal neutron energy range. The scattering cross-section contains contribution from the Bragg, incoherent, small angle, and inelastic scattering. The captured image, as explained earlier, is given by

$$I(x,y) = \int I_o(x,y,E)\varepsilon(E) e^{\int \Sigma_{tot}(x,y,z,E)dz} dE, \tag{1.4}$$

where $I_o(x,y,E)$ is the spatial energy distribution of the initial beam intensity, $\varepsilon(E)$ is the energy dependent efficiency of the detection system and z is the direction of propagation of the neutron beam. Equation (1.4) assumes the validity of the exponential attenuation (Beer-Lamberts law) which is true only in the first order. The inversion of Eq. (1.4) can be performed to obtain the material cross-section information if the thickness of the material is known. This process of inversion gets simplified if the energy spread of the neutron spectrum is reduced to a very small value. Moreover, if the mean energy is made to coincide with one of the Bragg edges of the material, which are discontinuous jumps in the material cross-section (see Figure 1.8), then the inversion can lead to very accurate material composition information. The texture of the material can also be obtained through this if $R(\beta_{hkl})$, which is the ratio of the number of crystallites in the Debye-Scherrer cone of the textured material to the corresponding number for a perfectly random sample, is included in the inversion process [27].

Energy selective neutron imaging requires high energy resolution of the neutron beam as the Bragg edges are very narrow in the energy range. This is usually specified by $\Delta\lambda/\lambda$ of the

beam where λ is the wavelength of the beam and $\Delta\lambda$ is the spread in the wavelength of the beam. There are several ways in which this is achieved in the cold energy range [28]:

- With a turbine type energy selector (chopper) – the velocity and the tilting angle are used to select the energy band. Most of the turbine selectors provide an energy resolution of $\Delta\lambda/\lambda \sim 10\%$ or higher [27].

- With a single crystal monochromator – Bragg reflected neutrons are used in pre-selected angular ranges, corresponding to defined energy bands. Graphite, silicon and germanium crystals are suitable as monochromators. The properties of the out scattered neutron beam is defined by the mosaicity (deviation of the crystal used from the ideal crystal) with respect to the energy dispersion and the beam divergence. A double monochromator can be used in order to keep the initial beam direction.

- By making use of the timing structure of a pulsed source – energies are selected by the time of flight (TOF) measurements. They have excellent timing/energy resolution.

Thus, it can be observed that energy selective attenuation contrast can provide better contrast and can provide structural properties (texture, crystal orientation, phase content) of the material but imposes stringent energy/timing resolution requirements on the neutron beam. This reduces the beam intensity significantly compared to a white neutron beam thereby increasing the exposure time. Further, its implementation requires more equipment to be installed which can be very expensive. Moreover, the energy selection depends on the object being imaged and thus object material composition should be known beforehand. All these things make energy selective neutron imaging much more complicated than the conventional neutron imaging.

A few of the application which has been performed using this technique are strain imaging, phase transformation study, evaluation of cross-sections and change in the microstructure of the material [29]-[31]. The technique seems to be quite promising and brings together two different communities working with neutrons: neutron scattering community and

neutron imaging community. With the advent of new high intensity pulsed neutron sources this technique is expected to grow further in future.

1.1.7.2 Non-Interferometric Phase Contrast Neutron Imaging

An altogether different contrast mechanism which has been demonstrated with neutrons is the *phase contrast* effect. The wave-particle duality of matter is well known and is also applicable to neutrons. The attenuation contrast generated by the particle nature of neutrons is utilized in the imaging techniques presented above. Phase contrast technique utilizes the wave nature of neutrons along with the particle nature to obtain higher contrast in the image for some material combinations. Figure 1.9(a) and (b) depict this phenomenon pictorially where the contrast in the image of the object gets enhanced when the neutrons *duel nature* is utilized and the distance between the object and screen is increased. In this case, the contrast gets better as the energy of the neutron beam is decreased. The technique itself has been known for a long time and was being successfully used in X-ray and electron imaging to obtain higher contrast [32]-[34]. For neutrons this out-of-focus phase contrast technique was demonstrated in the recent past [35]. The potential of this technique lies in its ability to be performed using a polychromatic neutron beam without using any interferometry techniques.

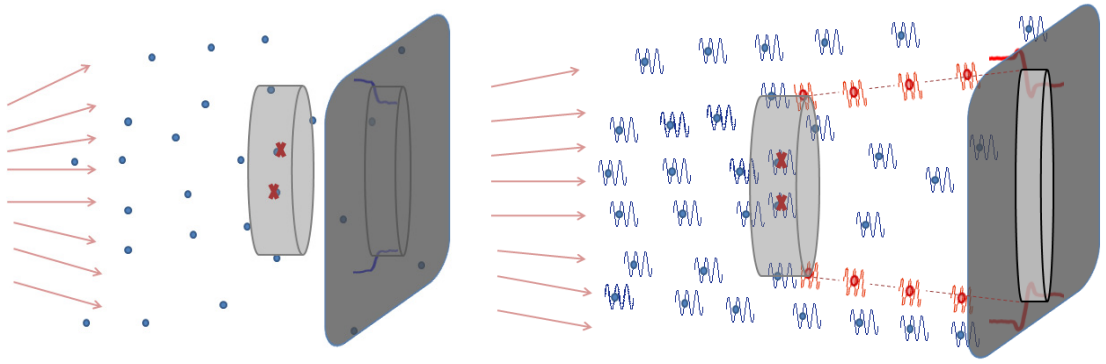

(a) **(b)**

Figure 1.9. (a) Attenuation contrast image of the object obtained using particle nature of the neutrons. (b) Phase contrast image of the same object obtained using both particle and wave nature of neutrons.

The requirement imposed on the neutron beam is not its chromatic (longitudinal) coherence as in the energy selective neutron imaging (as long as the mean energy of the beam is in the cold/thermal region) but, on its spatial (transverse) coherence. In order to achieve the spatial coherence of the neutron beam the source dimensions are reduced to a pinhole and the emerging neutron beam from it is limited to have a small divergence angle. This again leads to a large reduction in the neutron flux reaching the image plane from the source as in the case of Bragg-edge imaging, thereby increasing the exposure time proportionately. A detailed discussion on this technique will be presented in Chapter 3 and 4.

1.1.7.3 Polarized Neutron Imaging

Very recently Kardjilov et al. demonstrated an experimental method that used polarized neutrons to yield a new contrast mechanism for neutron radiography that enables two and three dimensional investigations of magnetic fields in matter [36]. This technique combines the neutron imaging technique with the Ramsey's technique of separated oscillating fields, which is well known in the field of neutron scattering, to image magnetic fields [37]. Figure 1.10 depicts the schematic of the polarized neutron imaging [36].

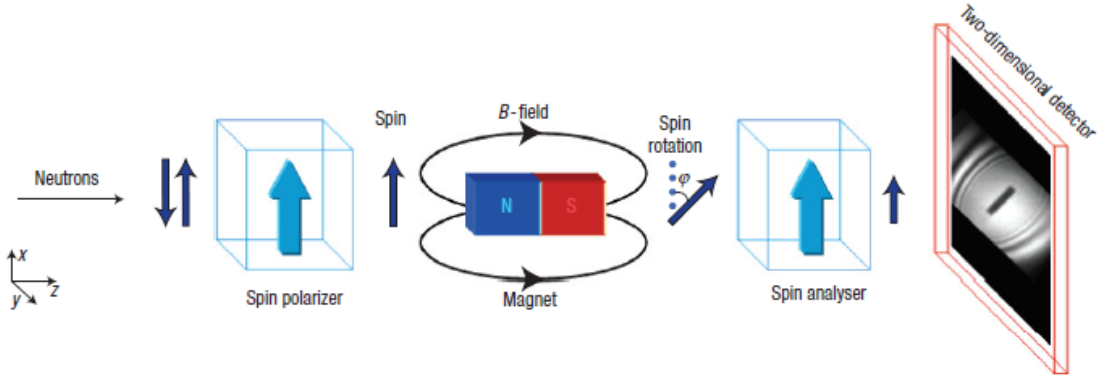

Figure 1.10. The schematic of polarized neutron imaging. The spin rotation of the neutrons depends on the magnetic field along the neutron path [36].

Neutrons are neutral particles but possess magnetic moment and spin. The magnetic moment of neutrons make them highly sensitive to magnetic fields. Also, neutrons being

neutral can penetrate even massive samples. The combination of these properties with radiographic and tomographic imaging is suitable for investigations of macroscopic magnetic phenomena inside solid materials. From quantum mechanics it is known that in a magnetic field, the spin component of neutrons polarized perpendicular to the field will undergo a Larmor precession. Thus, the fundamental idea in this method is the analysis of spin states of neutrons in the beam after its interaction with the sample for each pixel of the imaging detector and to determine the spatially resolved information about the spin rotation induced by the magnetic field of the sample.

In this technique a monochromatic polarized neutron beam is incident on the sample. The transmitted beam from the sample passes through a polarization analyzer before it is recorded on the detector. The analyzer is aligned parallel to the polarizer to guarantee the passage of neutrons carrying a spin parallel to the initial polarization and to absorb the neutrons with anti-parallel spins. The image of the sample detected behind the analyzer is a superposition of the attenuation contrast $I_{att}(x,y)$ and the spin contrast $I_{mag}(x,y)$ variations as given by [36]

$$I(x,y) = \underbrace{I_o(x,y)e^{-\int \Sigma_{tot}(s)ds}}_{I_{att}(x,y)} \cdot \underbrace{\frac{1}{2}\left(1+\cos\theta(x,y)\right)}_{I_{mag}(x,y)}, \tag{1.5}$$

where $I_o(x,y)$ is the incident beam intensity, Σ_{tot} is the macroscopic cross-section, (x,y) are the coordinates on the detector plane and θ is the precession angle. The precession angle has a dependence on the neutron magnetic moment, neutron velocity and the magnetic field presented by the sample. Since, the neutron velocity is directly related to its energy thus, a polychromatic beam, if used, would de-phase upon precession resulting in a loss of polarization [38]. This explains the requirement of a monochromatic beam.

With the development of this technique for the first time three dimensional visualization of the materials magnetic field becomes possible. The technique is very recent and has already shown promising results in imaging magnetic field effects in samples like $YBa_2Cu_3O_7$ (YBCO) that is a type II superconductor, superconducting lead and ferromagnetic materials [36]-[38]. It can turn out to be a very useful technique in future to study magnetic properties of materials.

1.1.7.4 Multi-Pinhole Imaging

Multi-pinhole imaging is not a contrast enhancement technique like the three imaging techniques presented above. It is a technique to improve the SNR of the image when pinhole imaging is being performed like in the case of phase contrast imaging. Pinhole imaging offers both, gain in the spatial resolution as well as the contrast resolution. The gain in spatial resolution is obtained simply by the large L/d ratio in this case. The contrast improvement happens in specific materials due to the phase effects as explained above and detailed in Chapter 3. Even if contrast gain is not always desirable/achievable depending upon the type of application and the kind of sample, the spatial resolution is always a desirable feature in any kind of imaging exercise. As an example, the resolution of the images in the Bragg-edge imaging or the polarized neutron imaging will increase if the source size is decreased to a pinhole with the other beam characteristics required for the performance of such imaging exercises being kept the same.

But, the problem associated with the pinhole imaging is the low intensity of the neutron beam emanating out of the pinhole that reaches to the sample and eventually to the detector. This problem gets aggravated further if the neutron flux intensity incident on the pinhole aperture initially is itself low. The incident neutron intensity can be low either because of the low intensity neutron source being used at the first place or the intensity decreased in the process of conditioning the neutron beam to meet certain desired characteristics like chromatic coherence, neutron to gamma (N/G) ratio, lowering the neutron beam average energy etc. This large reduction in the beam intensity leads to large reduction/increment in the image SNR/ exposure time, although there is a gain in the spatial resolution.

In order to gain the spatial resolution without sacrificing the SNR multiple pinholes can be used. This technique is associated with an additional burden of reconstruction of the raw image data collected to get an image of the object. The performance and the resolution of this technique depend upon how effectively and efficient the image reconstruction can be performed on the raw data. The technique will be presented in greater detail in later chapters.

1.2 Objective

The objective of the work was to investigate the phase contrast neutron imaging and its experimental performance at the PULSTAR reactor using single and multiple pinhole apertures. The investigation of phase contrast imaging included development of its better theoretical understanding and simulation tools to simulate phase contrast images that can help in determining the usefulness of this technique for any specific object. In this regard theory for mixed phase-amplitude objects and a technique to simulate images using this was developed.

The experimental performance of phase contrast imaging at the PULSTAR reactor had some associated design challenges. Phase contrast imaging has been demonstrated elsewhere. But, the few facilities where it has been performed are located at high intensity neutron sources. The PULSTAR reactor is an intermediate intensity neutron source with high gamma content in the beam. These kinds of neutron sources are more commonly available for such imaging applications around the globe. Thus, the demonstration of its performance on a routine basis at this facility without using elaborate expensive equipments to change the neutron beam characteristics can make this technique accessible to multiple imaging facilities located on other such low/intermediate power reactor sources, thereby making this technique practical for NDT applications to a large extent.

Phase contrast imaging suffers from low SNR problem due to pinhole source requirement as discussed above. To improve the SNR in such images multi-pinhole imaging was investigated. The associated image reconstruction techniques to process the raw data obtained were also explored in this work. After giving an overview of the neutron imaging facility on the PULSTAR in Chapter 2, details on this work will be presented in Chapters 3, 4 and 5.

CHAPTER 2

NEUTRON IMAGING AT THE PULSTAR: AN OVERVIEW

2.1 Introduction

A thermal neutron imaging facility has been set up at the NCSU PULSTAR reactor. Design of the facility was performed in a systematic fashion to achieve certain design objectives. Radiation transport simulation techniques were used to design and predict the performance of the facility before its construction. This Chapter presents an overview of the facility design, its performance and its capabilities for which the facility can be used. The details of the design have been already documented in [39]. But, this overview will help the readers relate to the later chapters on phase contrast neutron imaging to the specifics of the designed facility in a better manner.

2.2 The PULSTAR Reactor

The PULSTAR is the fourth reactor to be operated on the campus of N.C. State University. This reactor became fully operational in 1972. It is a swimming pool type 1-MWth research reactor with the core placed inside a 15,000 gallon open tank of water that provides access for observation and maintenance. Water acts as both the coolant and the moderator. The water temperature is about 105^{o}F. An aluminum tank acts as the pool liner, which is surrounded by concrete shielding [40]. The core having a size of 15" (38.1cm)×13" (33.0cm) and 24" (61.0cm) high, is loaded with 359-kg of Uranium Dioxide (UO_2) pin-type fuel with 4% enrichment. It is loaded with a 5×5 array of rectangular fuel assemblies. Each fuel assembly includes 25 UO_2 fuel pins. Uranium dioxide fuel pellets are enclosed in zircaloy cladding. To enhance the neutron economy, two sides of the core are reflected by graphite and beryllium.

This fuel gives the PULSTAR response characteristics that are very similar to commercial light water power reactors. There are 6 Beam Tubes (BT's) positioned around the core. A picture the reactor core along with all the beam tubes is shown in the Figure 2.1. It can be observed that all the beam tubes except BT #2 (which is a through tube) have the direct view of the reactor core. The top left hand corner of the picture shows the "*blue glow*" of the reactor core when it is operating at 1MWth.

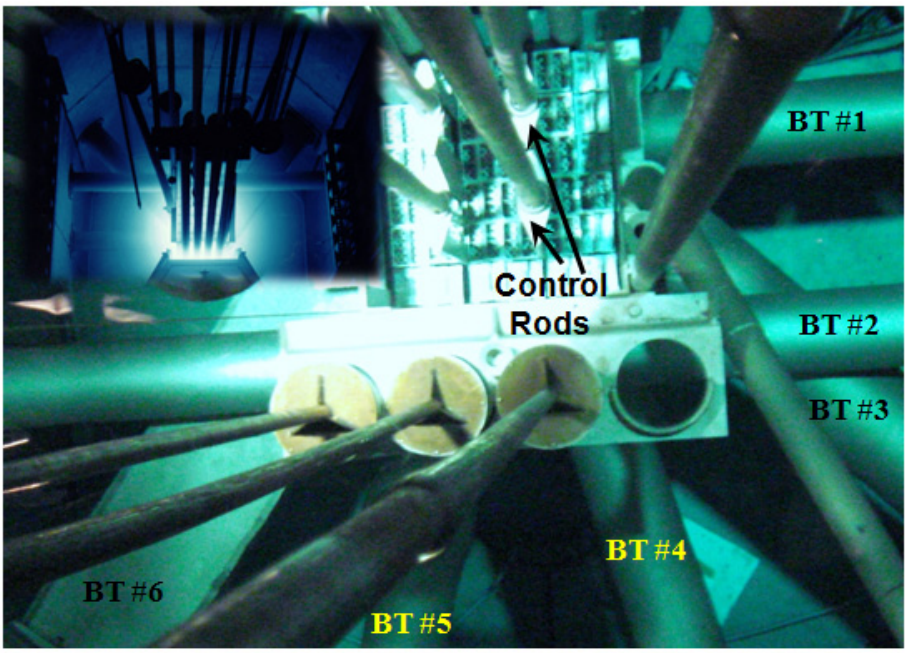

Figure 2.1. A picture showing the PULSTAR reactor core with all the 6 beam tubes.

A normalized neutron flux map across the reactor core is shown in Figure 2.2. It can be observed that the thermal neutron flux peaks at the edges of the reactor core where as the epithermal and the fast neutron flux peaks at the center of the core. This happens because the reactor core was designed to be highly under-moderated. Thus, most of the fast neutrons produced in the core during the fission escape the core and get moderated at the edges of the core by the water. Such a design may not be good for the neutron economy inside the core but is well suited for thermal neutron extraction through the beam tubes. This increases the thermal neutron content of the neutron beam emanating from the beam tubes.

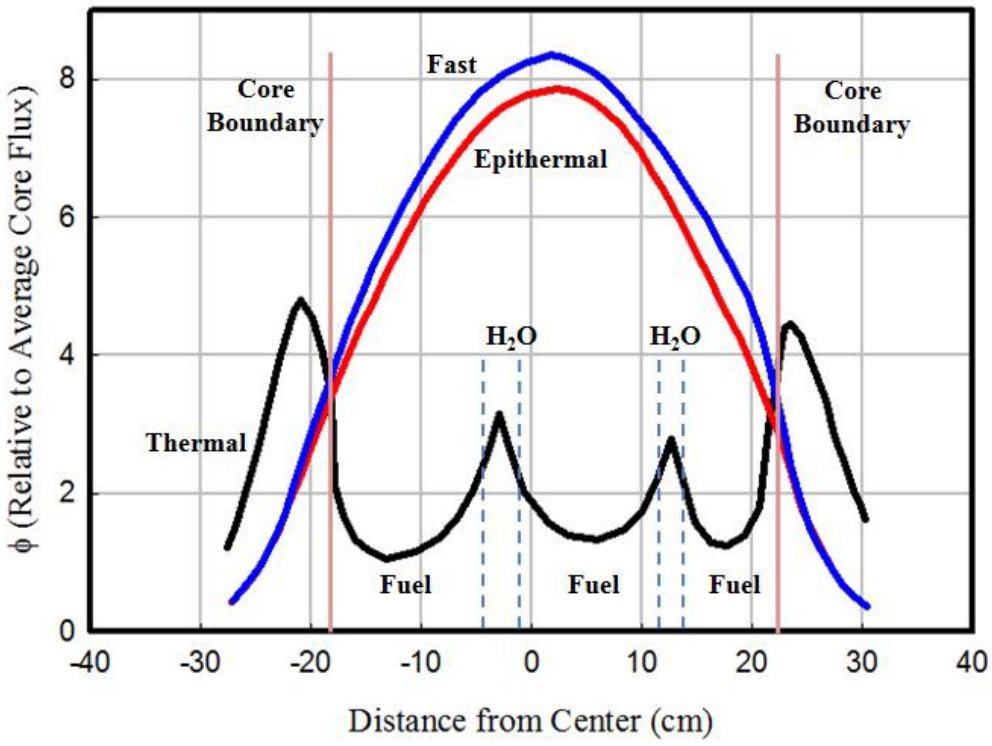

Figure 2.2. The relative neutron flux profile across the PULSTAR reactor core.

The imaging facility has been setup on BT #5 of the reactor. BT #5 was selected for this purpose as it has the longest available beam line length. A layout of the facility is shown in Figure 2.3 showing the reactor core, the collimator inside the beam tube and the shielding cave of the facility. The facility shown next to it on BT #4 is the powder neutron diffractometer. The beam tube is circular with two steps. The diameter at the entry of the beam tube (reactor side) is 6 inches which increases to 9 inches at the first step and to 12 inches at the second step which comes out of the biological shield of the reactor. The measured thermal neutron flux at the beam port entry is ~5 × 10^{12} n/cm^2.sec at the full reactor power. The measurement of the neutron flux was performed using cobalt foil activation. The Cadmium ratio, which is an indicator of thermal neutron content of the beam, was measured to be ~90. The gamma flux (~5x10^{14} γ/cm^2.sec at full reactor power) is also high in the beam tube due to its direct view of the core.

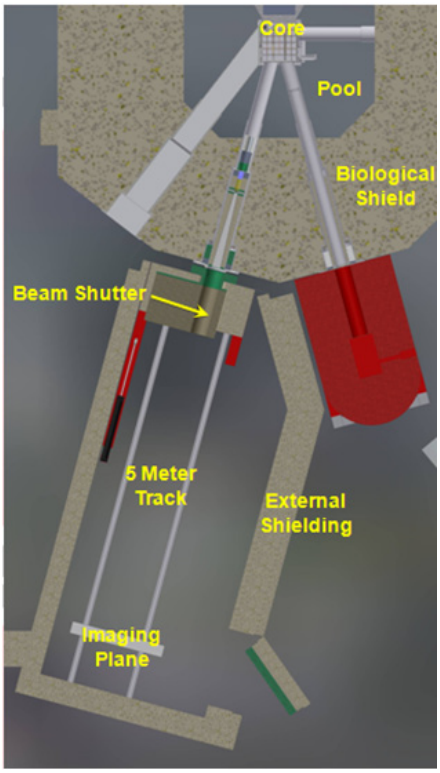

Figure 2.3. Layout of the imaging facility on BT #5.

2.3 Design of the Neutron Imaging Facility

2.3.1 Design Criteria and Constraints

The principal component of this facility is its neutron collimator, which is based on the commonly used divergent beam approach. The design was performed to meet the following objectives:

- an L/d ratio of ~150;
- a quality I^A beam as designated by the ASTM standards [16];
- a maximum N/G ratio;
- a maximum thermal neutron content (TNC);

- a uniform beam profile at the image plane of ~48 cm size to accommodate large size conventional radiography film; and
- the ability to vary these parameters to suit a given application.

Furthermore, several constraints were considered during the design process. This includes

- a maximum available beam line length of 6m;
- a reasonable thermal neutron flux at the farthest image plane (> 10^6 n/cm^2.sec); and
- a dose rate of ≤ 1 mR/hour at full power around the facility outside the shielding.

Based on an L/d ratio of 150 and a maximum beam line length of 6-m, the aperture size was selected to be 4 cm with a square cross-section. The aperture defining material is boral. The divergence angle of the collimator was obtained to be ~2.29°.

2.3.2 Design Performance using Simulations

The detailed collimator design and its expected performance were investigated using MCNP Monte Carlo simulations [41]. The simulation was carried out in two stages. In the first stage, the PULSTAR reactor core simulation was performed to obtain the neutron and gamma source energy spectrum at the beam tube entrance. The MCNP model of the reactor core is shown in Figure 2.4. The obtained neutron and gamma energy spectra at the beam tube entrance are shown in Figure 2.5 and Figure 2.6 respectively. The normalized neutron energy spectrum indicates high thermal neutron content in the beam with relatively low but significant epithermal and fast neutron flux. The 2.2 MeV peak in the gamma spectrum shown in Figure 2.6 is due to the neutron capture in hydrogen present in water that is used as a moderator. Water increases the gamma background and reduces the neutron signal at the same time.

Second stage of the simulation included the transport of neutron and gamma radiation incident on BT #5 entrance, through the collimator up to the image plane. To achieve the

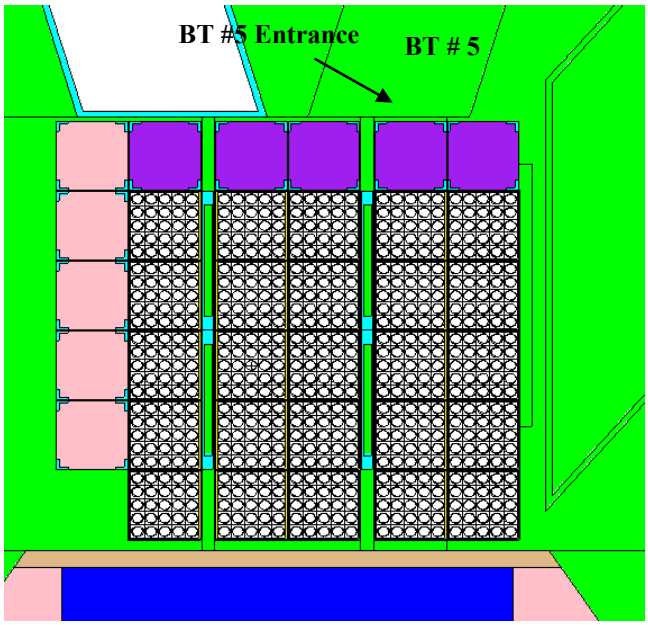

Figure 2.4. MCNP model of the PULSTAR reactor core.

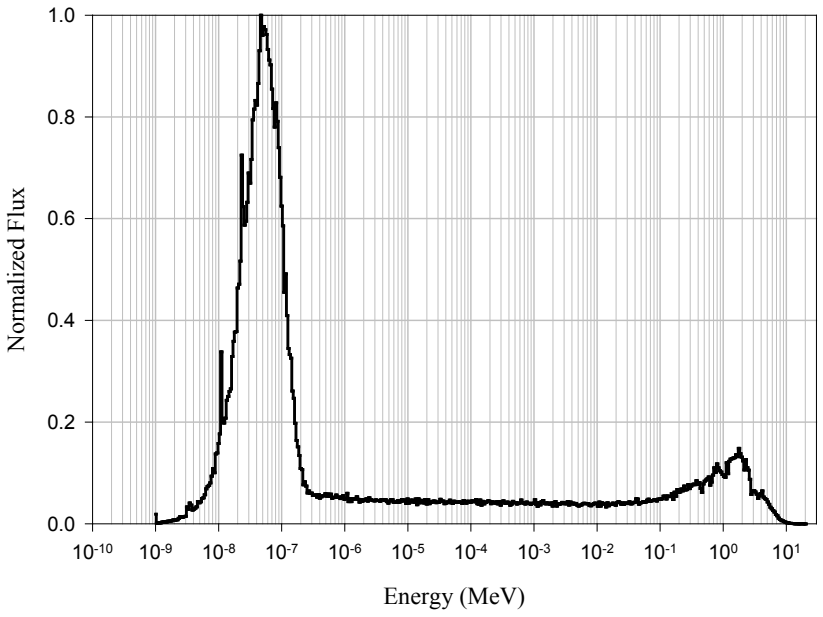

Figure 2.5. Normalized neutron energy spectrum at BT #5 entrance.

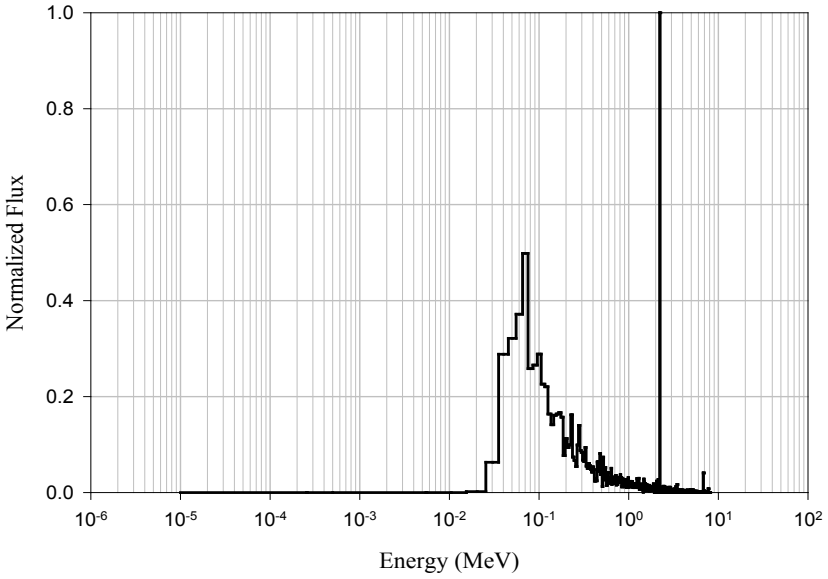

Figure 2.6. Normalized gamma energy spectrum at BT #5 entrance.

design objectives stated above, the first aspect studied was the beam filter requirement. The neutron transport calculations revealed that the fast neutron content, which is already significant in the source neutron beam entering BT #5 (see Figure 2.5), further increases during the transport through the beam-tube to the image plane because of the preferential absorption of thermal neutrons in the collimator. Consequently, to meet the objectives of a high N/G ratio and a high TNC, the use of fast neutron and gamma filters was deemed necessary.

The possible choices considered for fast neutron filtering included beryllium, silicon, quartz, sapphire, bismuth and lead. Single crystals of all these materials are known to have a filtering effect on the fast neutrons up to different degrees [42]-[48]. It has been shown that high quality single-crystal sapphire at room temperature is a better fast neutron filter than silicon and quartz even when they are cooled to liquid nitrogen temperature [46]. Its transmission for neutrons of wavelengths less than 0.04nm (500 meV) is less than 3% for a filter thickness of 100mm [47]. There is a great density of high-order reflections available to scatter the incident neutrons of wavelengths less than 0.1nm. Also, the transmission properties of sapphire are not altered by irradiation even after years within a beam-tube of a reactor [49].

Along with that, cooling of sapphire to liquid nitrogen temperature is not required as with other filters since neutron attenuation is reduced by only about 30% by cooling it to 80K. This attenuation would translate into just about 18% increase in the transmission from sapphire on cooling from 300K to 80K in comparison to 125% increase for beryllium where cooling is highly desirable [46]. This makes sapphire the best option to choose.

Sapphire is not a good gamma filter because of its low molecular weight and mass density. For filtering the gamma rays materials with high atomic number like lead, bismuth, depleted uranium etc. are suitable. Bismuth along with being a good gamma filter has also a thermal neutron window in its cross- section. Thus, single crystal sapphire and bismuth were selected as filtering materials for fast neutrons and gammas respectively. The diameter of the filters was selected to be 2.5 inches in order to fit the aperture in cross sectional area without any alignment issues.

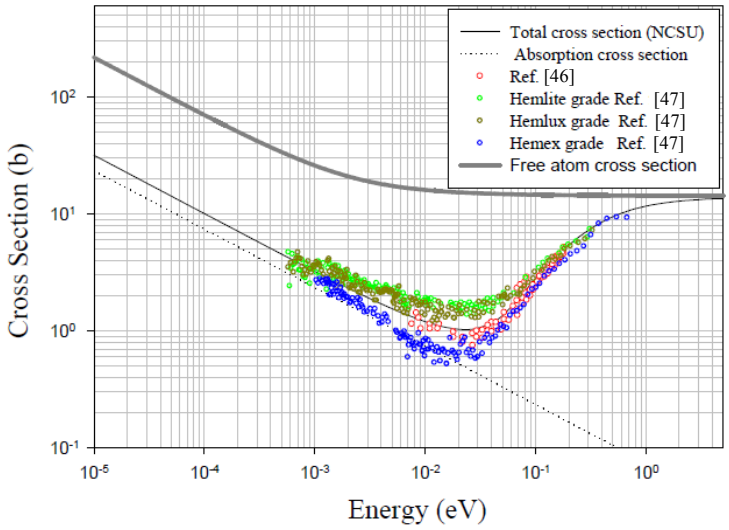

Figure 2.7. The calculated single crystal sapphire thermal neutron total cross-sections and comparison with experimental data. Hemex, Hemlux and Hemlite are three grades of sapphire mainly differing in the degree of crystal alignment and the photon transparency.

In order to observe the effect of filtering performed by these filter materials as well as to optimize their lengths based on the filtering requirements while maintaining the desired neutron

flux, MCNP radiation transport calculations were performed. Accurate thermal neutron cross-section libraries for filter materials like sapphire and bismuth are not available in MCNP. Simulation results using free atom cross-section libraries available in MCNP did not show any filtering effect [50]. Thus, in order to perform accurate neutronic calculations using MCNP, thermal neutron cross-section libraries for sapphire and bismuth were calculated [51]. The difference between the calculated neutron cross-section and the free-atom cross-section for both these materials can be observed in Figure 2.7 and Figure 2.8. These cross-section libraries were used in the calculations to optimize lengths of both the filters.

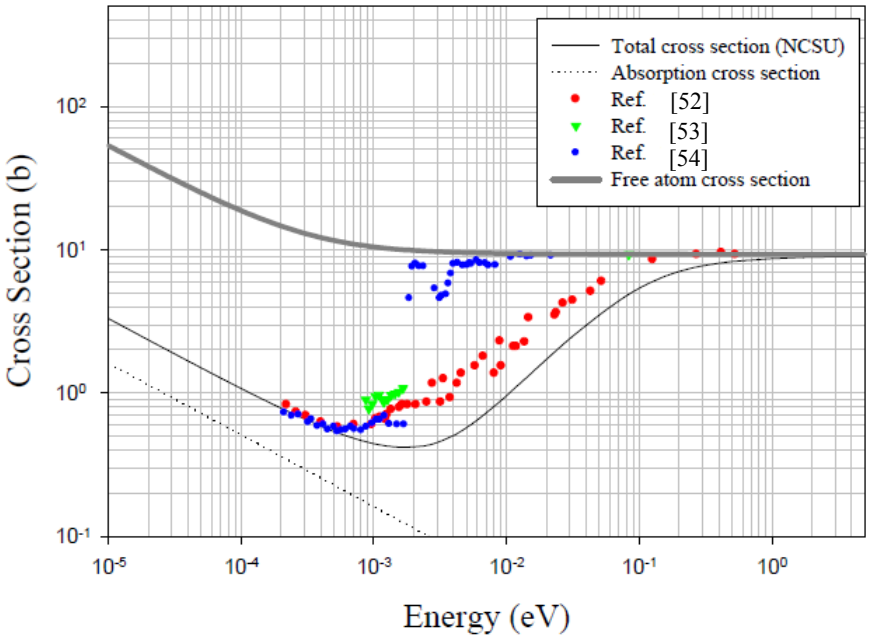

Figure 2.8. The calculated single crystal bismuth thermal neutron total cross-sections and comparison with experimental data.

Four inches of bismuth followed by six inches of sapphire filter was selected to maximize the TNC and the N/G ratio while maintaining the flux requirements. The neutron energy spectrum at the image plane obtained using the generated cross-section libraries for the 6 inches sapphire and the 4 inches bismuth single crystals is shown in Figure 2.9. From the figure it can be clearly observed that the fast neutron flux has been filtered out and the beam consists mainly

of the desired thermal neutrons. The gamma content in the beam was also reduced significantly by the use of 4 inches of bismuth. The final MCNP collimator design is shown in Figure 2.10.

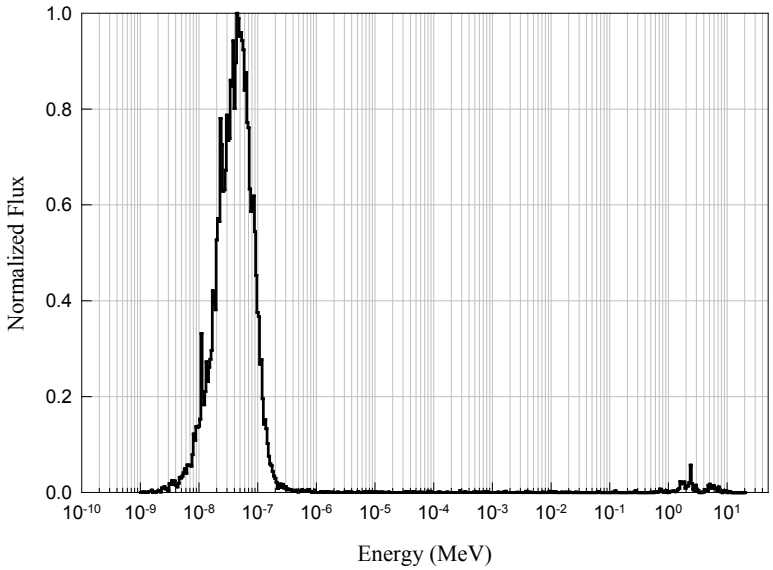

Figure 2.9. The neutron energy spectrum (dϕ/d(ln(E)) at the 6m image plane with 4 inch Bi and 6 inch sapphire filters using the generated thermal neutron scattering cross-sections.

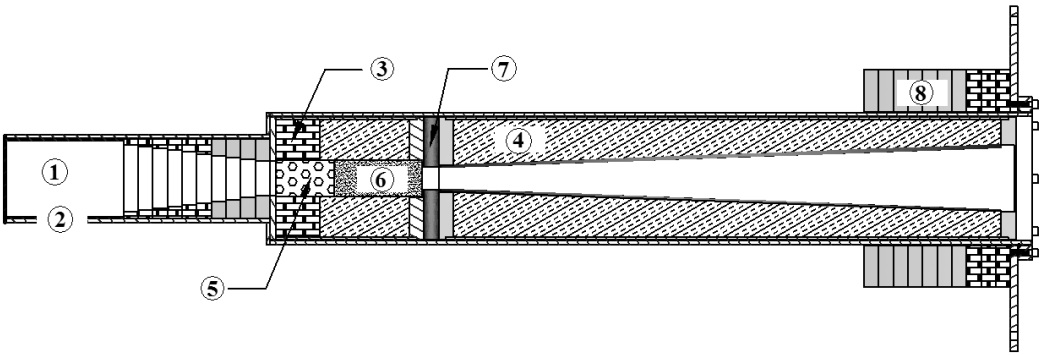

Figure 2.10. The collimator model used in the MCNP simulation. The various components that are shown in the figure are: (1) air, (2) aluminum, (3) lead, (4) SWX-277 (concrete type material with 1.6% boron content), (5) bismuth filter, (7) boral, and (8) borated polyethylene.

2.3.3 Design Verification using Simulations

The design of the collimator was verified against the design objectives using MCNP simulations. A beam uniformity simulation was conducted using the designed collimator. The obtained neutron flux spatial distribution clearly indicated that the flux is uniform over a length of 40cm [50].

ASTM specifies standards for the neutron beam used for conventional neutron imaging. It involves taking radiograph of two specified phantoms, referred to as beam purity indicator (BPI) and sensitivity indicator (SI), on the film. Details on the geometry and material composition of these phantoms can be found in serial number E-545 of the Annual Book of ASTM Standards, Section 3, Vol. 3.03 [16]. This volume includes the standards for various non-destructive testing methods. Most of the beam parameters like the TNC and the N/G ratio are calculated from the densitometer readings obtained from the BPI film radiograph. The SI radiograph is mainly used for visual inspection to figure out the smallest size of the hole and the smallest gap in the phantom that is visible which in some sense defines the spatial resolution of the radiograph.

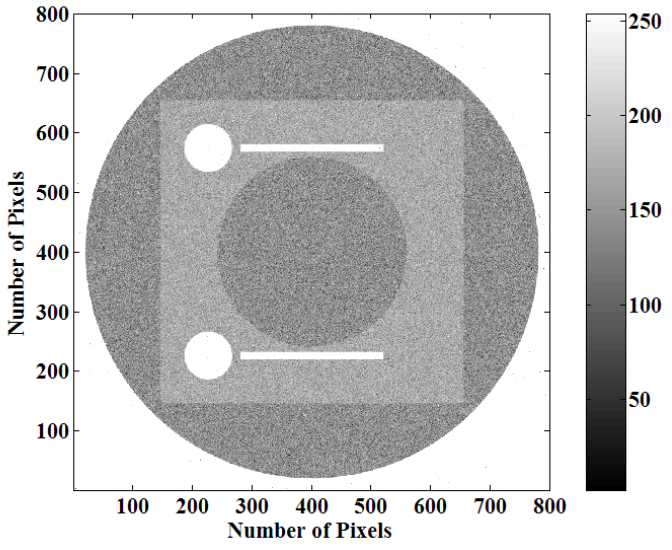

Figure 2.11. MCNP simulated radiograph of BPI. The pixel resolution is 50µm.

A simulation of the ASTM BPI was performed in order to obtain the approximate ASTM beam parameters. The obtained radiograph is shown in Figure 2.11 and the calculated parameters are listed in Table 2.1. From the predicted parameters it can be concluded that the beam, as designed, is anticipated to meet ASTM I^A quality standards. Table 2.1 also gives the final parameters for the designed thermal neutron imaging facility.

Table 2.1. Final parameters of the designed neutron imaging facility.

Parameter	Value
Neutron Flux	$1.8x10^6$ to $7x10^6$ n/cm^2·s
TNC	~70%
N/G	$4.43x10^4$ to $1.34x10^6$ cm^{-2}mR^{-1}
L/D	100 to150
Divergence	~2^o
Cd Ratio	~450
Scatter content	~1.8%

In addition, the expected resolution performance, using the designed collimator, for radiography film, image plate (IP) systems, and scintillation screens with CCD imaging media was estimated by including various components that contribute to the resolution in the simulation. Specifically, the geometric unsharpness, the recorder resolution and the grid resolution effects were taken into account. For the geometric unsharpness, an L/d ratio of 150 with an object-to-image plane distance of 2.5mm (typical thickness of the recorder holding cassette) was considered. The recorder resolution of radiography film, image plates and scintillation screens was taken as 20µm, 93µm and 100µm respectively [17], [55], [56]. This component was included in the simulation by estimating an effective object-to-image plane distance that would result in a combined resolution equivalent to the linear sum of the recorder resolution and the geometric resolution [21], [57]. Finally, the grid resolution effect was modeled by adjusting the pixel size that is used in the simulation. The grid resolution for the digitization of film, the IP scanning system and the CCD were taken as 25µm, 50µm and 25µm respectively. The resulting PSF distributions are shown in Figure 2.12. Sharp edges in the PSF

appear due to the grid discretization process considered in the calculation. Resolutions, as quantified by the FWHM of the PSF, are ~35μm, ~105μm and ~115μm respectively for film, IP and scintillation screen with CCD systems.

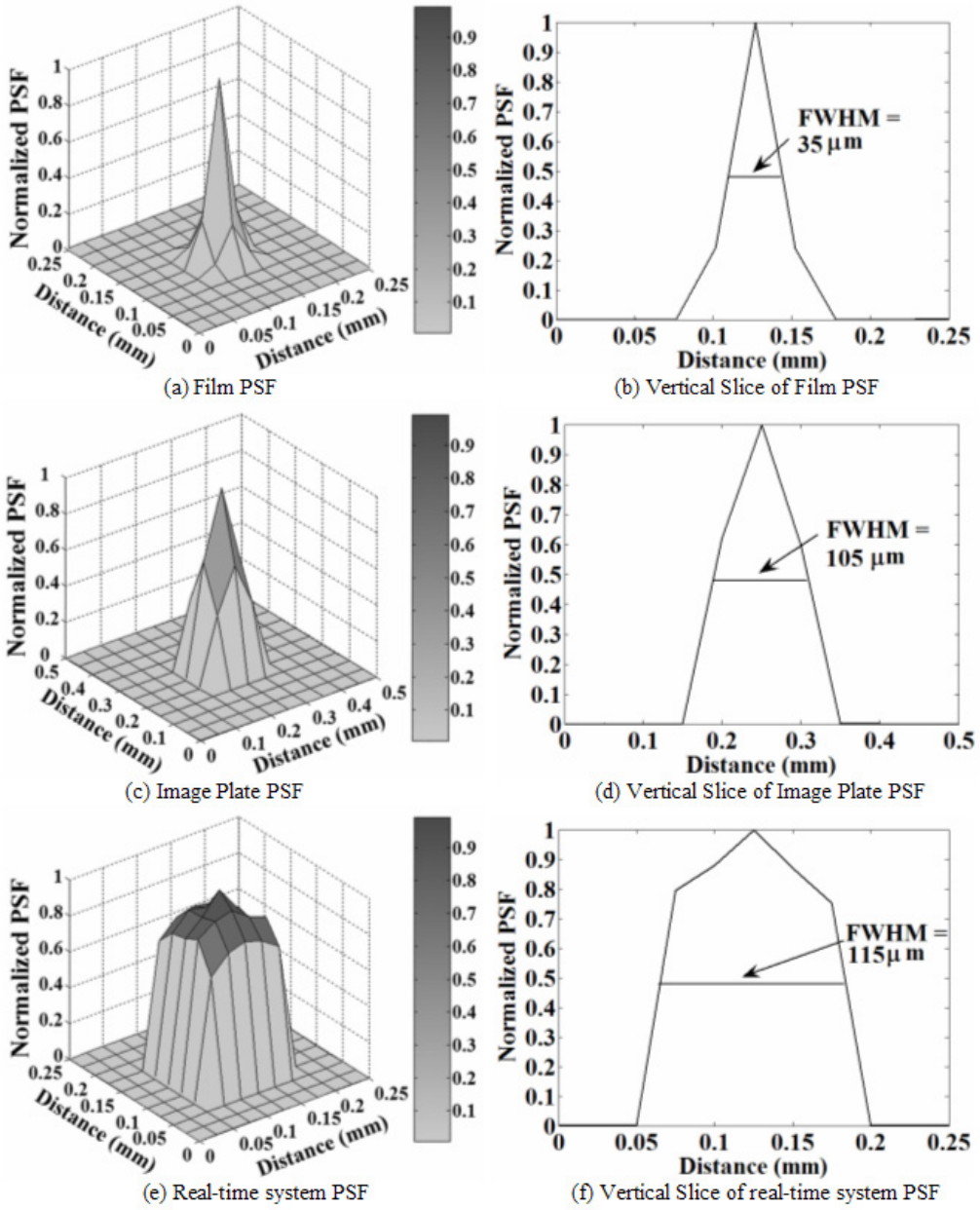

Figure 2.12. Simulated PSFs for different imaging media.

2.3.4 Facility Construction

The mechanical design and fabrication of the collimator was performed in a modular fashion. This eases the modification of beam characteristics by changing beam filter length, incorporating cooling mechanisms and changing aperture size without requiring the change of the entire collimator. The whole collimator was divided into three sections, namely the initial converging section, the filter section and the diverging section consisting of the aperture. These three sections were manufactured separately and then assembled inside the collimator casing, manufactured out of aluminum, confirming to the inside diameter of the beam-tube along with the steps present in it. The collimator casing was sealed at the front face (the reactor core end) by welding a 0.25 inch aluminum plate so that it can be helium filled if required and also the beam-tube can be flooded with water whenever required to reduce the dose. As an example, flooding of beam-tube is desired while changing the filters or changing the diverging section of the collimator as needed, to perform other kinds of imaging exercises as will be discussed in the next few chapters.

The converging section of the collimator was made in the form of stepped cylinders instead of the continuous cone section for the ease of manufacturing (see Figure 2.10). This change does not affect the collimator characteristics. Just before the converging section is an 8-inches long aluminum spacer as can be seen in Figure 2.10, which has been placed to keep the space for any other inserts which may be required in future.

The converging section is followed by the filter section. Sapphire and bismuth filters that were used are shown in the Figure 2.13. The sapphire crystal was obtained from the Crystal Systems Inc. of Salem, Massachusetts USA. There are different grades of sapphire crystals available which differ in terms of crystal distortion and the number of voids (see Table 2.2) [47]. Highest grade (Hemex A-1) crystals are not available in large sizes. In our case the desired size of the crystal was 6 inches in length and 2.5 inches in diameter which happened to be too large for the Hemex grade. Therefore, crystals of Hemlux grade (two in quantity) were obtained. The crystal distortion reported on both of them was type B. The light scattering grade, which is related to the number of voids, reported on the two crystals was between 1 and 2, and 3 and 4 (even though according to [47], Hemlux grades cannot have light scattering grade

of 3 or 4) respectively. As the wavelength of the neutrons (< 1nm) is much smaller than the visible light (> 100nm), the presence of light scattering voids do not really scatter the neutrons significantly. Therefore, the number of voids present is not a matter of concern for neutron filtering purposes as long as these voids are not very small (in that case they give rise to crystal distortion). The crystal distortions on the obtained crystals were reported to be ±15 minutes (B-1,2) and ±28 minutes (B-3,4) from the '*c*' axis. The distortion is known to have an effect of increasing the cross-section of the sapphire in the thermal neutron window [47]. This may be of significance if the crystal has to be used as a monochromator. But, for the fast neutron filtering, as is the case here, the effect is not known to be significant. The bismuth filter was obtained from the Monocrystals Company, Cleveland, Ohio, USA. The filter is composed of crystals with average size of ~0.5 inch oriented randomly. The filter holder is fabricated in separate pieces in order to hold the bismuth and sapphire crystals. Separate filter holders allow for a change in beam characteristics by changing the filters in the beam. Three different combinations of filters: only 6-inches sapphire, only 4 inches bismuth or 4 inches bismuth followed by 6 inches sapphire can be obtained. Moreover, depending upon the application filter inserts with other filter materials can also be inserted easily like inserting both the sapphire crystals to get 12-inch sapphire filter.

Table 2.2 Grades of single crystal sapphire [47].

Scatter of Light (No. of Voids)	Lattice Distortion (Crystal Mosaic)			
	A	**B**	**C**	**D**
1	Hemex	Hemlux	Hemlite	Hemcor
2	Hemlux	Hemlite	Hemcor	
3	Hemlite	Hemcor		
4	Hemcor			Recycle

The aperture and the diverging section of the collimator follow the filters. The aperture is defined by a one inch thick boral piece with a 4cm×4cm square hole cut using a water jet. The diverging section is defined by the 0.1 inch thick boral sheets in a manner such that they lock against each other making the divergent, square cross-section, frustum. This frustum was aligned in the aluminum casing of the collimator using three aluminum aligners at different

distances along the length of the collimator. The space between the frustum and the aluminum tube is filled with RX-277 (now known as SWX-277). It is a castable material like cement with boron in it which acts as neutron absorber. The length of the divergent section is ~120cm.

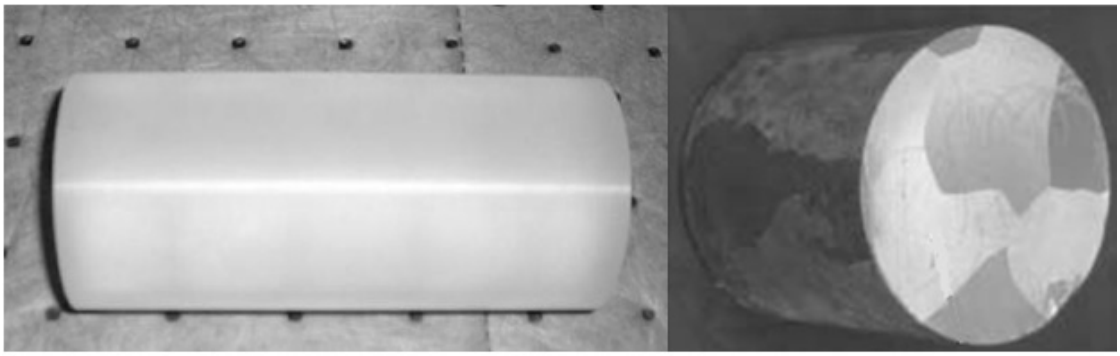

(a) (b)

Figure 2.13. (a) Six inches long single crystal sapphire filter. (b) Four inches long bismuth filter with large monocrystals.

In addition to the collimator, other components of the imaging facility include the beam shutter, the shielding enclosure, the beam stop, and the detection system. The beam shutter has a rotating drum type design, which is opened by an air cylinder. The closing of the shutter is gravity controlled, which provides passive safety. A picture of the beam shutter is shown in Figure 2.14. The rotating drum, the opening and the closing switches have been clearly indicated in the figure. These opening and closing switches are connected to the control system and send signal about the beam shutter status (open/close/in between) at any given time. The pressing of the switches indicate the complete opening/closing of the shutter. The shielding enclosure of the beam shutter has walls that include a 0.25 inch thick boral plate, 6 inches of lead followed by ~19 inches of RX-277.

The shielding enclosure of the facility was initially constructed using ordinary concrete bricks 2 feet thick on each side except the beam stop. Presently, it has been replaced with permanent cast concrete block enclosed in steel moulds. A picture of the new shielding

enclosure is shown in Figure 2.15. The picture also indicates the beam stop and the safety and control systems which will be discussed in the next Section.

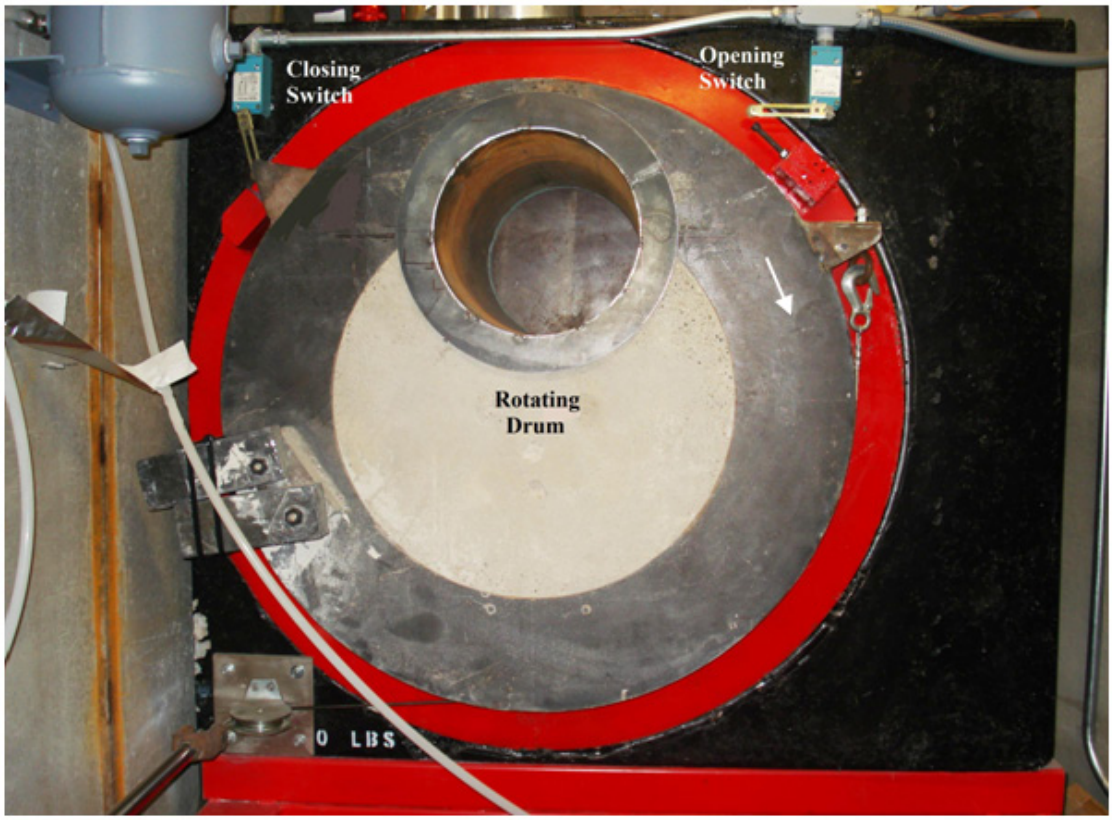

Figure 2.14. Photograph of the beam shutter used to open/close imaging beam.

2.3.5 Safety and Control Systems

Radiation safety has been thoroughly considered from personnel dose point of view while designing the control system of the facility. At the same time, ease of setting the exposure time and observing the experiment while running has been implemented into the design of the control system for the facility. A picture of the computer control panel of the facility is shown in Figure 2.16. The control system has been designed using LABVIEW (a virtual instrumentation software from National Instruments). Four different safety switches are provided whose status is indicated by the indicators on the computer control panel (see

Figure 2.15. The imaging facility shielding enclosure and the control system.

Figure 2.16). The switches are provided at different locations namely, the reactor control room, inside the shielding cave, outside the shielding cave and at the shielding door to secure it using the magnetic lock. Unless all switch indicators are green the beam shutter cannot be opened. Further, even while the beam shutter is open, it closes as soon as even one of the switch positions is altered. Also, the beam indicator light shown in Figure 2.15 turns red from green when the shutter is open. To observe the experiment as well as the conditions inside the shield cave while the beam is open, a video camera has been placed inside the shielding cave whose picture can be observed live on the computer control panel. The camera can be rotated and zoomed using the provided camera controls in the panel. Digital radiation monitoring devices have been placed inside and outside the shielding cave at different locations to monitor the neutron and the gamma dose rates. The Reactor Health Physicist also monitors radiation levels from time to time to make sure that the 'As low As Reasonably Achievable' (ALARA)

principles are being observed. A few of the safety switches, locks and radiation monitors are shown in Figure 2.15.

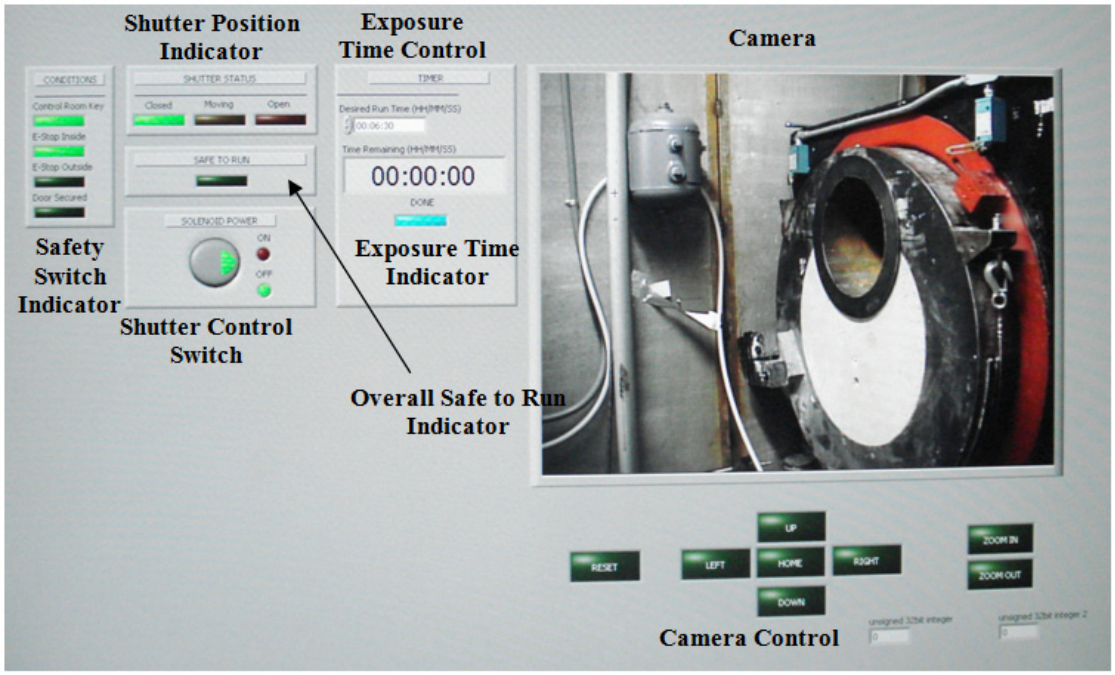

Figure 2.16. A view of the computer screen showing the safety and control system.

Computerized control system also enables easy operation of the facility. For example, the exposure time can be controlled very easily. The system can be operated using a remote desktop connection if all the safety switches are green. The experiment can be observed through the video camera remotely. The safety mechanism also does not require any personnel to be present there all the time while the beam is open.

2.3.6 Detection Systems

Detection systems covering a range of spatial resolution, time resolution as well as gamma sensitivity are present. The available detection systems are:

- Film with convertor screen

- Digital image plates
- Thompson Tube
- Scintillation screen with the CCD
- Micro Channel Plate (MCP)

2.3.6.1 Film with the Convertor Screen

This system consists of the following equipments:

- Single coated film
- The 14”×17” Gd conversion screen
- Automatic film developer
- Film scanner
- Film viewer
- Dark room

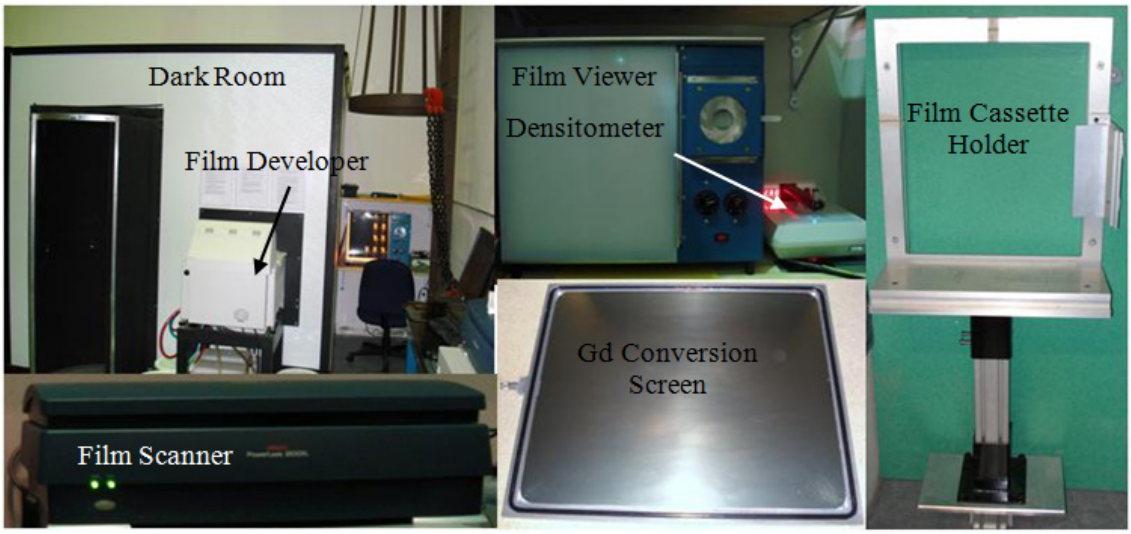

Figure 2.17. A picture of different equipments associated with the film detection system.

Equipments associated with the detection system are shown in Figure 2.17. This system is really important as most of the NDT using neutron imaging is still performed using films. The spatial resolution of the films is ~30μm which is much better than many other detection systems present. The time resolution and the gamma sensitivity characteristics of the films are poor but, for the conventional neutron imaging with moderate neutron flux, and N/G ratio meeting the ASTM requirements, it is satisfactory. The estimated exposure time at the PULSTAR facility is ~7 min. to obtain a densitometer reading of ~2.6. Availability of 14"×17" conversion screen provides the capability to image large size imaging parts. The working of the film detection system is well known and has been discussed in detail in [39]. Some of the key characteristics of the films and the conversion screen were also detailed in Chapter 1.

2.3.6.2 Digital Image Plates

Equipments associated with the image plate detection system as shown in Figure 2.18 are:

- NDG neutron image plates
- BAS-1800 II Fuji Film image plate (IP) reader
- Fuji Film image plate eraser

Figure 2.18. Equipments for the image plate detection system.

Image plates have poor spatial resolution than films. But, they have better time resolution, gamma characteristics and have linearity over a large range compared to films. Other advantages offered by this system are multiple times usability of the image plates, the ease of data storage and data transfer, and ability to apply image processing techniques. The lowest pixel size available in the present system is 50μm. But, its spatial resolution is worse that this because of other sources of unsharpness like the inherent grain size, the geometric factors as well as the spread of the laser used for the optical readout in the IP reader. The convertor material used is gadolinium oxide (Gd_2O_3). Exposure time for the image plates placed at the farthest position in the present facility is ~25sec. This order of magnitude improvement in time resolution over films turns out to be very useful in the phase contrast imaging which suffers from low SNR problem as will be presented in later chapters. For a detailed discussion on the working and characteristics of this system the readers are referred to [58]-[60].

2.3.6.3 Thompson Tube

Thompson tube is a real-time detection system consisting of the following devices:

- Neutron Image Intensifier tube
- Analog Vidicon camera
- Mirror
- Analog-to-digital convertor (ADC)
- Acquisition software (XCAP)

A photograph of the Thompson tube system is shown in Figure 2.19. The system was supplied by Precise Optics/ PEM Inc. Bay Shore, New York, with all the connection and optics already performed. The conversion material in this is also gadolinium used in the form of gadolinium oxy-sulphide. Gadolinium absorbs the thermal neutrons which results in emission of internal conversion (IC) electrons. Scintillation light is emitted subsequently when the vacancies in the K-shell left by the emission IC electrons are filled [61]. The scintillation light strikes the photocathode that emits an electron which is then focused onto an output screen that converts

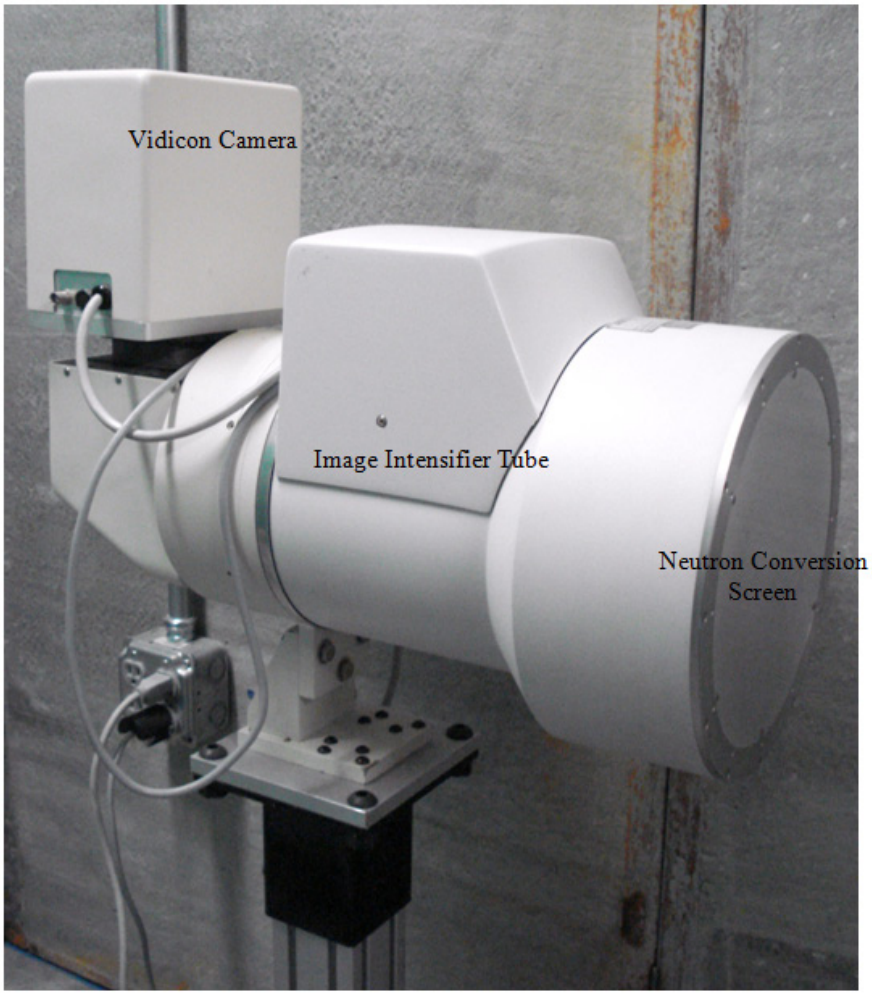

Figure 2.19. Thompson tube detection system.

the electron back into visible light which is sent to the vidicon camera. The focusing of the electron from the photocathode onto the output screen intensifies the radiographic image. Since the vidicon camera has analog output therefore, an analog-to-digital convertor (ADC) card was installed in order to obtain its output on a computer. The system is capable of taking 30 frames per second. But, in order to reduce the noise in the image as desired, frame averaging can be performed. The detection area is ~12cm in diameter. The camera has two optical zoom settings which can zoom on the object at 1.5X and 2X magnifications. The system works at a normal 120V 60Hz AC power supply. In order to reduce the noise in the image, care should be taken to

reduce the noise from the power supply, to avoid ground loop noise and electromagnetic fields. The optimum impedance of the cables attached to the camera is 75Ω. It has a 45 ° mirror arrangement to remove the camera from the direct radiation beam-line. This is required in order to protect the camera from radiation damage. The spatial resolution of the system is about ~300µm but has high time resolution as required for the real-time systems.

2.3.6.4 Scintillation Screen with the CCD

This is another detection system apart from the Thompson tube which gives visible light as the output which is captured by the CCD focused on it. It involves the following equipments:

- Scintillation Screen
- Light tight camera Box
- Mirror
- Lens and the CCD

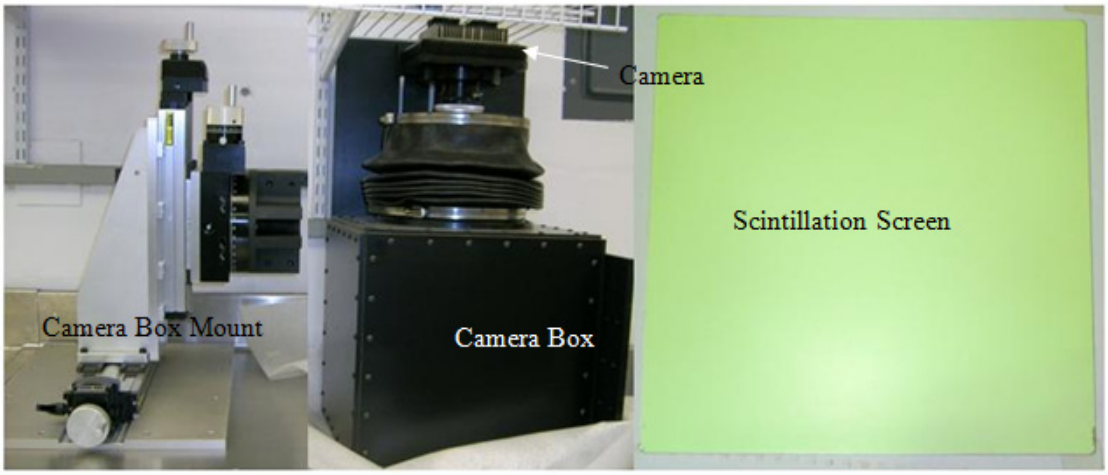

Figure 2.20. Equipments associated with the scintillation screen detection system.

Photograph of these equipments are shown in Figure 2.20. The scintillator in our case is NDG neutron sensitive screen of size 8×8 inch^2 obtained from Applied Scintillation Technologies.

The screen is a blend of Li^6F:ZnS:Cu,Al,Au [62]. The screen uses Li^6 as the converter. Emitted light by the screen has a wavelength peak at 540nm which is green in color. This is especially suited for the CCDs. To obtain the image on the 2 megapixel CCD again a 45° mirror arrangement is used in order to keep the CCD out of the direct beam path. The system is custom made and that is why good focusing is necessary in order to get a sharp image. This system can also be used for real-time imaging. The spatial resolution of the scintillation screen is comparable to the Thompson tube system. But, blurring due to inaccurate optics can lower the system resolution.

2.3.6.5 Micro Channel Plate Detection System

In this system the scintillation screen is replaced by the MCP keeping the rest of the system as it is. MCP detectors are well known in the field of photons and charged particles detection and have high spatial and timing resolution [63], [64]. They are relatively new for the detection of thermal neutrons. For thermal neutron detection the MCP making glass is doped with boron (B^{10}) atoms. The neutron capture reaction $B^{10}(n,\alpha)Li^7$ takes place within the bulk of the B^{10}-doped glass of the MCP [65]. Subsequently, some alpha and/or Li^7 particles escape from the bulk into the adjacent MCP pores, impinge on the secondary electron emissive surface of the MCP pore wall, thereby releasing a number of secondary electrons. A schematic of the detection and signal amplification through electron avalanche formation is shown in Figure 2.21 [66]. Once the electrons are created by the products of the neutron capture they are accelerated in the pores by the electric field created by the high DC voltage supply. In the process they hit the pore walls and the well known avalanche phenomena takes place, thereby amplifying the signal. This avalanche of electrons is then converted into visible light signal using phosphor materials. The light emitted is detected by the CCD camera after being reflected by the 45° angle mirror.

The pores in the MCP can be either square or circular and have a size of about 10-15μm. The wall thickness of the pores is about 2-3μm. These pores are parallel to each other and are usually at an angle to the surface (which is also the direction of the electric field). This ensures the collision of the electrons to the wall surface while accelerating in the electric field. The

small pore size makes the spatial resolution of the MCP to be high (~40μm). Also, the timing resolution of this detection device is good and can be used for real-time imaging if the neutron flux is high enough.

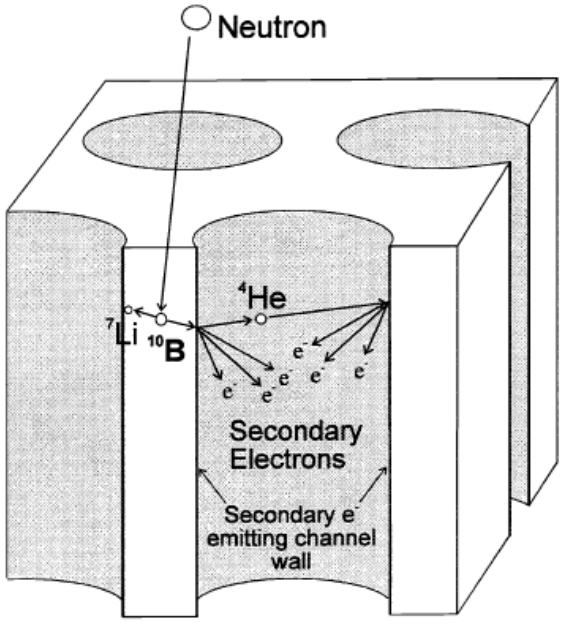

Figure 2.21. Schematic of the neutron detection within a boron doped MCP structure [66].

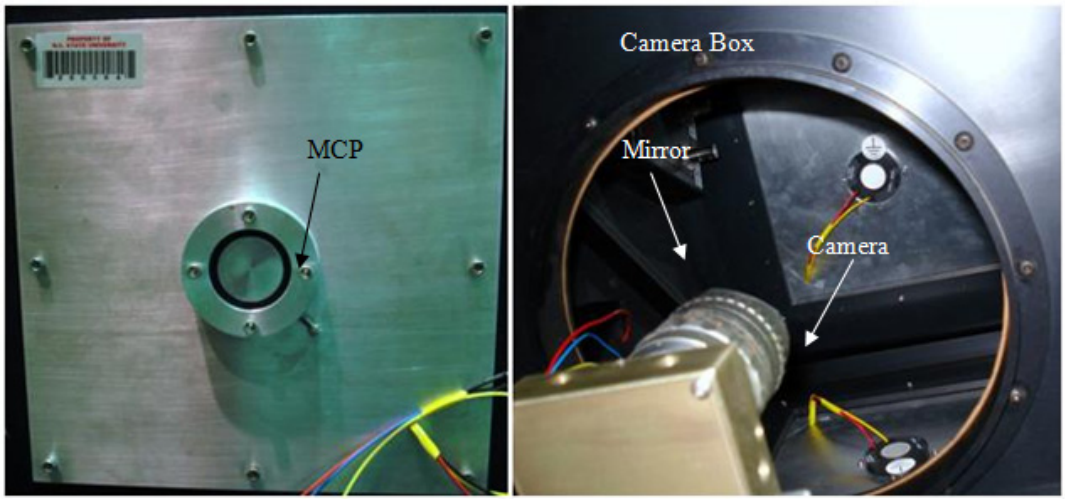

Figure 2.22. The micro-channel plate detection system.

In our case, the size of the MCP detector is 12mm and was supplied by Nova Scientific (see Figure 2.22). It needs a high voltage DC power supply of +5000V and -2000V on its two surfaces for the electron avalanche to take place. Optimum voltage settings are necessary as low voltage may not provide enough amplification and high voltage may increase the noise in the image produced by the gammas and the scattered neutrons. This system can be used for high resolution real-time imaging of a small section of an object.

2.3.7 Facility Characterization

Preliminary characterization of the facility was performed after inserting the collimator in the beam tube. Neutron flux measurements were performed using gold foil activation. The measured flux was $1.8\times10^{6}\pm6\%$ n/cm^2.sec with a Cd ratio of ~450 at the 6m image plane. The beam uniformity test was also performed using image plates and the profile is shown in Figure 2.23. The result indicates a uniform beam profile with a standard deviation of 1.0% which is considered consistent with the design objective. Later, the test was also performed using the 14"×17" films with Gd conversion screen. The variability in the densitometer readings at the corners was found to be within 4% of the center. This variability is well below the limit of 15% followed for practical neutron imaging.

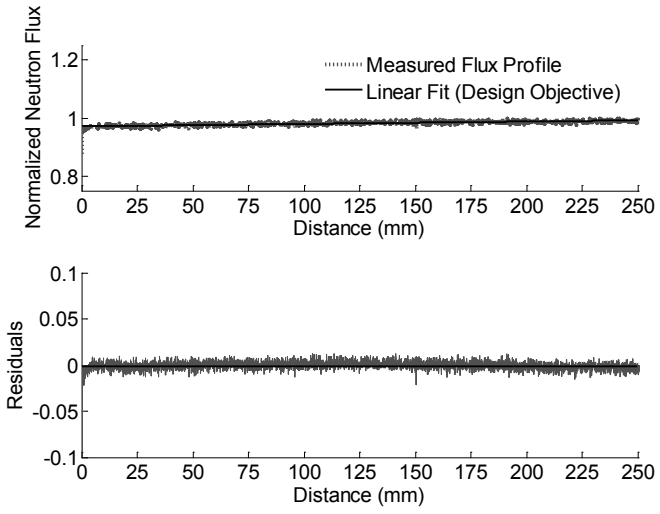

Figure 2.23. Measured neutron beam profile at the image plane located at a distance of 6m from the aperture. The pixel size is 50µm.

ASTM standard E545 was followed to determine the quality of the beam [16]. BPI and SI radiographs were taken using both the films and the image plates. It should be mentioned that ASTM testing method just prescribes film radiograph of these phantoms. The IP radiograph was taken and all the parameters were calculated using it for comparison purposes. The obtained radiographs are shown in Figure 2.24. Clearly from Figure 2.24 it can be observed that film images have better spatial resolution and less noise content. The noise is less because of the greater exposure time which provides more time for the noise to average out. Table 2.3 presents the parameters of the beam, as defined by the ASTM standard, calculated using the above film radiographs. These calculated parameters indicate an ASTM I^A beam quality.

Table 2.3 Measured beam parameters according to ASTM (E-545) standard. The 3rd column has parameters calculated using an IP image even though it is not prescribed by the ASTM.

ASTM Parameters	Conventional film	Digital Image Plate
Effective TNC	73.45 ± 3.5%	77.58 ± 5.0%
Scatter content	2.41 ± 3.5%	1.96 ± 5.0%
Gamma content	0.69 ± 5.0%	0.19 ± 7.1%
Pair production content	1.72 ± 3.5%	0.38 ± 5.0%
Holes visible	7	4
Gaps visible	7	7

Table 2.1 also contains the data measured using digital image plates. The values obtained using image plates are comparable to those obtained using film except that the number of visible holes in the radiograph of the SI is only 4 which constitute the first row of the holes in the SI. This is attributed to the fact that image plates have less spatial resolution than film. In addition, the gamma and the pair production contents obtained using image plates are much less than film. This is attributed to their reduced gamma sensitivity. Uncertainties in the parameters have been calculated using the uncertainties in the readings of film and image plates. Uncertainties in the densitometer readings of the lead and boron nitride discs images were comparatively negligible and therefore were not considered in the calculations.

To investigate the resolution of the system, measurement of edge spread function (ESF), was performed for both radiographic film and digital image plates. The edge was realized using

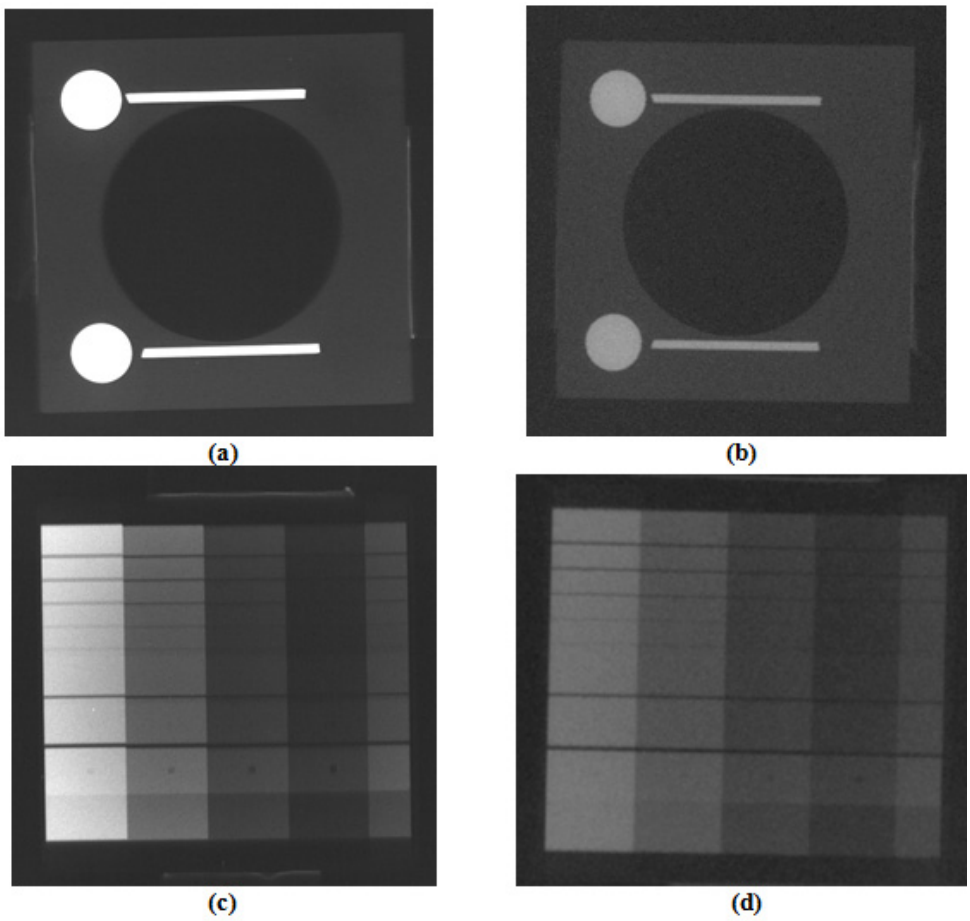

Figure 2.24. (a) Scanned neutron radiograph of the ASTM BPI using film. (b) Neutron radiograph of the ASTM BPI using an IP. (c) Scanned neutron radiograph of the ASTM SI using a film. (d) Neutron radiograph of the ASTM SI using an IP.

a 50μm thick gadolinium foil. Subsequently, the line spread function (LSF) was obtained by differentiating the measured ESF. Figure 2.25 depicts the LSF obtained using the film. In this case the experimental data was fitted using a Lorentzian spread functions [21], [25]. The film resolution, as defined by the FWHM of the LSF, is found to be in the range of 33±3μm. In the case the IP, a Gaussian function was used to fit the LSF. The Gaussian spread function is more suitable for the IP LSF as the laser intensity spread in the IP reader is Gaussian in shape [67]. Figure 2.26 presents the result of this analysis. The image plate resolution was found to be in the range of 110±15μm. The spatial resolution ranges obtained from the curve fittings for the

film and image plate is within the resolution range published for these detection systems [17]. The difference in resolution between film and IP is due to the larger recorder unsharpness of the digital image plates, which is known to be approximately ~93μm as opposed to the ~20μm recorder unsharpness of conventional radiography film [55].

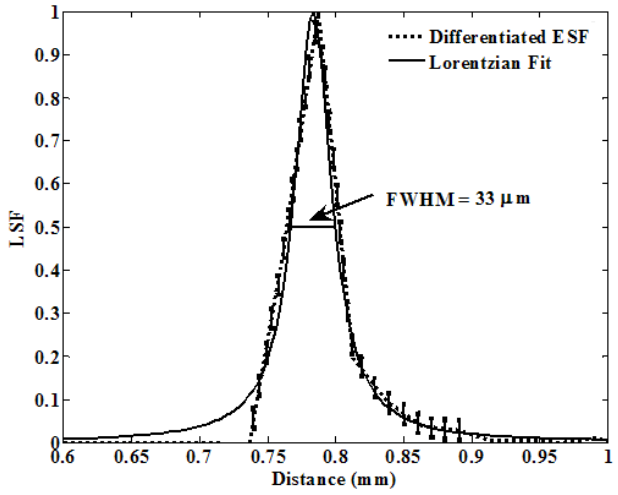

Figure 2.25. Measured LSF using a radiography film. The data was fitted to a Lorentzian function and the FWHM was extracted from the fit result.

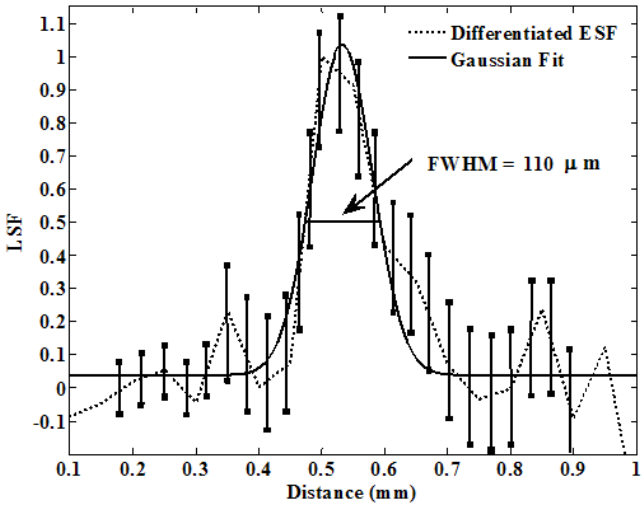

Figure 2.26. Measured LSF using digital image plates. The data was fitted to a Gaussian function and the FWHM was extracted from the fit results.

Finally, it can be seen that good agreement exists between the resolution estimates that were obtained from measurement and simulation. This verifies the assumptions made in the simulations. Consequently, the models developed in this work will be valuable for exploring further developments of this facility.

CHAPTER 3

PRINCIPLES OF PHASE CONTRAST AND MULTI-PINHOLE NEUTRON IMAGING

3.1 Phase contrast Neutron Imaging

In 1924 Louis de Broglie hypothesized the existence of '*matter wave*' in his Ph.D. dissertation [68]. The hypothesis states that any matter has an associated wave property whose wavelength λ is inversely proportional to the momentum of the matter and whose frequency ν is directly proportional to the kinetic energy of the matter. The constant of proportionality is Plank's constant *h* whose value is well known to be 6.626×10^{-34} J.sec. This was later termed as wave-particle duality of matter for obvious reasons. Phase contrast imaging is a novel example of wave-particle duality and in particular de-Broglie's postulate. In this case, both the particle like nature of the radiation namely its attenuation while passing through an object because of absorption and scattering, and the wave like nature of the radiation namely diffraction are utilized to generate contrast in the transmission image of the object. In this context it should be mentioned that '*particle like*' and '*wave like*' properties are not differentiated in quantum mechanics and the same Schrödinger equation applies in each case. This notion comes from the traditional thinking of relating some physical quantities like mass, kinetic energy etc. and some physical phenomena like collision, scattering etc. to particles, and other physical quantities like frequency, wavelength, amplitude etc. and physical phenomena like interference, diffraction etc. to waves.

Phase contrast imaging is a technique in which small phase shifts in the wave transmitted through a partially transparent object are converted into amplitude or contrast changes in the image. The advantages of this technique lie in it being a non-interferometric technique and to be able to provide an alternative contrast mechanism for objects for which attenuation contrast

is not sufficient. Phase contrast imaging can be performed with X-rays, electrons, gamma rays, neutrons etc. In the present chapter the focus will be on the phase contrast imaging with neutrons. Demonstration of phase contrast imaging with neutrons was performed a few years ago and the utilization of its full potential is still awaited [35].

3.2 Background of Phase Contrast Neutron Imaging

The non-interferometric phase contrast effect has been known in the field of X-ray or electron imaging for many years and has been utilized extensively in various applications [32]-[34]. The demonstration of this contrast mechanism for neutron imaging was reported by Allman et al. in 2000 [35]. They conducted experiments at the beam port of the Neutron Interferometry Facility at National Institute of Standards and Technology (NIST), Gaithersburg, Maryland using a monochromatic beam of neutrons with a wavelength of 4.43Å (4.14meV). Later, a polychromatic neutron beam with a Maxwellian distribution around a thermal neutron wavelength of 4.32Å (4.38meV) at the NG0 Neutron Depth Profiling Facility at NIST was used to obtain the phase contrast effect in the image by McMahon et al [69]. Similar experiments were conducted at the thermal neutron radiography station NEUTRA at Paul Scherrer Institut (PSI) in Villigen, Switzerland [70] and the ANTARES neutron imaging facility at the FRM II research reactor of Technische Universität München (TUM), Garching, Germany [71]. The demonstration of non-interferometric phase contrast technique was the key step towards bringing together two separate scientific communities of 'Neutron Imaging' and 'Neutron Scattering'. Table 3.1 lists the imaging facilities along with their salient characteristics where phase contrast neutron imaging has been performed.

3.3 Motivation

The motivation of this work is to study and perform phase contrast neutron imaging at small/medium size facilities. Table 3.1 clearly indicates that all the facilities where phase contrast neutron imaging has been performed are located at high intensity neutron sources with source fluxes reaching $>10^{14}$ n/cm^2·s. However, the 1-MWth PULSTAR reactor represents a medium flux (thermal flux 5×10^{12} n/cm^2·s at BT #5 entrance (see Figure 2.4)) facility with a neutron flux more than 20 times lower than the other facilities listed in Table 3.1. Moreover,

Table 3.1 The list of various facilities where phase contrast neutron imaging has been performed.

Imaging Facility	Neutron Source Characteristics	Other Remarks about the Facility
NIST Imaging Facility	20 MW Reactor Source Flux: 4×10^{14} n/cm^2/sec [72] Reactor core has split-core design, D_2O moderated.	Thermal Neutrons. Filter: LN cooled 10cm thick single crystal Bi. L/D Range 100-6000 with Neutron Flux: $5.1 \times 10^{7} - 4.3 \times 10^{4}$ n/cm^2/sec [72], [73].
NEUTRA at PSI	Swiss Spallation Neutron Source (SINQ). Source Flux: 10^{14} n/cm^2/sec [74].	Thermal Neutrons. Filter: 5cm thick 8cm diameter Bi [12]. L/D Range 200-550 with Neutron Flux: $2.8 \times 10^{7} - 4 \times 10^{6}$ n/cm^2/sec [75].
ANTARES at TUM	20 MW FRM II Reactor Source Flux: 8×10^{14} n/cm^2/sec. Reactor core designed for high thermal neutron flux and low background. D_2O moderated [76].	Cold and Thermal Neutrons. L/D Range: 400: 14000 with Neutron Flux: 10^{8} n/cm^2/sec (at L/D of 400) [76].
NRF at KAERI	30 MW HANARO Reactor Source Flux: 10^{14} n/cm^2/sec D_2O moderated [77]	Thermal Neutrons.
CONRAD at HMI	10 MW BER II Reactor Source Flux: > 10^{14} n/cm^2/sec [78]	Cold Neutrons wavelength range 2-12 Å. Located on curved neutron guide. L/D Range: 70-500 with Cold neutron flux: $2 \times 10^{8} - 6 \times 10^{6}$ n/cm^2/sec [79].
ICON at PSI	Swiss Spallation Neutron Source (SINQ). Source Flux: 10^{14} n/cm^2/sec [74].	Cold Neutron Wavelength Range 2-8 Å. Filter: Be [80].
NCSU Imaging Facility	1 MW PULSTAR Reactor Source Flux: ~5×10^{12} n/cm^2/sec H_2O moderated. High Gamma Flux.	Thermal Neutrons. Filter: 12" single crystal sapphire, L/D Range: 70-160 with neutron flux: 5×10^{6} n/cm^2/sec (L/D of 160).

the high gamma noise, the neutron energy spectrum and the available beam-line space at the PULSTAR makes such an imaging exercise more challenging, which is expected to be the case at other medium flux facilities that may be available at, e.g., university campuses worldwide. Thus, a successful demonstration of this imaging modality here and the ability to perform it on a routine basis will make this technique available to small/medium sized facilities for performing

practical neutron imaging. This will lead to its increased usage thereby expanding its applications as well as performing better NDT of the practical objects by providing higher contrast.

3.4 The Physics of Phase Contrast Imaging

The physical understanding of phase contrast imaging comes from wave optics and coherence theory. Wave optics is a branch of optics which studies interference, diffraction, polarization and other phenomena for which the ray approximation or geometric optics is not valid. Coherence theory deals with the study of optical effects arising from partially coherent waves. In this section the physics of phase contrast imaging will be presented in detail. An extension of it to phase-amplitude objects will also be presented. These formulations will be used in the later sections to develop design strategies and simulation techniques.

3.4.1 Kirchhoff's Formulation

The theoretical basis of the phase contrast imaging comes from Kirchhoff's formulation which is the Green's function approach to the wave equation. According to the Kirchhoff's formula the disturbance at any point P due to any wave field u, representing a solution of the wave equation, is given by

$$u_P = \frac{1}{4\pi}\oint_S \left(\frac{\exp\{-ik\boldsymbol{r}\}}{\boldsymbol{r}} \cdot \nabla u - u \cdot \nabla \left[\frac{\exp\{-ik\boldsymbol{r}\}}{\boldsymbol{r}} \right] \right) dS \,, \tag{3.1}$$

where ∇u is the gradient of u, S is a closed surface enclosing the point P, $\boldsymbol{r}$ is the position vector of the point P relative to the location of the wave field, $i = \sqrt{-1}$ and $k = 2\pi/\lambda$, λ being the wavelength of the wave [81]. Application of Eq. (3.1) to the wave field u due to a point source of unit strength at a point Q (wave function given by $\exp\{-ik\boldsymbol{r}_q\}/\boldsymbol{r}_q$) gives

$$u_P = \frac{1}{4\pi}\int \frac{\exp\{-ik\boldsymbol{r}\}}{\boldsymbol{r}} \cdot \frac{\exp\{-ik\boldsymbol{r}_q\}}{\boldsymbol{r}_q} \left\{ \left(\frac{1}{\boldsymbol{r}} + ik \right) \cos\xi - \left(\frac{1}{\boldsymbol{r}_q} + ik \right) \cos\zeta \right\} dS \,, \tag{3.2}$$

where ξ and ζ are the angles between the surface normal $\hat{\boldsymbol{n}}$ and the vectors $\boldsymbol{r}$ and $\boldsymbol{r}_q$ to the points P and Q respectively as shown in Figure 3.1. Making the approximation that all the dimensions involved are much greater than the wavelength λ, Eq. (3.2) can be written as

$$u_P = \frac{i}{2\lambda}\int \frac{\exp\{-ik\boldsymbol{r}\}}{\boldsymbol{r}} \cdot \frac{\exp\{-ik\boldsymbol{r}_q\}}{\boldsymbol{r}_q}\{\cos\xi - \cos\zeta\}\, dS\,. \tag{3.3}$$

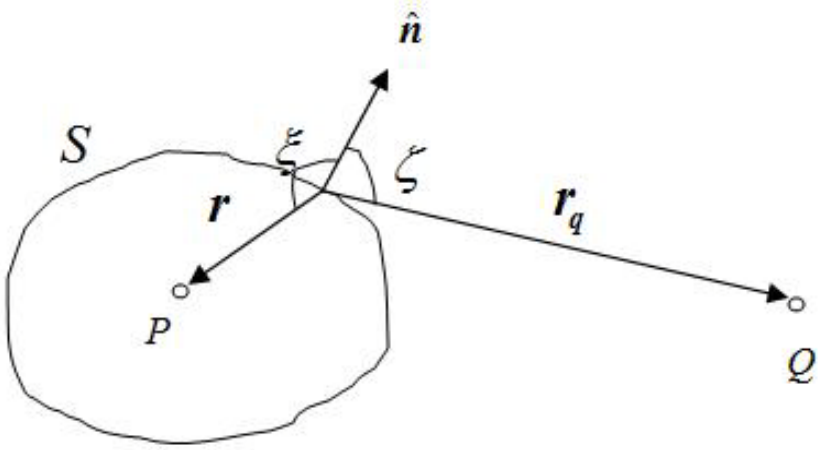

Figure 3.1. Diagram illustrating Kirchhoff's derivation of the amplitude at *P* due to a point source at *Q*.

Huygens-Fresnel principle makes the physical interpretation of the Kirchhoff's formula quite intuitive. The principle explains the propagation of a wave through space by the creation of secondary waves created at each point of the advancing wave front. The '*envelop*' of the secondary waves defines the new wave front. For example, Eq. (3.3) can be interpreted in terms of Huygens concept as implying that the secondary spherical waves emitted from each surface element, $\frac{\exp\{-ik\boldsymbol{r}\}}{\boldsymbol{r}} dS$, have relative amplitude proportional to the amplitude of the incident wave from Q, $\frac{\exp\{-ik\boldsymbol{r}_q\}}{\boldsymbol{r}_q}$. There is a scale factor of λ^{-1} and a phase change of $\pi/2$, represented by the multiplication of i. Further, an obliquity factor $\{\cos\xi - \cos\zeta\}$ ensures that

the waves add up with maximum amplitude in the forward direction and are not propagated backwards.

Kirchhoff's formula is very useful to obtain the wave function at a particular location P after it has been modified by an object. For a two dimensional planar object placed between the points P and Q a transmission function $q(X,Y)$ can be defined such that when this function is multiplied to the incident wave function the resulting wave function represents the effect of the object on the amplitude and the phase of the incident wave. For example, for a point source the emergent wave function will be $q(X,Y)\dfrac{\exp\{-ik\boldsymbol{r}_q\}}{\boldsymbol{r}_q}$. Applying Kirchhoff's law (see Eq. (3.3)) to the emergent wave, the wave function $\psi(x,y)$ at a point on the plane of observation

$$\psi(x,y)=\frac{i}{2\lambda}\iint\frac{\exp\{-ik\boldsymbol{r}\}}{\boldsymbol{r}}\cdot q(X,Y)\cdot\frac{\exp\{-ik\boldsymbol{r}_q\}}{\boldsymbol{r}_q}\{\cos\hat{Z}\boldsymbol{r}+\cos\hat{Z}\boldsymbol{r}_q\}dXdY \tag{3.4}$$

is obtained. In the equation X, Y, Z are the orthogonal coordinate axes with the Z axis being the direction of wave propagation, $\hat{Z}\boldsymbol{r}$ is the angle between the Z axis and the position vector $\boldsymbol{r}$ and $\hat{Z}\boldsymbol{r}_q$ is the angle between the Z axis and the position vector $\boldsymbol{r}_q$. The closed surface S is considered to be the X, Y plane plus a closing surface at the infinity.

3.4.2 Fresnel Diffraction

From the general Kirchhoff's formula, a relatively simple form can be derived when the point of interest is close to the two-dimensional object which is illuminated by a plane parallel incident wave as shown in Figure 3.2. This approximation is the small angle approximation which typifies the class of diffraction effects called '*Fresnel diffraction*'. If the object plane is perpendicular to the direction of incidence, the wave function of the incident wave can be replaced by ψ_o. Thus, the incident wave has amplitude ψ_o and zero phase at $Z = 0$. The amplitude on any plane of observation at a distance R from the object is given by

$$\psi(x,y)=\frac{i}{2\lambda}\psi_o\iint\frac{\exp\{-ikr\}}{r}\cdot q(X,Y)\{\cos\hat{Z}r+1\}dXdY\,, \tag{3.5}$$

where $r^2=(x-X)^2+(y-Y)^2+R^2$ as shown in Figure 3.3. Under the small angle approximation $\cos\hat{Z}r=1$, $r\approx R+\frac{(x-X)^2+(y-Y)^2}{2R}$ in the numerator (which is first order approximation using binomial expansion) and $r=R$ in the denominator can be further substituted in Eq. (3.5) to obtain

$$\psi(x,y)=\frac{i\exp\{-i\boldsymbol{k}\cdot\boldsymbol{R}\}}{R\lambda}\psi_o\iint\frac{\exp\left\{-ik\left[(x-X)^2+(y-Y)^2\right]\right\}}{2R}\cdot q(X,Y)dXdY\,. \tag{3.6}$$

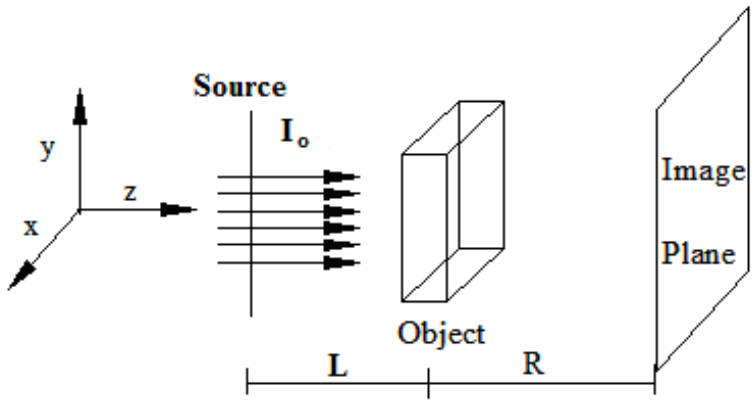

Figure 3.2. Schematic for the small angle approximation of the Kirchhoff's formula.

It can be clearly observed from Eq. (3.6) that

$$\psi(x,y)=\psi_o q(x,y)*\underbrace{\left[\frac{i\exp\{-ikR\}}{R\lambda}\exp\left\{\frac{-ik\left(x^2+y^2\right)}{2R}\right\}\right]}_{\text{Fresnel Propagator}}, \tag{3.7}$$

where '*' denotes the two-dimensional convolution operation defined as $(f*g)_{(x,y)}=\iint f(x',y')g(x-x',y-y')dx'dy'$ for two functions $f(x,y)$ and $g(x,y)$. The

function in the square bracket in Eq. (3.7) is called the Fresnel propagation function for a propagation distance of *R*.

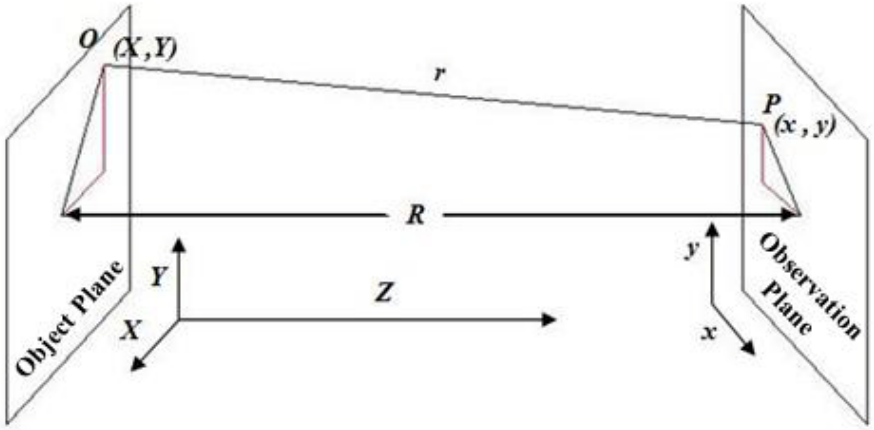

Figure 3.3. The geometry and coordinate system for the Fresnel diffraction.

3.4.3 Phase and Amplitude Objects

As mentioned in the above Section, the effect of a two-dimensional object on the wave function is totally described by its transmission function $q(X,Y)$. Thick objects can be considered to be a stack of planer objects with transmission function $q_n(X,Y)$, where $\sum_{n=1}^{N}\Delta t = t$, Δt being the thickness of each planer slice, *N* being the total number of slices and *t* is the thickness of the object.

The transmission function $q(X,Y)$ for a planer object can be written as

$$q(X,Y) = \exp\{i \cdot n(X,Y)\}, \tag{3.8}$$

where, $n(X,Y) = \Phi(X,Y) + i\mu(X,Y)$ and is referred to as object's '*transmission characteristic*'. It should be mentioned that this notation of the transmission characteristics $n(X,Y)$ as a complex quantity having two components, the real component as $\Phi(X,Y)$ and

the imaginary component as $\mu(X,Y)$, just provides notational simplicity and makes the math more tractable. The real component $\Phi(X,Y)$ provides information of the phase change of the incident wave as it passes through the object and therefore, is referred to as '*phase shift characteristic*' of the object. It is dependent upon the real part of the neutron refractive index of the material and the thickness of the object. The imaginary component $\mu(X,Y)$ provides the information on the amplitude change of the incident wave as it passes through the object and therefore, is referred to as '*amplitude characteristic*' of the object. It is dependent upon the neutron complex refractive index (or the microscopic cross-section) of the material and the thickness of the object. The modulus of transmission function, which is the factor by which the intensity of the incident wave is changed by the object, is given by

$$\left|q(X,Y)\right|^2 = \exp\left\{-2\mu(X,Y)\right\}. \tag{3.9}$$

Thus, the intensity of emergent wave from the object is only changed by the imaginary component $\mu(X,Y)$, as expected. Objects with transmission function given by Eq. (3.8) are called phase-amplitude objects.

There exists an idealized concept of a pure phase object in which the amplitude characteristic $\mu(X,Y)$ is assumed to be zero. For such ideal objects the transmission function becomes

$$q(X,Y) = \exp\left\{i\Phi(X,Y)\right\} \tag{3.10}$$

with a modulus of unity, thereby causing no change in the amplitude of the incident wave.

Another concept is that of a pure amplitude object. In this case it is assumed that the object only attenuates the incident beam but does not cause any phase change. In this case the objects transmission function becomes

$$q(X,Y) = \exp\left\{-\mu(X,Y)\right\}. \tag{3.11}$$

In the conventional neutron imaging all objects are treated as pure amplitude objects with just attenuation property producing the contrast in the image.

3.4.4 Non-Interferometric Phase Contrast

From Eq. (3.7), when a plane wave ψ_o is incident perpendicular on a planar object with transmission function $q(x,y)=\exp\{i\cdot n(x,y)\}$ then the transmitted wave function at a distance R from the object is given by

$$\psi(x,y,R,\lambda)=\psi_o q(x,y)*Fs(x,y,R,\lambda), \tag{3.12}$$

where $Fs(x,y,R,\lambda)$ is the Fresnel propagator. Equation (3.12) involves a two-dimensional convolution operation which is simple to handle in the Fourier domain. The Fourier transform of the Fresnel propagator $\Im s(\varsigma,\eta,R,\lambda)=\mathcal{F}\left[Fs(x,y,R,\lambda)\right]$ is given by

$$\Im s(\varsigma,\eta,R,\lambda)=\exp(-ikR)\exp\left\{i\pi\lambda R(\varsigma^2+\eta^2)\right\} \tag{3.13}$$

where ς and η are spatial frequencies in x and y directions. A detailed derivation of this is given in Appendix A. For small values of λR the Fourier transform in Eq. (3.13) can be approximated by the first order term of the Taylor's series expansion given by

$$\Im s(\varsigma,\eta,R,\lambda)=\exp(-ikR)[1+i\pi\lambda R(\varsigma^2+\eta^2)]. \tag{3.14}$$

If the Fourier transform of the transmission function is given by $Q(\varsigma,\eta)=\mathcal{F}\left[q(x,y)\right]$ then, using property 5 of the Fourier transforms given in Appendix B, Eq. (3.12) can be written as

$$\mathcal{F}\left[\psi(x,y,R,\lambda)\right]=\psi_o Q(\varsigma,\eta)e^{-ikR}\left[1+i\pi\lambda R\left(\varsigma^2+\eta^2\right)\right]. \tag{3.15}$$

Using property 4 from Appendix B, Eq. (3.15) can be written as

$$\psi(x,y,R,\lambda)=\psi_o e^{-ikR}\left[1-\frac{i\lambda R}{4\pi}\nabla^2\right]q(x,y), \tag{3.16}$$

where ∇^2 is the Laplacian operator defined as $\nabla^2\Omega = \frac{\partial^2\Omega}{\partial x^2} + \frac{\partial^2\Omega}{\partial y^2}$ for any function $\Omega(x,y)$. The Laplacian of the transmission function is given by

$$\nabla^2 q(x,y) = q(x,y)\left[\left\{\left\|\nabla\mu(x,y)\right\|^2 - \nabla^2\mu(x,y) - \left\|\nabla\Phi(x,y)\right\|^2\right\} + i\left\{\nabla^2\Phi(x,y) - 2\nabla\mu(x,y)\cdot\nabla\Phi(x,y)\right\}\right], \tag{3.17}$$

where ∇ is the gradient operator give by $\nabla f(x,y) = \left(\frac{\partial f}{\partial x}, \frac{\partial f}{\partial y}\right)$ for any function $f(x,y)$ and $\left\|\boldsymbol{\Omega}\right\|^2 = \Omega_x^2 + \Omega_y^2$ for any vector $\boldsymbol{\Omega} = \left(\Omega_x, \Omega_y\right)$. The intensity $I(x,y)$ at a point is given by the modulus of the wave function $\left|\psi(x,y)\right|^2 = \psi^*(x,y)\psi(x,y)$, where $\psi^*(x,y)$ denotes the complex conjugate of $\psi(x,y)$. Performing this operation and using Eq. (3.16) and Eq. (3.17) the intensity at a distance *R* is obtained to be

$$I(x,y,R,\lambda) = I_o e^{-2\mu(x,y)}\left[\begin{array}{l}\left\{1 + \frac{\lambda R}{4\pi}\left(\nabla^2\Phi(x,y) - 2\nabla\mu(x,y)\cdot\Phi(x,y)\right)\right\}^2 \\ + \left\{\frac{\lambda R}{4\pi}\left(\left\|\nabla\mu(x,y)\right\|^2 - \left\|\nabla\Phi(x,y)\right\|^2 - \nabla^2\mu(x,y)\right)\right\}^2\end{array}\right], \tag{3.18}$$

where $I_o = \psi^*{}_o\psi_o$ is the intensity of the beam incident on the object. Taking the linear terms in $R\lambda$ assuming higher order terms are negligible (as $R^2\lambda^2 << R\lambda$) the intensity can be written as

$$I(x,y,R,\lambda) \approx I_o e^{-2\mu}\left[1 + \frac{R\lambda}{2\pi}\nabla^2\Phi - \frac{R\lambda}{\pi}\nabla\Phi\cdot\nabla\mu\right]_{(x,y)}. \tag{3.19}$$

Thus, for a phase-amplitude object the intensity at a distance *R* from the object is given by the algebraic sum of three terms, where

- the first term is the pure attenuation contrast term arising due to the amplitude characteristic $\mu(x,y)$ of the object,

- the second term is the pure phase contrast term arising due to the difference in phase shift characteristics $\Phi(x,y)$ of the materials forming the object, and

- the last one is the mixed phase-amplitude contrast arising due to the interaction between the phase and amplitude characteristic of the object. Physically, the difference in the attenuation coefficients of the edge forming materials is modified by the difference in the phase characteristics of the objects.

It should also be noticed from Eq. (3.19) that the last two terms which arise because of the phase change of the incident wave are linearly dependent on *R* whereas the pure attenuation contrast term is independent of *R*. Therefore, the phase contrast effect cannot be observed when the detector plane is in contact with or very close to the object, which is usually the case in the conventional neutron imaging. This is one of the reasons why in conventional neutron imaging, where the object is placed close to the detector, only attenuation contrast forms the image of the object. Another reason, which is dependent upon the neutron beam coherence property, will be discussed later. Further observation of Eq. (3.19) indicates that the phase contrast effect also increases with the increasing value of the incident neutron wavelength λ (or decreasing energy). Thus, colder neutron beams are better suited for this modality.

From Eq. (3.19) the intensity distribution obtained at a distance *R* for pure phase objects and pure amplitude objects can be derived easily. For pure phase (PP) objects the imaginary component of the refractive index, $\mu(x,y)$ is assumed to be zero, which reduces Eq. (3.19) to

$$I_{PP}(x,y,R,\lambda) \approx I_o\left[1+\frac{R\lambda}{2\pi}\nabla^2\Phi\right]_{(x,y)}. \tag{3.20}$$

Similarly for pure amplitude (PA) objects Eq. (3.19) reduces to the well know intensity equation

$$I_{PA}(x,y,\lambda) \approx I_o e^{-2\mu(x,y,\lambda)}. \tag{3.21}$$

Equation (3.19) can be used to simulate phase contrast images of phase-amplitude object if all the relevant data is available. The simulation technique and results will be presented in the

next Chapter. The investigation on the phase-amplitude objects has been already published by the author [82]. Similar result has been obtained for X-rays before [83] but, phase amplitude interaction was always neglected as in the case of X-ray imaging often objects like thin tissue samples are of interest which behave like pure phase objects.

3.4.5 Multi-Component Systems

In the above derivation of the phase contrast effect (Eq. (3.19)) it was assumed that the transmission function $q(x,y)$ is defined for a thin planer object. For this case, the small angle approximation is valid. Thick multi-component objects can be handled by partitioning it into a series of thin planer objects with transmission functions $q_n(x,y)$ and thicknesses R_n as shown in Figure 3.4. Propagation over a distance R_n, from the n^{th} to the $(n+1)^{th}$ partition is represented by the convolution with the propagation function $p_n(x)$ given by the one-dimensional Fresnel propagator as

$$p_n(x) = \sqrt{\frac{i}{R_n \lambda}} \exp\{-ikR_n\} \exp\left\{\frac{-ikx^2}{2R_n}\right\}. \tag{3.22}$$

Here, the one-dimensional case is being presented for simplicity and clarity. The two-dimensional case is an easy extension of it. From Eq. (3.13) it can be easily observed that the Fourier transform $P_n(\varsigma)$ of the propagator $p_n(x)$ is given by

$$P_n(\varsigma) = \exp(-ikR_n) \exp\left\{i\pi\lambda R_n \varsigma^2\right\}. \tag{3.23}$$

Thus, the wave function at the observation plane, regarded as the $(N+1)^{th}$ plane is given by,

$$\psi_{N+1}(x) = q_N(x)\Big[q_{N-1}(x)\Big[....\Big[q_1(x)\Big[\psi_o q_o(x) * p_o(x)\Big] * p_1(x)\Big]....\Big] * p_{N-1}(x)\Big] * p_N(x), \tag{3.24}$$

where '*' is a one-dimensional convolution operation. Equation (3.24) can also be written in the iterative form as

$$\psi_0(x) = \psi_o \; ; \; \psi_{n+1}(x) = \left[\psi_n(x) q_n(x)\right] * p_n(x) \text{ for } n = 0 \text{ to } N \,. \tag{3.25}$$

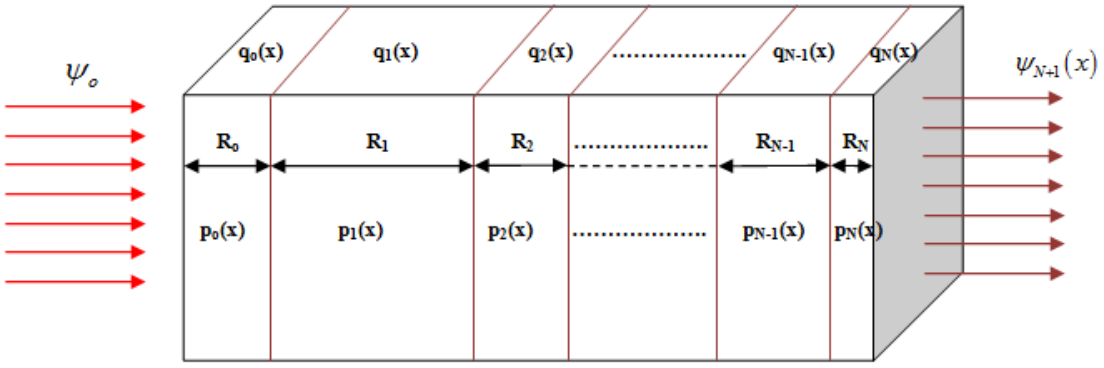

Figure 3.4. Diagram illustrating the description of wave propagation through a multi-component system.

Once, $\psi_{N+1}(x)$ is obtained the intensity at that location can be obtained to be $I_{N+1}(x) = \psi^*_{N+1}(x)\psi_{N+1}(x)$. No explicit expression can be derived for this case like Eq. (3.19) because the successive convolutions are no more with plane waves. But, Eq. (3.19) and the Fourier transform properties can be used to solve for $\psi_{N+1}(x)$ iteratively and obtain the intensity distribution at the observation plane. In the limit when the number of partitions reach to infinity ($N \to \infty$) and the thickness of each partition tends to zero, expressions of the form as in Eq. (3.24) can be used to rigorously represent the scattering from any three-dimensional object.

3.4.6 Neutron Transmission Function of Materials

The '*phase shift characteristic*' $\Phi(x,y)$ and the '*amplitude characteristic*' $\mu(x,y)$ need to be defined in order to completely specify the transmission function $q(x,y)$. As mentioned before, both these characteristics depend on the neutron refractive index of the object and the object thickness. The index of refraction for neutrons is analogous to the index of refraction of light except that the two definitions are reciprocal. Also, it has an imaginary

component to take into account the attenuation of the neutron wave in the material. So, for neutrons the index of refraction n_{Ref} is defined as

$$n_{\mathrm{Ref}} = \mathrm{Re}\left(n_{\mathrm{Ref}}\right) + i\,\mathrm{Im}\left(n_{\mathrm{Ref}}\right), \tag{3.26}$$

where $\mathrm{Re}\left(n_{\mathrm{Ref}}\right)$ is the real part of the neutron refractive index defined as

$$\mathrm{Re}\left(n_{\mathrm{Ref}}\right) = \frac{\mathrm{v}_{med}}{\mathrm{v}_{vac}}, \tag{3.27}$$

and $\mathrm{Im}\left(n_{\mathrm{Ref}}\right)$ is the imaginary part of the refractive index which, along with the real part, defines the neutron microscopic cross-section as will be explained later. In Eq. (3.27) v_{med} is the magnitude of the velocity of neutrons in the medium and v_{vac} is the magnitude of the velocity of neutrons in vacuum.

The existence of refractive index requires existence of an optical potential or a mean interaction potential v_{opt} in quantum mechanics. Physically, the neutron actually scatters and re-scatters from each nucleus to create this mean optical field as shown in Figure 3.5 [84]. From the figure the refractive index $\mathrm{Re}\left(n_{\mathrm{Ref}}\right)$ can also be defined as

$$\mathrm{Re}\left(n_{\mathrm{Ref}}\right) = \frac{K}{k}, \tag{3.28}$$

where K and k are wave vector magnitudes in the medium and the vacuum. This definition is equivalent to Eq. (3.27). The magnitudes of these wave vectors are determined by the incident neutron energy

$$E = \frac{\left(\hbar K\right)^2}{2m} + v_{opt} = \frac{\left(\hbar k\right)^2}{2m}, \tag{3.29}$$

where E is the neutron energy, m is the mass of the neutron and $\hbar = h/2\pi$, h being the Plank's constant. The energy of the neutron is conserved because it is elastic scattering. Using Eq. (3.28) and Eq. (3.29) it can be easily obtained that

$$\left[\mathrm{Re}\left(n_{\mathrm{Ref}}\right)\right]^2 = 1 - \frac{v_{opt}}{E} = 1 - 2\delta . \tag{3.30}$$

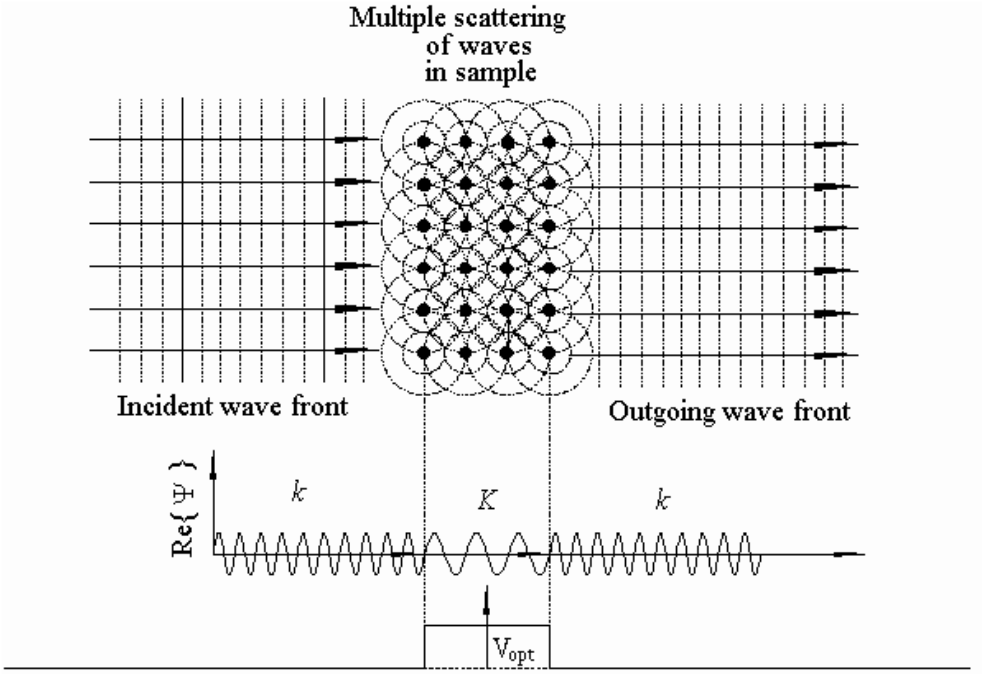

Figure 3.5. Schematic showing the interaction of neutron with atoms leading to the creation of mean optical potential [84].

From the elementary theory of dispersion, the optical potential v_{opt} can be obtained as

$$v_{opt} = \frac{2\pi\hbar^2}{m} a_c \rho , \tag{3.31}$$

where a_c is the bound coherent scattering length and ρ is the number density of atoms. Using Eq. (3.29) and Eq. (3.31) 2δ can be written as

$$2\delta = \frac{4\pi}{k^2} a_c \rho \,. \tag{3.32}$$

Substituting the value of 2δ from Eq. (3.32) to Eq. (3.30), the first order approximation of $\mathrm{Re}\left(n_{\mathrm{Ref}}\right)$ can be obtained as

$$\mathrm{Re}\left(n_{\mathrm{Ref}}\right) \approx 1 - \delta = 1 - \frac{2\pi}{k^2} a_c \rho \,. \tag{3.33}$$

More elaborate theory of neutron refractive index can be found in [85], [86]. Although it might seem from Eq. (3.33) that $\mathrm{Re}\left(n_{\mathrm{Ref}}\right)$ is always less than unity, for some materials like titanium (Ti) and vanadium (V) a_c is negative which makes $\mathrm{Re}\left(n_{\mathrm{Ref}}\right)$ greater than unity. The positive and negative sign of a_c indicates whether the system has bound or unbound states. A positive scattering length signifies that a bound state of the system exists, whereas a negative scattering length signifies that the system has no bound states. The bound state of the system implies that the particles cannot move to infinity and are confined within the potential walls. The unbound state of the system implies that the motion of the system is not confined. Moreover, the coherent scattering length can also have an imaginary component for some materials like boron, cadmium, gadolinium etc. The imaginary component of the scattering length takes into account absorption of the neutrons in the object and leads to the imaginary component of the refractive index [87].

The '*phase shift characteristic*' $\Phi\left(x, y\right)$ which gives the phase shift for a ray path through the object relative to vacuum is given in the classical optics approximation by

$$\Phi = kL \,, \tag{3.34}$$

where L is the '*optical path difference*' [88]. The optical path difference is given by

$$L = \int_C \mathrm{Re}\left(n_{\mathrm{Ref}}\right) \hat{\boldsymbol{K}} \bullet \boldsymbol{dl} \,, \tag{3.35}$$

where $\boldsymbol{K} = \mathrm{Re}\left(n_{\mathrm{Ref}}\right)k\hat{\boldsymbol{K}}$ (see Eq. (3.28)), $\hat{\boldsymbol{K}}$ being the unit vector in the direction of $\boldsymbol{K}$, $\boldsymbol{dl}$ is the vector along the closed counter $C \equiv \bigcup_{j=1}^{4} C_j$ defined through the material and the vacuum as shown in Figure 3.6 and '$\bullet$' denotes the scalar product of the two vectors. The optical path difference can be written as the sum of two different components L' and L'' as

$$L = L' + L'', \tag{3.36}$$

where $L' = \int_C \hat{\boldsymbol{K}} \bullet \boldsymbol{dl}$ and $L'' = \int_C \left[\mathrm{Re}\left(n_{\mathrm{Ref}}\right) - 1\right]\hat{\boldsymbol{K}} \bullet \boldsymbol{dl}$. Thus, L' denotes the actual difference in length between the paths 1(through the object) and 2 (through the vacuum), and L'' denotes the additional contribution in the optical path difference due to the index of refraction of the material (see Figure 3.6). In the present case the actual path length difference is zero. Further, the contribution by L'' just comes from the region where object is present. This gives the total optical path difference to be

$$L = \int_t \left[\mathrm{Re}\left(n_{\mathrm{Ref}}\right) - 1\right]dz, \tag{3.37}$$

where t is the thickness of the object. Using Eqs. (3.33), (3.34) and (3.37) the phase shift characteristic can be written as

$$\Phi\left(x,y\right) = k\int_t \left[n_{\mathrm{Ref}}\left(x,y,z,k\right) - 1\right]dz \;\; = -k\int_t \delta\left(x,y,z,k\right)dz \;\;, \tag{3.38}$$

where t is the thickness of the material in the z direction. Equation (3.38) can be simplified and written as

$$\Phi\left(x,y,t,\lambda\right) = -\lambda\int_t a_c(x,y,z)\rho\left(x,y,z\right)dz\,. \tag{3.39}$$

Thus, the phase characteristic function depends on the integrated coherent scattering length density $a_c(x,y,z)\rho\left(x,y,z\right)$ of the material over its thickness and the wavelength λ of

the neutrons. For most materials the coherent scattering length is positive and thus by Eq. (3.39) induce a negative phase difference by the propagation of coherent neutron waves through them. The negative phase difference corresponds to phase lead in the material. But, as mentioned before, there are materials with negative coherent scattering length. For such materials the phase difference will be positive (by Eq. (3.39)) which corresponds to the phase lag.

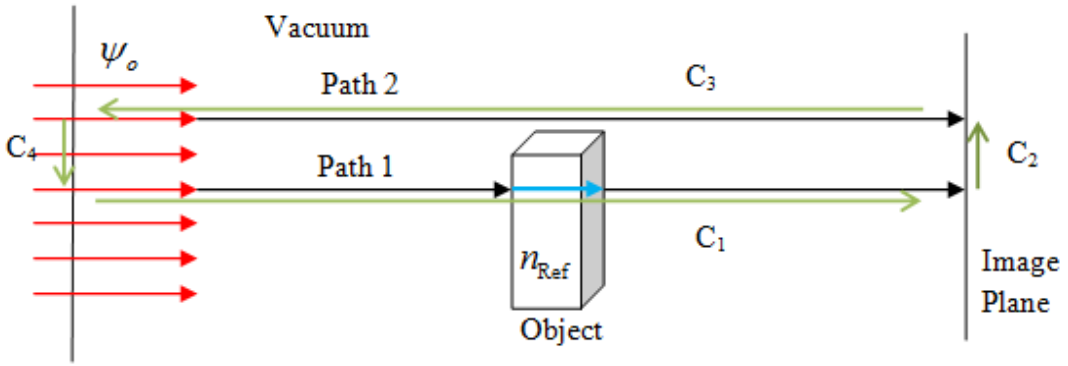

Figure 3.6. Diagram depicting the optical path difference between the neutron waves passing through the object and the vacuum.

The '*amplitude characteristic*' $\mu(x,y)$ of the material depends on both the real and imaginary part of the neutron refractive index. In this case the relationship between the amplitude characteristic and the neutron refractive index is not as simple as the one between the phase shift characteristic and the refractive index. It can be shown using conventional collision theory that for an incident plane wave of neutrons scattered by a spherically symmetric center of force the total neutron microscopic cross-section σ_{Tot}, which is the sum of scattering cross-section and the absorption cross-section, is given by

$$\sigma_{Tot} = \frac{2\pi}{k^2}\sum_n (2n+1)\left\{1-\cos\left[2\,\mathrm{Re}\left\{n_{\mathrm{Ref}}(n)\right\}\right]e^{-2\,\mathrm{Im}\{n_{\mathrm{Ref}}(n)\}}\right\}, \tag{3.40}$$

where *n* is the Legendre polynomial order used in defining the scattering amplitude $f(\theta)$ [86], [88]. The scattering amplitude $f(\theta)$ can be obtained using theory of partial waves [88]. Once

the microscopic cross-section is known either using Eq. (3.40) or otherwise the amplitude characteristic of the material can be obtained by

$$\mu(x,y,\lambda) = \frac{1}{2}\int_t \sigma_{Tot}(x,y,z,\lambda)\rho(x,y,z)dz \ . \tag{3.41}$$

Thus, it can be observed from Eq. (3.39) and Eq. (3.41) that if the objects coherent scattering length, the total microscopic cross-section and the atomic number density is known then the transmission characteristic of the object can be obtained. This transmission characteristic will define the transmission function of the object.

3.4.7 Assumptions and Beam Requirements

The theory of non-interferometric phase contrast and the related physics presented above has some inherent assumptions which translate into neutron beam requirement while implementing the technique to perform imaging.

3.4.7.1 Coherence

One of the assumptions that is made in almost any kind of neutron optics theory is some type of coherence in the neutron waves. Coherence of two neutron waves follows from how well correlated the waves are as quantified by the cross-correlation function. The cross-correlation quantifies the ability to predict the value of the second wave if the value of the first wave is known. There are various different kinds of coherence that can be defined which have different effects. Two of the most important coherence types are *absolute* coherence and *relative* coherence [88]. Scattering is said to be *coherent in the absolute sense* if the scattered waves interfere with the incident wave. For most of the optical phenomena such coherence is desirable. The scattering is said to be *coherent in the relative sense* if the waves scattered by different atoms interfere with each other, though not necessarily with the incident wave. In addition to *absolute* and *relative* coherence, there are other kinds of coherence like *temporal* and *spatial* coherence, *second-order* and *fourth-order* coherence, etc.

A system that can be described by a single wave function ψ is said to be in a *pure state*. Otherwise, it is in a *mixed state* and an appropriate ensemble of different wave functions is required for its description. A collimated neutron beam from a thermal fission reactor is an example of a system in a *mixed state*. The number density of the neutrons in such a beam is sufficiently small that neutron-neutron collision can be neglected and the beam can be regarded as a system of free neutrons. Therefore, the state of a single free neutron can be described by a wave packet $\psi(\boldsymbol{r},t)$, which is a coherent superposition of plane waves, as

$$\psi(\boldsymbol{r},t) = \int a(\boldsymbol{k}) \exp\left[i(\boldsymbol{k} \bullet \boldsymbol{r} - \omega_k t) \right] d\boldsymbol{k}, \tag{3.42}$$

where $\boldsymbol{r}$ is the position vector of the neutron with respect to a co-ordinate axes, t is the time, ω_k is the angular frequency of the neutron corresponding to the wave vector $\boldsymbol{k}$ given by $\omega_k = \hbar k^2 / 2m$, m being the mass of the neutron, and $a(\boldsymbol{k})$ is the amplitude of the state with wave vector $\boldsymbol{k}$. Thus, the beam can be described by an appropriate ensemble of such wave packets. Density matrix $\Gamma(\boldsymbol{r},t)$ is one such ensemble average describing the macroscopic properties of a thermal neutron beam. It is defined as

$$\Gamma(\boldsymbol{r},t) = \left\langle \psi^*(0,0)\psi(\boldsymbol{r},t) \right\rangle, \tag{3.43}$$

where $\psi(\boldsymbol{r},t)$ is the wave packet given by Eq. (3.42) and $\langle ... \rangle$ denotes the ensemble average [88]. Thus, $\Gamma(\boldsymbol{r},t)$ is the autocorrelation function of $\psi(\boldsymbol{r},t)$ and describes the coherence of the neutron beam.

The matrix $\Gamma(0,t)$ describes the *temporal* (*longitudinal*) coherence. Thus, the *temporal* coherence is the measure of the average correlation between the values of a wave at a particular point at any pair of times, separated by delay, t. The duration of the delay over which it produces visible interference is known as the *coherence time* of the wave, τ_c. Figure 3.7(a) and (b) depict cases of temporal coherence with infinite coherence time and finite coherence time respectively [89]. The temporal coherence of a wave is related to the spectral bandwidth of the

source. A truly monochromatic (single frequency) wave would have perfect temporal coherence with infinite coherence time. In practice, no wave is truly monochromatic (since this requires a wave-train of infinite duration), but in general, the coherence time of the source is inversely proportional to its bandwidth.

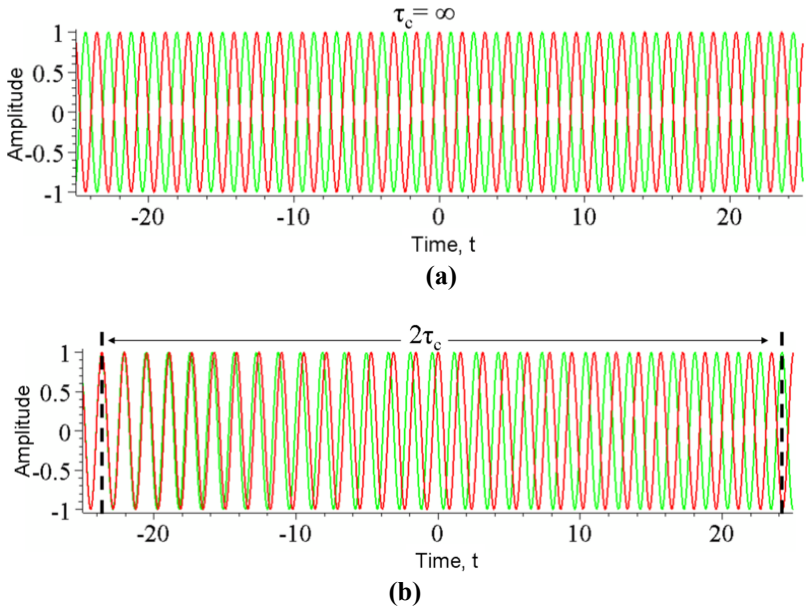

Figure 3.7. (a) Two monochromatic waves with a delay of τ. The coherence time τ_c is infinite since they are perfectly correlated with each other for all delays τ. (b) The amplitude of a wave whose phase drifts significantly in time τ_c as a function of time *t* (red) and a copy of the same wave delayed by $2\tau_c$ (green). At any particular time *t* the wave can interfere perfectly with its delayed copy. But, since half the time the red and green waves are in phase and half the time out of phase, when averaged over *t* any interference disappears at this delay [89].

The matrix $\Gamma(\boldsymbol{r},0)$ describes the *spatial* (*transverse*) coherence of the beam. In other words, *spatial* coherence is the cross-correlation between two points in a wave for all times. If the wave has a single value of amplitude over an infinite length, then it has perfect spatial coherence. Figure 3.8 depicts a few cases of spatially coherent waves [89]. Waves in Figure 3.8(a) and Figure 3.8(b) are perfectly spatially coherent whereas the wave in Figure 3.8(c) has partial spatial coherence. Spatial coherence is high for plane and spherical waves as it is related to the wavelength, size and coherence of the source. For example, a polychromatic point source of zero diameter emits spatially coherent waves, while the wave from a collection of mutually

incoherent point-sources would have lower coherence (as the point sources are not coherent with each other, the resulting wave has low spatial coherence). Spatial coherence can be increased by use of *spatial filters*; a very small pinhole which excludes all neutrons apart from that coming from a very small central region of the source , thus converting a source of finite size into a point source. Spatial coherence also increases as the wave travels away from the source because the source appears smaller (more point-like) and the waves become more like a sphere or plane wave. Both these spatial filters will be used later on to increase the spatial coherence of the neutron beam.

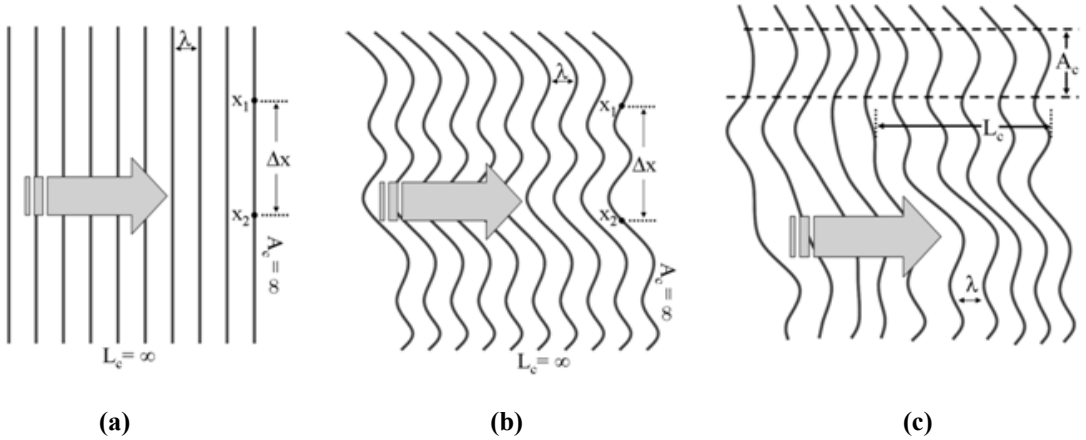

Figure 3.8. (a) A plane wave with an infinite coherence length. (b) A wave with varying wave-front and infinite coherence length. (c) A wave with varying wave-front and finite coherence length [89].

The distance along the wave propagation direction from the source to a point where the wave maintains a specified degree of coherence is called coherence length, L_c. The degree of spatial coherence is a measure of the correlation which exists between the phases of the radiation at two points and is measured by the visibility (V) of fringe patterns in the image. V is defined as

$$V = \frac{I_{\max} - I_{\min}}{I_{\max} + I_{\min}}, \tag{3.44}$$

where $I_{\max}$ and $I_{\min}$ are the maximum and minimum intensities in the obtained fringe patterns. In the case of perfect coherence it is unity, and for complete incoherence it is zero. For a

circular source of uniform intensity and diameter d the degree of coherence is given by $J_1(\pi du)/(\pi du)$, where $u = x_p/R\lambda$, λ is the wavelength of the neutron beam, J_1 is the first order Bessel function of the first kind, x_p is the distance between the two points whose spatial coherence is of interest (located on the object), and R is the object to image-plane distance. This defines the coherence patch or the coherence area A_c, which is the range of separation between the two points over which there is significant interference. The radius of the first zero of the above Bessel function is taken as a measure of the width of this patch (area). This radius is given by

$$x_p \approx \frac{\lambda L}{d}, \tag{3.45}$$

where L is the distance between the source and the object. It is also referred to as the transverse coherence length (L_t) (i.e. $x_p = L_t$).

3.4.7.2 Neutron Beam Requirement

For the phase contrast neutron imaging the requirement imposed on the neutron beam to obtain the intensity variation as given by Eq. (3.19), is a high degree of *spatial* (*transverse*) *coherence*. On the other hand, high degree of *temporal* (*longitudinal*) *coherence*, necessary for most interferometic techniques, is not required. The extent of the observable phase contrast effect is given by the width of the coherence patch (L_t) which is dependent on the beam energy and the L/d ratio of the system as indicated by Eq. (3.45). Here, the L/d ratio is the same that appeared in Chapter 1 in relation to the geometric unsharpness of images. From Eq. (3.45) it can be observed that the transverse coherence length L_t and hence, the coherence area A_c will increase if the expected wavelength of the neutron beam spectrum is increased. Also, the transverse coherence length is directly proportional to the L/d ratio of the beam, which is a combination of both the *spatial filters* discussed above. Large L/d ratio, obtained either by increasing L or decreasing the source diameter d or both, makes the wave-front reaching the object more like a plane wave thereby increasing the width of the coherence area A_c as shown in

Figure 3.9 [89]. This will be used as a design tool for phase contrast neutron imaging system in the next Chapter.

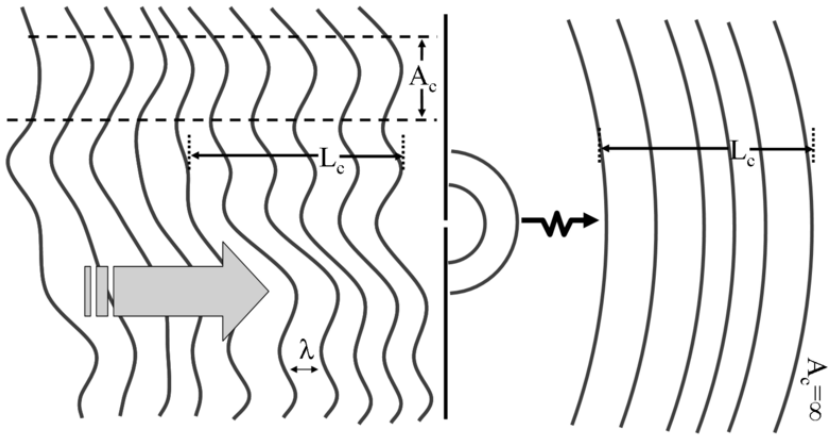

Figure 3.9. Schematic depicting the increase in the coherence area A_c of a wave incident on a pinhole at a large distance from the pinhole [89]. The coherence length L_c remains unchanged.

Upon substitution of L_t (from Eq. (3.45)) for x_p, the expression $u \approx L/dR$ is obtained. The degree of coherence for a circular aperture defined by the visibility (see Eq. (3.44)) thus becomes

$$V_{circ} \approx \frac{J_1\left(\pi L/R\right)}{\left(\pi L/R\right)}. \tag{3.46}$$

From Eq. (3.46) it can be observed that the degree of spatial coherence does not depend on the wavelength of the beam or the source diameter. Further, it can also be observed from Eq. (3.46) that V_{circ} is dependent only on the L/R ratio and thus for a given L, (obtained using Eq. (3.45) or limited by the beam line length) to observe the coherence effect the object to image-plane distance R must be large enough (within the Fresnel limit).

The physics and principles discussed above for the phase contrast neutron imaging will be used in the system design and development of image simulation techniques that will be presented in the next Chapter.

3.5 Introduction to the Multi-pinhole Neutron Imaging

Multi-pinhole source neutron imaging is a technique where the image of the object is taken using multiple point-like neutron sources. The schematic of such an imaging system is shown in Figure 3.10. The technique offers the advantage of improving the signal-to-noise ratio (SNR) while maintaining the benefits of pinhole imaging systems like high image resolution. Multiple pinholes increase the signal at the image plane (the neutron flux at the image plane in the case of pinhole neutron imaging) linearly with the number of pinholes present. The pattern of the holes at the source plane is collectively referred to as the source mask. Due to multiple pinholes the image formed on the detector is an overlap of multiple object images formed by every single pinhole. Thus, the additional burden associated with this technique is the requirement of image reconstruction which will process the raw image data collected into the image of the object. Availability of a good image reconstruction technique is therefore crucial for retaining the resolution improvements offered by the pinhole imaging in the reconstructed images. The image reconstruction will be discussed in greater detail in Chapter 5.

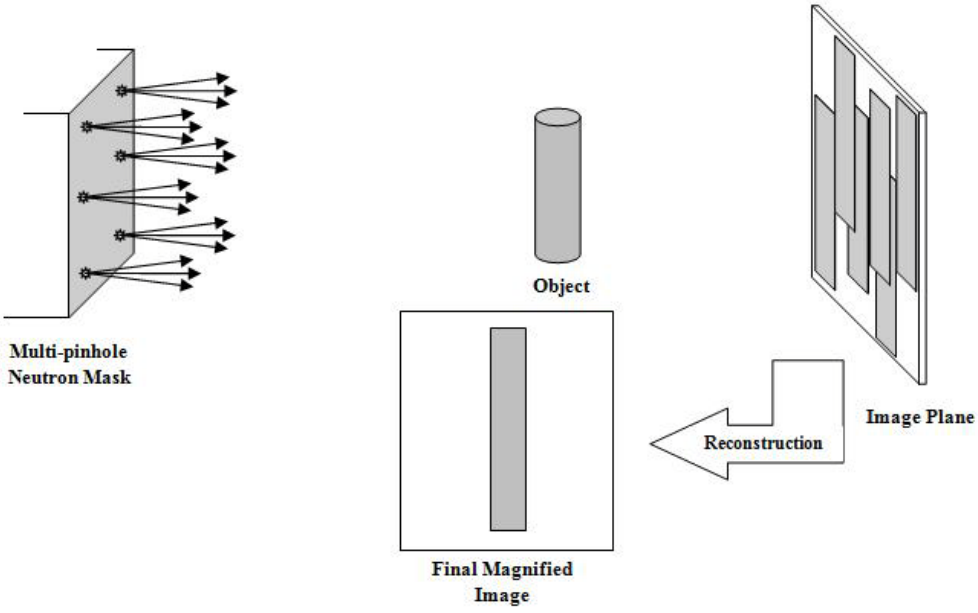

Figure 3.10. Schematic of the multiple pinhole neutron source imaging.

Multi-pinhole source imaging is a concept derived from the multi-pinhole cameras. Multi-pinhole cameras are used to image faint radiation sources itself, rather than an object using the radiation source. In this case the multi-pinhole mask is placed in front of the detector which forms multiple overlapping images of the source on the detector. The multi-pinhole camera was first introduced in the field of X-ray and γ-ray astronomy by Dicke [90] and Ables [91] in the year 1968 for obtaining high angular resolution along with good photon statistics while imaging celestial objects. Since then this concept has been used in various fields to improve the SNR [92]-[95]. In most of these cases specially designed pinhole patterns, referred to as '*coded masks*' or '*coded apertures*' were used for imaging. These masks were designed to provide ease in image reconstruction along with a large open area fraction A_o. The open area fraction is defined as the ratio of the total area of all the holes and the area of the mask (which is the sum of the total area of the holes and the area of the 'no-hole' region). It is always between 0 and 1 with the ideal value for the coded masks to be 0.5. Various different coded aperture pattern generation schemes have been presented in the literature [96], [97]. These schemes are mainly based on binary arrays (arrays containing elements that are either 0 or 1) like the uniformly redundant arrays (URAs), the modified uniformly redundant arrays (MURAs), the hexagonal uniformly redundant arrays (HURAs) etc. These introduced schemes have different properties in terms of image reconstruction and open area fraction [98]. Figure 3.11 depicts one such coded mask based on the URA scheme.

These kinds of coded masks impose some constraints on the imaging system for the reconstruction to work, which may not be desirable depending upon the application. Binary arrays which are used to design coded masks have a specific relationship between the number of rows N_x and the number of columns N_y. Thus, coded masks of some specific aspect ratios only are possible which are usually close to unity. This can be a severe constraint for the highly rectangular neutron sources where the lesser dimension will dictate the size of mask thereby restricting the neutron optimum usage. Further, the number of pinholes being used and hence the open area fraction can take some particular fixed values only depending on the type of coding and the binary array size. Therefore, the open fraction other than some specific values cannot be selected even if desired. Moreover, the spatial resolution of the reconstructed image

is limited by the diameter of the pinholes present in the mask. The cross-correlation technique used to reconstruct the image also introduces an inherent noise in the reconstruction even when the collected data has no background and shot noise, thereby imposing an upper limit on the possible SNR [96]. Last but not the least, all the holes present in the mask must illuminate the entire object to be imaged (in the coded source imaging) for the reconstruction technique to work. Thus, with pinhole locations fixed as defined by the coding scheme, often a large beam divergence is required to illuminate the whole object by every single pinhole.

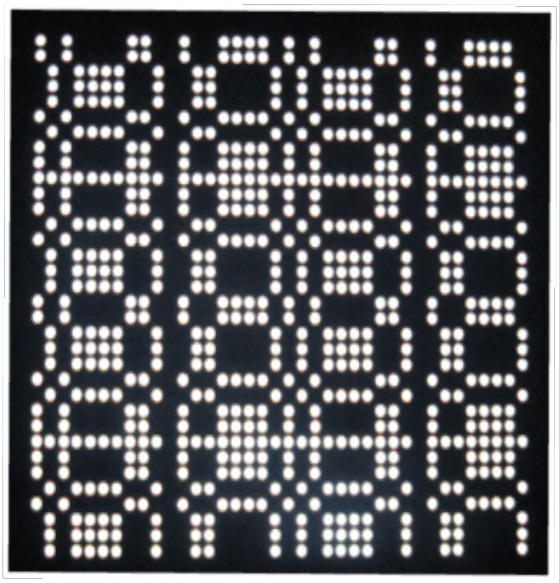

Figure 3.11. A coded mask with pinhole pattern based on the URA scheme.

In the present case the focus was mainly on performing phase contrast neutron imaging using multi-pinhole masks. Increasing the SNR without compromising the spatial and contrast resolution was the main objective of this exercise. If coded masks were to be used as the multi-pinhole neutron source then the diameter of the holes to be used in the coded mask is of the order of 100μm or less in order to meet the spatial resolution requirements. Such coded masks for neutrons are difficult to manufacture and will be expensive. Also, for phase contrast imaging very low beam divergence (or very large L/d ratio) is required which is not well suited the for coded mask technique.

Therefore, in this work an approach using un-coded masks where, the number of pinholes and their relative location can be decided using design requirements rather than the ease of reconstruction, was taken. In the next section mathematical formulation of the process of image formation using multi-pinhole masks will be presented. The design and the experimental verification will be presented in the next Chapter.

3.6 Image Formation using Multi-Pinhole Masks

Figure 3.12 presents a 1-dimensional ray diagram of the process of image formation. It can be observed that each of the single pinholes form a magnified and shifted image of the object on the image plane. Their algebraic sum along with the noise is the raw image collected at the image plane.

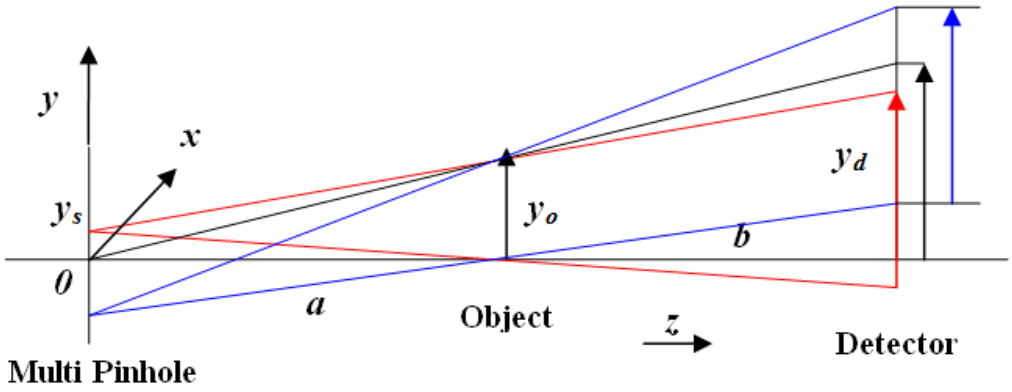

Figure 3.12. Ray diagram depicting the formation of overlapped images of the object on the detector by the multi-pinhole source.

In Figure 3.12 y_s, y_o and y_d are the Y axes at the source plane the object plane and the detector plane respectively. If Δy_o and Δy_d denote the difference in the Y co-ordinates between two points taken on the y_o and y_d axes respectively then using geometry it can be shown that the magnification of the object co-ordinate can be written as

$$\Delta y_d = \frac{(a+b)}{a}\Delta y_o, \tag{3.47}$$

where, a and b are the distance from the source plane to the object plane and the object plane to the detector plane respectively. Thus, the magnification obtained from each individual pinhole does not depend on the location of the pinhole on the source. Moreover, in this regard it should be mentioned that for a solid object of extended dimensions the distances a and b for different planes of the object will be different resulting in different magnification of each plane in the image. Further, the object imaged should be fairly large (but also within the field of view) compared to the size of the mask otherwise rays from each pinhole will have different ray path through the object resulting into a different view of the object on the image plane. In this case all the overlapping images formed will not have the same information and the obtained raw image will resemble to a limited angle tomography.

The relative shift of the formed images on the detector by each pinhole is given by

$$\Delta y_d = -\frac{b}{a}\Delta y_s , \tag{3.48}$$

where, all the symbols have their usual meaning. The negative sign in Eq. (3.48) indicates that the relative shift of the pinhole location and the formed image with respect to the Z axis is in opposite direction. Thus, a pinhole on the negative y_s axis will have the formed image shifted in the positive y_d axis by a factor of b/a.

Thus using Eq. (3.48), the image of the source mask $S_{img}(x_d, y_d)$ at the location of the detector plane obtained through a single pinhole object placed on the Z axis without taking into account the spreading due to geometric blurring can be written as

$$S_{img}(x_d, y_d) = S\left(-\frac{b}{a}x_s, -\frac{b}{a}y_s\right). \tag{3.49}$$

Further, using Eq. (3.47) the image obtained from a single pinhole $I_{pin}(x_d, y_d)$ can be related to the object reference system as

$$I_{pin}(x_d, y_d) = I\left(\frac{a+b}{a}x_o, \frac{a+b}{a}y_o\right). \tag{3.50}$$

The image formed by all the pinholes in the multi-pinhole mask at the image plane $I_{mask}(x_d, y_d)$ is sum of all the images as given by

$$I_{mask}(x_d, y_d) = \iint S_{img}(x_d', y_d') I_{pin}(x_d, y_d) dx_d' dy_d' . \tag{3.51}$$

Using Eq. (3.49) and Eq. (3.50), Eq. (3.51) can be written as

$$I_{mask}(x_d, y_d) = \iint S\left(-\frac{b}{a}x_s', -\frac{b}{a}y_s'\right) I_{pin}\left(\frac{a+b}{a}x_o, \frac{a+b}{a}y_o\right) dx_d' dy_d' . \tag{3.52}$$

From Figure 3.12 the relationship between the source, object and image plane co-ordinates can be written as

$$(x_d, y_d) = -\frac{b}{a}(x_s, y_s) + \frac{a+b}{a}(x_o, y_o), \tag{3.53}$$

which can be used along with Eq. (3.52) to show that

$$I_{mask}(x_d, y_d) = \iint S_{img}(x_d', y_d') I_{pin}(x_d - x_d', y_d - y_d') dx_d' \; dy_d' . \tag{3.54}$$

Thus, it can be observed that as in the case of coded aperture the raw image obtained in the case of multi-pinhole source too is a convolution between the source mask image at the detector and the image obtained using one pinhole mask on the detector and can be written as

$$I_{mask}(x_d, y_d) = S_{img}(x_d, y_d) * I_{pin}(x_d, y_d), \tag{3.55}$$

where, '*' denotes the two dimensional convolution operator.

To account for various unsharpness effects a blurring function needs to be taken into account. If $PSF_{pin}(x_d, y_d)$ is the point spread function of a single pinhole obtained at the image plane then the actual raw image obtained at the image plane can be written as

$$I_{raw}(x_d, y_d) = S_{img}(x_d, y_d) * I_{pin}(x_d, y_d) * PSF_{pin}(x_d, y_d) + \text{Noise}, \tag{3.56}$$

where, the noise consists of all the random noise in the collected raw data due to the counting statistics, detector inherent noise, scattering noise and gamma noise.

Next chapter will present the design of a multiple pinhole imaging system. The data collected from that system will be reconstructed using the inverse techniques applicable to the above presented formulation of the image formation process. The reconstruction technique and the results will be addressed in detail in Chapter 5.

CHAPTER 4

DESIGN AND TESTING OF PHASE CONTRAST AND MULTI-PINHOLE NEUTRON IMAGING SYSTEMS

4.1 Introduction

This chapter presents the system design for the phase contrast and multi-pinhole neutron imaging. The experiments conducted with the designed system are also presented which verify the working of the system as designed.

Starting from the next Section the design of the single pinhole phase contrast neutron imaging system will be presented. Along with the design a simulation technique developed to predict phase contrast neutron image of a given object will also be presented. Experiments conducted with the single pinhole system will follow its design. Lastly, the design of the multi-pinhole collimator and its experimental testing will be outlined.

4.2 Design Considerations for Phase Contrast Imaging

In Chapter 3 the physics of phase contrast neutron imaging was presented. From the physics of phase contrast imaging it becomes clear that for obtaining phase contrast intensity variation in the neutron image as indicated by Eq. (3.19), high spatial coherence of the neutron beam is necessary. Further, to achieve the high spatial coherence in the beam the average energy of the beam should be lowered and the L/d ratio of the system should be maximized. In order to quantify these requirements better for thermal neutron beam simple calculations can be performed using practical values of different parameters. Thermal neutrons have wavelength λ of the order of 10^{-10} m. Thus, to achieve a L_t of the order of micrometers (i.e. of the order of

detection resolution of neutron radiographs) $L/d \geq 10,000$ is required which is much higher than the L/d for conventional neutron imaging. To achieve such a high L/d ratio, the neutron source effective diameter d must be reduced to a pinhole. For example if the beam line length L is 10 meters then d is 1mm to obtain the $L/d = 10,000$.

Above were the design considerations dictated by the physics in order to perform phase contrast imaging. But, along with these there are some practical considerations which must be accounted for in the design. Two of the most important practical considerations are, obtaining enough neutron flux at the image plane and to maintain a good signal to noise ratio in the presence of gammas in the beam. Most of the available neutron sources have flux intensity much lower than X-ray sources available. If the source size is reduced to a pinhole, as required here, then the available neutron flux (φ_n) at the image plane reduces drastically as indicated by Eq. (4.1). This increases the exposure time (T_E) required to collect the image.

$$\frac{1}{T_E} \propto \varphi_n \propto \left(\frac{d}{L}\right)^2 . \tag{4.1}$$

Further, neutron beams, specifically those obtained from reactors, are often contaminated with gamma rays. Thus, if the imaging detector is sensitive to gamma rays, then the SNR of the collected data might be very low because of the reduced intensity of the neutrons at the image plane. Thus, the design requirement for the phase contrast neutron imaging is:

- Objective: Maximization of the neutron beam expected wavelength and the L/d ratio;

- Constraint: (i) Maintain a required minimum amount of neutron flux at the image plane and (ii) Maintain moderate beam N/G ratio (if gamma sensitive detectors are being used).

Hence, a constrained maximization of the objective defined above has to be performed. To achieve the optimum between maximizing the transverse coherence length (L_t) and the neutron flux (φ_n) radiation transport simulations can be used as a design tool.

4.3 Image Simulation Technique

Phase contrast enhancement in the neutron images only occurs at the material edges of the sample differing in coherent scattering length density. Therefore, the degree of edge enhancement depends on the kind of material edges present in the sample. In such a situation it may be desirable to have a simulation tool which can predict the contrast obtainable through this technique for a particular sample given the beam and the design parameters, in order to evaluate the usefulness of the technique for that particular sample. Further, it also provides the luxury to use different design parameters and observe the changes in the contrast of the image. This gives the insight into design modifications which can possibly be performed in order to make this modality suitable for some particular application. Thus, the simulation technique can be used as a decision making tool for choosing this technique in any particular setting and for some specific application. Therefore, a simulation strategy was developed keeping the above objective in consideration.

As mentioned before, phase contrast imaging does not require temporal coherence and thus can be performed with polychromatic neutron beam. For a polychromatic beam and a material with varied composition an approximate approach to obtain the intensity image would be to use the expectation value of the parameters involved in Eq. (3.19) that is taken over the neutron energy spectrum as

$$E_\lambda\left[I(x,y)\right] = E_\lambda\left[I_o e^{-2\mu}\left[1+\frac{R\lambda}{2\pi}\nabla^2\Phi - \frac{R\lambda}{\pi}\nabla\Phi\cdot\nabla\mu\right]_{(x,y)}\right], \tag{4.2}$$

where $E_\lambda[.]$ is the expected value of $[.]$ taken over all wavelengths. In order to perform the expectation operation the neutron energy spectrum should be known. Moreover, in obtaining Eq. (3.19) it has been assumed that the functions $\Phi(x,y)$ and $\mu(x,y)$ are at least twice differentiable with respect to x and y. Although in most of the practical cases we have an edge function (as most of the samples are made out of different materials with explicit edges) which is not differentiable, the above formulation is applicable because the edge function is smoothed by the convolution '*' with the point spread function ($PSF(x,y)$), thus making it

differentiable. This is the same point spread function which was responsible for image blurring in Chapter 1. The final neutron intensity image ($I_{tot}(x,y)$) obtained on the screen is given by

$$I_{tot}(x,y) = E_{\lambda}\left[I(x,y)\right] * PSF(x,y). \tag{4.3}$$

Equation (4.3) along with Eq. (3.39) and (3.41) are the working equations which should be used for formulating the simulation technique for phase contrast images.

The working equations need to be discretized in order to use them for numerical simulations. In general the Laplacian operator ∇^2 can be discretized up to the first order as

$$\nabla^2_{\alpha} = \frac{1}{\alpha+1}\begin{bmatrix} \alpha & 1-\alpha & \alpha \\ 1-\alpha & -4 & 1-\alpha \\ \alpha & 1-\alpha & \alpha \end{bmatrix}, \tag{4.4}$$

where $0 \le \alpha \le 1$. ∇^2_{α} is called the Laplacian filter whose convolution with the function returns the approximation of the Laplacian of the function. With $\alpha = 0$ it becomes the regular second order central differencing scheme which is isotropic. Other values of α make ∇^2_{α} anisotropic. The gradient operator in general can be discretized up to the first order using isotropic central differencing scheme which is given for any function f by

$$\nabla_d f(x,y) = \left(\frac{f_{i+1,j} - f_{i-1,j}}{2\Delta x}, \frac{f_{i,j+1} - f_{i,j-1}}{2\Delta y} \right), \tag{4.5}$$

where Δx and Δy is the width of the pixel in x and y direction which is often equal. Thus, it is simple difference operation and no convolution is required to perform this. Other gradient filter which can approximate the gradient operator is the *Sobel* filter ∇_s [99] given by

$$\nabla_{sx} = \begin{bmatrix} 1 & 0 & -1 \\ 2 & 0 & -2 \\ 1 & 0 & -1 \end{bmatrix}; \nabla_{sy} = \begin{bmatrix} 1 & 1 & 1 \\ 0 & 0 & 0 \\ -1 & -2 & -1 \end{bmatrix}; \nabla_s = \left(\nabla_{sx}, \nabla_{sy}\right). \tag{4.6}$$

In this case the convolutions of the image with ∇_{sx} and ∇_{sy} return gradients in x and y direction respectively. Both these discretization techniques are also used for the edge detection in the image. Using these discretization techniques Eq. (4.2) can be written as

$$E_\lambda\left[I(x_i,y_j)\right]=E_\lambda\left[I_o e^{-2\mu}\left[1+\frac{R\lambda}{2\pi}\nabla_\alpha^2\Phi-\frac{R\lambda}{\pi}\nabla_d\Phi\cdot\nabla_d\mu\right]_{(x_i,y_j)}\right], \tag{4.7}$$

where $\left(x_i,y_j\right)\ i=1:I;\ j=1:J$ are the coordinate locations of the discretized image.

If the energy spectrum (as energy histogram) of the neutron beam is known then the wavelength spectrum can be obtained by converting histogram energy bins into the wavelength bins. The wavelength of the neutron can be calculated from its energy by

$$\lambda=\frac{h}{\sqrt{2mE}}. \tag{4.8}$$

A good approximation to the wavelength probability density function $p\left(\lambda_m\right)\ m=1:M$, M being number of histogram bins, can be obtained from the wavelength histogram by normalizing it to have a total area of unity. This approximate wavelength density function can be used to calculate the expected value in Eq. (4.7) as

$$E_\lambda\left[I(x_i,y_j)\right]=\sum_{m=1}^{M}I_o p\left(\lambda_m\right)e^{-2\mu(\lambda_m)}\left[1+\frac{R\lambda_m}{2\pi}\nabla_\alpha^2\Phi\left(\lambda_m\right)-\frac{R\lambda_m}{\pi}\nabla_d\Phi\left(\lambda_m\right)\cdot\nabla_d\mu\left(\lambda_m\right)\right]_{(x_i,y_j)}, \tag{4.9}$$

where

$$\Phi\left(x_i,y_j,\lambda_m\right)=-\lambda_m\int_t a_c(x_i,y_j,z)\rho\left(x_i,y_j,z\right)dz\text{, and} \tag{4.10}$$

$$\mu(x_i,y_j,\lambda_m)=\frac{1}{2}\int_t\sigma_{Tot}(x_i,y_j,z,\lambda_m)\rho(x_i,y_j,z)dz. \tag{4.11}$$

It should be noticed that the coherent scattering length is not taken as a function of neutron wavelength (or energy) whereas the microscopic cross-section energy dependence must be considered. This is because coherent scattering lengths do not have strong energy dependence unlike the microscopic cross-section. Moreover, energy dependent scattering length data for different materials is not easily available.

In order to perform these calculations radiation transport calculations can be performed. But most radiation transport codes do not perform wave optics calculations (which include phase contrast calculations). Hence, for that purpose custom computer codes may be required. The information on the neutron energy dependent cross-section and the coherent scattering length required in order to perform phase contrast calculations for the given material can be obtained through various sources like neutron transport codes cross-section libraries and various reliable online resources [100], [101]. These sources mostly provide the data for elements and its isotopes. The data for polyatomic systems, like compounds, mixtures, alloys etc., can be calculated if its elemental composition and mass density is known. For a polyatomic system the coherent scattering length density, $a_c\rho$ can be written as

$$a_c\rho = \sum_l a_{c_l}\rho_l \,, \tag{4.12}$$

where l labels the contributions of various atomic species [88]. For a system of identical molecules, on the other hand, ρ can be taken as the average number of molecules per unit volume, in which case a_c is the bound coherent scattering length of a single molecule is given by

$$a_c = \sum_l N_l a_{c_l} \,, \tag{4.13}$$

where N_l is the number of atoms of type l per molecule. The cross-section for the polyatomic systems can be calculated in a similar fashion.

Equation (4.9) along with Eq. (4.10) and Eq. (4.11) present the fully discretized version of Eq. (4.2). In order to obtain the effect of blurring in the image the PSF for the specific

geometry must be simulated. For the simulation of PSF radiation transport calculations can be performed in a similar fashion as in Chapter 2. The calculated PSF can be used to obtain the final intensity variation of the image using Eq. (4.3) in discrete form as

$$I_{tot}\left(x_i, y_j\right) = E_\lambda\left[I(x_i, y_j)\right] * PSF\left(x_i, y_j\right), \tag{4.14}$$

where '*' denotes the discrete two-dimensional convolution operator.

4.4 Design Performance for PULSTAR

Design calculations were performed keeping in consideration the design objectives and constraints specified in Section 4.2. Monte Carlo radiation transport calculations were performed using MCNP5 to design the collimator. The calculations were similar in nature to the once presented in Chapter 2 and therefore details of these calculations are being skipped.

As mentioned in Chapter 2, the available beam line length at the facility is limited to 6 meters (can be increased to ~7m with some geometry changes) which has to be divided between the pinhole to object distance L and the object to detector distance R. For the phase contrast effect to develop in the image usually about a meter to two meters of distance between the object and the detector is desired. Taking this into account, the pinhole-to-object distance L for the design was taken to be 5m. With the requirement of $L/d \geq 10,000$ for a thermal neutron beam (which is the beam characteristic at the PULSTAR) the required pinhole diameter was calculated to be $d \leq 0.5mm$. The pinhole defining material was selected as 500μm thick foil of gadolinium as it is the best absorber of the thermal neutrons. Further, the beam divergence had to be lowered as discussed Section 4.2. In order to be able to accommodate objects a few centimeters wide it was decided to have a beam divergence big enough to get a beam diameter of 130mm at the farthest image plane.

Radiation transport simulations revealed that the pinholes with diameter smaller than 0.5mm are not feasible to have in terms of getting sufficient neutron flux at the image plane. Thus, the pinhole diameter was fixed to be 0.5mm. With this diameter of the pinhole, the available beam line length and the required size of the beam at the image plane, the beam

divergence was calculated using simple ray tracing to be 0.6 degrees. This angle of divergence was also verified by performing radiation transport to obtain the beam size and uniformity at the actual image plane. The obtained beam size using MCNP5 at the 6m image plane is shown in Figure 4.1. From the figure it can be clearly observed that the beam is very uniform at the image plane with a diameter of ~130mm.

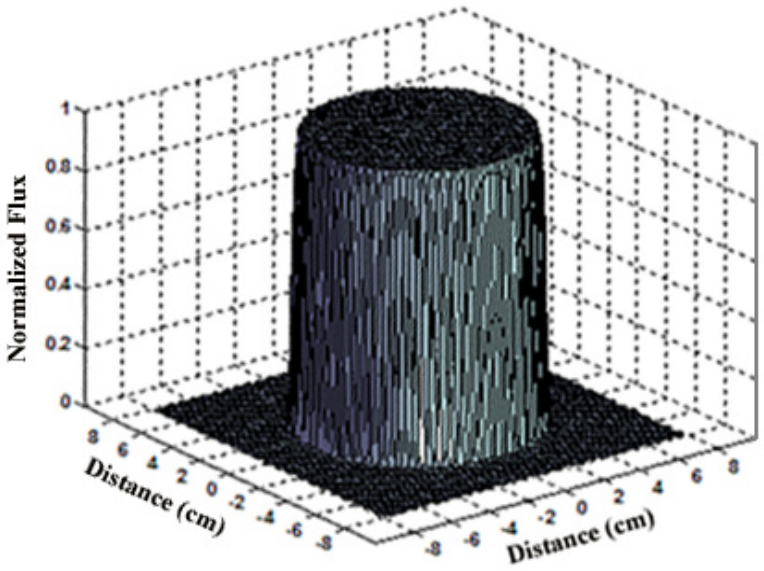

Figure 4.1. Simulated beam profile at the 6m image plane.

With the fixed L/d ratio, the beam transverse coherence length can be increased only by increasing the average wavelength (or decreasing the average energy) of the neutron beam. One way to achieve this is by cooling the neutron beam to shift the overall energy spectrum to lower energies. Cooling requires elaborate cryogenic setup which is expensive. Also, it will possibly consume some beam line space. Moreover, putting the cooling mechanism inside the beam tube will require design alterations in multiple other components. Therefore, this option was not viable to implement at the facility. The alternative approach was to increase the thermal neutron content (TNC) of the beam by filtering the fast neutrons while maintaining sufficient neutron flux at the image plane. Further, for the reduction of gamma noise in the beam that reaches the image plane gamma filtration had to be performed. Same filter materials as before

(sapphire and bismuth) were selected for this purpose because of their comparatively better filtration properties over other materials (see Chapter 2 for details). Their length optimization was performed using MCNP simulations in the similar manner as in Chapter 2 with the objective of maximizing the neutron beam TNC (and hence the average wavelength) and the constraint of maintaining a minimum required neutron flux at the image plane that keeps the exposure time for the neutron image plates less than three hours. Neutron image plates were selected as the detector of choice for this purpose because they have highest neutron sensitivity (speed) among all the available detector options sited in Chapter 2. Also, they were also thought to be fairly insensitive to gamma rays.

MCNP simulations indicated that the bismuth, although desirable for gamma filtration, could not be used in the design because of significant neutron flux reduction. Significant attenuation of the neutrons occur in the bismuth because of the misalignment of bismuth cross-section energy window and the neutron energy spectrum thermal peak as shown in Figure 4.2. It can be further observed from the figure that the sapphire cross-section energy window has a good alignment with the neutron energy spectrum thermal peak, which makes it well suited for the present beam. From the MCNP calculations performed using only sapphire filter it was observed that 3 inches of sapphire provided enough increase in the TNC (neutron energy spectrum shown in Figure 4.3) to have a transverse coherence length (L_t) of 1.47μm. The neutron flux also seemed to be reasonable (towards the higher side), although the exact neutron flux requirement for obtaining a three hour exposure time was unknown (and was also not required). Moreover, decreasing the filter length will decrease the transverse coherent length below one micrometer which was not considered desirable. Hence, as far as filter optimization was concerned, it was decided to proceed with at least 3 inches of sapphire filter with the realization that increase in the filter length is preferable to obtain higher TNC if permitted by the neutron flux constraint during the testing phase.

The collimator design finalized through this design process is shown in Figure 4.4. It can be observed from the collimator design the angle of divergence of the divergent section has been decreased from 2.3^o to 0.6^o. Further, the material forming the diverging section (SWX-277) is replaced by borated polyethylene. This change was performed for the ease of

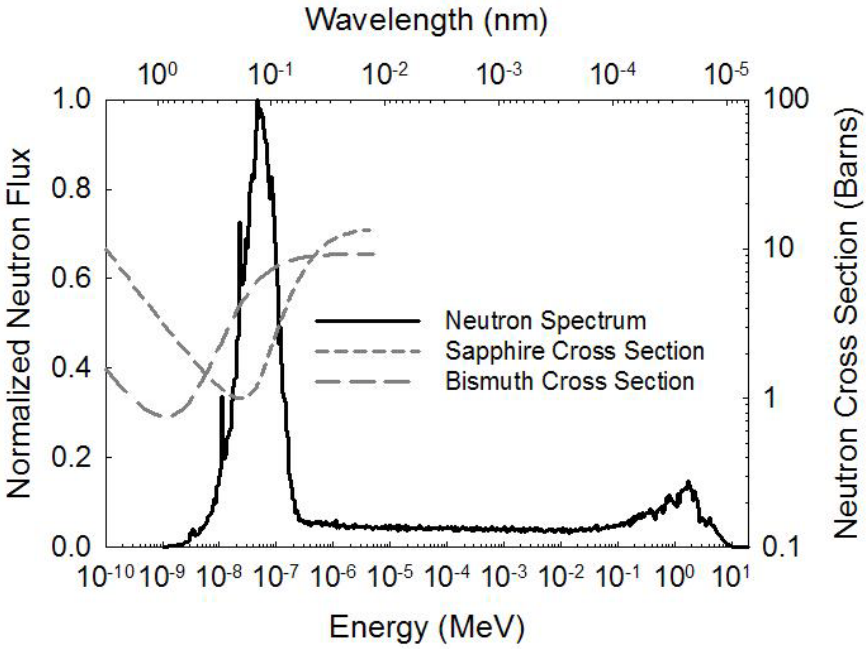

Figure 4.2. Neutron source energy spectrum plotted along with the sapphire and the bismuth thermal neutron cross-sections.

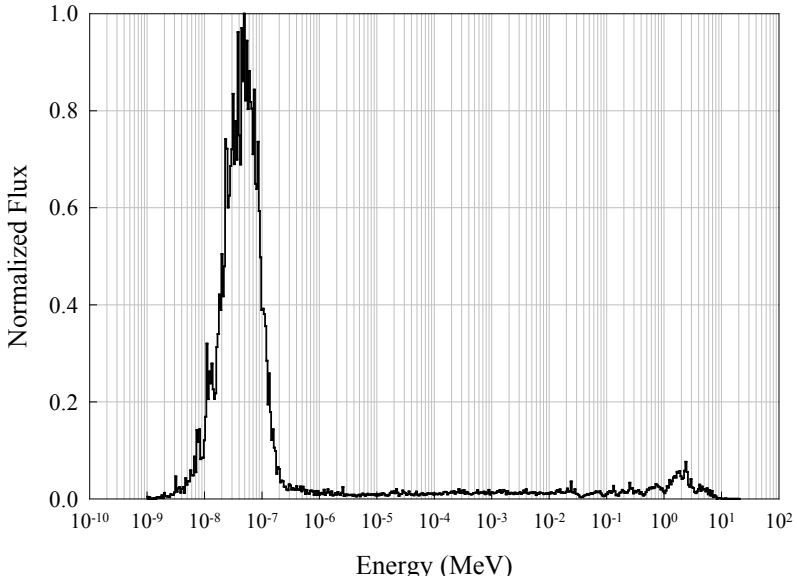

Figure 4.3. Neutron energy spectrum at the image plane using 3 inches of sapphire filter.

manufacturing and better precision and alignment of the parts. With SWX-277 casting has to be performed in which it is difficult to achieve good accuracy. In terms of attenuation of neutrons both the materials are sufficient to stop the thermal neutrons almost completely. Two and half inches of lead were used in the filter holder to decrease gamma ray streaming from that region. Lead was not used in defining the divergent collimator because it was thought to create machining and alignment problems. Moreover, as mentioned above the neutron image plates were being misconceived to be fairly insensitive to gamma rays. Due to these reasons the gamma noise issue was not handled sufficiently in this design process. Alterations to the presented design (in Figure 4.4), that were mainly guided towards eliminating the gamma noise and improving the TNC further, will be presented later.

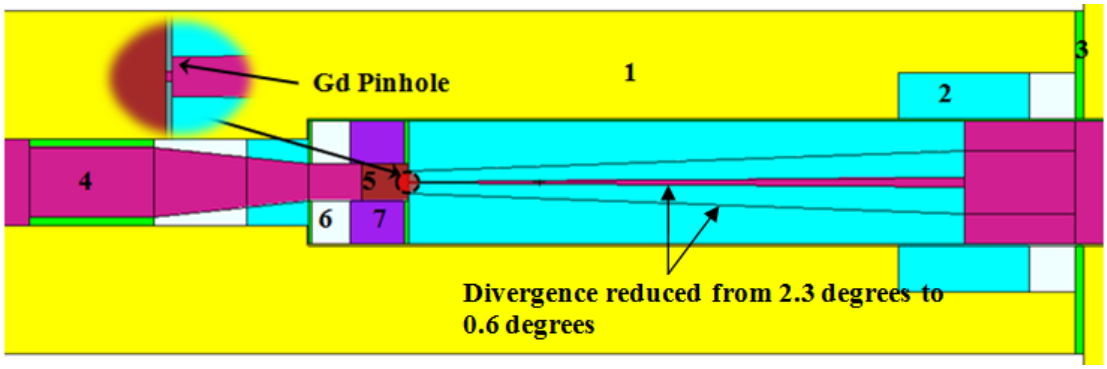

Figure 4.4. MCNP design of the collimator. The material specifications are (1) Concrete (2) 5% Borated Polyethylene (3) Aluminum (4) Air (5) Sapphire Filter (6) Lead (7) SWX-277 (look in Chapter 2).

4.5 Phase Image Simulations

Phase image simulations were performed of the designed phantoms using the simulation technique outlined in Section 4.3. The design parameters and the neutron beam characteristics required for this purpose, like the pinhole diameter, the L/d ratio, the neutron beam energy spectrum (shown in Figure 4.3) etc., were taken from the design presented above. This exercise was performed to verify the presented simulation technique and study phase contrast formulation for the phase-amplitude objects. It should be mentioned that the simulation

technique is applicable in general and other design parameters and characteristics can also be used.

The phantoms were designed to depict various edges that are possible in objects characterized by difference in the transmission functions of the edge forming materials. Phantom 1 was selected to include various engineering, structural, ornamental, nuclear and aerospace materials with moderate but almost similar attenuation contrast. For example, steel is a common structural material, titanium is an aerospace material, nickel-silver composites are used for electrical contacts and electrodes, zirconium and zircaloy is used in nuclear fuel cladding. It is these type of materials on which non destructive testing and non-invasive measurements need to be performed through imaging to locate possible cracks, voids, delaminations in composites, corrosion sites, misalignment etc. Precisely locating the edges constitutes an important step in performing any of the above tasks using the obtained images.

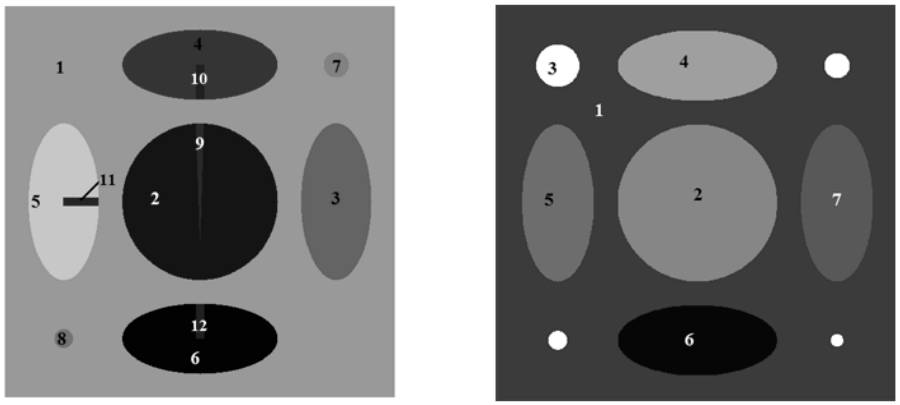

(a) **(b)**

Figure 4.5. Geometry of (a) Phantom 1 (b) Phantom 2. Table 4.1 gives the material composition of the phantoms.

Phantom 2 was selected to include organic and biological materials to investigate phase contrast enhancement in such samples. These materials are either present in plants or animal bodies or are very similar to them. For example, International Commission on Radiological Protection (ICRP) defined soft tissue and bone are equivalent to biological tissue and bone,

sapphire specks (Al_2O_3) are used in phantoms to simulate micro-calcifications, nylon fibers are used to simulate fibrous structures, acrylic is used to simulate breast tissues [102], urea is used as fertilizer for plants etc. The geometry of the phantoms and the material composition are shown in Figure 4.5 and Table 4.1 respectively.

Table 4.1 The material composition of the phantoms used in the simulations.

Mat#	Phantom 1	Phantom 2
1	Iron	ICRP Soft Tissue
2	Fe-57	ICRP Bone
3	Platinum	Sapphire
4	Zircaloy-4	Urea
5	Nickel	Ethyl Acrylate
6	Titanium	Water
7	SS304	Nylon
8	CS A501	
9	Niobium	
10	Zirconium	
11	Silver	
12	Chromium	

To simulate neutron images of the phantoms, the $PSF(x,y)$ values were calculated at different object to image plane distances assuming a 0.5mm diameter point source and a beam divergence of 0.6^o. Attenuation radiograph $I_{att}(x,y)$ simulation of the selected phantoms were performed using MCNP5 at the same object to image-plane distances. The simulations were executed on a Linux cluster available in the High Performance Computing (HPC) Center at NCSU. The cluster has 612 dual Xeon nodes. Each node has two Xeon processors (mix of single-, dual- and quad-core) that have 2 Gigabytes (GBs) of memory per core and 36-37GBs of disk-space. For each image simulation 2×10^9 particles were run in four cycles with each cycle run on 24 processors for two hours. To further improve the counting statistics pinhole detectors were used to bring the relative error in every pixel inside the field of view of the pinhole down to ~0.6%. The magnification of the attenuation images were obtained accurately using the *Sobel* edge detection algorithm [99]. The calculated magnification and the obtained PSFs were used to obtain the pure phase and the phase-amplitude interaction images of the corresponding phantom at the same object to image-plane distance. From Eq. (4.9) it is clear that the final image is the algebraic sum of these three images. The coherent scattering length densities

$a_{coh}(x,y,z)\rho(x,y,z)$ for different materials required for simulating phase images were calculated using the data obtained from the National Institute of Standards and Technology (NIST) database [100]. For the purpose of simulation $\alpha = 0$ was used in Eq. (4.4) to approximate the Laplacian performing isotropic filtering. Central finite difference scheme was used to discetize the gradient operator (see Eq. (4.5)). A pixel size of 50μm was selected in the image simulation.

4.5.1 Simulation Results

The simulated radiographs of Phantom 1 are shown in Figure 4.6. All the radiographs are on the same gray scale. Figure 4.6(a), Figure 4.6(b) and Figure 4.6(c) depict the attenuation only, pure phase effect and phase-amplitude interaction effect radiographs respectively corresponding to the first, second and the third term in Eq. (4.9). Figure 4.6(d) depicts the total phase effect which is the algebraic sum of the pure phase and the phase-amplitude interaction effects. Figure 4.6(e) and Figure 4.6(f) depict radiographs of the object considering it as a pure phase object and as a phase-amplitude object respectively.

Clearly, the attenuation only radiograph does not provide enough contrast for all the edges of the object to be distinguishable in the image. As is clear from the phase images, the phase effect does not provide different intensities in different materials which may be important for obtaining material makeup information of the object but, it enhances the edges between the materials providing the geometry information of the object. Comparing Figure 4.6(b) and Figure 4.6(c), it can be observed that the phase-amplitude interaction term provides less contrast than the pure phase term but still is not negligible. This happens because the pure phase term involves a higher order derivative which increases the frequency and amplitude of intensity oscillation and hence higher contrast on the gray scale is visible. Also, the magnitude of the phase-amplitude interaction effect depends on the difference in the coherent scattering length densities of the edge forming materials. For example, the nickel-silver edge has more interaction effect than other edges even with a little difference in their attenuation coefficients. The difference in the contrast due to these interaction effects can also be observed when Figure 4.6(e) and Figure 4.6(f) are compared. This indicates that for some material edges the

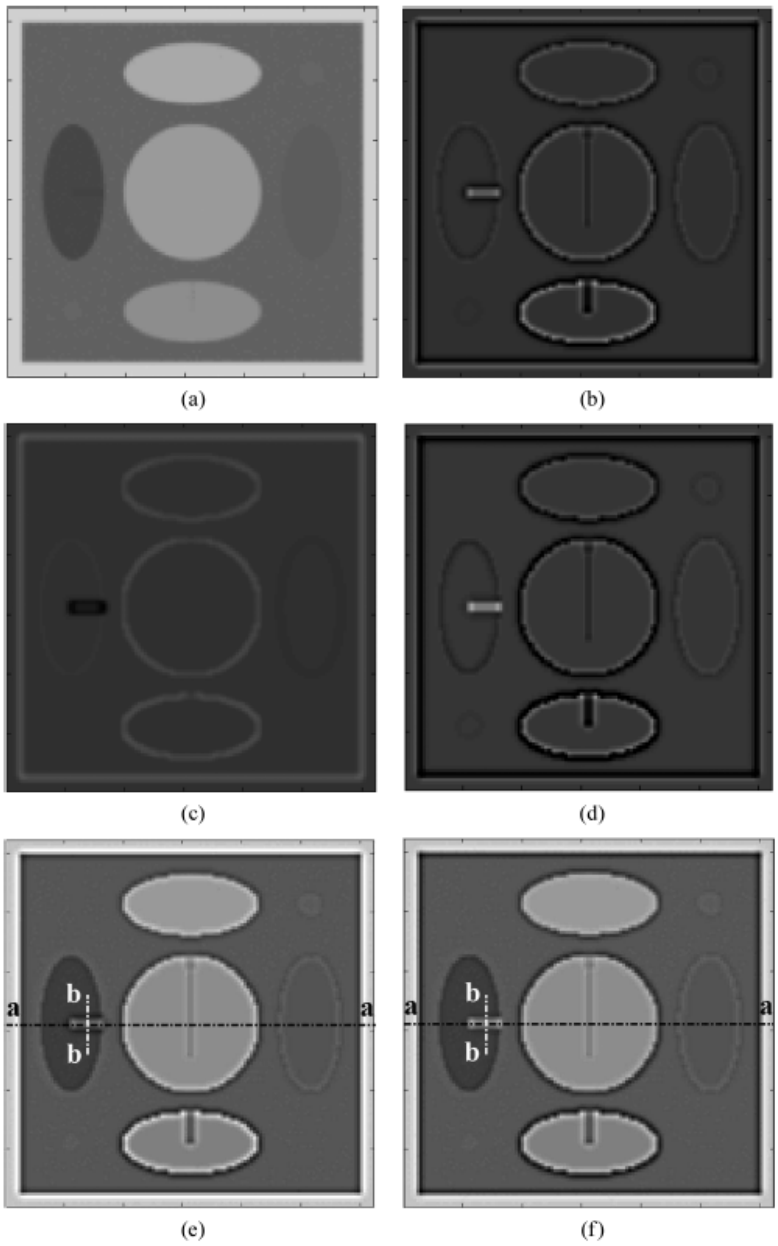

Figure 4.6. Phantom 1 Simulation Results: (a) Normal Attenuation Radiograph (1st term in Eq. (4.9)) (b) The pure phase image (2nd term in Eq. (4.9)) (c) The phase amplitude interaction image (3rd term in Eq. (4.9)) (d) The phase image with phase-amplitude interaction which is the difference of (b) and (c) as given by Eq. (4.9) (e) Phase contrast radiograph with pure phase approximation (1st and 2nd term in Eq. (4.9)) (f) Phase contrast radiograph with phase-amplitude interaction (all terms in Eq. (4.9)). The object to detector distance *R* = 80cm. The grayscale for all six images is the same.

interaction effect (i.e., the third term in Eq. (4.9)) can become really important. Comparing Figure 4.6(a) and Figure 4.6(f), it can be observed that features like cracks and material intrusions, which were not visible in the attenuation image due to similar attenuation coefficients, become visible in the phase enhanced image because of the difference in their scattering length densities.

Figure 4.7(a) and Figure 4.7(b) depict the normalized intensity profiles taken across the horizontal slice '*a*-*a*' and the vertical slice '*b*-*b*' that are shown in Figure 4.6(e) and Figure 4.6(f). These figures illustrate the sharp intensity changes at the edges because of the phase effect. Quantitative effect of the phase-amplitude interaction term can also be observed in these figures. A significant interaction effect appears at the nickel-silver edge in the profiles. In addition, an edge overlap effect arises in the profiles due to the spread of the contrast from adjacent silver edges as silver intrusion in the nickel is considerably thin. Moreover, it can be observed that at the edges phase-amplitude interaction image profile has a higher maximum and a lower minimum, which is due to the asymmetry introduced by the interaction term in Eq. (4.7). This observation can be interpreted with the aid of Figure 4.8. The figure depicts the shape of a generic intensity variation introduced by the pure phase and the phase-amplitude interaction terms of Eq. (4.7) for a material edge in a given sample. As it can be seen, the pure phase consideration leads to an intensity redistribution that has odd symmetry about the mean intensity at the edge. The minimum appears in the material with higher neutron scattering length density. The phase-amplitude interaction term leads to an intensity profile with even symmetry about the edge. Thus, the difference of these two terms (as in Eq. (4.7)) offsets the intensity symmetry by adding intensity on one side and subtracting on the other side of the edge, which results in the profile shown in Figure 4.8.

The simulated radiographs of Phantom 2 are shown in Figure 4.9 and Figure 4.10. Figure 4.9(a), Figure 4.9(b) and Figure 4.9(c) depict the attenuation only radiograph, pure phase approximation radiograph and mixed phase-amplitude approximation radiograph respectively. The gray scale of the radiographs is also shown along with the figures. Figure 4.9(a) clearly indicates that there is small attenuation contrast present in the sample except at the sapphire specks. On the other hand, Figure 4.9(b) and Figure 4.9(c) indicate the presence of significant

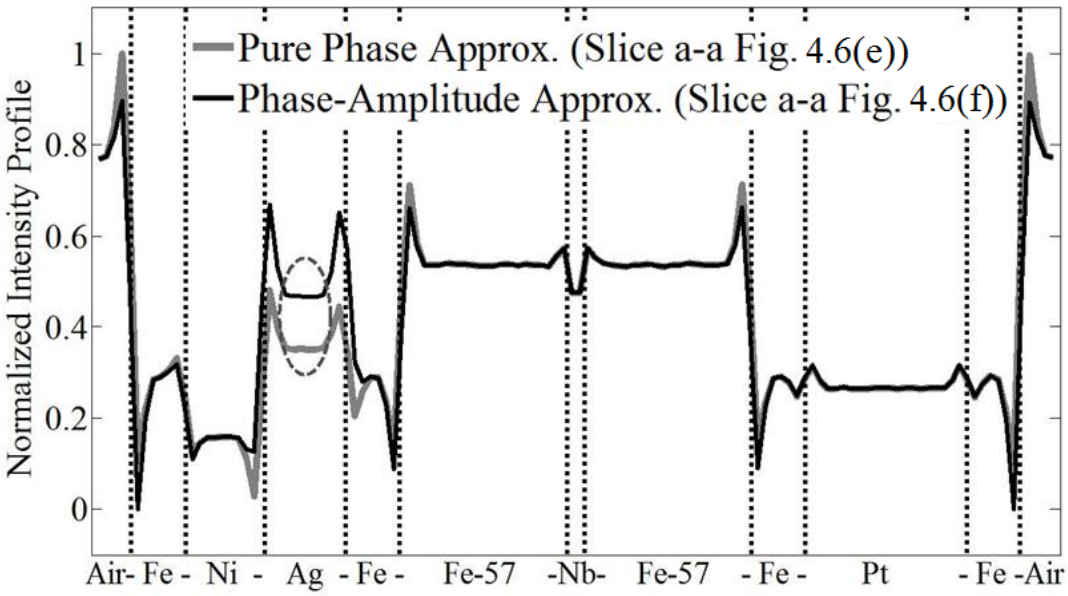

(a)

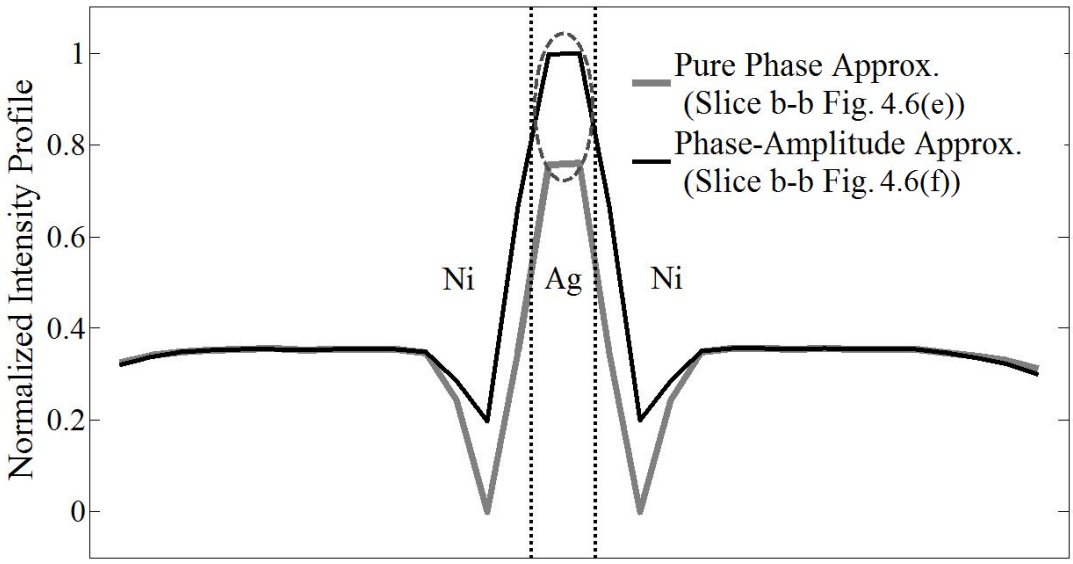

(b)

Figure 4.7. An intensity profile taken across (a) slice '*a-a*' of Figure 4.6(e) and Figure 4.6(f) and (b) slice '*b-b*' of Figure 4.6(e) and Figure 4.6(f). The profiles compare the pure phase and the mixed phase-amplitude approximations. The circled regions show the edge overlap effect.

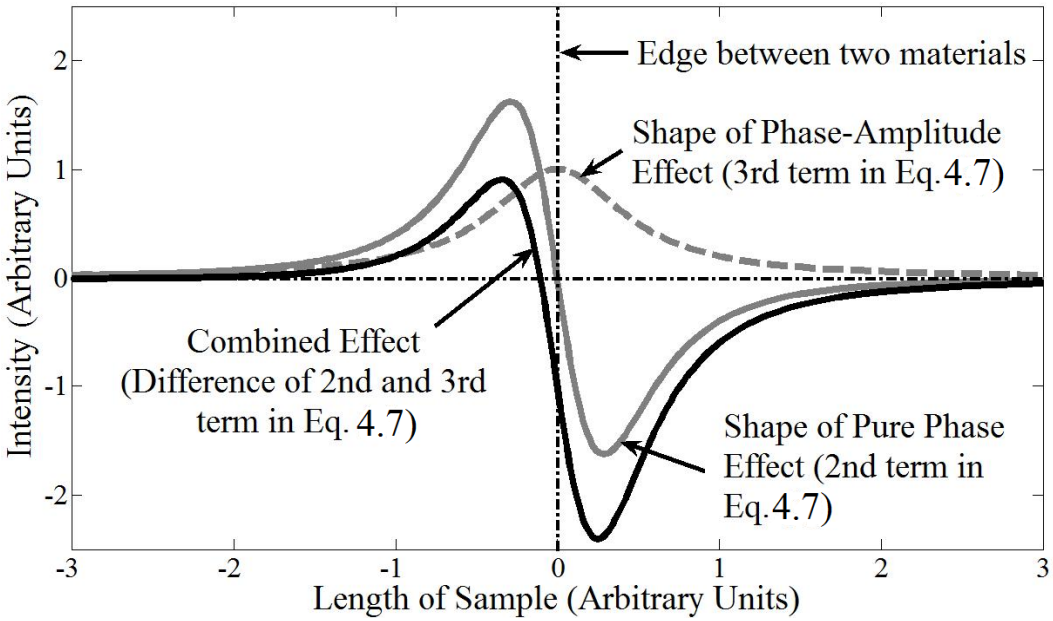

Figure 4.8. The shape of the pure phase term with odd symmetry about a material edge in a sample, the phase-amplitude interaction term with even symmetry about the edge in the sample and their difference which is asymmetric about the edge.

phase contrast effect in these organic and biological materials especially between ICRP soft tissue and urea, which was invisible in attenuation contrast. The presence of such a high phase contrast among these materials makes neutron phase contrast imaging suited for imaging biological and organic samples. Observing the phase images obtained for Phantom 2 in Figure 4.10 it is clear that little phase-amplitude interaction is present in these biological materials except at the sapphire-tissue edge. At this edge the interaction is large because of the comparatively large difference in the attenuation coefficient and not so much due to the large difference in the neutron scattering length densities as was the case for the nickel-silver edge in Phantom 1. The effect of this interaction is also clearly visible in the final phase image in Figure 4.10(c).

Therefore, for these biological materials it can be concluded that for thin samples the pure phase approximation works fine, nevertheless the combined phase-amplitude analysis will always perform better. Phantom 2 constitutes an example where there are some material edges

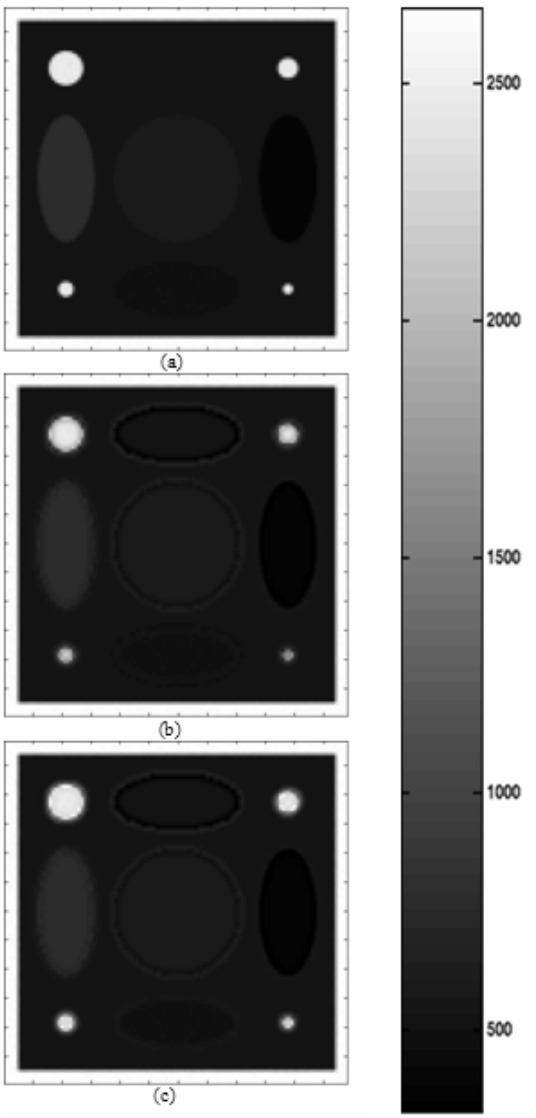

Figure 4.9. Phantom 2 simulation results: (a) Normal Attenuation Radiograph (b) Phase contrast radiograph with pure phase approximation (c) Phase contrast radiograph with phase-amplitude interaction. The object to detector distance *R* = 50cm.

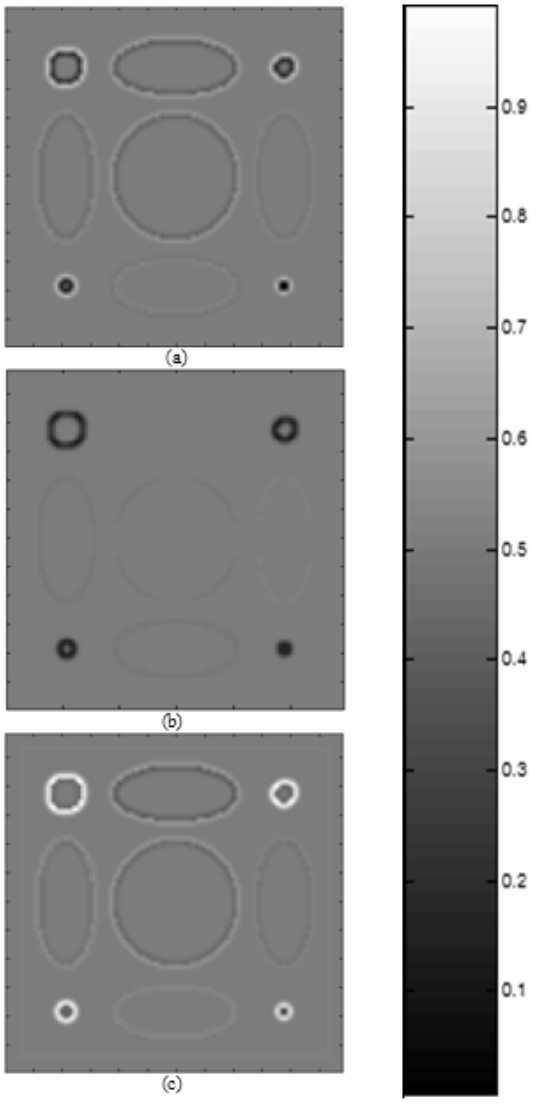

Figure 4.10. Phantom 2 Simulation Results: (a) Phase image using pure phase approximation (b) Phase-amplitude interaction image (c) The phase image with phase-amplitude interaction which is the difference of (a) and (b) as given by Eq. 4.9. The object to detector distance *R* = 50cm. The images were normalized between zero and one.

present which have significant phase-amplitude interaction and other edges where it is not significant. In such samples the interaction term will decrease the contrast at those edges that

already have high attenuation contrast and thus virtually expand the gray scale for the lesser contrast edges to become more prominent in the digital image. This effect can be observed in Figure 4.10(c) where the sapphire edges are suppressed by the interaction term to make other edges more prominent. Thus, the phase-amplitude interaction term can increase the contrast at those edges where it is needed by providing rescaling of the gray scale in the digital image.

4.6 Design Verification and Experimental Results

4.6.1 Design Verification

The designed collimator presented in Section 4.4 was manufactured for testing and performance of phase contrast experiments. The pinhole aperture was made of a 500μm thick gadolinium (Gd) foil. The divergent section of the collimator, ~36 inches long, is made up of discs of an inch thick borated polyethylene (5% boron content) with holes of increasing diameter in steps of 0.5mm starting at a diameter of 1.5mm. This provided ease of machining and also renders itself to easy design alterations if required without compromising with any design objectives. The design provides a beam divergence of 0.6 degrees which translates into a beam size of 135mm at the farthest image plane located at 685cm from the aperture. The borated polyethylene prevents the streaming of neutrons through the regions other than the central holes. All the borated polyethylene discs were encased inside an aluminum tube as shown in the designed collimator in Figure 4.4.

The manufactured divergent collimator section along with 3 inches of sapphire filter and its holder was inserted in the beam-tube for its testing. This was easy to perform by removing the other filter section and the diverging collimator (the filter arrangement and the collimator presented in Chapter 2) because of the modular design of the whole collimator assembly. Various image plate bare beam (no object placed) exposure exercises for different exposure time ranging from 30 minutes to 4 hours were performed. The images obtained indicated that the whole image plate was being exposed with a central circular region having a little higher density values. From this it was concluded that the image plates are getting exposed by the gamma rays which are not being stopped by the borated polyethylene and the gadolinium. Due to this reason the gamma flux was many orders of magnitude higher than the neutron flux at the

image plane. During the long exposure time required to obtain enough neutron fluence at the image plate the large gamma fluence builds up a huge background almost saturating the image plates. Hence, the neutrons do not produce significant difference in the density in the central circular region of the image plates. Thus, the conception of neutron image plates being almost insensitive to gamma rays turned out to be wrong.

In order to rectify this problem of gamma exposure the collimator design had to be altered. To reduce the gamma noise three 0.5 inch thick lead discs were introduced having central holes of diameter 1.5mm, 1.5mm and 2mm. In order to accommodate them in the aluminum tube one of the borated polyethylene disc was removed. The lead discs were kept close to the gadolinium pinhole end of the collimator with the diameters of the holes in them made to match the divergence angle. One borated polyethylene disc preceded the lead discs because it had the required arrangements to attach the gadolinium pinhole aperture on it. The altered design of the divergent section is shown in Figure 4.11.

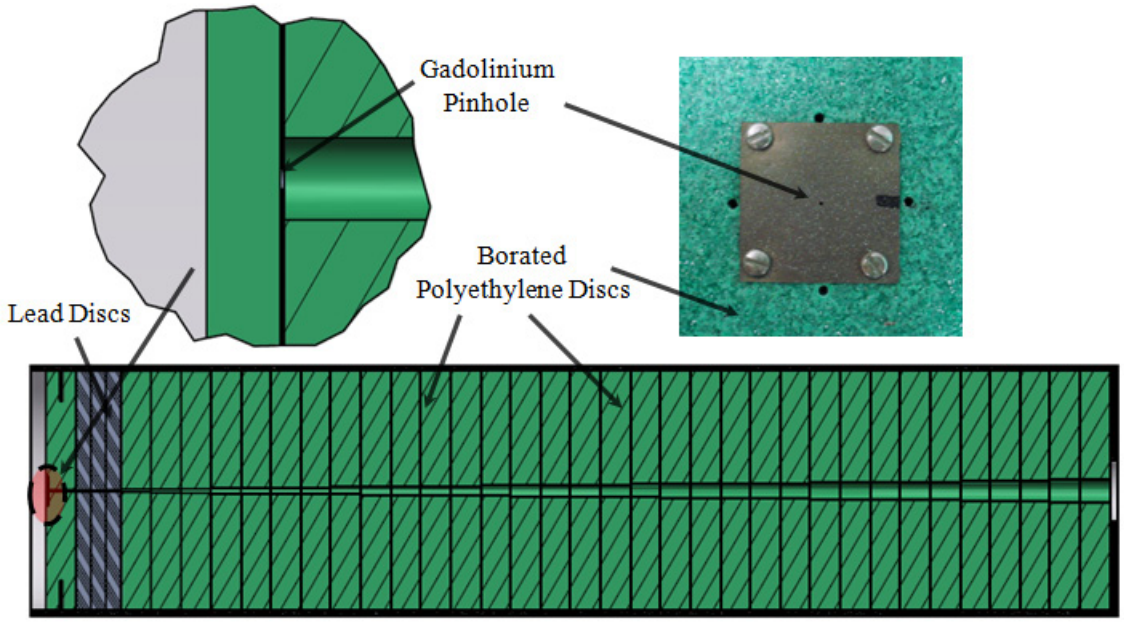

Figure 4.11. The divergent section of the collimator with the lead discs. The gadolinium pinhole is shown in the blowup section. The diameter of the pinhole is 0.5mm.

With the replacement of the discs there were hole misalignment issues as the lead discs are much heavier than the polyethylene discs and even a slight clearance between the discs and the aluminum tube will cause a misalignment. Thus, hole alignment was performed using lasers by rotating the discs relative to each other until laser spot can be clearly observed at the other end as shown in Figure 4.12.

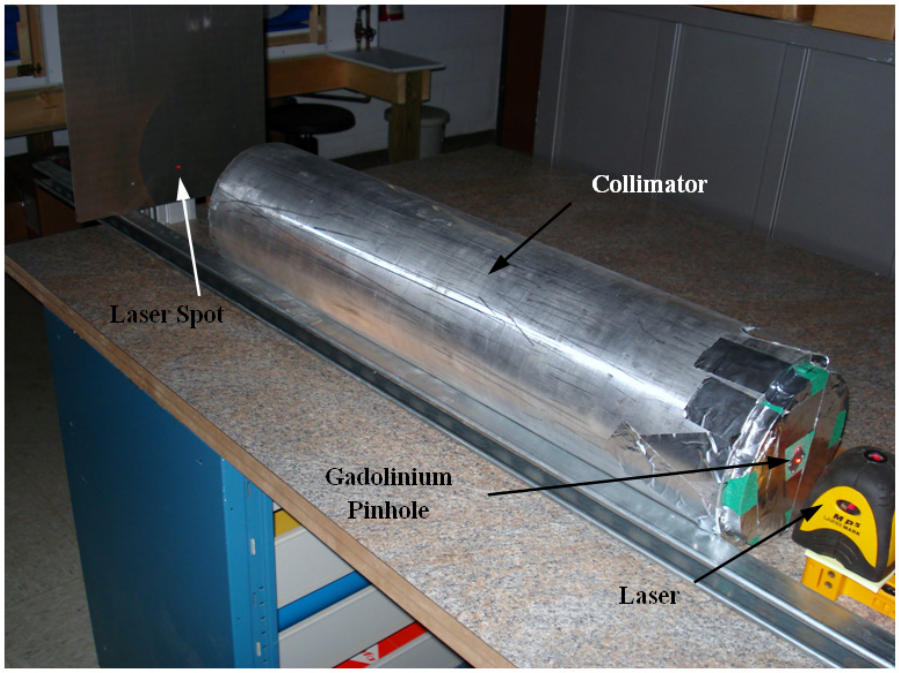

Figure 4.12. Alignment of the gadolinium pinhole with the lead discs using laser.

The aligned collimator was inserted inside the beam-tube for testing. Again bare beam exposures of image plates were performed. Significant improvement was observed in the images taken on the image plate with the lead in the collimator. Figure 4.13 depicts one of the bare beam images taken using the neutron image plate. The central circular neutron exposure area almost 135mm (close to the design target of 130mm) in diameter is clearly visible in comparison to earlier images where it was hardly visible. Also, the beam is fairly uniform which indicates that the discs in the collimator were aligned fairly well using the laser. The image in Figure 4.13(a) is the raw image as obtained through the scan of the image plate. The

image in Figure 4.13(b) is the processed image using the spike noise filter and the 9×9 median filter available in the Multi Gauge software provided by Fuji Films along with the scanner. These filters are used for noise filtering. The spike noise filter is used to remove unexpectedly high or low values of density in some of the pixels due to various reasons. The median filter is good for removing speckle and '*salt and pepper*' noise from the image. Also, it has the edge preserving property which is desirable in neutron imaging (see Appendix D for details on these filters). As it can be observed, use of these two filters has lead to significant improvement in the SNR of the image.

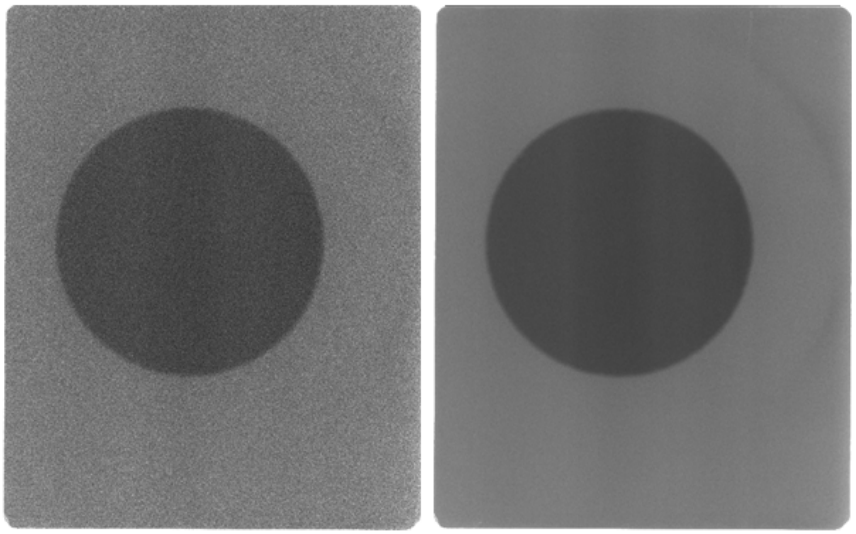

(a) **(b)**

Figure 4.13. Bare beam neutron image of the gadolinium pinhole taken using image plates. (a) The raw image as obtained by reading the image plate. (b) The image processed in the multi gauge software using the spike noise filter and the 9×9 median filter. The exposure time was 60 minutes at a 6m distance between pinhole and the detector. The size of the image plate is 20×25 cm^2.

Another observation that can be made from Figure 4.13 is about the beam intensity. The exposure time for the image was 60 minutes with the pinhole-to-detector distance of 6 meters. The observed density on the image plate is very good indicating that the neutron flux intensity is more than sufficient and can be sacrificed some to gain on the transverse coherence length by

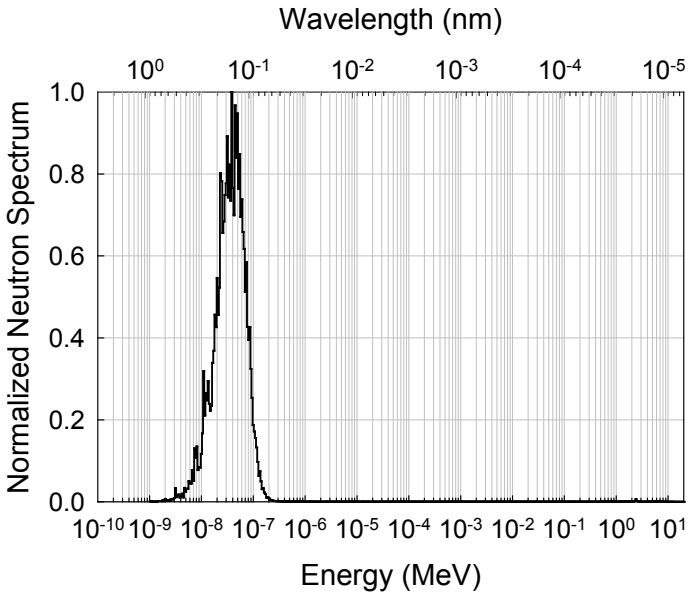

Figure 4.14. The neutron energy spectrum at the 6m image plane using 12 inches of single crystal sapphire.

increasing the sapphire filter length. Therefore, 6 inches, 9 inches and 12 inches sapphire filters (as these were the available length of sapphire filters) were tested using both simulations and the experiment. Although the 12 inch sapphire filter increased the exposure time to three hours to get similar density as 3 inch of sapphire but also provided significant gain in the transverse coherence length by reducing the average energy of the neutron beam. This can be easily observed by comparing the neutron energy spectrum obtained using 12 inches of sapphire shown in Figure 4.14 with the spectrum obtained using 3 inches of sapphire shown in Figure 4.3. The transverse coherence length increased from 1.47μm to 1.81μm (at a L/d ratio of 11,000 with d = 0.5mm). Hence 3 inches of sapphire was replaced with 12 inches (two filters of 6 inches length) of sapphire. Both the filter holder for the 6 inch sapphire filter contained 2.5 inches of lead followed by SWX-277. In order to not lose the beam line length after the pinhole while increasing sapphire length the filters were inserted further inside in the 6 inch diameter beam tube section. Moreover, to reduce the gamma noise further without decreasing the neutron signal 4 inches of lead shield with a 3mm diameter hole at its center was inserted after

the filter holder which is followed by the Gd aperture. The sectional view of the final collimator design is shown in Figure 4.15.

4.6.2 Performance of Neutron Phase Contrast Imaging Experiments

With the above changes performed to tackle the gamma noise and to increase the coherence area of the beam the redesigned collimator was better suited to perform phase contrast neutron imaging. Imaging exercises were performed with this collimator for different kinds of sample. The geometry of imaging setup used to perform phase contrast imaging is shown in Figure 4.16. Both the detector stand and the sample stand are placed on the aluminum rails on which they can slide.

Initial imaging of samples revealed that the aluminum rail (shown in Figure 4.16) is not perfectly aligned to the neutron beam direction. In the case of conventional neutron imaging where the sample is kept almost in contact with the detector slightly misaligned setup does not cause any problem. But in the case of phase contrast imaging where the sample is kept at a distance of a few meters from the detector a slight misalignment can cause a shift in the sample location relative to the beam when the distance R is increased or decreased. In a perfectly aligned system only magnification of the sample should take place without any shift.

In order to align the rail with the beam, bare beam images were taken at different distances from the pinhole aperture and overlapped on each other as shown in Figure 4.17. Center of the beam should not shift in such images taken at different distances for a perfectly aligned setup. Regression of the beam center calculated transverse shift with the distance from the source indicated an angular misalignment of 0.88^{o} (slope = -0.0153) as shown in Figure 4.18. Based on this the alignment correction was performed. The measurements performed at the corrected position yielded an angular misalignment of 0.15^{o} (slope = 0.0026) which was considered to be within the tolerable error.

Phase contrast imaging of different samples were performed after the beam alignment exercise was completed. A few example radiographs are being presented here illustrating different aspects of this imaging exercise.

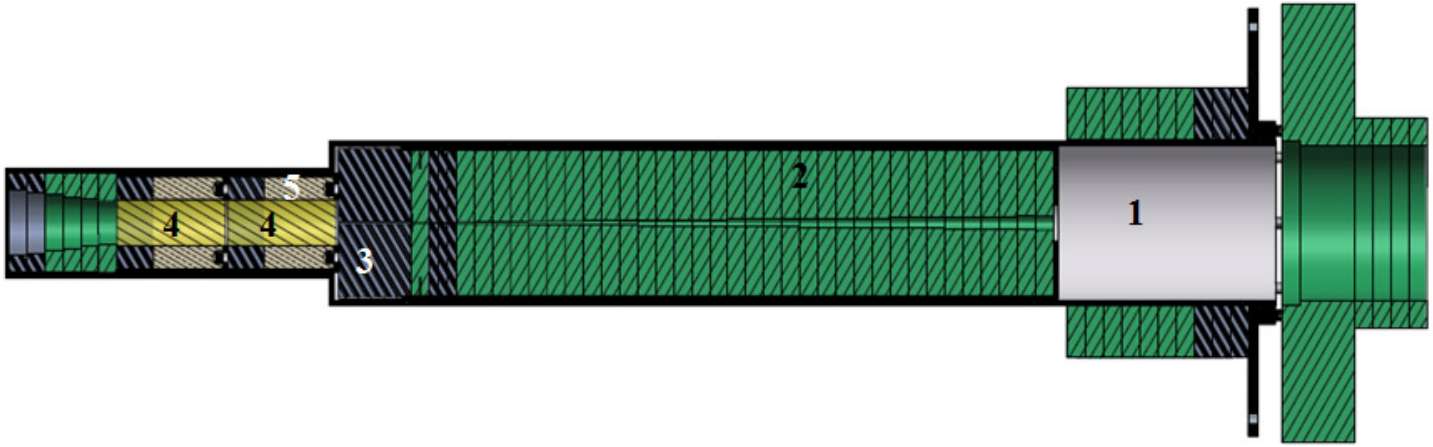

Figure 4.15. The sectional view of the final design of the pinhole collimator used for phase contrast neutron imaging. The material specifications are (1) aluminum tube (2) 5% borated polyethylene (3) lead (4) sapphire filter (5) SWX-277 (look in Chapter 2).

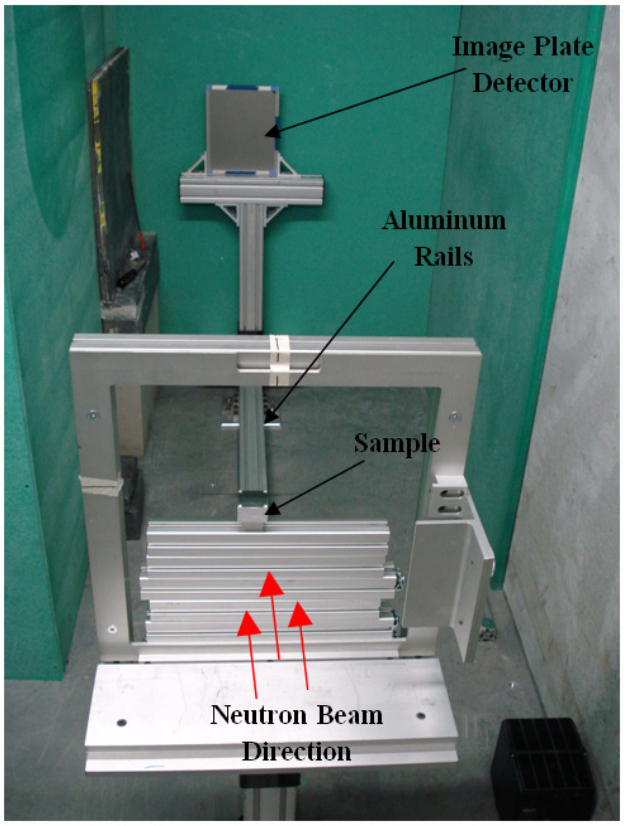

Figure 4.16. Geometry of imaging setup used to perform phase contrast neutron imaging.

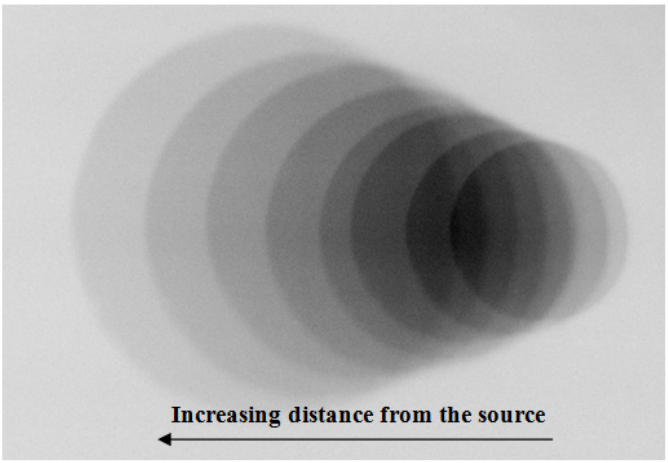

Figure 4.17. Overlapped image of the bare beam taken at different distances from the source depicting rail misalignment.

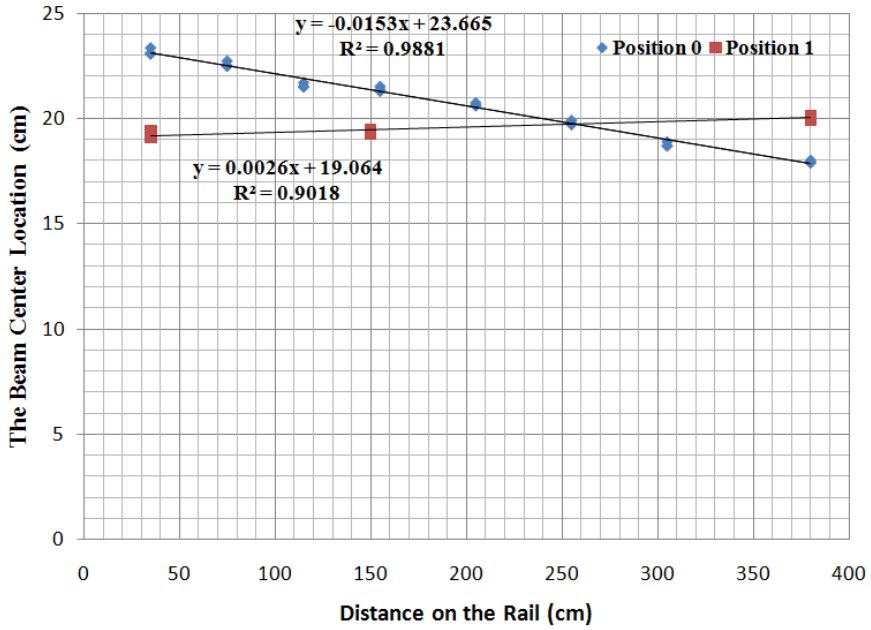

Figure 4.18. Plot of beam center location against the distance on the rail (which has a fixed offset from the source). Position 0 indicates the misaligned position of the rail and Position 1 indicates the corrected position.

4.6.2.1 Sample 1: Stack of Aluminum Plates

First sample was a stack of five 0.25 inch thick aluminum plates as shown in Figure 4.19. The thickness of each aluminum plate along the beam direction was 5cm. Two images of this sample were taken using the neutron image plates at an object-to-detector distance (R) of 8cm and 200cm. From the phase contrast formulation (Eq. (4.9)) it is expected to observe this effect at large object-to-detector distances. For small R only attenuation contrast image will be formed. Obtained images of the sample are shown in Figure 4.20. These are the post processed images from the raw data collected using the spike noise filter and the 11×11 median filter. Further, since the image taken at R = 200cm gets magnified due to the beam divergence, the magnification of the other image (R = 8cm) was also performed to almost match with the R = 200cm image. It was performed just to make the visual comparison easier to perform.

Comparison of both the images shown in Figure 4.20 clearly indicates higher edge contrast present in the image taken at R = 200cm. The phase contrast effect is clearly visible at

the aluminum edges with the air. Moreover, it is due to this effect that the slight air gap between different aluminum plates stacked on top of each other is clearly visible when R = 200cm. These edges are not visible in the attenuation image shown in Figure 4.20(a).

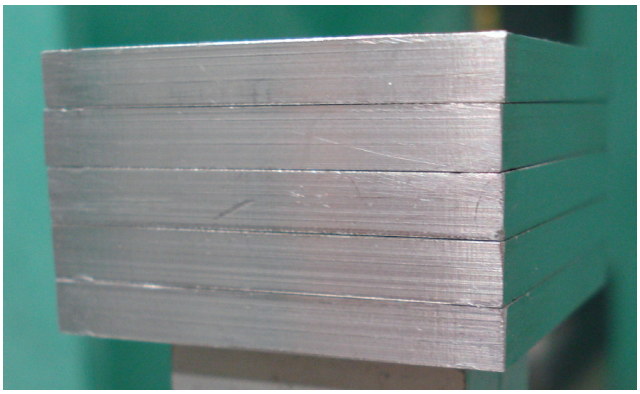

Figure 4.19. Photograph of Sample 1 (Stack of Aluminum Plates).

A normalized intensity profile of the top edge of aluminum with air is shown in Figure 4.21. From the intensity profile of the image taken at R = 200cm the phase contrast effect is clearly visible. The effect is prominent because of large difference in the coherent scattering length density (CSLD), $a_{coh}(x,y,z)\rho(x,y,z)$ between air (CSLD = 4.47×10^{11} atoms/m^2) and aluminum (CSLD = 2.11×10^{14} atoms/m^2) which makes the pure phase contribution (2nd term in Eq. (4.9)) large. Further, the asymmetry introduced as a result of the phase amplitude interaction term (3rd term in Eq. (4.9)) can also be observed in the intensity profile shown in Figure 4.21 for R = 200cm. The trough of the intensity in the aluminum is larger than the peak in the air. This asymmetry can be explained with the help of Figure 4.8.

4.6.2.2 Sample 2: The Designed Phantom

Sample 2 is a designed phantom consisting of different materials as shown in Figure 4.22. The phantom consisted of iron (Fe), titanium (Ti), lead (Pb) and vanadium (V) 1cm×1cm×1cm cubes inserted inside an aluminum block. The aluminum block thickness along the beam direction was 3cm (three 1cm thick blocks screwed together). There were four through holes of

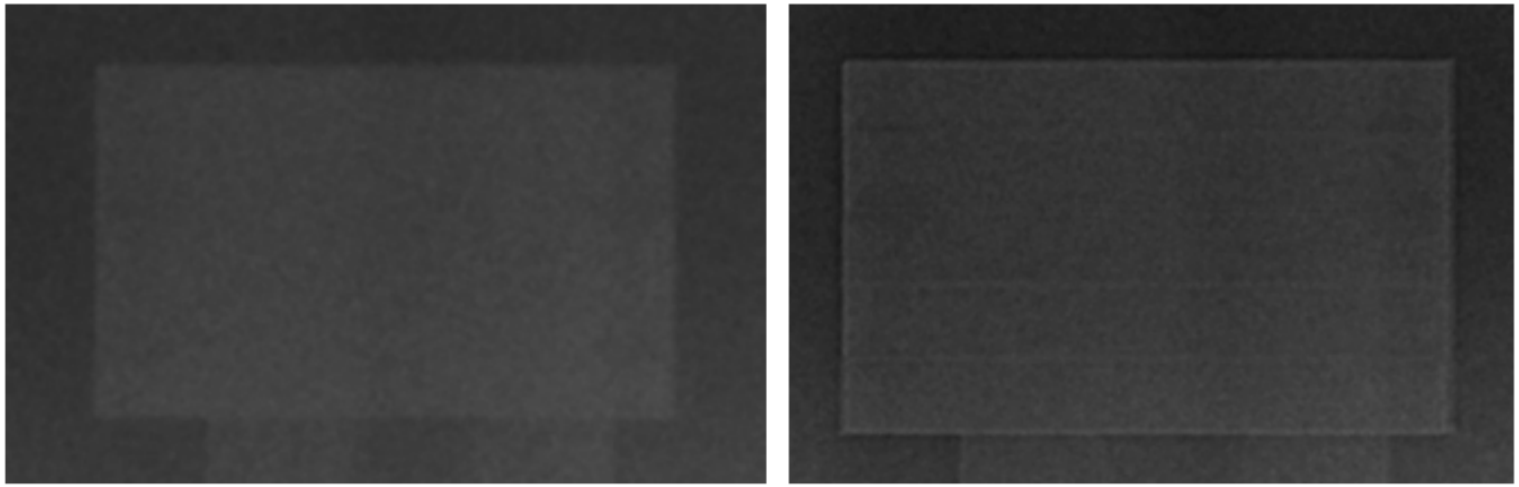

(a) (b)

Figure 4.20. Image of the aluminum stack taken (a) at *R* = 8cm (b) at *R* = 200cm. The exposure time for both of them was 120 minutes at the 1MW reactor power.

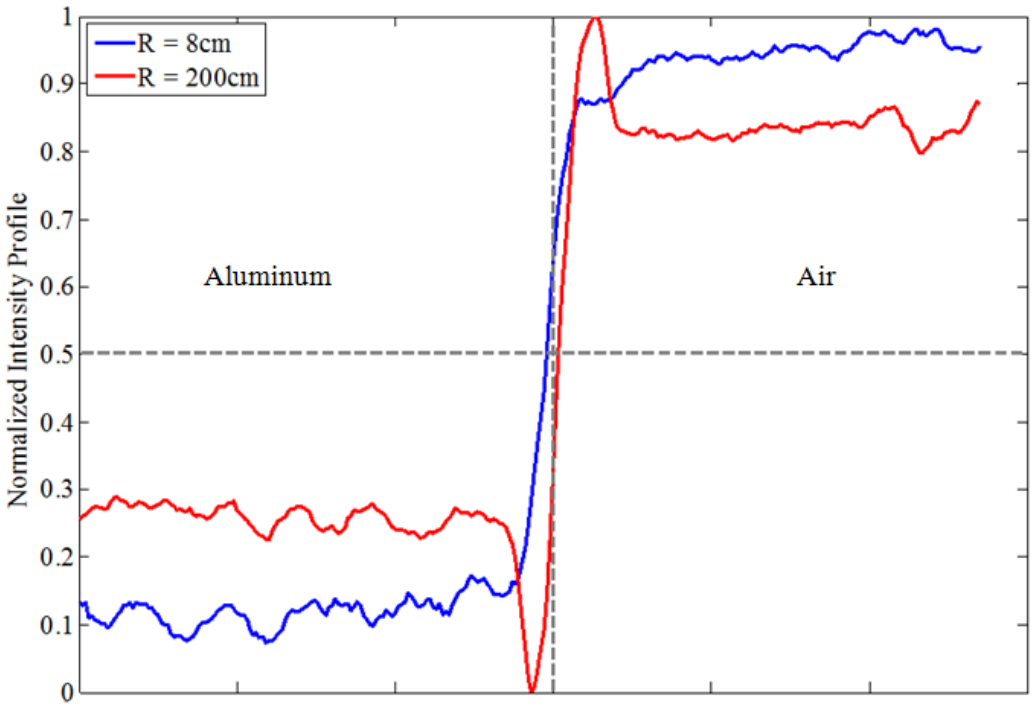

Figure 4.21. A normalized intensity profile of the top edge of the aluminum with air for Sample 1 for both the radiographs shown in Figure 4.20. Image of the aluminum stack taken (a) at *R* = 8cm (b) at *R* = 200cm. The exposure time for both of them was 120 minutes at the 1MW reactor power. The intensity clearly indicates the phase contrast intensity variation at the aluminum edge. Both the shown profile has been averaged over 400 edges to reduce the fluctuation due to noise.

different sizes drilled in the aluminum. The whole phantom was placed on two aluminum plates as shown in the figure.

The neutron radiograph of the sample was taken at object-to-detector distance, *R* = 3cm and 250cm using neutron image plates. The exposure time in this case was reduced to 75 minutes from the 120 minutes (used for Sample 1) in order to observe if lower exposure time provides sufficient SNR and the exposure. Raw images obtained at the two object-to-detector distances are shown in Figure 4.23. In spite of high noise content in the raw image the higher edge contrast in Figure 4.23(b) is clearly visible. All the holes and edges can be clearly demarcated in the radiograph taken at *R* = 250cm whereas in the radiograph taken at *R* = 3cm many of the edges are hardly visible.

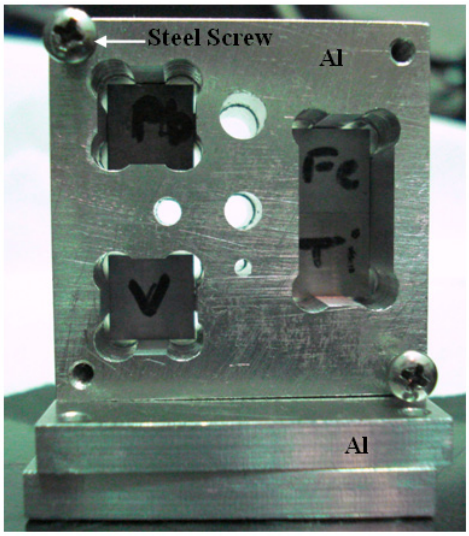

Figure 4.22. Photograph of the designed phantom with the different material marked (Sample 2).

The raw image was de-noised using the spike noise filter and the 11×11 median filter as used before for Sample 1. Figure 4.24 and Figure 4.25 depict the radiograph of the sample after filtering the raw image with the spike noise filter and the spike noise filter followed by the median filter respectively. It can be observed that spike noise filter does not de-noise the image considerably. It removes some unexpectedly high pixel values from the image. The median filter performs better in terms of noise removal from the image but also smoothens the image in the process. But still it is better than averaging filter in terms of edge preserving characteristics.

The material and geometry selection for the phantom were performed in a manner to define material edges with varying degrees of differences in coherent scattering length densities. This will achieve various degree of phase contrast enhancement in the image. Table 4.2 lists the coherent scattering length densities of various materials present in the sample. It can be observed that most of the metals have much higher coherent scattering length density than air because of their higher mass densities. Thus, edges of the sample formed with air (or air like material) will always produce higher contrast using this technique. Further, titanium and steel edge have the largest difference in their coherent scattering length density. Also, titanium has negative coherent scattering length. Therefore, their edge should have the highest phase

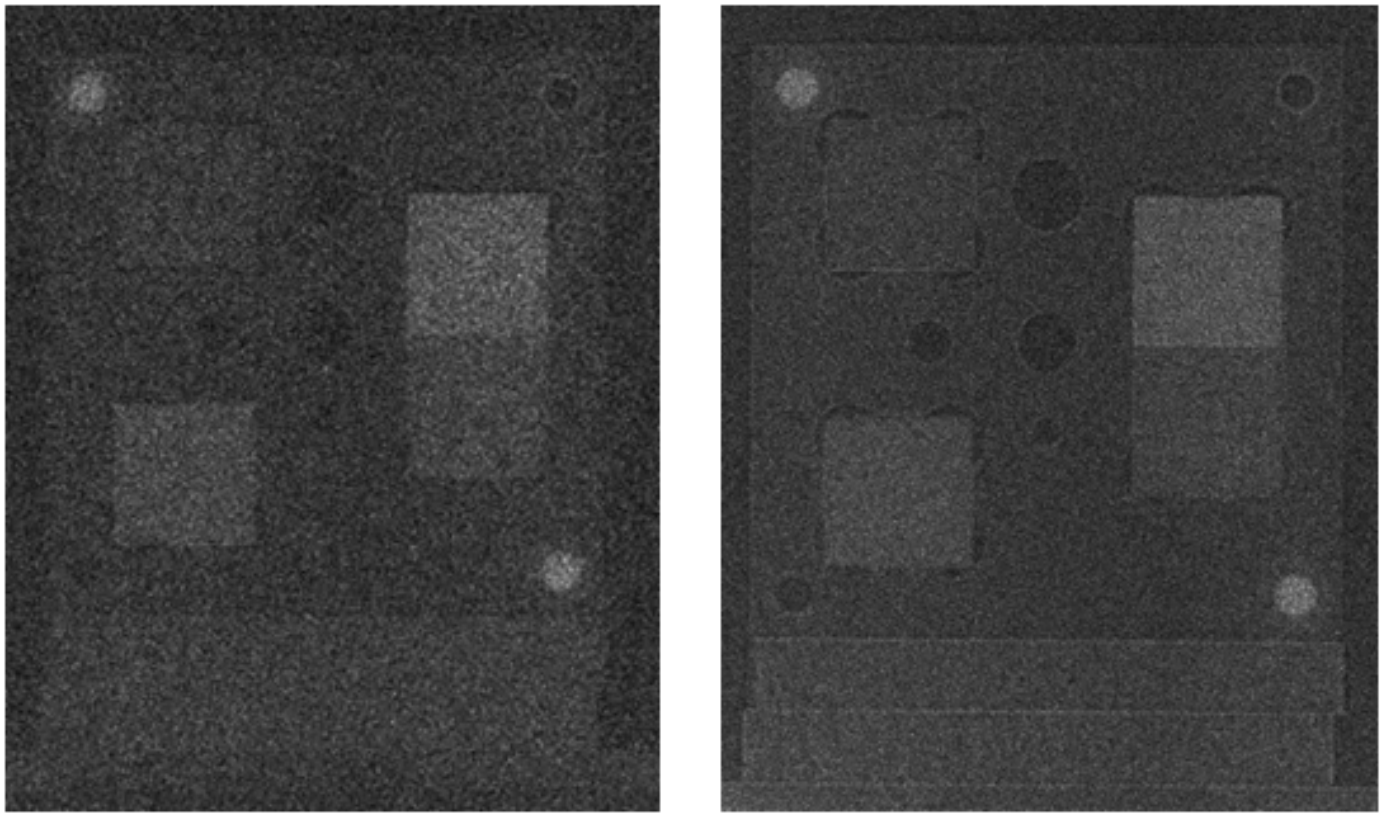

(a) (b)

Figure 4.23. Neutron radiograph (without post processing) of Sample 2 (designed phantom) for the object-to-detector distance (a) R = 3cm and (b) R = 250cm.

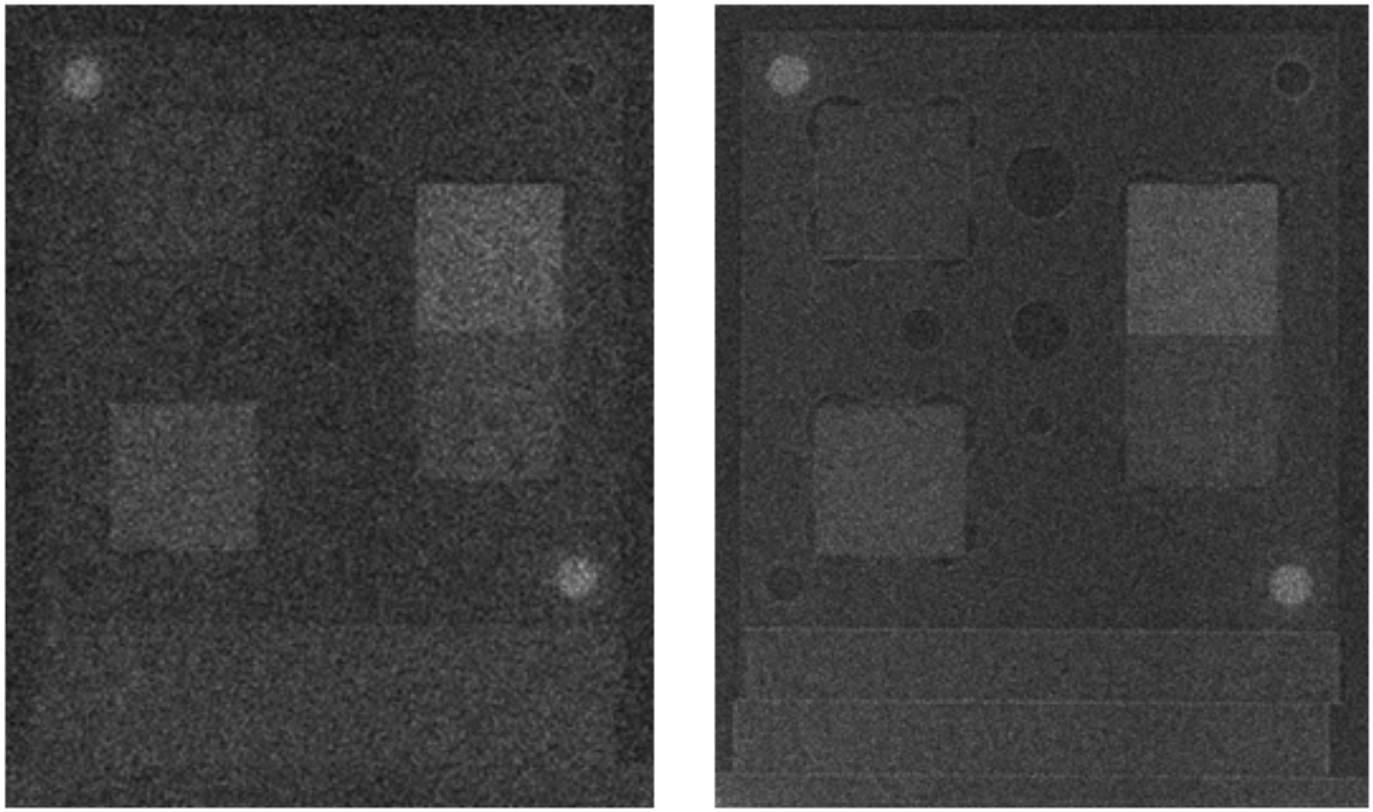

(a) **(b)**

Figure 4.24. Neutron radiograph of Sample 2 (designed phantom) for the object-to-detector distance (a) *R* = 3cm and (b) *R* = 250cm. The image was de-noised using spike noise filter.

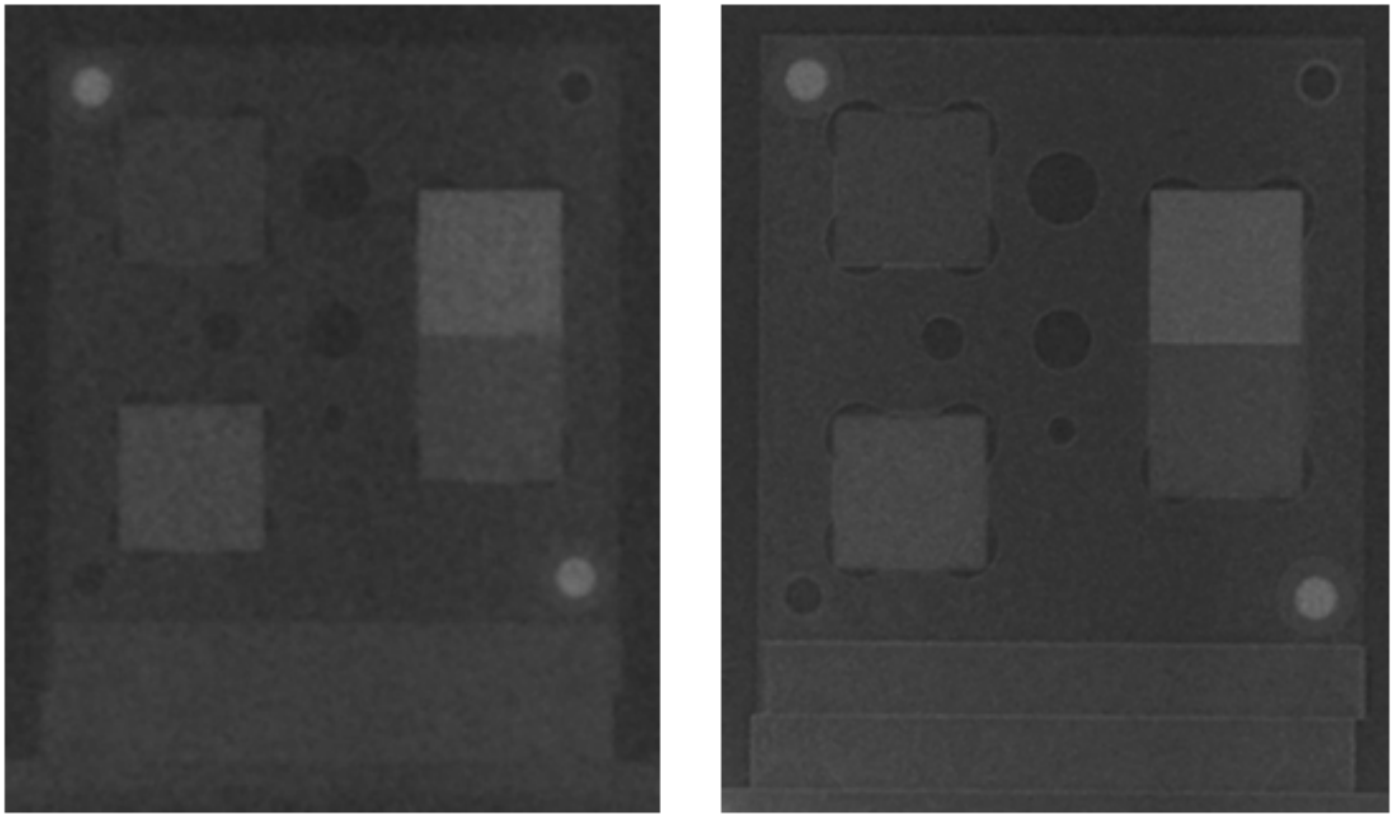

(a) **(b)**

Figure 4.25. Neutron radiograph of Sample 2 (designed phantom) for the object-to-detector distance (a) *R* = 3cm and (b) *R* = 250cm. The image was de-noised using spike noise filter and 11×11 median filter.

contrast effect if pure phase object assumption is used with the intensity maximum occurring in the titanium. The image in Figure 4.25 does not depict the highest contrast at this edge. This may be because pure phase assumption is not valid as both materials have significant attenuation as pointed out by their microscopic cross-sections which is 14.18 barns for steel and 10.41 barns for titanium. For such cases phase-amplitude formulation can better describe the intensity variation. The least difference in the CSLD is between lead and aluminum where very little intensity jumps due to phase effect is visible.

Table 4.2 The coherent scattering length densities of materials in Sample 2.

Material	Coherent Scattering Length (in fm)	Mass Density (in gm/cm^3)	Coherent Scattering Length Density (in atoms/m^2)
Aluminum	3.5	2.7	2.11×10^{14}
Steel	9.45	7.87	8.02×10^{14}
Titanium	-3.4	4.51	-1.93×10^{14}
Lead	9.43	11.4	3.12×10^{14}
Vanadium	-0.38	6.0	-2.71×10^{13}
Air	8.66	0.00124	4.47×10^{11}

4.6.2.3 Sample 3: A Stainless Steel and Copper Sample

The 3rd sample whose phase contrast images are being presented is made of stainless steel circular plate ~2.5cm in diameter and ~0.25 inch thick in the neutron beam direction. A photograph of the sample is shown in Figure 4.26. The sample has a copper 'O' ring as shown in the figure. Also, the stainless steel has multiple holes and intrusions.

The neutron radiograph of the sample taken at R = 2.5cm, R = 250cm and R = 300cm are shown in Figure 4.27. Physical size of each image is proportional to the magnification of the object that happens at the image plane. Again, clearly enhancement in image quality is clearly visible at larger object-to-detector distances. This enhancement can be attributed to phase contrast effect as well as the magnification of the sample. The contrast enhancement in the images happens due to the phase effect whereas the magnification leads to an improvement in the spatial resolution in terms of the details of the object being captured in the image. Very large L/d ratio of the system leads to very small geometric blurring even when the object-to-

detector is large. Thus, with such a system an overall image quality improvement, which includes improvement in the spatial and the contrast resolution, can be achieved if signal-to-noise ratio is maintained in the imaging process.

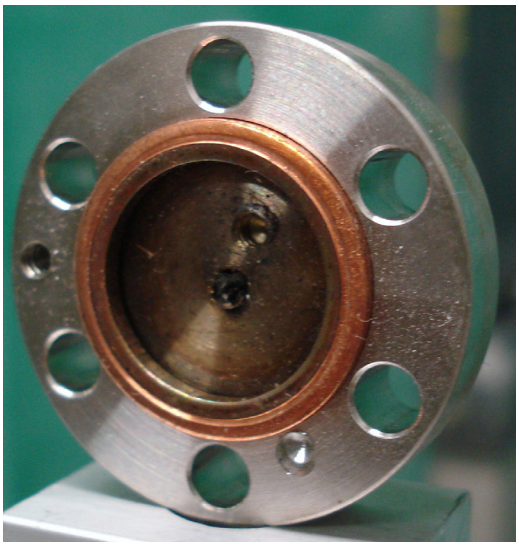

Figure 4.26. Photograph of Sample 3.

4.6.3 Routine Performance of Phase Contrast Neutron Imaging

The natural extension of the successful demonstration of the phase contrast neutron imaging at the PULSTAR imaging facility is to be able to perform it on a routine basis to obtain higher contrast in different samples suited for such application. Two of the important factors in performing such imaging exercises on a routine basis are the length of the exposure time and the ease of system changeability required to shift back and forth from conventional to phase contrast imaging. In the present case the exposure time required is about 45 minutes (as used for Sample 3). The system changes required to perform this is just the diverging collimator section. This change is easy and can be performed in about 30 minutes. A few imaging exercises were performed using different objects as samples in order to verify if 45 minutes exposure time is adequate in general and also observe the contrast enhancement obtainable in such objects. The radiographs of a Duracell battery and a BNC connector (photographs of the

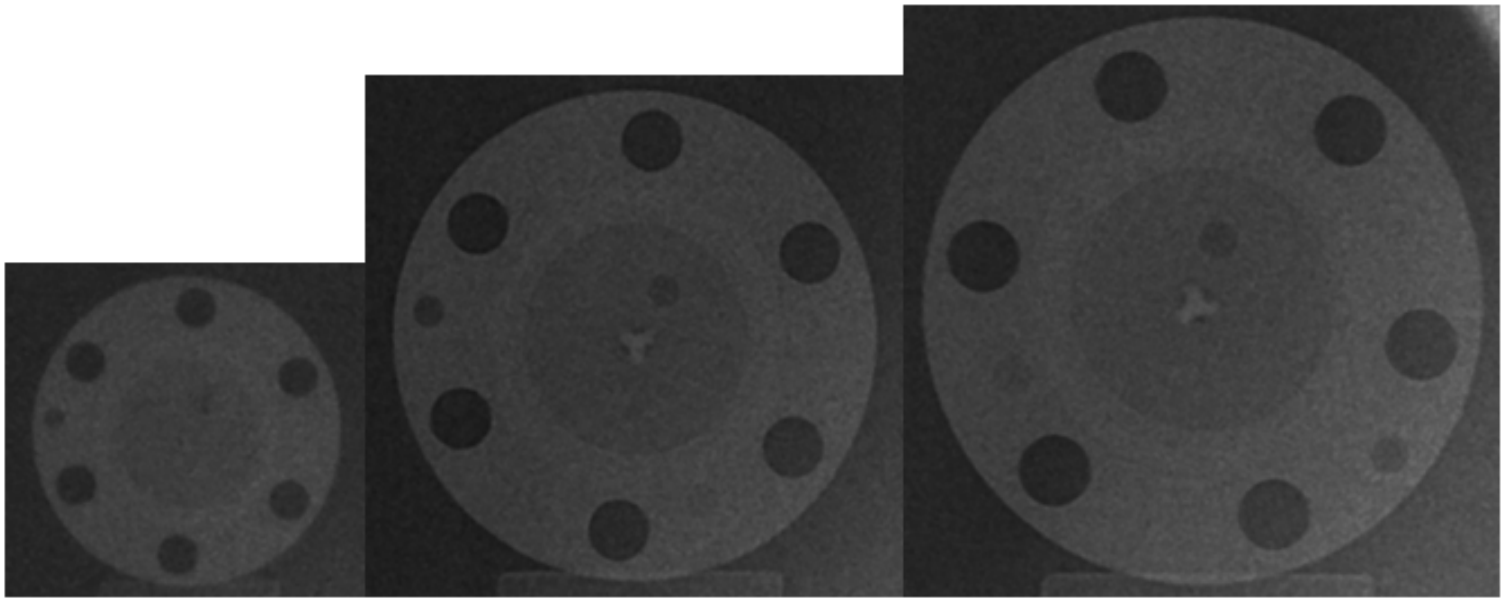

(a) **(b)** **(c)**

Figure 4.27. Neutron radiograph of Sample 3 at (a) *R* = 2.5cm (b) *R* = 250cm and (c) *R* = 300cm. The image sizes are proportional to the magnification of the object at the image plane. The exposure time for each of the images was 45 minutes.

samples shown in Figure 4.28) comparing the attenuation radiograph and the phase contrast radiograph are shown in Figure 4.29 and Figure 4.30 respectively. The edge enhancement due to phase contrast effect is clearly visible in the radiographs of both the samples. Also, 45 minutes exposure time seems reasonable to get enough exposure of the image plates such that after using de-noising filters the radiographs have visual clarity. The design and experimental results for the phase contrast have been published by the author [103].

(a) **(b)**

Figure 4.28. Photograph of (a) a Duracell battery (b) a BNC connector.

Even though 45 minutes exposure time is not very long, further reduction in it without compromising SNR of the image and the coherence area of the beam is always desirable. In order to achieve this reduction in exposure time the neutron signal at the image plane has to be increased. With the fixed source strength and the spatial coherence of the beam the solution to this is offered by the multi-pinhole phase contrast imaging. This technique can reduce the exposure time significantly while maintaining or even improving the SNR of the image.

4.7 Design Considerations for Multi-Pinhole Collimator

The design objectives and constraints specified for the single pinhole collimator (see Section 4.2) also hold for the multi-pinhole phase contrast collimator design. Some of the additional design considerations which had to be taken into account were:

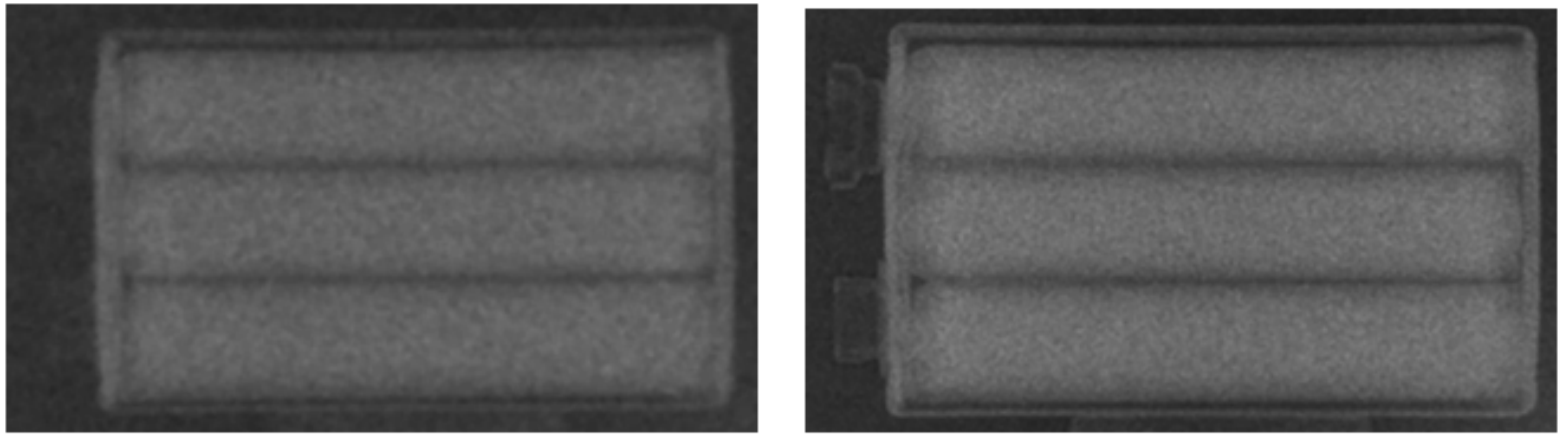

(a) **(b)**

Figure 4.29. Neutron radiograph of a battery taken at (a) *R* = 2.5cm and (b) *R* = 250cm. The exposure times for both the radiographs were 45 minutes.

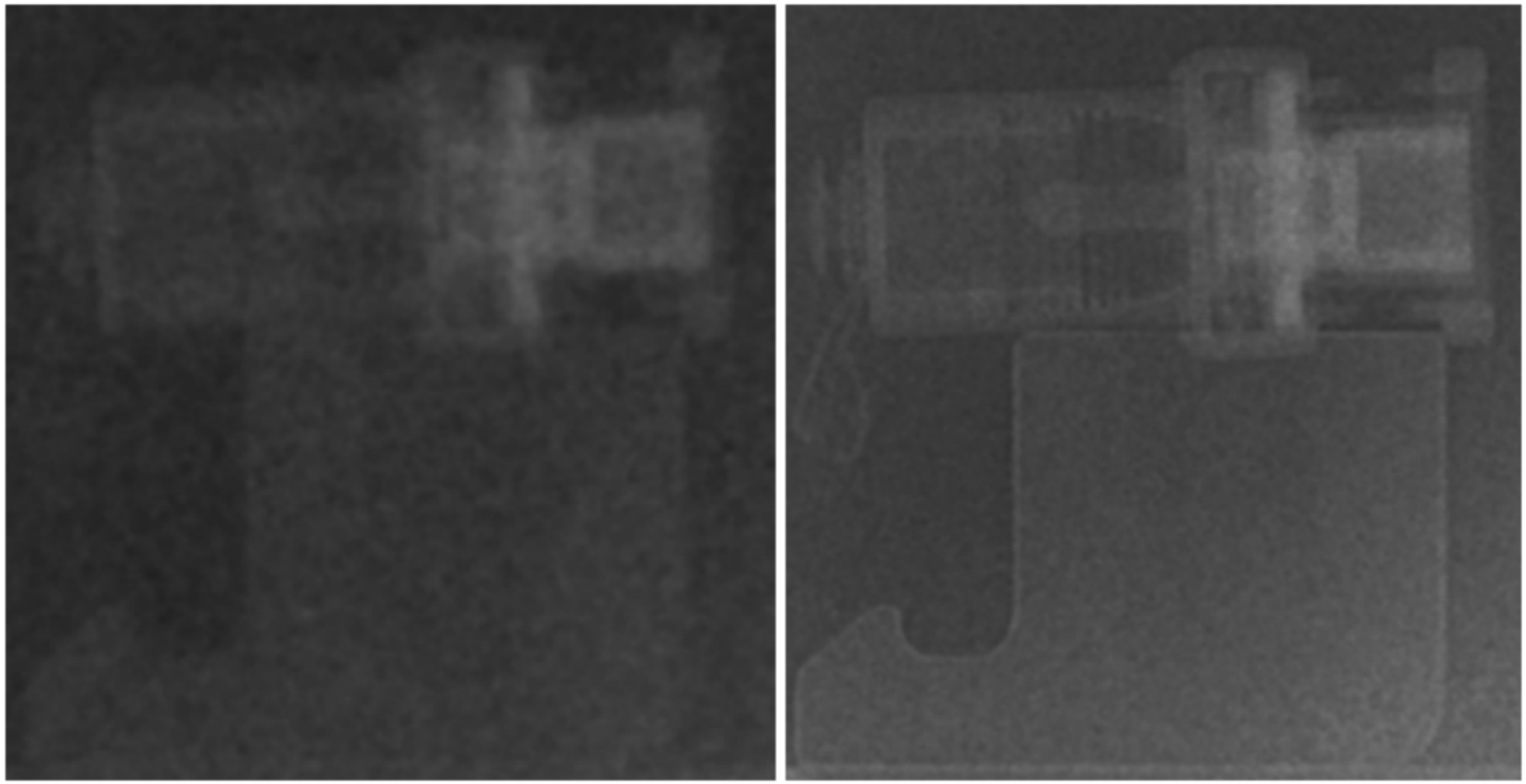

(a) **(b)**

Figure 4.30. Neutron radiograph of a BNC connector taken at (a) *R* = 2.5cm and (b) *R* = 250cm. The exposure times for both the radiographs were 45 minutes.

- Objective: (i) Maximization of the number of pinholes in the mask to improve the SNR; (ii) Maximization of the beam cross-sectional area that is illuminated by all the holes

- Constraint: The sapphire filter diameter is 2.5 inches which defines the maximum mask size.

In order to achieve the design objectives that were common to the single pinhole collimator, the parameters crucial in achieving those objectives like the diameter of the pinhole, the divergence angle associated with the pinholes, the sapphire filter length, the thickness of the gadolinium foil were taken from the previous design. This eliminated redesigning for those objectives from the start and also it made sure that the design will perform as expected for phase contrast neutron imaging. The thickness of lead was increased from 1.5 inches to 2 inches to contain the gamma noise as the 4 inch thick lead shield between the sapphire and the mask had to be removed. Thus, the characteristics of the collimator in terms of providing a spatially coherent neutron beam should remain like the single pinhole collimator presented before.

To achieve the additional design objectives within the constraint specified three different geometries (see Figure 4.31) of pinhole arrangements were considered. These three geometries were natural choices that fit within the filter diameter of 2.5 inches (6.35cm) taking into account the pinhole divergence. The diameter of the holes in the mask is 0.5mm as in the case of single pinhole collimator. Each hole is followed by its conical diverging section with a beam divergence of ~0.6^{o}. These diverging cones have a diameter of ~2cm at a distance ~1m (length of the conical collimating section) as is clear from Figure 4.32. In order to maintain the beam divergence these cones should not intersect with each other in the collimating section (clearly indicated in Figure 4.32). Further, all these holes should be inscribed in the circle of 2.5 inch diameter (diameter of the sapphire filter) to the extent possible to minimize the leakage of neutrons coming through unfiltered regions. Also, the holes should be located as close to each other as possible, because the largest distance between the hole centers will be limiting the beam size illuminated by all the holes i.e. size of the common illumination region. The calculated beam size of each of the single hole at the object plane (taken at 505cm from the

mask) is 10cm in diameter. The calculated beam size at the image plane taken at 668cm from the pinhole mask) is 13.2cm in diameter.

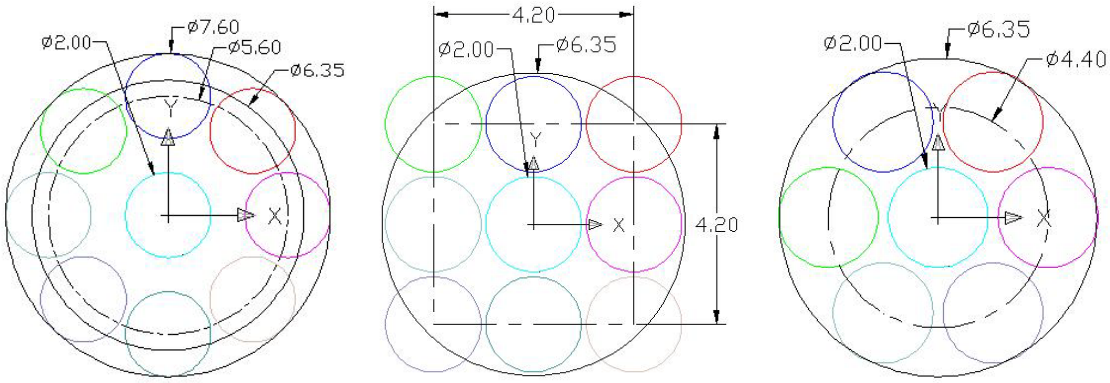

(a) **(b)** **(c)**

Figure 4.31. The multiple pinhole geometries considered in the design of the mask. (a) A circular 9 hole geometry (Geometry 1) (b) A square 9 hole geometry (Geometry 2) (c) A circular 7 hole geometry (Geometry 3). All dimensions are in centimeters.

Mask Geometry 1, shown in Figure 4.31(a), has 8 holes located in a circular geometry around one central hole. The eight non-central holes are located on vertex of a regular octagon with the circle passing through the vertices having a diameter of 5.6cm. In this case the length of the conical section up to which all the cones are inscribed inside the filter diameter is 38.4cm. It can be clearly observed in Figure 4.31(a) that at the end of the collimating section the cone cross-section for the non-central holes lies outside the filter. But, area outside the filter section is same for all the non-central holes which will make the neutron leakage from all the non-central holes to be same on an average. Further, the largest distance between any two hole centers is 5.6cm. This gives a common illumination area at the object plane (at 505cm from the mask), as given by the circle inscribed in the intersection region, to be 4.4cm in diameter (see Figure 4.33).

Mask Geometry 2, shown in Figure 4.31(b), has 9 holes arranged in rectangular fashion with center of each hole lying on a square of side length 4.2cm. In this case the length of the

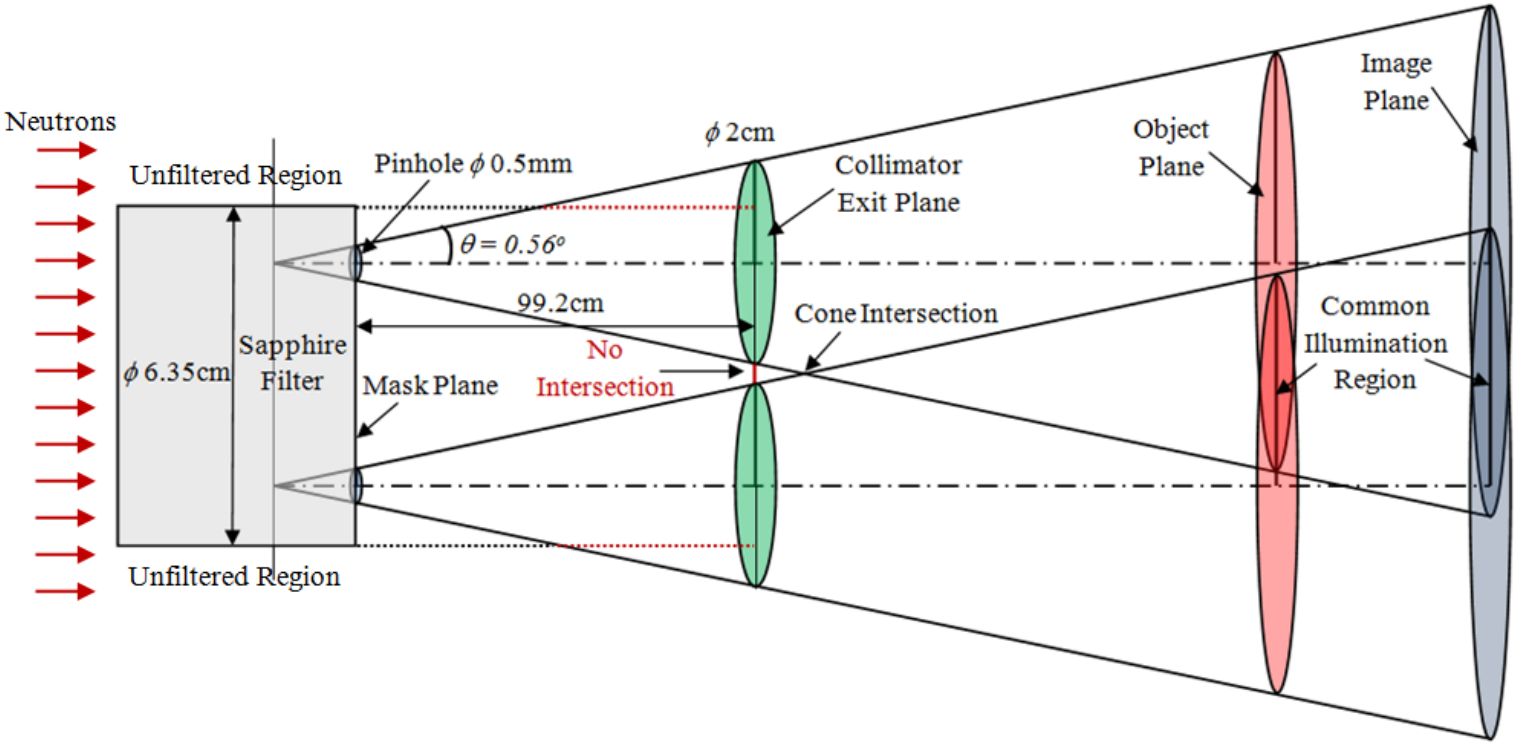

Figure 4.32. Schematic of the diverging conical section of the multi-pinhole collimator.

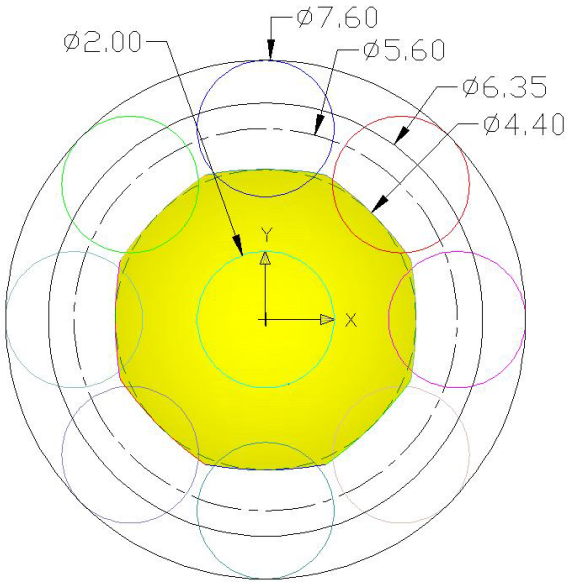

Figure 4.33. The common illumination area at the object plane for the pinholes arranged as shown in Fig. 4.31(a) (Geometry 1). All dimensions are in centimeters.

conical section up to which all the cones are inscribed inside the filter diameter is 19.6cm. In this case the holes located on the corners of the square escape outside the filter cross-section in a symmetric fashion before reaching the end of the collimating section. Thus, the leakage of neutrons from the corner holes will be same on an average that is different from the other holes located on the sides of the square and the center. The largest distance between the centers of any two holes is 5.94cm which is more than Geometry 1. The common illumination area obtained with this geometry can be given by the largest size square inscribed in the intersection region of all the cones as shown in Figure 4.34. In the present case the sides of the inscribed square is 3.45cm in length.

Mask geometry 3, shown in Figure 4.31(c), has 6 non-central holes located on the vertices of a regular hexagon and a central hole. In this geometry the numbers of holes are less than the previous geometries but the distance between the adjacent holes is same for all the holes. Also, the largest distance between the centers of any two holes is 4.4cm, which is the smallest of all the three geometries considered. Thus, in spite of losing the neutron signal due to less number of pinhole this geometry has other advantages over the previous two geometries considered.

Firstly, all the holes almost lie inside the filter even at the end of the collimating section thereby minimizing the neutron leakage. Secondly, it offers the largest common illumination area among all the three geometries which is better for accommodating somewhat bigger samples. Figure 4.35 depicts the common illumination area for this geometry with the largest circle inscribed in it of diameter 5.6cm. Considering these advantages offered by the present arrangement of pinholes, it was selected for the collimator and the mask design. Using this arrangement the neutron beam cross-sectional area at the image plane (668cm from the pinhole mask) as illuminated by every single hole is shown in Figure 4.36.

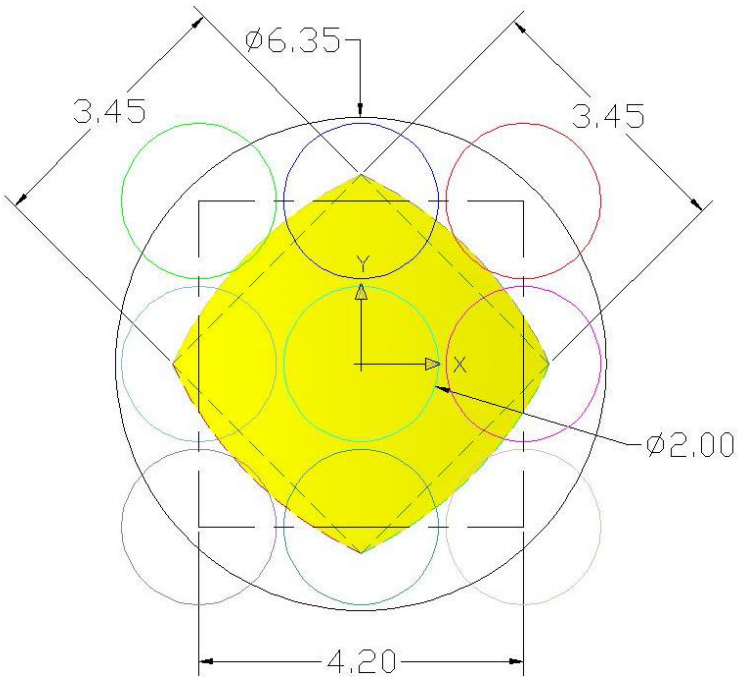

Figure 4.34. The common illumination area at the object plane for the pinholes arranged as shown in Fig. 4.31(b) (Geometry 2). All dimensions are in centimeters.

The mechanical design of the collimator was performed taking into consideration the alignment issues which were faced in the single pinhole collimator design. Better alignment methods are needed in this case as all the holes have to be aligned simultaneously. Also, it should not get misaligned while handling the collimator to insert or remove it from the beam tube. Thus, mechanical rigidity was needed in the design with the discs in the divergent section

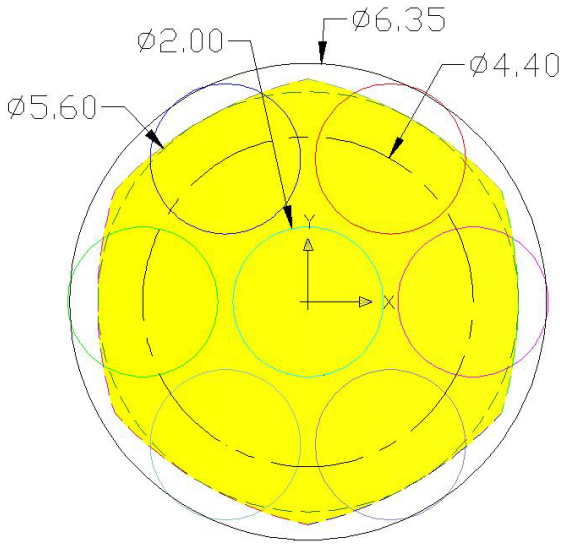

Figure 4.35. The common illumination area at the object plane for the pinholes arranged as shown in Fig. 4.31(c) (Geometry 3). All dimensions are in centimeters.

not free to rotate with respect to each other like in the single pinhole collimator. This was achieved by removing the outer aluminum casing completely and providing four steel rods going through all the borated polyethylene and lead discs. These rods restrict motion of the discs with respect to each other. There are two aluminum discs at the beginning and the end of the collimating section in order to provide the sturdiness to the design. In order to prevent streaming of the neutrons and gamma rays from the four steel rods borated polyethylene and lead discs were mounted on the front end with no holes at the location of the rods. The sectional view of the collimator is shown in Figure 4.37. The figure also depicts the mask which is made out of gadolinium with the arrangement of holes. Figure 4.38 depicts the manufactured divergent section assembly of the collimator along with the picture of the gadolinium mask. It can be observed that there is no aluminum casing on the collimator. The thickness of the gadolinium foil used to make the mask is 0.02 inches (508μm). This is the thickness that is available off the shelf and is close to 500μm (the optimum thickness reached by MCNP calculations taking the neutron beam energy spectrum into consideration). The actual length of the collimator is 38 inches (96.5cm) with the last borated polyethylene disc having holes of diameter 1.95cm (instead of 2cm as mentioned above). But, this does not affect

any design considerations. Also, the two inches of lead used after the gadolinium mask has holes of diameter 1mm which is less than the single pinhole collimator lead discs. This reduces the gamma streaming further by reducing the effective aperture size available to gamma rays.

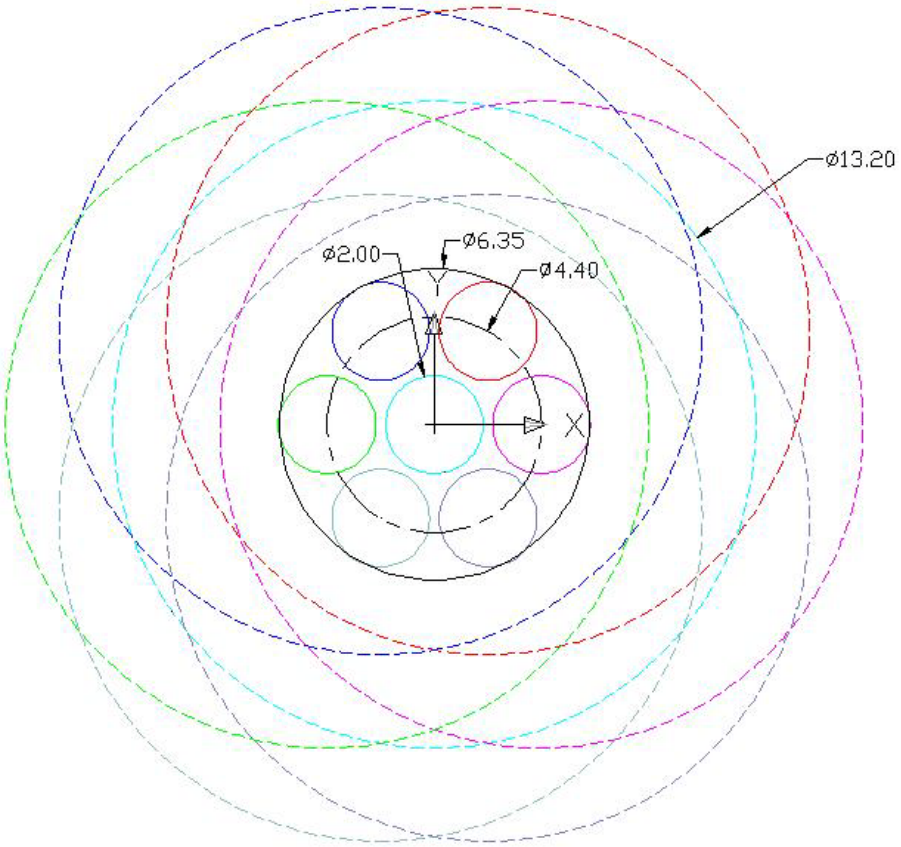

Figure 4.36. Schematic of the diverging beam cross-section at the image plane for Geometry 3 (shown in Figure 4.31(c)). All dimensions are in centimeters.

4.8 Experimental Results

Various imaging exercises were conducted to test the collimator in terms of its alignment and its ability to capture neutron phase contrast effect. The alignment of all the holes can be best verified by taking a bare beam image. Figure 4.39 shows the bare beam image taken on an image plate placed at the farthest image plane using the multi-pinhole collimator. The bare

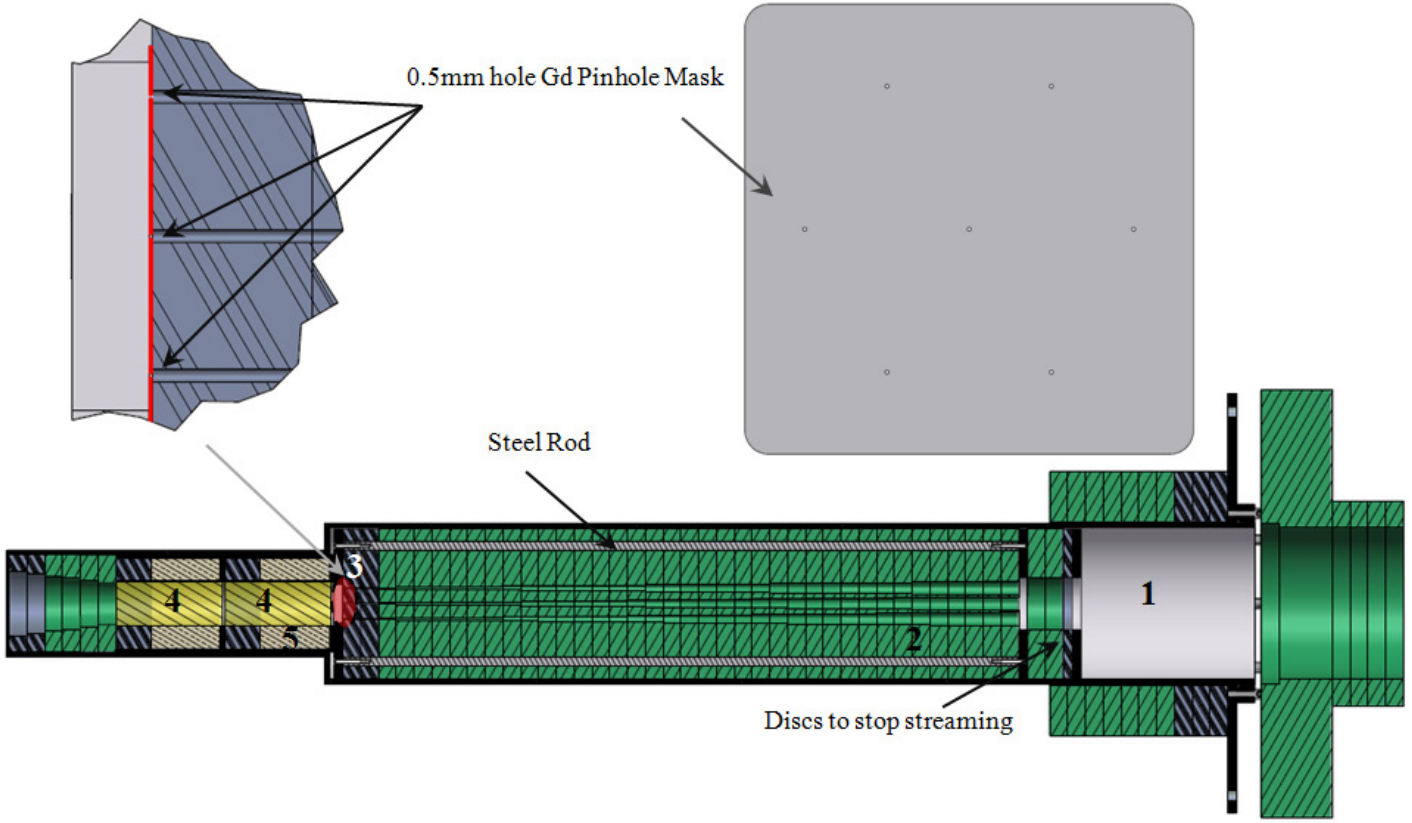

Figure 4.37. The multi-pinhole phase contrast neutron imaging collimator design. The materials as indicated in the figure are (1) aluminum (2) borated polyethylene (3) lead (4) sapphire filter (5) SWX-277. The gadolinium mask design with the pinhole pattern is also shown in the figure.

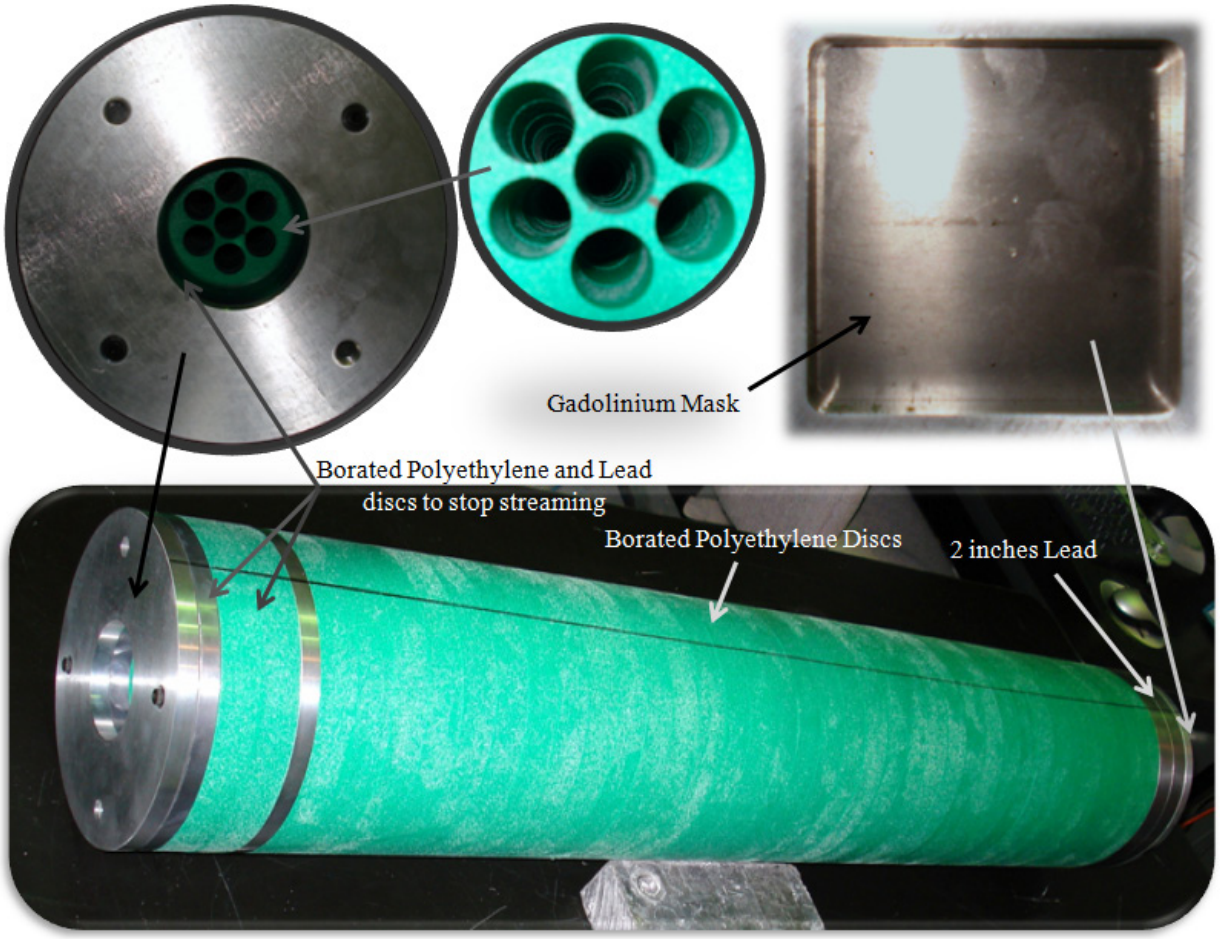

Figure 4.38. Photograph of the manufactured multi-pinhole collimator divergent section assembly.

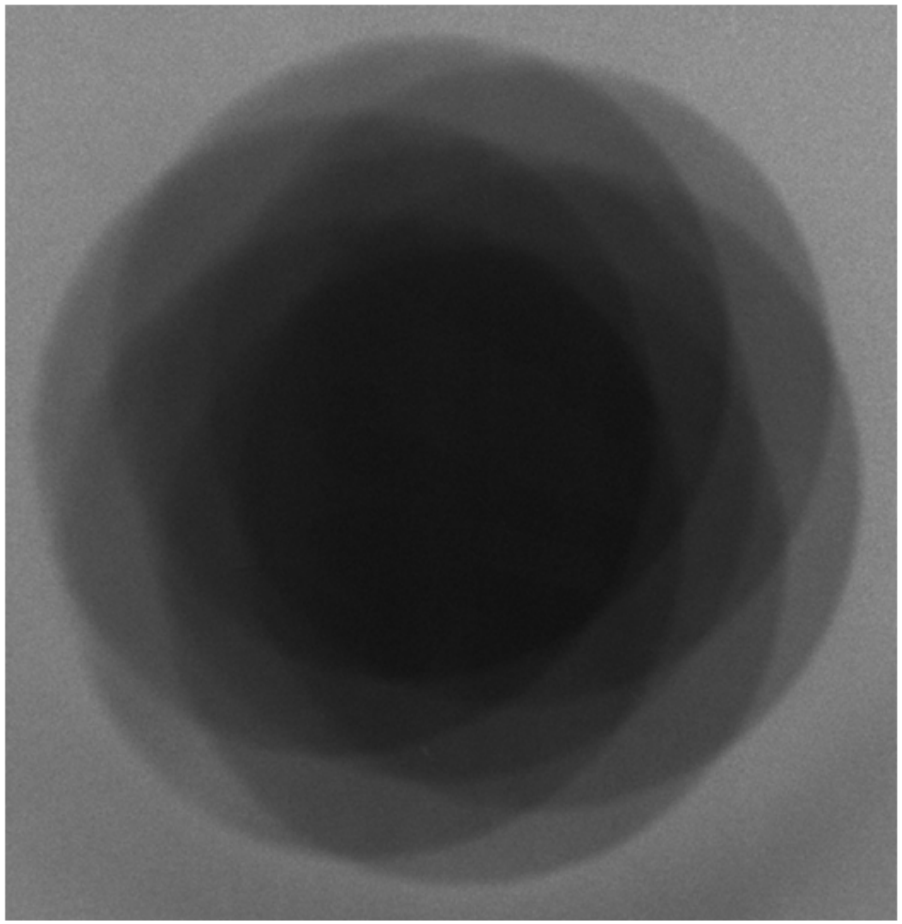

Figure 4.39. Bare beam image taken on an image plate placed at the farthest image plane using the multi-pinhole collimator. The exposure time is 40 minutes at 1MW reactor power.

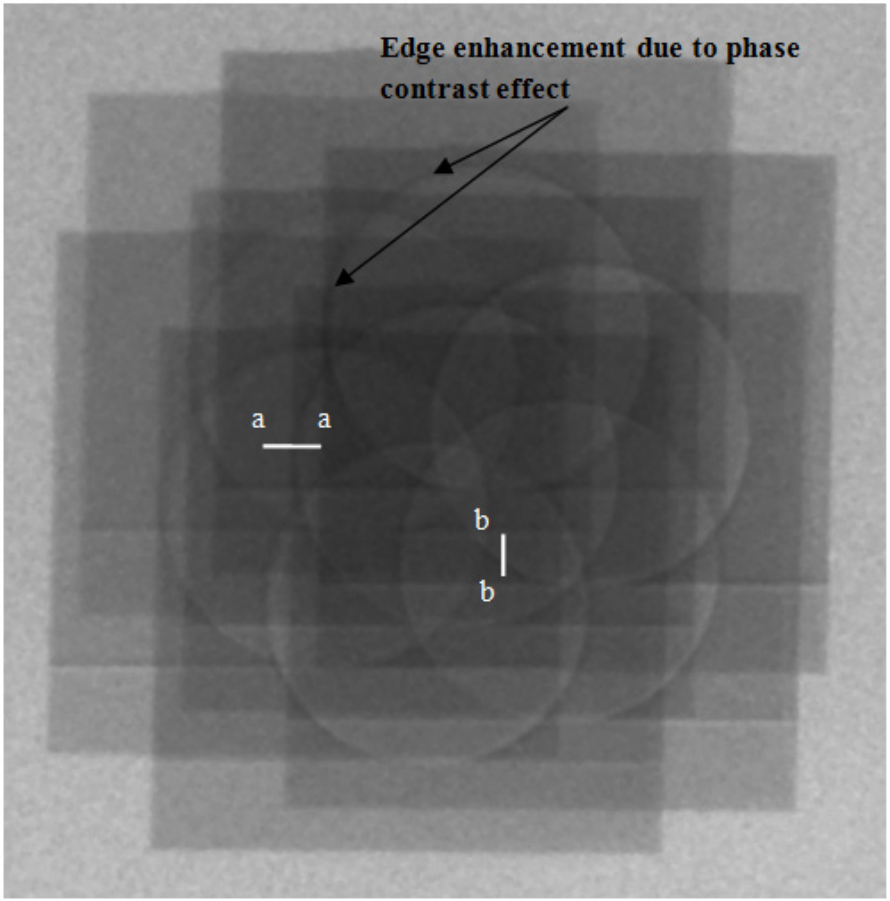

Figure 4.40. Radiograph of an aluminum rod 2 inches in length 1cm in diameter taken using the multi-pinhole collimator. The object to image plane distance is 170cm. The exposure time was 120 minutes at the 1MW reactor power.

beam profile resembles the expected profile shown in Figure 4.36. The intensity obtained by each of the holes is reasonably uniform indicating good alignment of different lead and borated polyethylene discs with the gadolinium pinholes. The size of the common illumination area is also very close to the calculated size of 7.6cm (diameter of the largest circle inscribed in the common illumination region at the image plane).

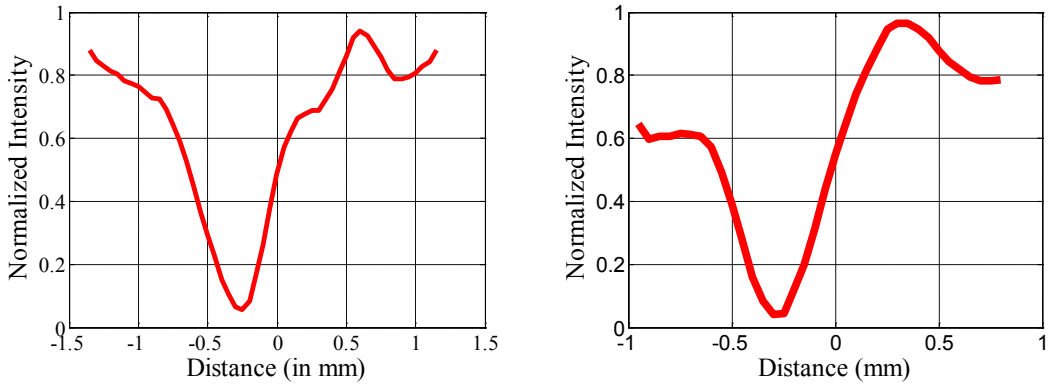

(a) **(b)**

Figure 4.41. Normalized intensity profile along the edges (a) 'a-a' and (b) 'b-b' shown in Figure 4.40.

Imaging of an aluminum cylindrical rod 1cm in diameter and 2 inches in length was performed to verify if the phase contrast effect is being captured by the collimator. Figure 4.40 shows the radiograph of the aluminum rod taken using the multi-pinhole collimator. The object to image plane distance was kept to be 175cm in this case. The rod was surrounded by cadmium sheet with a 1inch×1inch square hole in the center. Edges of the square hole in the cadmium can be observed in the figure. Image of the circular aluminum cross-section can be clearly observed in the image shown even without reconstructing the image. Moreover, the phase contrast effect at the aluminum edge is also clearly visible which makes the aluminum edges more enhanced than even the cadmium edge. The normalized intensity profile of the edges 'a-a' and 'b-b' are shown in Figure 4.41(a) and Figure 4.41(b) respectively. The intensity profiles were smoothed by three point moving average. From the profile the intensity redistribution at the edges due to the phase effect can be clearly observed. This verifies the

design of the multi-pinhole collimator which was mainly performed to capture phase contrast effect along with improved SNR.

In this Chapter design and experimental results of phase contrast neutron imaging at the PULSTAR facility using single and multi-pinhole apertures was presented. In the next Chapter, image reconstruction technique that might be used to reconstruct the images obtained from multi-pinhole un-coded masks has been investigated.

CHAPTER 5

MULTI-PINHOLE IMAGE RECONSTRUCTION

5.1 Introduction

As was pointed out in the previous chapters, reconstruction of the raw image data, collected using the multi-pinhole system, is the major burden associated with this imaging technique. Image reconstruction is in general an inverse problem which is often ill-posed. The reconstruction technique gets simplified if a coded mask is being used as a source as will be shown briefly in Section 5.3. But, in the present work, coded masks were not used because of certain constraints associated with them as outlined in Chapter 3. Therefore, in the present chapter the reconstruction technique applicable to the so called un-coded masks will be mainly discussed.

5.2 Image Reconstruction: An Inverse Problem

Inverse problems are ubiquitous in science and engineering. An inverse problem in general can be written as

$$K(f) = g\,, \tag{5.1}$$

where f is the quantity of interest, g is the observed data, and $K(.)$ is the *operator* connecting the quantities f and g. The operator $K(.)$ may be either known, which is often the case in physical science and engineering, or unknown, like in biological and social sciences most of the times. When $K(.)$ is unknown it is modeled using *influence* variables (which are perceived to influence the outcome). The observed data g contains noise due to various

reasons like experimental errors, un-modeled influences, numerical round-offs etc. Thus, different methods of solving inverse problems try to obtain an estimate of f i.e. $\hat{f}$ given $K(.)$ and g (which contains noise), such that $\hat{f}$ is closest to the true value f according to some specific criteria defined by the solution method. The method used to solve a particular inverse problem depends on the nature of the operator equation i.e. Eq. (5.1). Equation (5.1) is said to be well-posed provided [104]

i. for each g there exists a f, called a solution ,for which Eq. (5.1) holds;

ii. the solution f is unique; and

iii. the solution is stable with respect to perturbations in g. This means that if $K(f^*) = g^*$ and $K(f) = g$, then $f \to f^*$ whenever $g \to g^*$.

If a problem is not well-posed then it is called *ill-posed*. It is ill-posed problems which are often of interest.

Usually, the kind of inverse problems of interest cannot be solved analytically and computational methods play a fundamental role in it. In order to use computational techniques and computers, Eq. (5.1) is converted into a set of algebraic linear equations by discretizing the problem space, given by

$$A\underset{\sim}{f} = \underset{\sim}{g}, \tag{5.2}$$

where $\underset{\sim}{f}$, $\underset{\sim}{g}$ are the discretized value of f, g, and A is the matrix obtained by linearizing and discretizing the operator $K(.)$ in some specific domain of the problem. Linearization is only necessary if the actual operator $K(.)$ happens to be non-linear. In that case the matrix A changes in different discretized domains of the problem. Taylor's series expansion is often used to perform linearization. If the problem is linear then the matrix A is valid over the whole problem space and solution of the linear system of equations as given by Eq. (5.2) provides the

estimate $\hat{\underset{\sim}{f}}$ of discretized values $\underset{\sim}{f}$. The nature of the matrix depends on the nature of the operator $K(.)$.

Inverse problems that are encountered in the field of image reconstruction often involve solving the Fredholm integral equation of the first kind given by

$$g(x,y) = \iint_{\mathbb{R}^2} k(x,x',y,y') f(x',y') dx'dy', \tag{5.3}$$

where f is ideal image of the object, g is the blurred image, and k is known as the system point spread function (SPSF). Equation (5.3) is a linear operator equation and therefore linearization is not required in this case. The SPSF k depends on the system specification and the geometry of imaging. Often, in imaging, the SPSF is either invariant under spatial translation or is assumed to be so thereby converting Eq. (5.3) to a two-dimensional convolution integral given by

$$g(x,y) = \iint_{\mathbb{R}^2} k(x-x',y-y') f(x',y') dx'dy'. \tag{5.4}$$

This simplifies the problem by reducing it from four variables to two variables operator equation.

In order to solve for f given g and k using computational methods, Eq. (5.4) needs to be discretized. Actually images are often discretized automatically by the device it is taken into small picture elements (pixels). The discrete form of Eq. (5.4) is given by

$$g_{ij} = \sum_{i'=0}^{N_x-1} \sum_{j'=0}^{N_y-1} k(x_i - x_{i'}, y_j - y_{j'}) f(x_i, y_j) \Delta x \Delta y, \tag{5.5}$$

where N_x and N_y are the number of pixels in the x and y directions. It should be mentioned that Eq. (5.5) is not exact as there is an error involved in averaging the integral in Eq. (5.4) over each pixel. This error decreases with the decrease in the pixel size. Equation (5.5) is a linear system of equations and can be posed as Eq. (5.2). The right hand side of Eq. (5.2) ($\underset{\sim}{g}$) is

obtained from g_{ij} using e.g. lexicographical ordering. It should be mentioned here that g_{ij} also includes noise in the collected image due to various sources like counting statistics, background noise, electronics noise etc.

Various inverse techniques exist in the literature to solve Eq. (5.2) obtained from Eq. (5.5). These techniques are called de-convolution techniques (as the forward problem is a convolution equation). One of the well known techniques is by using Fourier transforms which is uses property (5) in Appendix B to give the inversion formula as

$$f = F^{-1}\left\{\frac{F\{g\}}{F\{k\}}\right\}, \tag{5.6}$$

where $F\{\cdot\}$ is the Fourier transform of $\{\cdot\}$. If $F\{k\}$ takes on zero values, Eq. (5.6) is not valid. If it takes small non-zero values, the reconstructed f is unstable with respect to the perturbations in g that happens due to the noise. This makes the technique not suitable for the present problem as often the SPSF are such that $F\{k\}$ will have values near zero. Least square technique can also be used to solve Eq. (5.2). But even this technique will be unstable. Other methods of de-convolution include use of wavelet transforms, expectation maximization, Bayesian techniques and their combination [105]-[109]. But in general all these techniques are unstable as the actual de-convolution problem is ill-posed. In order to bring stability in the solution regularization techniques are used. In general, regularization means approximation of an ill-posed problem by a family of neighboring well-posed problem [110]. In this the matrix A in Eq. (5.2) is modified in order to favor some particular kind of solutions that are close to f in some sense, thereby making the system stable. A regularization method consists of a regularization operator, a parameter and a selection rule. The regularization operator defines the rule of modifying the matrix A. The parameter controls the extent of modification of A performed by the regularization operator. The selection rule provides the basis for selecting optimum value of the parameter. Multiple different regularization methods exist like Tikhonov regularization (will be discussed later in detail), total variation regularization, regularization by projection etc.

Usually, the SPSFs encountered in imaging are unimodal having a single peak. Therefore, most of the above de-convolution techniques are designed for that kind of SPSF. In the case of multi-pinhole imaging the SPSF is multimodal with the number of peaks equal to the number of pinholes in the source mask. Thus, above techniques need to be adapted to include the multimodality along with the spread happening due to every single pinhole.

5.3 Coded Mask Image Reconstruction

Reconstruction of the data collected using coded masks is performed using a reconstruction mask designed following a specific algorithm. This algorithm depends upon the type of the coded mask being used as the source. If the coded mask image is represented by a binary array ***A*** then the image data collected, ***I***, can be written using Eq. (3.55) (blurring due to single pinhole spread is not considered) as

$$I = A * O + Noise \tag{5.7}$$

where, ***O*** is the ideal image of the object that can be obtained using a single pinhole and '*' is the two dimensional convolution operation. Corresponding to the coded mask ***A*** there exists a reconstruction mask ***G*** whose autocorrelation with ***A*** results into a Dirac delta function ***δ*** which is zero everywhere else except at the center. The obtained image data ***I*** is cross-correlated with the reconstruction mask ***G*** to obtain the reconstructed image $\hat{I}$ as detailed in Eq. (5.8). In the equation $\otimes$ denotes the auto-correlation operation which is like the convolution but without flipping. Thus, it can be observed that the noise in the reconstructed image comes from the noise in the raw data which also gets cross-correlated with the reconstruction mask ***G***. More details about the coded mask reconstruction technique can be found in [96]-[98].

$$\begin{aligned} \hat{I} &= I \otimes G \\ &= \left(O * A + Noise\right) \otimes G \\ &= O * \left(A \otimes G\right) + Noise \otimes G \\ &= O * \delta + Noise \otimes G \\ &= O + Noise \otimes G \end{aligned} \tag{5.8}$$

5.4 Image Reconstruction for Un-coded Masks

The process of image reconstruction for an un-coded mask relies on directly de-convolving the image $I_{pin}(x_d, y_d)$ from the obtained raw image $I_{raw}(x_d, y_d)$. As is clear from Eq. (3.56) the raw image $I_{raw}(x_d, y_d)$ obtained can be expressed as the convolution of desired image $I_{pin}(x_d, y_d)$ with two functions, namely the source mask image on the detector with no spreading $S_{img}(x_d, y_d)$ and the spread function of each of the pinholes at the image plane $PSF_{pin}(x_d, y_d)$ along with an added noise. A discritized form of Eq. (3.56) can be written in the matrix notation as

$$g = P \cdot M \cdot f + N, \tag{5.9}$$

where $g \equiv vec\{I_{raw}(x_d, y_d)\}$, $f \equiv vec\{I_{pin}(x_d, y_d)\}$, M is the convolution matrix corresponding to the convolving function $S_{img}(x_d, y_d)$, P is the blurring matrix corresponding to the $PSF_{pin}(x_d, y_d)$ and N is the discritized noise in the image. Here, $vec\{{}_mA_n\}$ of a matrix ${}_mA_n$ is defined as the $mn \times 1$ vector formed by the lexicographical ordering of the elements of the matrix. Thus, assuming that the matrices M, P and $I_{raw}(x_d, y_d)$ are known the above reconstruction problem simplifies to solving the matrix Eq. (5.9) for $f \equiv vec\{I_{pin}(x_d, y_d)\}$ in the presence of noise N. If the matrices M and P are not known, which is usually the case, then they need to be estimated before this process can be implemented. One way of estimating these matrices will be presented in the later Section.

The solution to Eq. (5.9) can be performed using a two-step least square de-convolution as is given by

$$\tilde{g} = P^{ginv} g \quad \text{Step.1}; \qquad \tilde{f} = M^{ginv} \tilde{g} \quad \text{Step.2} \tag{5.10}$$

where, $P^{ginv} = \left(P^T P\right)^{-1} P^T$ and $M^{ginv} = \left(M^T M\right)^{-1} M^T$ are the generalized inverses of P and M respectively, $\tilde{g}$ is the PSF de-convolved image and $\tilde{f}$ is the reconstructed image. This

technique has the advantage of easy implementation but needs large memory space to store the matrix M whose size increases rapidly with the size of the source mask image and the size of the raw image. The error ε in the reconstructed image $\tilde{f}$ can be defined as

$$\varepsilon = \frac{\sigma_{(\tilde{f}-f)}}{\sigma_f}, \tag{5.11}$$

where σ_β is the standard deviation associated with the quantity β. The estimate of the error values ε will be denoted by $\hat{\varepsilon}$. This definition of error requires f to be known and therefore will only be used to study the performance of the reconstruction technique using simulation results where actual object is known. It should be mentioned that the de-blurring step (Step 1) may not be necessary in all the cases. If blur in the image does not seem to be significant then Step 1 in Eq. (5.10) can be skipped and just Step 2 can be performed. As mentioned in previous chapters, blurring of the image depends on two important factors namely, the L/d ratio of the imaging system and the distance between the object and the detector. Blurring increases with decreasing L/d ratio and increasing object-to-detector distance. In multi-pinhole imaging applications like phase-contrast imaging usually the L/d ratio is very large such that significant blurring does not take place even at large object-to-detector distances. Therefore, PSF de-blurring is not expected to be necessary in the case of phase contrast neutron imaging.

In the presence of noise N in the raw data the above outlined de-convolution process may result in reconstructed images $\tilde{f}$ having high noise content. This is because, as mentioned before, the de-convolution process falls in the class of ill-posed problem with the associated matrices being ill-conditioned and a small amount of noise in the raw data can lead to large errors in the estimates [104]. In the present case of multiple pinhole system, the system of equations become unstable when the spreading that happens due to the matrix P is significantly more than the distance between the pinholes in the source mask image at the image plane. In such cases slight changes in the pixel values of the raw image (which makes the right hand side of the system of equations) due to noise can lead to different solutions. This may not happen when the number of pinholes in the source mask is less and separated by large distance

compared to the detector resolution and the spread of the PSF. But as the number of holes in the source mask increase and the distance between them decreases, the condition number of the associated de-convolution matrix decreases causing ill-conditioning. In such cases regularization techniques can be used to tackle the instability. In this work Tikhonov regularization has been considered for that purpose [104]. In this scheme a L_2 penalty is imposed on the least square functional that is being minimized by Eq. (5.10). This minimization problem gives rise to the two step linear system

$$\tilde{g}^* = P^* g \quad \text{Step.1}; \quad \tilde{f}^* = M^* \tilde{g} \quad \text{Step.2}, \tag{5.12}$$

where $P^* = \left[P^T P + \alpha_1 \Gamma^T \Gamma\right]^{-1} P^T$ and $M^* = \left[M^T M + \alpha_2 \Upsilon^T \Upsilon\right]^{-1} M^T$, $\tilde{g}^*$ is the regularized PSF de-convolved image vector and $\tilde{f}^*$ is the regularized reconstructed image vector. Here, Γ, Υ are the Tikhonov matrices associated with the two steps and α_1, α_2 are the corresponding scale parameters to adjust the weight of regularization. Tikhonov matrices Γ and Υ can be selected to give importance to certain kind of solutions. When they are selected to be Identity matrix I then it gives preference to the solutions with smaller Euclidian norm. It can also be selected as difference operator or the Fourier matrix to give more importance to smoother solutions. In this work, Tikhonov matrices were selected as Identity because smaller norm was considered to be a desirable characteristics and the underlying object being reconstructed is not smooth. The scale parameters need to be adjusted to obtain optimal reconstruction in terms of minimizing the error ε as defined in Eq. (5.11). To minimize the error further, de-noising techniques can also be considered.

5.5 Simulation Results and Discussion

The above technique was applied to simulated test images to study its performance in being able to reconstruct the images. In the reconstruction, the source mask image $S_{img}(x_d, y_d)$ or the matrix M in Eq. (5.9) and $PSF_{pin}(x_d, y_d)$ or the matrix P in Eq. (5.9) are assumed to be known. This is a fair assumption to make since the source mask image $S_{img}(x_d, y_d)$ can be estimated from Eq. (3.49) with a, b and the location of holes on the mask being known.

Another way to estimate it will be explained later using simulations and experimental data. $PSF_{pin}(x_d, y_d)$ at known distances a and b can be obtained by imaging a very small pinhole through a single pinhole source mask. The diameter of the hole in the single pinhole source mask should be the same as the diameter of holes in the multi-pinhole mask.

5.5.1 Reconstruction of the System Point Spread Function

Reconstruction of the system point spread function (SPSF) can be used to study the performance of this technique. The system point spread function is the image of a point object as taken by the multi-pinhole imaging system. The point object in practice is materialized by a pinhole drilled on a neutron absorbing material like gadolinium where the neutrons just pass through the pinhole. The transmission function of such objects is described by a delta function which is zero everywhere except at the pinhole where its value is unity. An inverted delta function is defined as a function that is unity everywhere except at the center where it is zero. It can be realized approximately by a pinhole made in thin aluminum plate that is filled with neutron absorbing material like gadolinium. Thus, the image obtained, called the SPSF, of such object provides an idea of how the image of a point is going to look like if taken by that system. It is also sometimes referred to as impulse response of the system. Analysis of the SPSF provides a great deal of insight into the system characteristics and the performance of the algorithms which are being used for post processing.

Figure 5.1(a) depicts the random multi-pinhole mask used in the simulation. The mask is a 40×40 binary array with 300 randomly distributed holes denoted by '1s' in the array. The single pinhole spread function $I_{pin}(x_d, y_d)$ selected to be 5×5 normalized Gaussian with a standard deviation of 0.6. The delta function has a unit spike at the center where as the inverted delta function has a unit trough at the center surrounded by a plateau. The raw image obtained for the delta and the inverted delta function with no added noise is shown in Figure 5.1(b) and Figure 5.1(c) respectively. Figure 5.1(d) and Figure 5.1(e) show the reconstruction of the raw images using the two step least square de-convolution technique given by Eq. (5.10). The conjugate gradient (CG) method was used to implement the two-step least square technique as an iterative search algorithm (see Appendix C). Advantage of using the CG method is that the

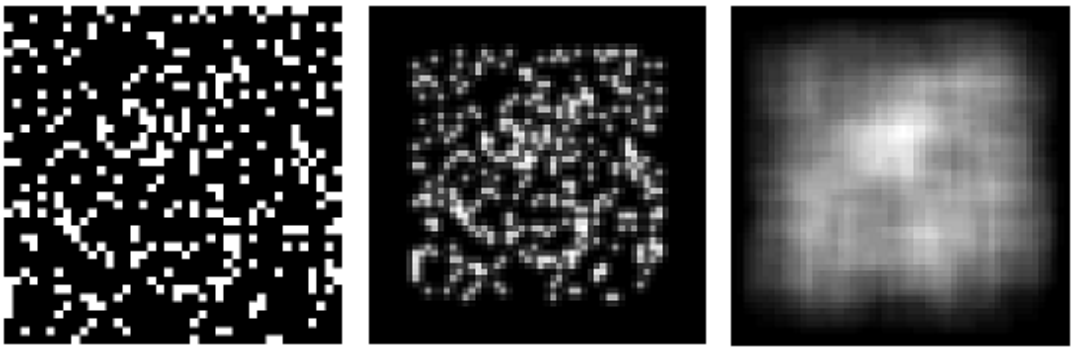

(a) (b) (c)

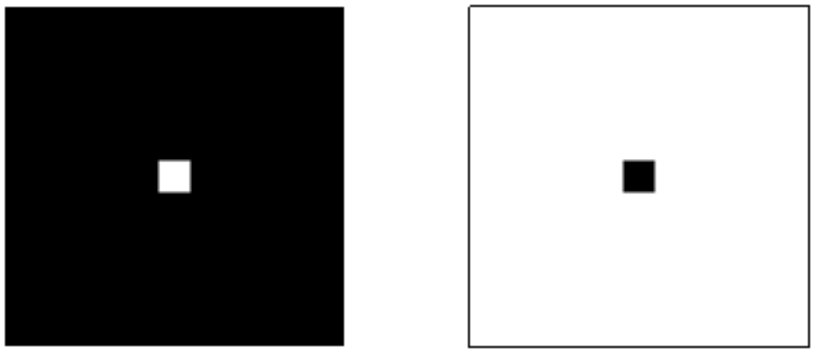

(d) (e)

Figure 5.1. (a) The random multi-pinhole mask image at the image plane with 300 holes. (b) The raw image at the image plane with no noise obtained for a delta function. (c) The raw image at the image plane with no noise obtained for an inverted delta function. (d) The reconstructed delta function from Figure 5.1(b) using two-step least square de-convolution process ($\varepsilon = 2.81\times10^{-7} \pm 4.73\times10^{-24}$). (e) The reconstructed inverted delta function from Figure 5.1(c) using two-step least square de-convolution process ($\varepsilon = 3.84 \times 10^{-6} \pm 7.26 \times 10^{-22}$). All the images are in the grayscale with white being the maximum.

prior information available about the object can be used to provide good initial estimate of the solution to reduce the iteration time. The error tolerance used in the CG method for all the cases was 10^{-9} unless otherwise stated. Reconstructed images as well as the error values given clearly indicate a good reconstruction using this technique in the absence of noise. The error in the reconstruction of inverted delta function is more because for this the '0s' in the mask array starts acting as effective holes, thus increasing the effective number of holes from 300 to 1300. This indicates that even with very large number of holes the technique performs quite well. The error values quoted for each reconstructed image was obtained as the mean of errors obtained in fifty iterations to decrease uncertainties in their estimates. The deviations quoted in the error estimates are twice the standard error obtained for the estimated error values $\hat{\varepsilon}$.

The performance of the generalized inverse technique was also investigated in the presence of the different levels of noise in the raw data. Main sources of noise in the present imaging exercise are the counting statistics, and the gamma noise. Noise due to counting statistics is usually modeled using Poisson process. That has not been considered in the model here because, when the SNR is sufficiently high, which turns out to be the case as number of pinholes is increased, the counting statistics is good and hence this component of noise is low. Thus, the noise only comes from gamma rays, which behaves as additive white noise (as it is independent of neutron signal). Therefore, the raw image collected in the experiment will mainly have additive white noise, which is the model considered in the present case. Four different levels of additive Gaussian noise with standard deviations of 0.05, 0.2, 0.5 and 1.0 were considered resembling situations from very low noise systems to very high noise systems. The raw images of the delta function obtained for these four cases are shown in Figure 5.2(a)-(d). Comparing the noisy raw images in Figure 5.2(a)-(d) with no noise images in Figure 5.1(b) clearly indicates that the spreading pattern in the images slowly gets lost with the increasing noise.

Reconstructions of the noisy raw images using the two-step least square de-convolution technique are shown in Figure 5.3. All the reconstructed images show the spike of the delta function but, the images as well as the error values indicate significant noise level in the images. Also, it can be observed that some of the estimated pixel values in the reconstruction are

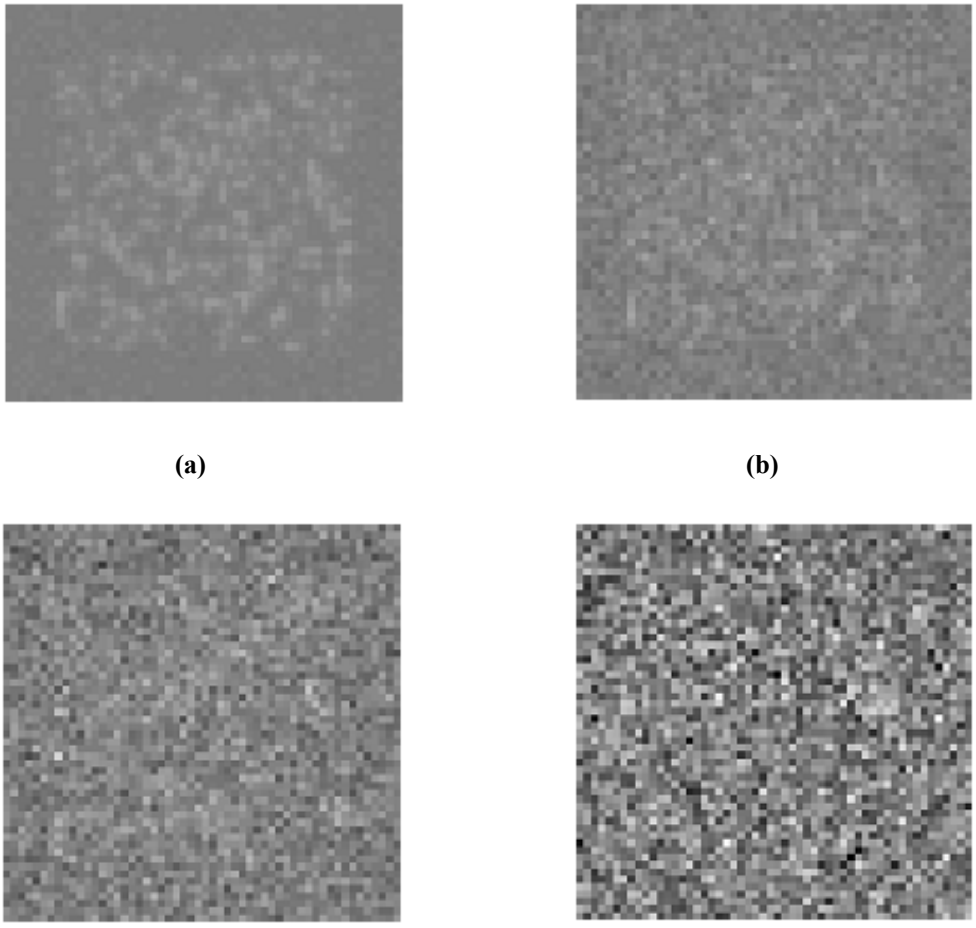

(a) **(b)**

(c) **(d)**

Figure 5.2. The raw image of the delta function with additive white noise (a) with 0.05 standard deviation (b) 0.2 standard deviation (c) 0.5 standard deviation and (d) 1.0 standard deviation. All the images have same grayscale.

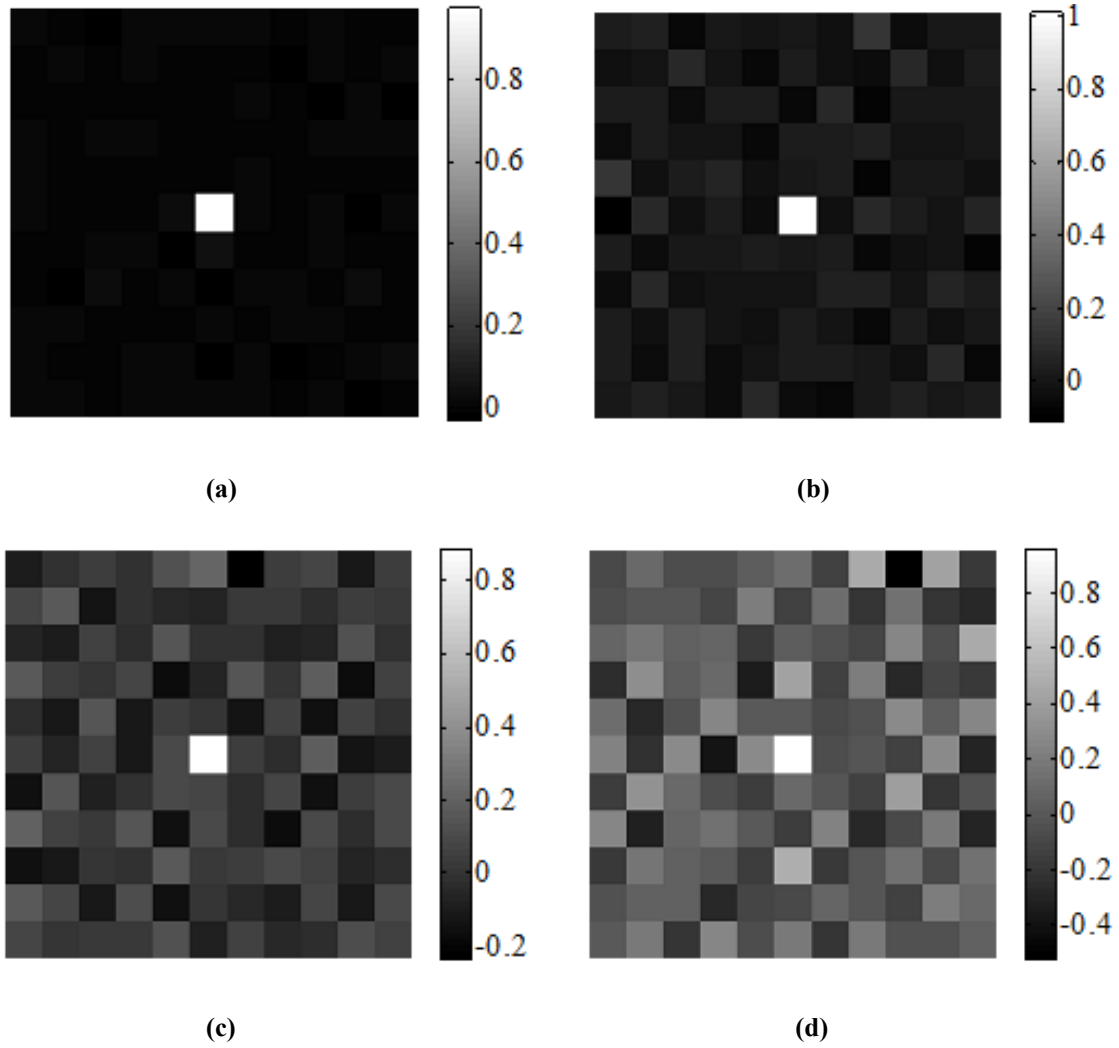

Figure 5.3. The reconstructed delta function using two-step least square de-convolution technique from the noisy raw images shown in (a) Figure 5.2(a) (b) Figure 5.2(b) (c) Figure 5.2(c) and (d) Figure 5.2(d). The error values of the reconstructed images from (a) to (d) are 0.121 ± 0.003, 0.484 ± 0.015, 1.254 ± 0.029 and 2.508 ± 0.059 respectively.

negative. This happens because no non-negativity constrained was imposed in the reconstruction technique. The noise and the negativity of pixels can be handled to a great extent by performing regularized inversion.

Tikhonov regularized reconstructed images at the optimum α_1 and α_2 values are shown in Figure 5.4. Clearly, from the images it can be observed that regularization has helped in lowering the noise and the pixel negativity in the reconstruction. For low noise raw data the scale parameter α_1 remains zero and significant difference is not observed in the estimated error values because of the change in scale parameter α_2. But, for the high noise content images the regularization significantly decreases the error. Also, the obtained reconstructed image gets smoother.

The surface plot showing the variation of the error with α_1 and α_2 values is shown in Figure 5.5. It does indicate that except for the lowest noise level a small positive α_1 value increases the stability of the matrix P to a large extent. The mask matrix M is quite stable and the error values are quite insensitive to α_2 values. This explains why the error values did not change significantly even when α_2 values were not zero for Figure 5.4(a) and Figure 5.4(b). Moreover, it also indicates that the generalized inverse technique performs well for binary matrices in contrast to the Fourier technique in which the problem of near zero Fourier coefficients is encountered [96]. Even in the Fourier technique the filtering of small Eigen values could be performed, which will have a similar effect as regularization if such a problem is observed.

As mentioned in the previous Section de-noising can also be performed along with regularization to reduce the error in the reconstructed image. In the present case both wavelets based de-noising and Wiener filtering was investigated (see Appendix D for details on these techniques). Wavelet based de-noising was performed by soft thresholding of wavelet coefficients of the raw images by using MATLAB Wavelet Toolbox. The thresholds were selected as the default values proposed by the Donoho [111]. Symlets of order four were used for two level pyramidal wavelet decomposition of the image. Soft thresholding using default global threshold was then performed for de-noising. Symlets were used because they possess

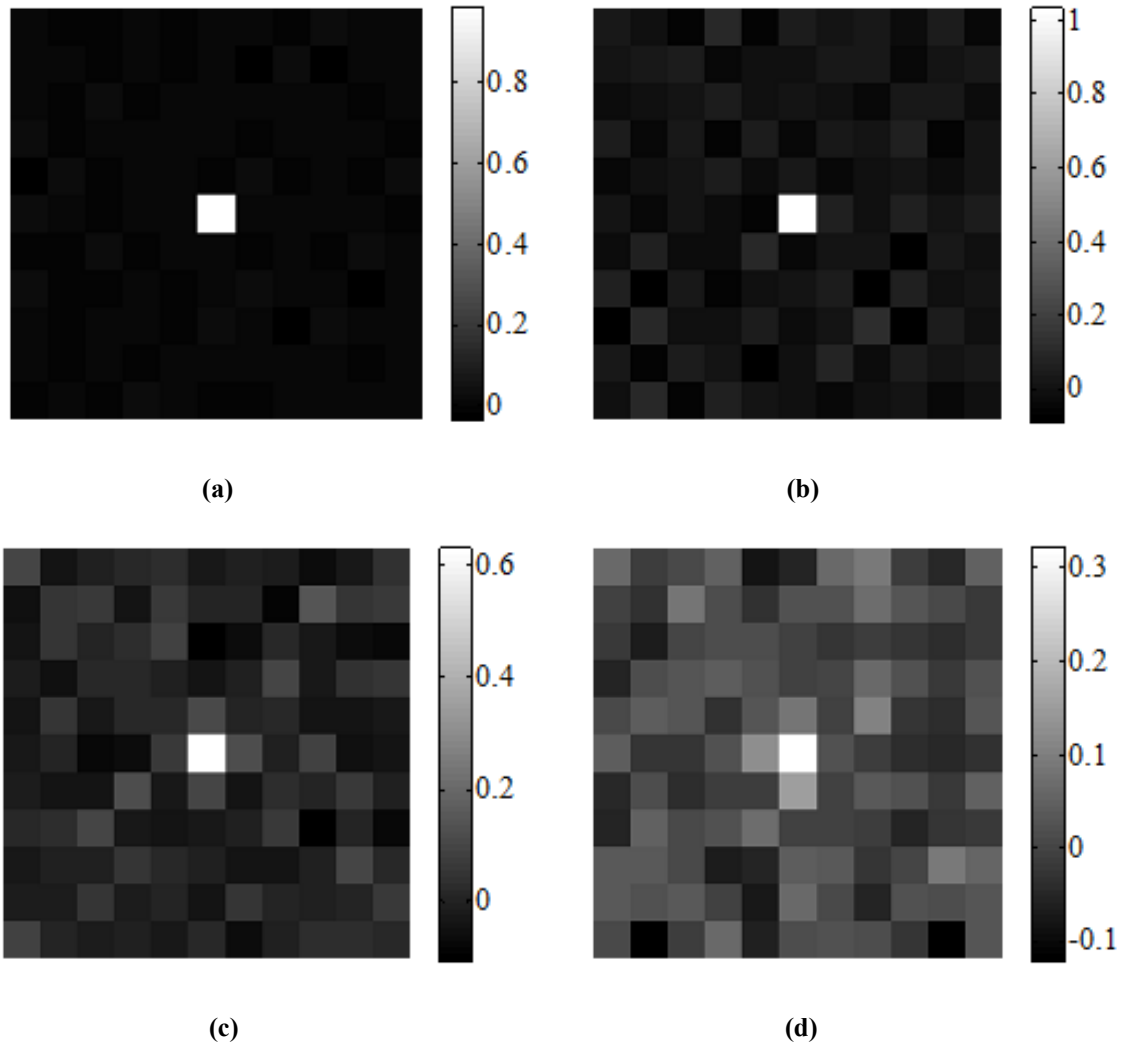

(a) **(b)**

(c) **(d)**

Figure 5.4. The reconstructed delta function using two-step regularized least square de-convolution technique at their respective optimum scale parameters from the noisy raw images shown in (a) Figure 5.2(a) (b) Figure 5.2(b) (c) Figure 5.2(c) and (d) Figure 5.2(d). Error values of the reconstructed images from (a) to (d) are 0.122 ± 0.004 (α_1= 0, α_2=0.06), 0.400 ± 0.010 (α_1= 0, α_2=0.15), 0.680 ± 0.012 (α_1= 0.1, α_2=0.9) and 0.845 ± 0.011 (α_1= 0.4, α_2=1.4) respectively.

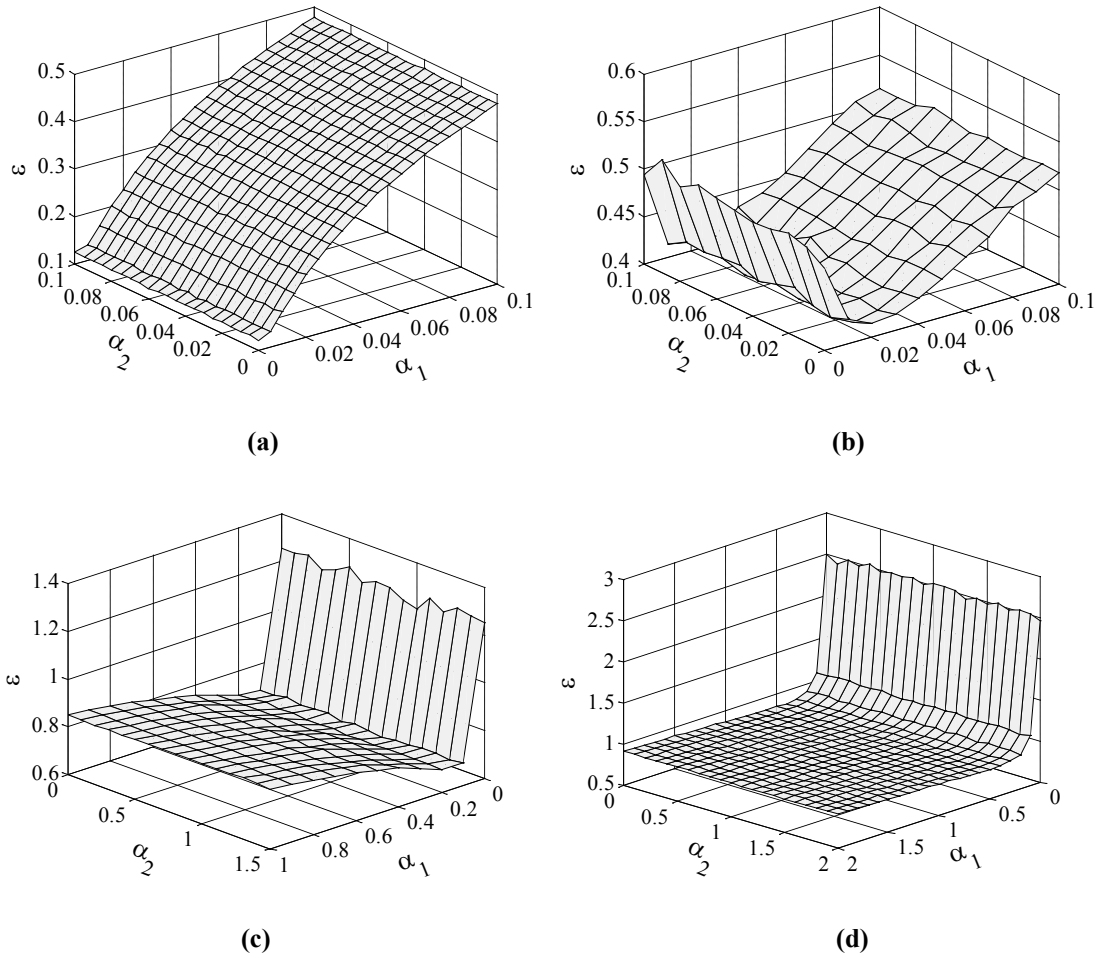

Figure 5.5. The surface plots depicting the variation of the error with the change in the scale parameter α_1 and α_2 in the two-step regularized least square de-convolution of the images shown in (a) Figure 5.2(a) (b) Figure 5.2(b) (c) Figure 5.2(c) and (d) Figure 5.2(d).

the characteristics of most vanishing moments for a given support width [112]. Adaptive Wiener filtering of images was performed using a 4×4 neighborhood to estimate means and standard deviations.

The de-noising can be performed either initially on the raw image i.e. before performing the de-convolution or at the end i.e. on the image obtained after the de-convolution or on both, using either of the two techniques mentioned above. Although, it was expected that initial de-noising of raw images before de-convolution is not suitable because of the high frequency signal content in the raw image obtained through multiple pinhole sources, all the eight possible combinations (initial wavelet de-noising (IWv), initial Wiener filtering (IWi), both wavelet de-noising (WvWv), both Wiener filtering (WiWi), initial wavelet de-noising with Wiener filtering at the end (WvWi), initial Wiener filtering with wavelet de-noising at the end (WiWv), Wiener filtering at the end (EWi), wavelet de-noising at the end (EWv)) were tested in order to study their effectiveness in reducing error in the reconstructed image. All the images were also de-convolved using regularized least square at their optimum scale parameters. The error values obtained for all these eight cases as well as the no de-noising (ND) case for the four noisy raw images shown in Figure 5.2 have been compared in Figure 5.6. For the least white noise case the de-noising does not seem to be necessary. Further, for all the four images adaptive Wiener filtering after the regularized de-convolution (EWi) performs the best with its error value being significantly lower than the others. This is because in the de-convolved image the signal should have a low frequency spectrum and thus, adaptive Wiener low-pass filtering is ideally suited for de-noising such images. The wavelet de-noising works well in removing the noise from the raw image even when the noise level is high but as mentioned earlier it also removes the signal in the raw image as the image has large wavelet coefficients arising due to multi-pinhole imaging. Thus, while thresholding the *detail* wavelet coefficients and taking an inverse wavelet transform the signal gets distorted. Because, of this effect the initial wavelet de-noising might even introduce some artifacts into the reconstruction. Thus, it can be clearly observed that initial de-noising on the raw image using any of the technique should not be performed even when the noise levels are high because of high gamma content in the beam or some other reasons. This is only applicable when there are large number of pinholes in the mask which in turn leads to high frequency signal content in the raw image. But, when the number of pinholes are less the raw

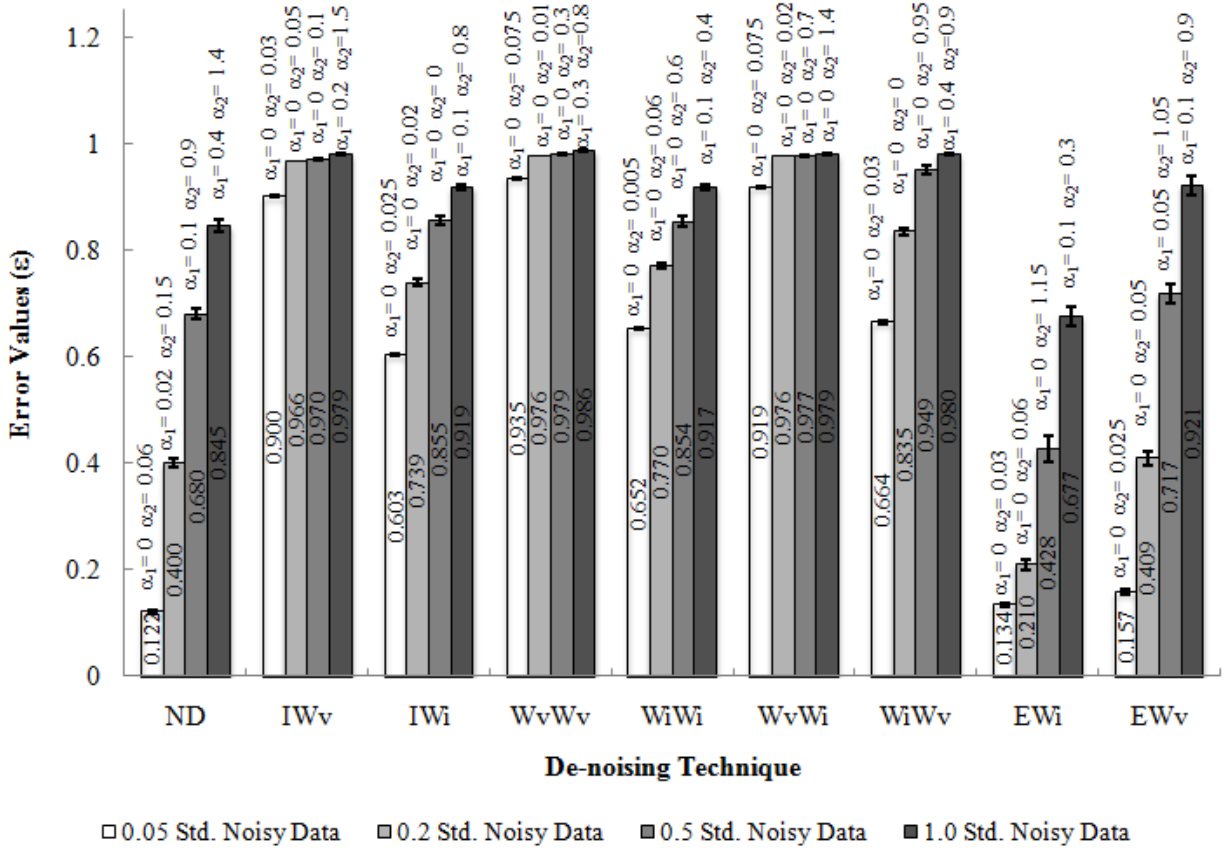

Figure 5.6. The bar chart comparing the error values obtained in the reconstructed images using two step regularized de-convolution at optimum scale parameter values and different de-noising techniques

image will not have high frequency signal content and thus initial de-nosing could be performed.

5.5.2 Reconstruction of Simulated Test Object

Reconstruction of an example object shown in Figure 5.7(a) is being presented using the above technique. The object contains different intensity regions resembling different material along with the edges between them. Usually, the samples which are imaged using neutrons have edges formed by different materials and this selected example relates to them in terms of their features. Moreover, NDE of such samples using neutron imaging necessitates good edge contrast as well as material differentiation capability. Therefore, the reconstructed image should retain these properties.

The selected mask in this case has 40 holes located randomly in the 30×30 array as shown in Figure 5.7(b). The noisy raw image of the object using this mask is shown in Figure 5.7(c). Additive white noise with a standard deviation of 0.5 was used to make the image noisy. The reconstructions of this image using the least square, regularized least square and, regularized least square with adaptive Wiener filtering of the de-convolved image are shown in Figure 5.8(a)-(c) respectively. Regularized reconstructions were performed at optimal scale parameter values. From the figure and the error values it is clear that the regularized reconstruction with Wiener filtering of the de-convolved image performs the best. But, some smoothing of the image is observed in this case which may or may not be desirable. Just regularized inversion (Figure 5.8(b)) also indicates significant improvement in the reconstruction over the least square technique. Also, no smoothing is observed in this case and thus can be suitable if smoothening is not desirable.

5.6 System PSF Estimation and Image Reconstruction: Simulated Results

The PSF of the designed system was simulated using MCNP radiation transport calculations. The geometry of the system used to perform the simulation is shown in Figure 5.9 and Figure 5.10. Simulations were performed in three stages. In the first stage the neutron source spectrum at the beam-tube entrance was obtained by running the MCNP reactor core

(a) **(b)** **(c)**

Figure 5.7. (a) Ideal image of the object. (b) Image of the pinhole mask at the image plane (c) The noisy raw image data at the image plane.

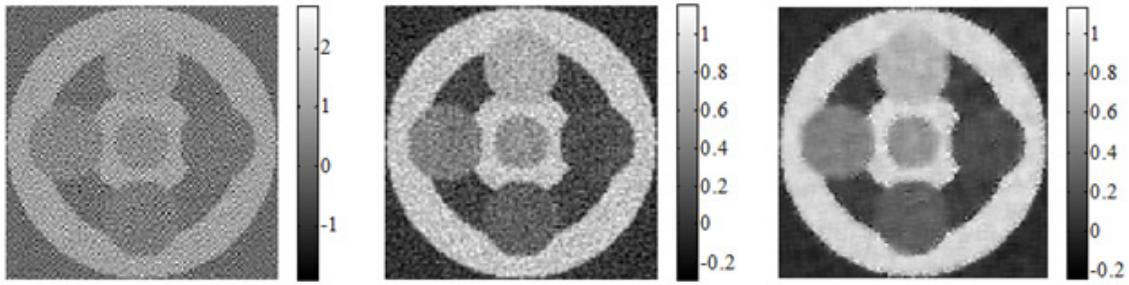

(a) **(b)** **(c)**

Figure 5.8. Reconstruction of the raw data shown in Figure 5.7(c) using (a) two-step least square de-convolution (ε = 5.061 ± 0.022) (b) two-step regularized least square de-convolution (α_1 = 0.2, α_2 = 1.7, ε = 1.666 ± 0.003) (c) two-step regularized de-convolution followed by adaptive Wiener filtering (α_1 = 0.1, α_2 = 0.3, ε = 1.222 ± 0.003).

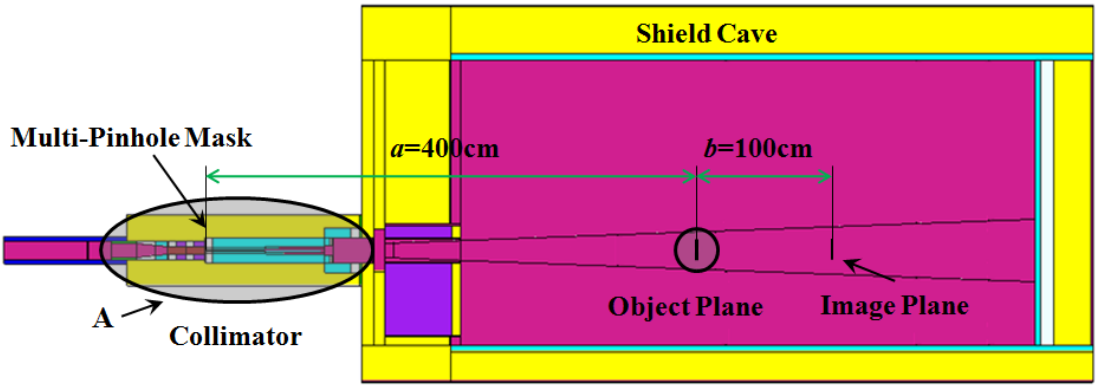

Figure 5.9. The MCNP model of the imaging system used to simulate the multi-pinhole images. The blow up of the Sections A is shown in Figure 5.10.

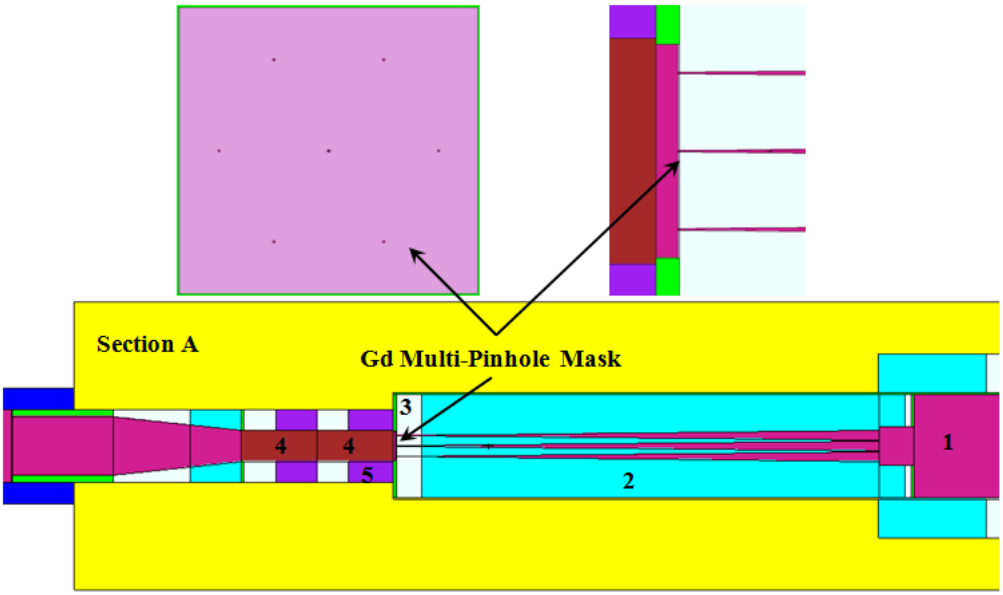

Figure 5.10. The collimator model used to perform simulation of system images. It can be compared with the designed collimator shown in Figure 4.37. The materials as indicated in the figure are (1) aluminum (2) borated polyethylene (3) lead (4) sapphire filter (5) SWX-277.

model as before (refer to Figure 2.4, Figure 2.5 and Section 2.3.2). In the second stage the obtained neutron source at the BT #5 entrance was transported through the 12 inches sapphire filter to obtain the neutron energy and spatial distribution incident on the gadolinium mask. In the third stage the source data obtained after the 12 inches sapphire filter was transported through the multi-pinhole collimator. In order to improve the statistics, the source was kept localized at the respective pinholes with a diameter of 0.6mm, as the pinholes have a diameter of 0.5mm. This should not affect the results because thermal neutrons which are emitted away from the pinholes will get absorbed in the gadolinium and will not affect the final tally. For the same reason the direction distribution of the initial source particles was defined to be a cosine distribution with a divergence of 2^{o}. Again, since the divergence of the collimator is only 0.6^{o} the neutrons which get emitted outside that angle have extremely low probability of getting tallied at the detector. These two techniques help a lot in improving the tally statistics and hence reducing the runtime.

Another technique which was used to improve the statistics is the use of detector tally. In all the simulations MCNP pinhole camera detector tally was used to obtain the images [41]. This tally is ideally suited for such simulations. The number of particles used in the third stage of the run was 2×10^{8}. The simulation was performed on the same Linux cluster available in the HPC Center at NCSU that was mentioned in Section 4.5. Each run took ~90 minutes to finish on 20 processors. In the first and the second stage the simulation was performed until good statistics were obtained.

The simulation was performed to provide an insight into different sources of error involved in the image reconstruction as they can be easily separated in this exercise. For example, in the simulation an ideal pinhole object can be used with exact known distances between the source and the object and, between the object and the image plane. Also, the angular orientation of the non-central holes is known in the simulation. These distances and angles are never measured exactly in the experiments. The present setup is such that the measured values of these parameters can have large associated error. Error in the reconstructed image due to error in the measurement/estimation of these parameters can be studied using simulations.

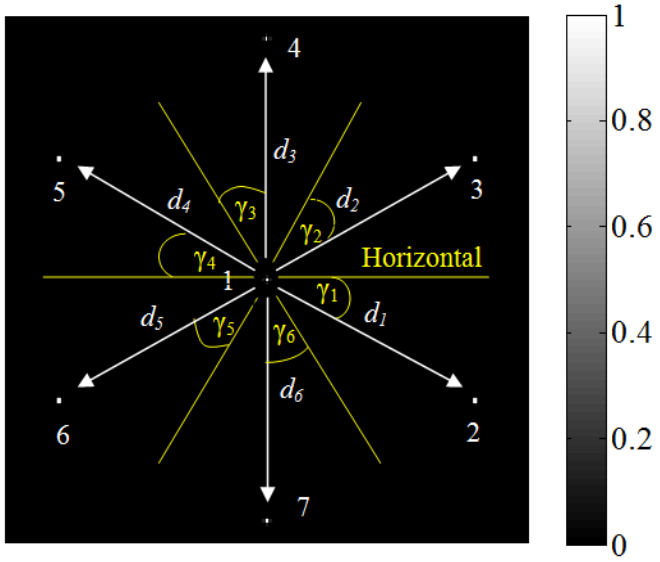

Figure 5.11. The simulated system PSF obtained using radiation transport calculations. The distance between the multi-pinhole mask and the object pinhole is 4m and the distance between the object and the image plane is 1m. The image plane grid resolution is 50μm. The image is normalized between 0 and 1.

The obtained system PSF using an ideal pinhole in the MCNP simulation is shown in Figure 5.11. In Figure 5.11 the source-to-object distance $a = 4m$ whereas the object-to-detector distance $b = 1m$ (see Figure 5.9). Thus, the relative shift multiplication factor $b/a = 0.25$. Also, the angular orientation (γ) of the non-central holes is 30° from the horizontal. Using these parameters SPSF or the source mask image at the detector $S_{img}(x_d, y_d)$ (see Section 3.6) can be obtained. In the calculation of the source mask image, the separation between the pinholes is given by d' and the centers of the non-central pinholes is calculated using both d' and γ. The radius of the pinholes centered at the calculated locations in the SPSF can be obtained using Eq. (3.48) to be 0.0625mm (0.25mm×0.25) for the mask pinhole radius of 0.25mm.

Figure 5.11 can be directly used as $S_{img}(x_d, y_d)$ but it is better to obtain it via calculations in order to avoid all the noise. Figure 5.11 hardly has any noise therefore the $S_{img}(x_d, y_d)$ calculations may not be very useful in this specific case but its usefulness will be clear when the

experimental results will be presented. Moreover, $S_{img}(x_d, y_d)$ calculation also helps in getting rid of the effect of non-zero object pinhole diameter used to obtain the SPSF image as will be described later on.

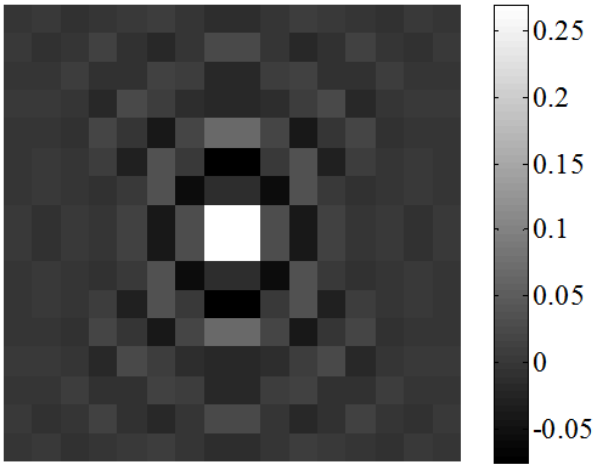

Figure 5.12. The reconstruction of the image shown in Figure 5.11 using conjugate gradient iterative least square with no regularization. The pixel size is 50µm. The source mask image for the reconstruction was calculated using known parameters $b/a = 0.25$, $\gamma = 30^o$ and the source mask pinhole diameter of 0.5mm.

Reconstruction of Figure 5.11 was carried out using the calculated source mask image. The known parameters $b/a = 0.25$, $\gamma = 30^o$ and the source mask pinhole diameter of 0.5mm were used to calculate the source mask image. Reconstructed image using the CG iterative least square without regularization is shown in Figure 5.12. The reconstruction was performed with a CG error tolerance limit of 10^{-10}. A CG error of 6.8×10^{-11} was obtained in 74 iterations. The reconstructed image indicates a single peak, as expected, corresponding to a single pinhole. The width of the pinhole is 100µm which is twice the grid resolution of 50µm in accordance with the Shannon's sampling theorem. It should be mentioned that in the reconstruction of the image no PSF de-blurring was performed as it is quite clear from Figure 5.11 that due to very high L/d ratio of the system, there is hardly any spreading of the pinholes. Thus, for the present system PSF de-blurring is not necessary but, if performed, will be better as will be presented later. Moreover, regularization was also not performed in the above reconstruction as

it was not required. This is because the source mask has only seven pinholes of 0.5mm diameter with center-to-center separation of 22mm. Also, from Figure 5.11 it is clear that in the source mask image at the image plane the holes are distinctly separated and is not affected by the PSF spreading. Regularization should not be performed if not required as it always smoothens the solution to some extent thereby reducing its sharpness, which is important in neutron imaging. Therefore, in further reconstruction of simulation and experimental images regularization will not be performed. But, in general for multi-pinhole imaging systems with large number of pinholes regularization may be necessary.

In the above case the object had an ideal pinhole with zero diameter. In experiments, the pinhole object will always have a finite diameter and the exact distances a, b and the angle γ is difficult to measure accurately from the setup. Therefore, in order to estimate the relative shift and the angular orientation of different pinholes in the image a different approach had to be considered which provides better accuracy.

One of the ways in which the relative shift multiplication factor can be estimated from the SPSF when accurate values of a and b are not available is by calculating the distances d_i's shown in the Figure 5.11, where $i = 1 \ldots 6$ and then taking their sample mean $\bar{d}$ which estimates d'. When the mean distance between the holes $\bar{d}$ is divided by the actual distance between the pinhole in the mask then an estimate of the relative shift multiplication factor is obtained. In the present case for the purpose of calculating these distances, the distance between the maximum/minimum pixel values occurring within each of the pinholes in the image was taken. The maximum/minimum value was selected because for every pinhole image it is more likely that the maximum will occur at the center of the pinhole or very close to it. For the image shown in Figure 5.11 the mean distance $\bar{d}$ was calculated to be 5.35mm using this method. The actual distance between the pinholes in the source mask is 22mm. Thus, the relative shift multiplication factor can be calculated to be $5.35/22 = 0.243$ which is close to the exact value of 0.25.

Similar estimation procedure can be used to estimate the angular orientation of the holes relative to the horizontal using the SPSF. From the geometry the angular spacing between the

non-central holes is 60°. Six different angles γ_1 to γ_6 (as shown in Figure 5.11) can be calculated and their mean $\bar{\gamma}$ estimates the angular shift of the non-central holes from the horizontal. In the simulated SPSF shown in Figure 5.11 the calculated angular shift through this method is 29.99° which is very close to the actual value of 30°.

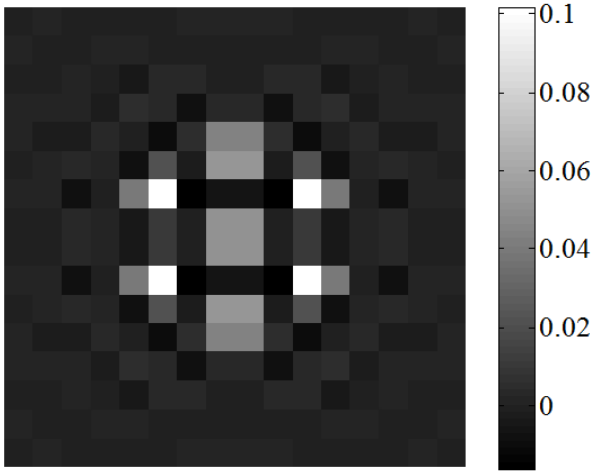

Figure 5.13. The reconstruction of the image shown in Figure 5.11 using conjugate gradient iterative least square with no regularization. The pixel size is 50μm. The source mask image for the reconstruction was calculated using estimated parameters $b/a = 0.243$, $\gamma = 29.99^o$ and the known source mask pinhole diameter of 0.5mm.

Once distance between the pinholes and their angular orientation has been estimated the image of the source mask at the image plane location $S_{img}(x_d, y_d)$ can be obtained through calculations as before. The formed source mask image can be used to reconstruct the image shown in Figure 5.11 (from which it was calculated) in order to verify the estimation process and to observe the effect on the reconstruction due to errors in the estimation process. The reconstructed image using the CG iterative least square without regularization is shown in Figure 5.13. The reconstruction was performed with an error tolerance of 10^{-10}. A CG error of 5.3×10^{-11} was obtained in 56 iterations. The reconstructed image indicates a single peak, as expected, but artifacts start appearing in the image due to estimation errors in $\bar{d}$ and $\bar{\gamma}$ even though the error did not seem to be large. In the present image the pixel size is 50μm. Thus, from the reconstructed image the artifacts seems to be localized near the object and for large

object it will mostly act like blurring. In order to tackle these artifacts the reconstruction can be performed choosing a small interval around the estimated $\bar{d}$ and $\bar{\gamma}$. The interval can be selected to be the confidence interval of these estimated parameters which can be obtained using the standard errors calculated from the different values d_i and γ_i. In this interval reconstruction should be performed at different combinations of the parameters and the best reconstructed image among them should be selected. Once the value is known it can be used for reconstruction of other object for the same system geometry.

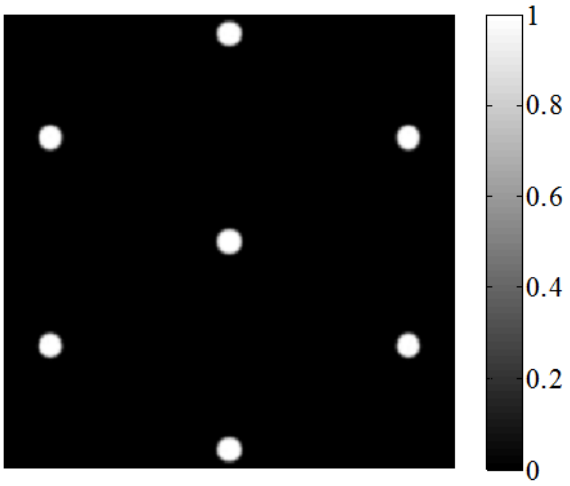

Figure 5.14. The simulated image of a black object with a central hole of 0.5mm diameter. The distance between the multi-pinhole mask and the object pinhole is 4m and the distance between the object and the image plane is 1m. The image plane grid resolution is 50μm. The image is normalized between 0 and 1.

Another simulation was performed with the same source-to-object and object-to-detector distances as above but with the object having a finite size pinhole of 0.5mm diameter. This resembles actual experiment where the SPSF is obtained using a non-zero diameter hole in the neutron absorbing object like gadolinium. The obtained image is shown in Figure 5.14. Using the above calculated $S_{img}(x_d, y_d)$ (using the estimated $b/a = 0.243$ and $\gamma = 29.99^o$) the reconstructed image via CG un-regularized least square is shown in Figure 5.15. In this case the CG error value was 2.7×10^{-11} in 51 iterations. In the reconstructed image clearly the object hole

has been diffused by blurring due to the error in $S_{img}(x_d, y_d)$, calculated using estimated b/a ratio and γ. This supports the previously pointed out notion of blurring caused by the estimation error as the object size increases.

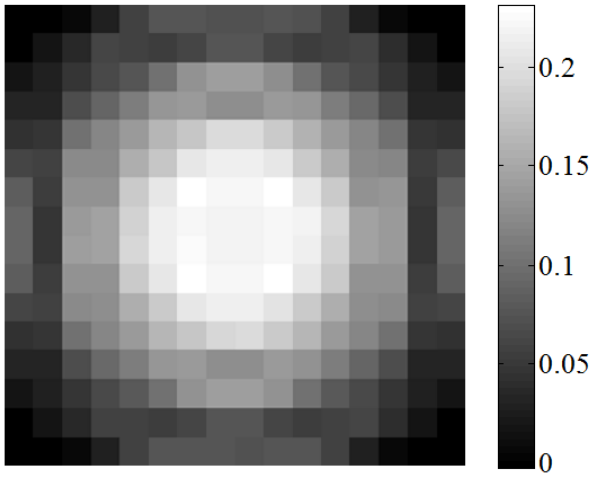

Figure 5.15. The reconstruction of the image shown in Figure 5.14 using conjugate gradient iterative least square with no regularization. The SPSF for the reconstruction was calculated using estimated values from Figure 5.11. The pixel size is 50µm.

The estimation of SPSF can be also performed using the above outlined technique from Figure 5.14. But due to non-zero diameter of the pinhole in the object the estimate can have more deviation depending upon the image. Using Figure 5.14 average hole distance $\bar{d}$ and the average angular shift $\bar{\gamma}$ were calculated to be 5.48mm and 30.25° respectively. From this the relative shift multiplication factor can be estimated to be $5.48/22 = 0.249$. Thus, it can be observed that the error in the shift multiplication factor decreased where as the error in the angular shift increased. The calculated SPSF using these parameters can be used to reconstruct the image shown in Figure 5.14 itself. The reconstructed image is shown in Figure 5.16. Clearly with improved estimate of the b/a ratio the reconstruction has significantly improved. This points out that an accurate estimate of $\bar{d}$ is critical for the reconstruction to perform well. Thus, the interval technique pointed out before should at least be followed for $\bar{d}$. It can be observed that the size of the reconstructed hole is 700µm. Ideally it should be 625µm

(500μm×1.25) using Eq. (3.47). The difference can be accounted by the grid resolution of 50μm which is not considered in Eq. (3.47). Spreading in the reconstructed image is mainly because of the grid effect and will not be visible for larger images. According to Shannon's sampling theorem the least spreading that is expected is twice the grid resolution. Here, the spreading seems to be a little higher because of the circular shape of the object that does not match with the rectangular grid.

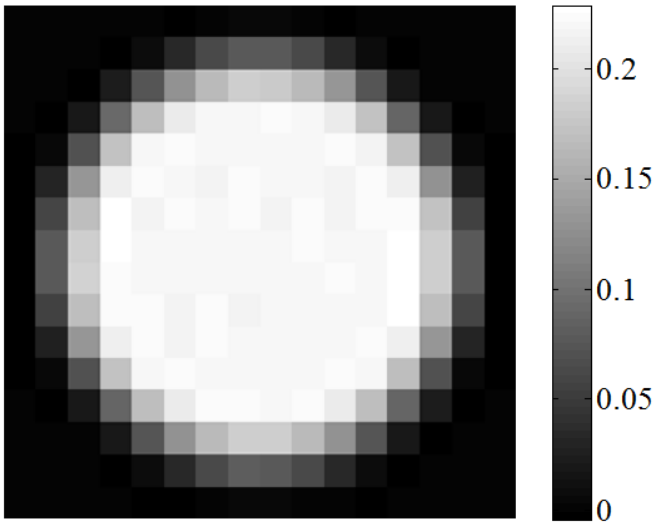

Figure 5.16. The reconstruction of the image shown in Figure 5.14 using conjugate gradient iterative least square with no regularization. The SPSF for the reconstruction was calculated using Figure 5.14. The pixel size is 50 μm.

In Figure 5.17 blurring due to non-zero pinhole diameter in the source mask is removed. This has been removed by constructing the SPSF without taking into account the effect of the finite size of the pinholes in the source mask. This is different than the de-convolution of PSF using the least square technique presented above. For the present system and other systems like this where images of different holes have much larger separation than the spread of the PSF this method will work and will perform better, as the centers of different holes can be located very precisely. PSF de-blurring increases the sharpness of the image as expected and also provides correct scaling of the gray scale. Thus, in this case the grid resolution is the limiting factor on the blurring other than the error in SPSF estimates.

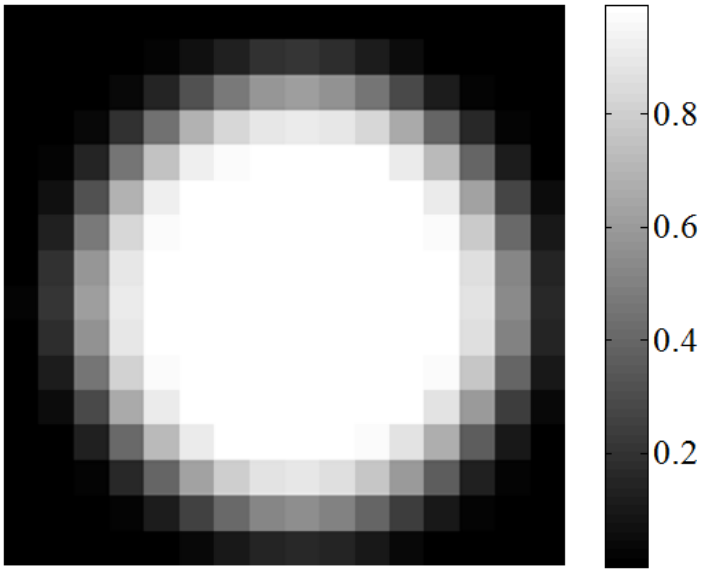

Figure 5.17. The reconstruction of the image shown in Figure 5.14 using conjugate gradient iterative least square with no regularization. The SPSF for the reconstruction was calculated using Figure 5.14 with the effect of the non-zero diameter of the source mask pinholes removed. The pixel size is 50μm.

A simple object made up of square piece of cadmium 1mm thick with a rectangular hole cut at the center (see Figure 5.18) was simulated with all the distances and angle same as before. The simulated raw image is shown in Figure 5.19(a) at 50μm resolution. Figure 5.19(b) is the same image as Figure 5.19(a) but every 4^{th} row and column is selected in it. In Figure 5.19(b) the edge degradation due to low resolution can be clearly observed. The circle in the image is the diameter of the pinhole used to cast the image on the detector plane. It behaves like the aperture of a camera which is used to take a photograph.

Large convolution matrix was associated with Figure 5.20(a). Therefore, reconstructions of Figure 5.19(b) using the ideal and the estimated SPSFs are shown in Figure 5.20(a) and Figure 5.20(b) respectively. Due to low resolution of the reconstructed image some artifacts appear in the reconstruction especially the reconstruction of the circular aperture. Representing a circle on a low resolution rectangular grid is difficult. On a low grid resolution the pixels representing the circle edge depict jumping effect as in Figure 5.19(b). When such an image is reconstructed due to pixel jumping some artifacts appear in the reconstruction as can be

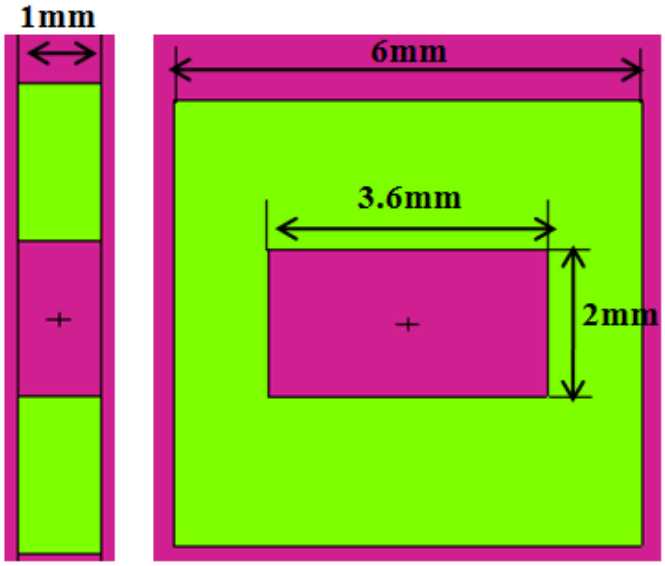

Figure 5.18. The cadmium sample used to perform MCNP simulation.

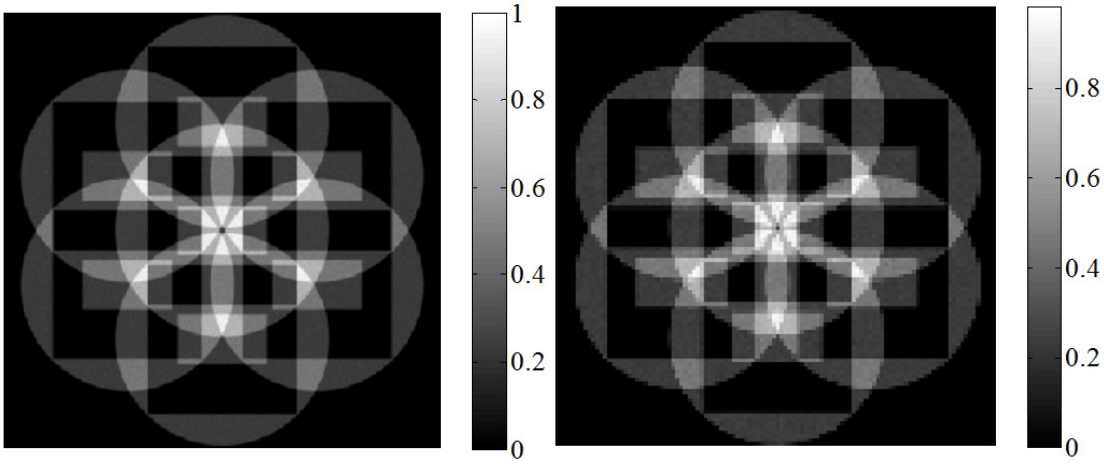

(a) **(b)**

Figure 5.19. The simulated image of 1mm thick cadmium square with a rectangular hole in it. The distance between the multi-pinhole mask and the object pinhole is 4m and the distance between the object and the image plane is 1m. The image is normalized between 0 and 1. (a) The image plane grid resolution is 50μm. (b) The image plane grid resolution is 50μm but every 4th row and column from Figure 5.19(a) is selected.

observed in Figure 5.20(a) and Figure 5.20(b). These artifacts will not appear on a higher grid resolution. Otherwise, the reconstructed images using ideal and estimated parameters clearly depict the cadmium square with a rectangular hole. Figure 5.20(c) and Figure 5.20(d) depict the reconstruction performed using SPSF obtained from somewhat larger errors in one of the estimated parameters $\bar{d}$ and $\bar{\gamma}$ which provides $b/a = 0.245$ in the first case and $\bar{\gamma} = 31^o$ in the second case. These reconstructions demonstrate the error introduced in them due to error in estimated SPSF. Due to error in the estimation of SPSF the alignment among the different overlapping images does not take place perfectly and therefore artifacts become pronounced wherever misalignment occurs. Other observation that be performed is even if the object extends outside common illumination area, the reconstruction technique works.

5.7 System PSF Estimation and Image Reconstruction: Experimental Results

Experiments were conducted using the manufactured collimator shown in Figure 4.38. The experimental setup was similar to the one shown in Figure 4.16 except that the multi-pinhole collimator was in the beam-tube instead of the single pinhole collimator. Neutron image plates were used to take the images. As the collimator is located inside the beam-tube, the measurement of mask to object distance, a (see Figure 5.9) can have error of a few centimeters. Also, since there is no alignment arrangement to accurately define the orientation of non-central holes, the angle γ differs each time the collimator is inserted. Moreover, the angular orientation cannot be measured directly. Thus, the estimation technique presented above will be used to estimate these parameters for the reconstruction of images.

The SPSF was obtained using a pinhole of ~650μm diameter in a 500μm thick gadolinium foil. The SPSF obtained at the object-to-detector distance of ~130cm is shown in Figure 5.21. The depicted image is the raw image with spike noise filter applied to it. This filter removed pixel values that are outliers. The gray scale was also adjusted to just contain the high intensity region on the image plate. This increases the contrast in the region of interest by providing more gray levels in the narrow intensity region. The image was obtained at 1MW reactor power with an exposure time of 60 minutes. The SNR of the image, as calculated by the

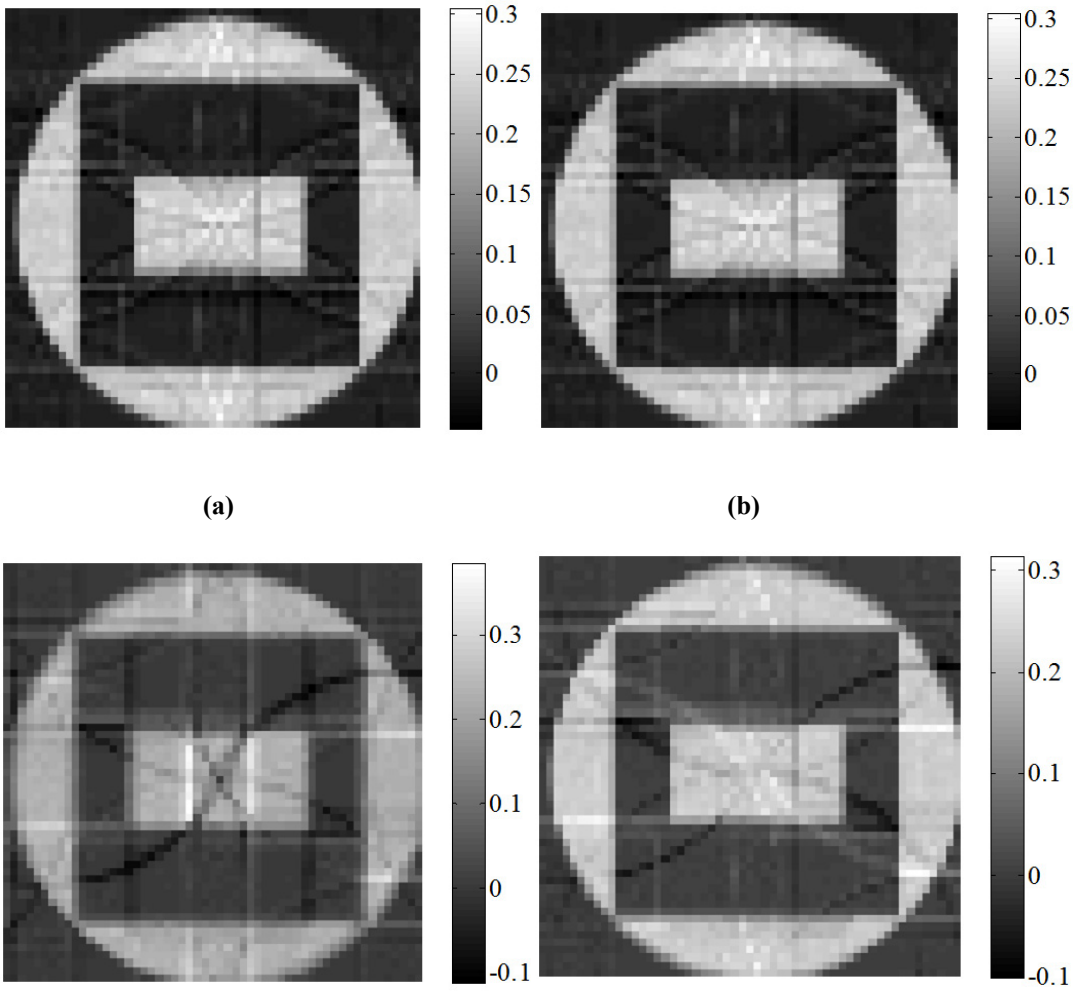

Figure 5.20. Reconstruction of the image shown in Figure 5.19(b) using conjugate gradient iterative least square with no regularization. The SPSF for the reconstruction was calculated using (a) ideal parameter values of $b/a = 0.25, \gamma = 30^o$, (b) parameters estimated using Figure 5.14 ($b/a = 0.249, \overline{\gamma} = 30.25^o$) (c) $b/a = 0.245, \gamma = 30^o$ (d) $b/a = 0.25$, $\overline{\gamma} = 31^o$ with the effect of the non-zero diameter of the source mask pinholes removed.

ratio of mean and standard deviation of all the pixels, is 7.71. The image has large noise content even with such a long exposure time because the pinhole size in the gadolinium foil used is very small and therefore not many neutrons go through it. This will not be a problem in imaging of regular objects.

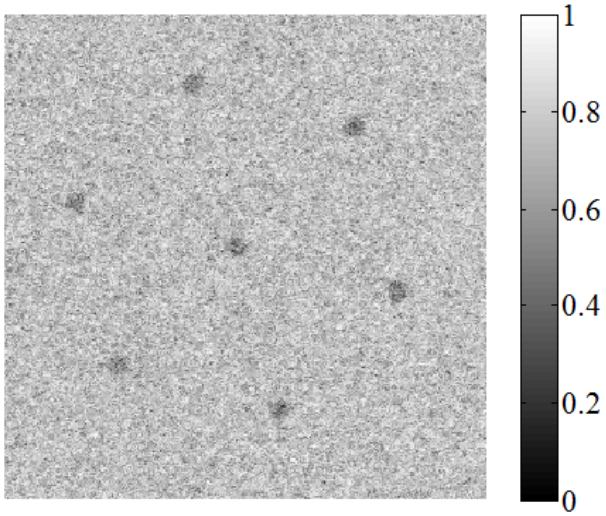

Figure 5.21. The system point spread function (SPSF) obtained using the multi-pinhole collimator. The distance between the pinhole and the detector was 130cm. The exposure time was 60 minutes at 1 MW reactor power. The image has been normalized between 0 and 1.

Various different de-noising techniques were applied to the raw image and the corresponding SNR was calculated. The de-noised images are shown in Figure 5.22 and the corresponding SNR values are quoted. In this regard it should be mentioned that comparison of SNR values should only be performed among similar images having same pixel dimensions. The de-noised images indicate that the Wiener filtering worked the best in terms of improving the SNR of the image. The soft thresholding using Symlets improves the SNR the least but visually from the image it seems that the edges are better preserved by this technique.

Wiener filtered image was used to estimate the SPSF calculation parameters $\bar{d}$ and $\bar{\gamma}$. The estimated $\bar{d}$ and $\bar{\gamma}$ values from Figure 5.22(b) are 5.2mm and 15.02° respectively. The standard errors of the estimates were 0.032mm and 0.72°. From this, the b/a ratio can be

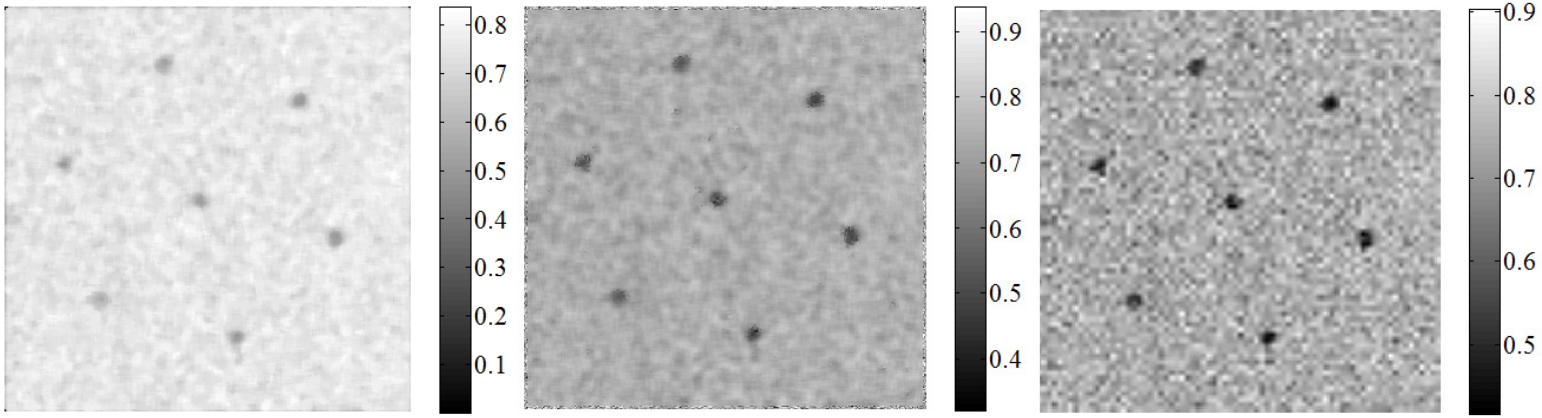

(a) **(b)** **(c)**

Figure 5.22. De-noised SPSF using (a) 7×7 Median filtering. (b) 7×7 Wiener filtering (c) soft thresholding of Symlet (of order 4) coefficients using a threshold of 0.3906. The SNR for these images are 21.98, 22.95, and 18.41 respectively.

estimated to be 0.236. The reconstruction of the image in Figure 5.22(b) itself (with alternate row and columns sampled) was performed for a range of values of d' from 5mm to 5.3mm and γ from 12° to 16°. Visually the best reconstruction was observed for $d = 5.22mm$ and $\gamma = 14.5^{o}$. The reconstructed image from the SPSF calculated using these parameters is shown in Figure 5.23. As expected the reconstructed image indicates a single hole with a size of ~800µm which is close to the calculated size of 804µm using the estimated $(a+b)/a$ ratio (magnification ratio) of 1.236.

The above calculated SPSF was used to reconstruct the raw image obtained using three pinholes in a gadolinium foil as the object. The diameters of the three pinholes were 650µm, 1000µm and 650µm. The raw image obtained after Wiener filtering is shown in Figure 5.24. The location of all the different pinholes can be clearly observed in the image. For the reconstruction every alternate row and column in the raw image was selected. The reconstructed image is shown in Figure 5.25. The three holes in the object have been reconstructed clearly.

Finally, using the above SPSF estimation and image reconstruction technique, the reconstruction of the phase contrast neutron radiograph of the aluminum cylinder, shown in Figure 4.40, was carried out. For the reconstruction every 5th row and column was selected from Figure 4.40. The reconstructed image is shown in Figure 5.26. It was smoothed using 2×2 Wiener filter. Enhanced edges of the aluminum cylinder can be clearly observed in the image. The spatial resolution of the image is not very good because of the down sampling of the original image by the factor of five. There are some artifacts in the image. They occur due to various kinds of error sources like experimental error, estimation error, error due to thick (non-planer) objects, discretization error and error due to down-sampling.

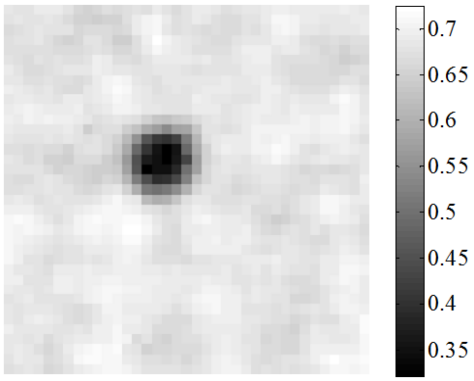

Figure 5.23. Reconstruction of the image shown in Figure 5.22(b) using conjugate gradient iterative least square with no regularization. The SPSF for the reconstruction was calculated using parameter values of $b/a = 0.237$, $\gamma = 14.5^{o}$.

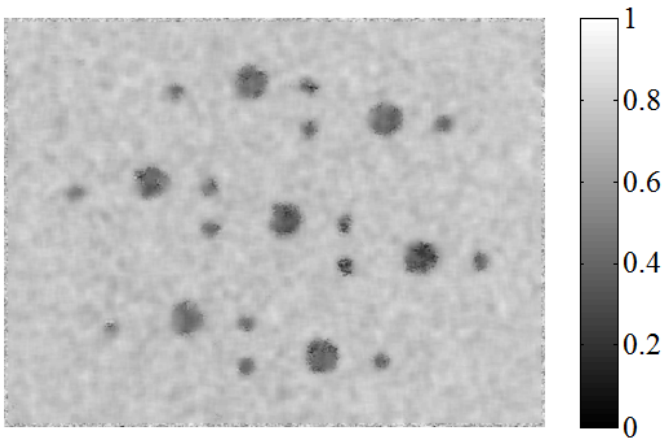

Figure 5.24. Raw image for the gadolinium foil with three pinholes after 7×7 Wiener filtering.

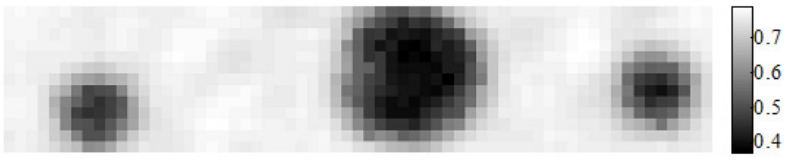

Figure 5.25. The reconstruction of the image shown in Figure 5.24 using the SPSF estimated using Figure 5.22(b).

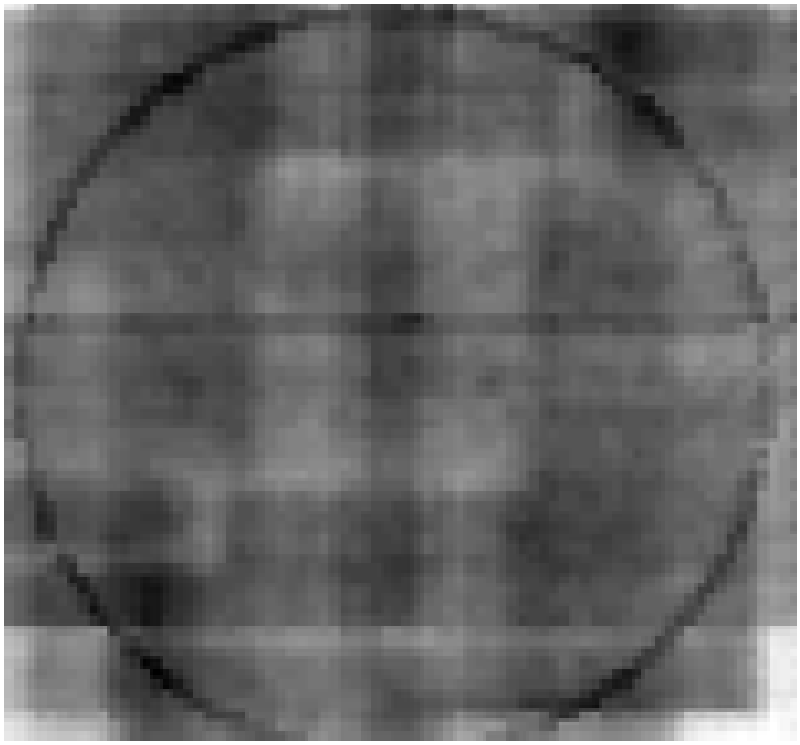

Figure 5.26. The reconstructed image of the aluminum rod from the multi-pinhole image shown in Figure 4.40.

CHAPTER 6

CONCLUSION AND FUTURE WORK

6.1 Conclusion

In the present work investigation of phase contrast neutron imaging was performed using single and multiple pinhole apertures and its feasibility at low/medium intensity neutron sources was studied. The investigation included its theoretical understanding, development of simulation techniques, system design and performance of experiments as well as exploring the image reconstruction techniques that can be applied to process the raw image obtained through multiple pinhole apertures.

A theory for phase contrast neutron imaging for mixed phase-amplitude objects was developed. It was found that a phase-amplitude interaction term, which depends on the scalar product of the gradients of the real and imaginary part of the transmission functions of the edge forming materials, needs to be included to extend the pure phase object approximation to mixed phase-amplitude objects. Also, it was observed that the phase-amplitude interaction effect counters the edge contrast effect provided by the pure phase contribution and leads to an asymmetry in the intensity distribution about the edge.

A technique for computational simulation of the phase contrast images was also developed through which contrast mechanisms in various samples could be understood and expected phase contrast could be predicted, which can help in examining this technique for a particular application. Parameters were identified based on which the feasibility and performance of phase contrast imaging experiments can be studied using neutron transport calculations. The transverse coherence length (L_t) along with the neutron flux at the image plane (ϕ_n), given the source characteristics and other constraints, can be optimized through computational simulations.

Through computational simulations, effects of the pure phase as well as phase-amplitude interaction terms on contrast enhancement in the images (for different mixed phase-amplitude materials) were investigated. It was observed that the interaction effect is less than the pure phase effect in terms of contrast enhancement; nevertheless it can be significant depending on the type of material edges present in the sample. The interaction effect can also lead to a higher overall contrast in samples having some material edges with significant phase-amplitude interaction and others where it is not significant. This is achieved by decreasing the contrast at those edges that already have high attenuation contrast thereby virtually expanding the gray scale in the digital image making other edges more prominent.

Further, phase contrast neutron imaging was demonstrated at the NCSU PULSTAR reactor which is a medium intensity neutron source. The requirements for such an imaging exercise are more difficult to achieve particularly for low/medium intensity neutron sources with high gamma noise like the PULSTAR. A step-by-step design methodology was followed to design the collimator according to the required objectives and constraints. Experiments depicting the phase contrast effect were performed using the designed collimator. The exposure time required to obtain such radiographs on a neutron image plate is reasonable (45 minutes). The system was designed in a fashion such that routine performance of such imaging experiments is possible. This demonstration at the PULSTAR makes the technique feasible to implement at other such facilities located on low/medium neutron flux sources. Such implementations will enable usage of this technique for practical neutron imaging applications on a routine basis as and when desired.

Lastly, phase contrast neutron imaging through multiple pinholes was investigated. Towards this goal a multi-pinhole collimator with seven pinholes was designed. Experiments with the designed collimator depicted edge enhancement (due to the phase contrast effect) in the collected images. Image reconstruction techniques that can be used to process the raw images were explored. Towards this end, a mathematical formulation for the image formation process through the multi-pinhole sources was developed. It was observed that the raw images collected is a convolution of the source mask image at the detector and the image recorded by the detector using a one pinhole mask. Based on this formulation, a regularized least square de-

convolution technique was explored for the reconstruction. In this work, Tikhonov regularization was investigated. Moreover, various de-noising methods like Wiener filtering, median filtering, wavelet based de-noising were also explored. It was observed that adaptive Wiener filtering performed the best in terms of improving the SNR of the images.

Thus, the main objective of making phase contrast neutron imaging available to facilities located on low/medium intensity neutron sources was achieved in this work. In addition, various other investigations were performed, as outlined above, that can help in further development of this technique as a useful tool in non-destructive testing.

6.2 Future Work

In future, it can be envisioned to use phase contrast neutron imaging for some applications like imaging of machine components made up of different materials, or biological applications like imaging of small animals. Further, in order to standardize this technique it is also necessary to develop standard phantom to quantify beam characteristics and a standard procedure to quantify the contrast. Also, better simulations techniques should be developed for system design and image prediction taking into account partial spatial coherence of the beam.

Multi-pinhole phase contrast neutron imaging should be tested with more number of pinholes in the mask and gain in the SNR should be investigated in greater detail. Since, the major burden in implementing multi-pinhole imaging technique is the availability of a good image reconstruction method, more effort should be directed towards exploring this aspect in future. The image reconstruction method used in the present work had some shortcomings and can be improved.

One of the shortcomings of the used method was, it can provide negative estimate of pixel values. This can be removed by putting a non-negativity constraint in the least square algorithm. There are fast non-negativity constrained least square algorithms proposed in the literature which can be used in the present case with a little modification [113], [114]. Other techniques like quadratic programming and gradient projection-reduced Newton-CG method can also be used to implement this [115].

Matrices associated with SPSFs of multi-pinhole imaging systems with large number of pinholes are much larger in size than the usual unimodal SPSFs encountered in the imaging field. But, with large memory computers getting increasingly available handling such matrices will become convenient soon. Moreover, since the matrices involved here arise from a convolution operation other numerical techniques can be used if needed. The matrix associated with the two dimensional convolution operation is Block Toeplitz with Toeplitz Blocks (BTTB) [104]. Efficient methods available in the literature requiring less storage space can be explored for solving such systems by taking into account its BTTB characteristics [116]-[118]. Circulant approximation to Toeplitz matrics can be used to lower the storage space requirements if needed. Moreover, multiplication of such matrices can be performed easily using Fourier transforms [104]. Another possibility that might be useful to explore is domain decomposition method [119]. In this case the large image is partitioned into small sub-domains and iterative techniques like CG can be used to solve the problem in every sub-domain. Solutions in different sub-domains are coordinated through suitable boundary conditions. The advantage of this technique is that it is inherently parallel and thus, can be implemented on parallel computers for fast computation.

It is also suggested to explore other regularization schemes especially total variation regularization. Total variation regularization is known to retain the blockiness of the image i.e. has edge preserving characteristics [104], [120]. In this case the least square functional with a penalty function that penalizes solutions with higher value of total variation is minimized [121]. Different pre-conditioners for total variation regularization in order to make the algorithm faster have also been proposed [122]. Along with this, edges in the reconstructed image can also be improved by applying appropriate boundary conditions in the least square image de-convolution [123].

Other methods of de-convolution as pointed out in Section 5.2 can also be explored. In this regard Bayesian techniques of de-convolution where prior information about the object can be easily incorporated may turn out to be useful. Expectation maximization de-convolution methods are also used in various applications and can be explored for its suitability in here.

Last but not the least, the feasibility of other advanced neutron imaging techniques at the PULSTAR imaging facility can also be investigated in distant future. With a possible upgrade in the reactor power to 5MW the available neutron flux will be five times higher. With this increase in the flux, cold neutron and energy selective neutron imaging (by using a beam chopper) can be envisioned.

REFERENCES

[1] H. Kallmann, Research 1 (1948), 254-260.

[2] J. P. Barton, "Neutron Radiography – An Overview," *Practical Applications of Neutron Radiography and Gaging, ASTM STP 586*, American Society for Testing and Materials, pp. 5-19, 1976.

[3] J. F. W. Markgraf, Neutron Radiography Working Group- Summary of activities and publications, International Neutron Radiography Newsletter, 2nd World Conference on Neutron Radiography, 59-67.

[4] J. P. Barton, "History and Foundation of ISNR," available at www.isnr.de.

[5] http://palaeo-electronica.org/2005_2/neutron/images/fig1.jpg

[6] I. S. Anderson, R. L. McGreevy, and H. Z. Bilheux, "*Neutron Imaging and Applications*," Springer Science + Business Media, New York, USA, 2009.

[7] H. Berger, "Neuton Radiography- Methods, Capabilities, and Applications," *Elsevier Publishing Company*, New York, USA, 1965.

[8] R.E. Faw, J.K. Shultis, "Radiological Assessment: Sources and Exposures," Prentice Hall New Jersey, 2nd Edition, 1993.

[9] H. Berger, Neutron Radiography- Annual Reviews, Argonne National Laboratory, Illionis, 1971.

[10] J. P. Barton, H. Berger, C. Hinsdale, Proc. 16th Conf. Remote Systems Technology, American Nuclear Society 276-288, 1969.

[11] R. Satija, D. L. Jacobson, M. Arif, and S. A. Werner, "In situ Neutron Imaging Technique for Evaluation of Water Management Systems in Operating PEM Fuel Cells," *J. Power Sources*, vol. **129**, pp. 238-245, 2004.

[12] K. K. Moghaddam, T. T. Taheri, and M. Ayubian, "Bone Structure Investigation using X-ray and Neutron Radiography Techniques," *Appl. Radiat. Isot.*, vol. **66**, pp. 39-43, 2008.

[13] M. Bastürk, H. Tatlisu, and H. Böck, "Nondestructive Inspection of Fresh WWER-440Fuel Assemblies," *Jour. Nucl. Mat.*, vol. **350**, pp. 240-245, 2006.

[14] U. Matsushima, Y. Kawabata, and T. Horie, "Estimation of the Volumetric Water Content in Chrysanthemum Tissues," *J. Radioanalytical Nucl. Chem.*, vol. **264** (2), pp.325-328, 2005.

[15] M. R. Hawkesworth, "Films for Neutron Radiography: An Investigation of Film-Intensifying Screen Image Recorders," *J. Scientific Instr. (Jour. Phys. E)*, 2, vol. **2**, pp. 235-242, 1969.

[16] Annual Book of ASTM Standards, Section 3, "Metals Test Methods and Analytical Procedures", vol. 03.03, Nondestructive Testing 1999.

[17] E. H. Lehmann, P. Vontobel, G. Frei, C. Bronnimann, "Neutron Imaging- Detector Options and Practical Results," *Nucl. Instr. Methods A*, vol. **531**, pp. 228-237, 2004.

[18] http://www.e-radiography.net/radtech/f/film.htm

[19] S. Masalovich, A. Ioffe, M. Schlapp, H. von Seggern, E. Küssel, and Th. Brückel, "Optimization of a Neutron Image Plate Detector with Low γ-Sensitivity," *Nucl. Instr. Methods A*, **539**, pp. 236-249, 2005.

[20] A. A. Harms, and D. R. Wyman, "Mathematics and Physics of Neutron Radiography," D. Reidel Publishing Company, Dordrecht, Holland, 1986.

[21] A. A. Harms, A. Zeilinger, "A new Formulation of Total Unsharpness in Radiography," *Phys. Med. Bio.*, vol. **22** (1), pp. 70-80, 1977.

[22] J. C. Domanus, "Practical Neutron radiography," NRWG, Kluwer Academic Publishers.

[23] C.E. Metz, and K. Doi, "Transfer Function Analysis of Radiographic Imaging Systems," *Phys. Med. Biol.*, vol. **24**, pp. 1079-1106, 1979.

[24] M.J. Day, "Specification and Additivity of Unsharpness in Diagnostic Radiology," *Phys. Med. Biol.*, vol. **21**, No. 3, pp. 399-405, 1976.

[25] A. A. Harms, B. K. Garside, and P. S. W. Chan, "Edge Spread Function in Neutron Radiography," J. Appl. Phys., vol. **43**, pp. 3863-3867, 1972.

[26] N. Kardjilov, S. Baechler, M. Basturk, M. Dierick, J. Jolie, E. Lehmann, T. Materna, B. Schillinger, and P. Vontobel, "New features in Cold Neutron Radiography and Tomography- II," *Nucl. Instr. Methods Phys. Res. A*, vol. **501**, 536-546, 2003.

[27] E. H. Lehmann, G. Frei, P. Vontobel, L. Josic, N. Kardjilov, A. Hilger, W. Kockelmann, and A. Steuwer, "The Energy-selective option in Neutron Imaging," *Nucl. Instr. Methods Phys. Res. A*, vol. **603**, pp. 429-438, 2009.

[28] W. Kockelmann, G. Frei, E. H. Lehmann, P. Vontobel, and J. R. Santisteban, "Energy-selective Neutron Transmission Imaging at a Pulsed Source," *Nucl. Instr. Methods Phys. Res. A*, vol. **578**, pp. 421-434, 2007.

[29] J. R. Santisteban, L. Edwards, M. E. Fizpatrick, A. Steuwer, and P. J. Withers, "Engineering Applications of Bragg-edge Neutron Transmission," *Appl. Phys. A*, vol. **74** [Suppl.], pp. 1433-1436, 2002.

[30] L. Josic, E. H. Lehmann, G. Frei, and M. Tamaki, "Cold Neutron Imaging near Bragg Edges as a tool for Material Research," *Nucl. Instr. Methods Phys. Res. A*, vol. **605**, pp. 21-25, 2009.

[31] K. Iwase, K. Sakuma, T. Kamiyama, and Y. Kiyanagi, "Bragg-edge Transmission Imaging of Strain and Microstructure using a Pulsed Neutron Source," *Nucl. Instr. Methods Phys. Res. A*, vol. **605**, pp. 1-4, 2009.

[32] F. Arfelli, et al., "Low-Dose Phase Contrast X-Ray Medical Imaging," *Phys. Med. Biol.,* vol. **43**, pp.2845-2852, June, 1998.

[33] C. J. Kotre, and I. P. Birch, "Phase Contrast Enhancement of X-ray Mammography: A Design Study," *Phys. Med. Biol.*, vol. **44**, pp. 2853-2866, 1999.

[34] K. Kanaya, and H. Kawakatsu, "Experiments on the Electron Phase Microscope," *J. Appl. Phys.,* vol. **29**, pp. 1046-1049, 1958.

[35] B. E. Allman, P. J. McMahon, K. A. Nugent, D. Paganin, D. L. Jacobson, M. Arif, and S. A. Werner, "Phase Radiography with Neutrons," (Brief Communications), *Nature*, vol. **408**, pp. 158-159, Nov. 2000.

[36] N. Kardjilov, I. Manke, M. Strobl, A. Hilger, W. Treimer, M. Meissner, T. Krist, and J. Banhart, "Three-dimensional Imaging of Magnetic Fields with Polarized Neutrons," *Nature Physics*, vol. **4**, pp. 399-403, 2008.

[37] F. M. Piegsa, B. van den Brandt, P. Hautle, J. Kohlbrecher, and J. A. Konter, "Quantitative Radiography of Magnetic Fields using Neutron Spin Phase Imaging," *Phys. Rev. Lett.*, vol. **102**, pp. 1-4, 2009.

[38] M. Dawson, I. Manke, N. Kardjilov, A. Hilger, M. Strobl, and J. Banhart, "Imaging with Polarized Neutrons," *New Jour. Phys.*, vol. **11**, pp. 1-19, 2009.

[39] K. K. Mishra, "Development of a Thermal Neutron Imaging Facility at the N.C. State University PULSTAR Reactor," Master's Thesis, Nucl. Engg., NCSU, 2005. (Available Online at: http://www.lib.ncsu.edu/theses/available/etd-06282005-103223/unrestricted/etd.pdf).

[40] *Visitors Guide to the NCSU Pulstar Reactor*, Raleigh, NC, n.p., n.d.

[41] X-5 Monte Carlo Team, "MCNP – A General Monte Carlo N–Particle Transport Code, Version 5," Los Alamos National Laboratory, Los Alamos, NM, Tech. Rep. LA-UR-03-1987, 2003.

[42] A. K. Freund, "Cross-sections of Materials used as Neutron Monochromators and Filters," *Nucl. Instr. Meth. Phys. Res.*, vol. **213**, pp. 495-501, 1983.

[43] M. Adib, K. Naguib, A. Ashry, and M. Fathalla, "On the use of Lead as Neutron Filter," *Annals of Nucl. Energy*, vol. **29**, pp. 1119-1130, 2002.

[44] M. Adib, N. Habib, A. Ashry, and M. Fathalla, "On the use of Silicon as Neutron Filter," *Annals of Nucl. Energy*, vol. **30**, pp. 1905-1917, 2003.

[45] M. Adib, and M. Kilany, "On the use of Bismuth as Neutron Filter," *Rad. Phys. Chem.*, vol. **66**, pp. 81-88, 2003.

[46] D. C. Tennant, "Performance of a Cooled Sapphire and Beryllium Assembly for Filtering of Thermal Neutrons," *Rev. Sci. Instr.*, vol. **59** (2), 1988.

[47] D. F. R. Mildner, M. Arif, and C. A. Stone, "Neutron Transmission of Single Crystal Sapphire Filters," *J. Appl. Cryst.*, vol. **26**, pp. 438-447, 1993.

[48] R. M. Brugger, "A Single Crystal Silicon Thermal Neutron Filter," *Nucl. Instr. Meth.*, vol. **135**, pp. 289-291, 1976.

[49] D. F. R. Mildner, and G. P. Lamaze, "Neutron Transmission of Single Crystal Sapphire," *J. Appl. Cryst.*, vol. **31**, pp. 835-840, 1998.

[50] K. K. Mishra, A. I. Hawari, and V. H. Gillette, "Design and Performance of a Thermal Neutron Imaging Facility at the North Carolina State University PULSTAR Reactor," *IEEE Trans. Nucl. Sci.,* vol. **53** (6), pp. 3904-3911, 2006.

[51] A. I. Hawari, I. I. Al-Qasir, and K. K. Mishra, "Accurate Simulation of Thermal Neutron Filter Effects in the Design of Research Reactor Beam Applications," PHYSOR-2006: Advances in Nuclear Analysis and Simulation, Vancouver, Canada, 2006.

[52] B. M. Rustad, J. Als-Nielsen, A. Bahnsen, C. J. Christensen, and A. Nielsen, **"**Single-Crystal Filters for Attenuating Epithermal Neutrons and Gamma Rays in Reactor Beams**,"** *Rev. Sci. Instr.*, vol. **36**, pp. 48-54, 1965.

[53] P. A. Egelstaff, and R. S. Pease, "The Design of Cold Neutron Filters," *J. Sci. Instr.,* vol. **31**, pp. 207-212, 1954.

[54] D. J. Hughes, and J. A. Harvey, "Neutron Cross Sections," Brookhaven National Laboratory Report 325, Office of Technical Services, Department of Commerce, Washington D. C., 1955.

[55] H. Kolbe, E. Lehmann, W. Gunia, and S. Korner, "Applications and Characteristics of Imaging Plates as Detectors in Neutron Radiography at SINQ," *Nucl. Instr. Meth. A*, vol. **424**, pp. 40-47, 1999.

[56] R. Baker, Applied Scintillation Technologies, Annapolis, MD, private communication, June 2005.

[57] A. Bouwers, *Fortschr. Geb. Röntgstrahal.*, **54**, pp. 87, 1936.

[58] M. Thoms, D. Myles, and C. Wilkinson, "Neutron Detection with Imaging Plates Part-I Image Storage and Readout," *Nucl. Instr. Meth. A*, vol. **424**, pp. 26-33, 1999.

[59] M. Thoms, "Neutron Detection with Imaging Plates Part II- Detector Characteristics," *Nucl. Instr. Meth. A*, vol. **424**, pp. 34-39, 1999.

[60] K. Takahashi, S. Tazaki, J. Miyahara, Y. Karasawa, and N. Niimura, "Imaging Performance of Imaging Plate Neutron Detectors," *Nucl. Instr. Meth. A*, **377**, pp. 119-122, 1996.

[61] M. R. Deinert, C. W. Lowe, J.-Y. Parlange, K. Ünlü, and K. B. Cady, "Performance and Calibration of a Neutron Image Intensifier Tube Based Real-time Radiography System," *IEEE Trans. Nucl. Sci.*, vol. **52**, pp. 349-355, 2005.

[62] Phosphor/Scintillator Data sheet 40, Applied Scintillation Technologies, USA.

[63] M. Ghioni, S. Cova, C. Samori, and F. Zappa, "True Constant Fraction Trigger Circuit for Picoseconds Photon-timing with Ultrafast Microchannel Plate Photomultipliers," *Rev. Sci. Instr.*, vol. **68**, pp. 2228-2237, 1997.

[64] A. S. Tremsin, O. H. W. Siegmund, J. V. Vallerga, J. S. Hull, and R. Abiad, "Cross Strip Readouts for Photon Counting Detectors with High Spatial and Temporal Resolution," *IEEE Trans. Nucl. Sci.*, vol. **51**, pp. 1707-1711, 2004.

[65] A. S. Tremsin, W. B. Feller, R. G. Downing, and D. F. R. Mildner, "The Efficiency of Thermal Neutron Detection and Collimation with Microchannel Plates of Square and Circular Geometry," *IEEE Trans. Nucl. Sci.*, vol. **52** (5), pp. 1739-1744, 2005.

[66] W. B. Feller, R. G. Downing, and P. L. White, "Neutron Field Imaging with Microchannel Plates," *Proc. SPIE*, **4141**, pp. 291-302, 2000.

[67] J. Hofmann, C. Rausch, "Performance of a Prototype Detector System for Thermal Neutron Based on Laser Stimulated Luminescence," *Nucl. Instr. Meth. A*, vol. **355**, pp. 494-500, 1995.

[68] L. de Broglie, "Recherches sur la théorie des quanta (Researches on the quantum theory)", Thesis (Paris), 1924; L. de Broglie, *Ann. Phys.* (Paris), vol. **3** (22), 1925.

[69] P. J. McMahon, B. E. Allman, K. A. Nugent, D. L. Jacobson, M. Arif, and S. A. Werner, "Contrast Mechanisms for Neutron Radiography," *Appl. Phys. Letters*, vol. **78** (7), pp. 1012-1013, Feb. 2001.

[70] N. Kardjilov, E. Lehmann, E. Steichele, and P. Vontobel, "Phase-contrast Radiography with a Polychromatic Neutron Beam," *Nucl. Instr. Meth. Phys. Res. A*, vol. **527**, pp. 519-530, 2004.

[71] B. Schillinger, "Various Neutron Imaging Methods at the FRM II Reactor Source and Potential Features at a Spallation Source Installation," *Nucl. Instr. Meth. Phys. Res. A*, vol. **600**, pp. 28-31, 2009.

[72] D. Hussey, "New Neutron Imaging Facility at the NIST," Power Point Presentation, July 27, 2004.

[73] http://physics.nist.gov/MajResFac/Nif/facility.html

[74] http://sinq.web.psi.ch/

[75] http://neutra.web.psi.ch/facility/index.html

[76] http://www.frm2.tum.de/en/technik/reactor/neutron-flux-density/index.html

[77] http://hanaro.kaeri.re.kr/english/nba_intro.htm

[78] http://www.hmi.de/grossgeraete/forschungsreaktor/daten_en.html

[79] A. Hilger, N. Kardjilov, M. Strobel, W. Treimer, and J. Bnahart, "The New Cold Neutron Radiography and Tomography Instrument CONRAD at HMI Berlin," Intl. Conf. Neutron Scattering, Sydney, Australia, vol. **385-86** (2), pp. 1213-1215, 2006.

[80] http://www.helmholtz-berlin.de/userservice/neutrons/instrumentation/neutron-instruments/v7/index_en.html

[81] J. M. Cowley, *Diffraction Physics*, New York, North-Holland Publishing Company, 1981.

[82] K. K. Mishra, and A. I. Hawari, "Investigating Phase Contrast Neutron Imaging of Mixed Phase-Amplitude Objects," *IEEE Trans. Nucl. Science*, **56**(3), pp. 1629-1636, 2009.

[83] A. V. Bronnikov, "Theory of Quantitative Phase-Contrast Computed Tomography," *J. Opt. Soc. Am. A*, **19**(3), 2002.

[84] http://physics.nist.gov/Divisions/Div846/Gp3/NIOF/web04c.html

[85] M. Warner, and J. E. Gubernatis, "Neutron Refractive Index: A Fermi-Huygens theory," *Phy. Rev. B*, vol. **32** (10), pp. 6347-6357, 1985.

[86] M. L. Goldberger, and F. Seitz, "Theory of the Refraction and the Diffraction of Neutrons by Crystals," *Phy. Rev.*, vol. **71** (5), pp. 294-310, 1947.

[87] W. Ketter, W. Heil, G. Badurek, M. BaronR. Loidl, and H. Rauch, "Measurement of Coherent Neutron Scattering Length of ^{3}He," *J. Res. Natl. Stand. Technol.*, vol. **110**, pp. 241-244, 2005.

[88] V. F. Sears, *Neutron Optics- An Introduction to the Theory of Neutron Optical Phenomena and their Applications*, New York, Oxford University Press, 1989.

[89] http://en.wikipedia.org/wiki/Coherence_%28physics%29

[90] R. H. Dicke, "Scatter-hole cameras for X-rays and Gamma Rays," *Astrophys. J.*, **153**, L101-L106, 1968.

[91] J. G. Ables, "Fourier Transform Photography: A New Method of X-ray Astronomy," *Proc. Astron. Soc. Aust.*, **1**, 172-173, 1968.

[92] H. H. Barrett, "Fresnel Zone Plate Imaging in Nuclear Medicine," *J. Nucl. Med.*, **13**, 382-385, 1972.

[93] G. K. Skinner, "Imaging with Coded-Aperture Masks," *Nucl. Instr. Meth. Phys. Res. A*, **221**, 33-40, 1984.

[94] W. L. Rogers, K. F. Koral, R. Mayans, P. F. Leonard, J. H. Thrall, T. J. Brady, and J. W. Keyes Jr., "Coded-Aperture Imaging of the Heart," *J. Nucl. Med.*, **21**, 371-378, 1980.

[95] E. Caroli, J. B. Stephen, G. Di Cocco, L. Natalucci, and A. Spizzichino, "Coded Aperture Imaging in X-ray and Gamma-ray Astronomy," *Space Sci. Rev.*, **45**, 349-403, 1987.

[96] E. E. Fenimore, and T. M. Cannon, "Coded Aperture Imaging with Uniformly Redundant Arrays," *Applied Optics*, **17**(3), pp. 337-347, 1978.

[97] S. R. Gottesman, and E. E. Fenimore, "A new Family of Binary Arrays for Coded Aperture Imaging," Applied Optics, 28 (20), pp. 4344- 4352, 1989.

[98] A. Busboom, H. Elders-Boll, and H. D. Schotten, "Uniformly Redundant Arrays," *Experimental Astronomy*, **8**, pp. 97-123, 1998.

[99] S. Jae Lim, *Two-Dimensional Signal and Image Processing*, Prentice Hall, Englewood Cliffs, NJ, 1990.

[100] V. F. Sears, "Neutron Scattering Lengths and Cross Sections," *Neutron News*, vol. 3, no. 3, pp. 29-37, 1992. Available: http://www.ncnr.nist.gov/resources/n-lengths/

[101] M. Hainbuchner, and E. Jericha, "Bound coherent neutron scattering lengths," 2001, Available: http://www.ati.ac.at/~neutropt/scattering/ScatteringLengthsAdvTable.pdf

[102] *Mammography Accreditation Phantom Gammex 156*, GAMMEX RMI, Middleton, WI, USA, 2002.

[103] K. K. Mishra, and A. I. Hawari, "Phase Contrast Neutron Imaging at a Medium Intensity Neutron Source," *Proc. IEEE Nucl. Sci. Symp.*, Orlando FL, Nov. 2009.

[104] C. R. Vogel, *Computational Methods for Inverse Problem*, Philadelphia, SIAM Publication on Frontiers in Applied Mathematics, 2002.

[105] L. V. Novikov, "Wavelet-based Deconvolution," *Instr. Expt. Techniques*, **50**(1), pp. 61-67, 2007.

[106] W. L. Richardson, "Bayesian-Based Iterative Method of Image Restoration," *J. Opt. Soc. Am.*, **62**, pp. 55-59, 1972.

[107] E. Y. Lam, and J. W. Goodman, "Iterative Statistical Approach to Blind Image Deconvolution," *J. Opt. Soc. Am. A*, **17**, pp. 1177-1184, 2000.

[108] M. A. T. Figueiredo, and R. D. Nowak, "An EM Algorithm for Wavelet-Based Image Restoration," *IEEE Trans. Img. Pros.*, **12**(8), pp. 906-916, 2003.

[109] J. M. Bioucas-Dias, "Bayesian Wavelet-Based Image Deconvolution: A GEM Algorithm Exploiting a Class of Heavy-Tailed Priors," *IEEE Trans. Img. Pros.*, **15**(4), pp. 937-951, 2006.

[110] H. W. Engl, M. Hanke, and A. Neubauer, *Regularization of Inverse Problems*, Series: Mathematics and Its Applications, Kluwer Academic Publishers, MA, USA, 2000.

[111] D. L. Donoho, "De-noising using Soft Thresholding," *IEEE Trans. Info. Theory*, **41**(3), 613-627, 1995.

[112] E. G. T. Swee, and S. Elangovan, "Application of Symlets for De-noising and Load Forecasting," *Proc. IEEE Signal Processing Workshop on Higher-Order Statistics*, 165-169, 1999.

[113] R. Bao, and S. D. Jong, "A fast Non-Negativity Constrained Least Square Algorithm," *J. Chemometrics*, **11**, pp. 393-401, 1997.

[114] K. H. Haskell, and R. J. Hansen, "An Algorithm for Linear Least Squares Problems with Equality and Non-Negativity Constraints," *Mathematical Prog.*, 21(1), pp. 98-118, 1981.

[115] J. M. Bardsley, and C. R. Vogel, "A Non-Negativity Constrained Convex Programming Method for Image Reconstruction," *SIAM J. Sci. Comput.*, **25**(4), pp. 1326-1343, 2003.

[116] M. K. Ng, *Iterative Methods for Toeplitz Systems*, Numerical Mathematics and Scientific Computation, Oxford Science Publications, New York, USA, 2004.

[117] Xiao-Qing Jin, "*Developments and Applications of Block Toeplitz Iterative Solvers*, Combinatorics and Computer Science, Kluwer Academic Publishers, MA, USA, 2002.

[118] R. Hon-Fu Chan, and Xiao-Qing Jin, "*An introduction to Iterative Toeplitz Solvers*, Fundamentals of Algorithms, SIAM, Philadelphia, 2007.

[119] A. Toselli, and O. Widlund, *Domain Decomposition Methods – Algorithms and Theory*, Springer Series in Computational Mathematics, **34**, 2004.

[120] D. C. Dobson, and F. Santosa, "Recovery of Blocky Images from Noisy and Blurred Data," *SIAM J. Appl. Math.*, **56**(4), pp. 1181-1198, 1996.

[121] R. Acar, and C. R. Vogel, "Analysis of Total Variation Penalty Methods, *Inverse Problems*, **10**, pp. 1217-1229, 1994.

[122] R. H. Chan, and T. F. Chan, and C. K. Wong, "Cosine Transform Based Preconditioners for Total Variation Deblurring," *IEEE Trans. Img. Pros.*, **8**(10), pp. 1472-1478, 1999.

[123] R. Vio, J. Bardsley, M. Donatelli, and W. Wamsteker, "Dealing with Edge Effects in Least-Squares Image Deconvolution Problems," *Astrom. Astrophys.*, **442**(1), pp. 397-403, 2005.

[124] http://www.cs.cmu.edu/~quake-papers/painless-conjugate-gradient.pdf

[125] W. H. Press, S. A. Teukolsky, W. T. Vetterling, and B. P. Flannery, *Numerical Recipes-The Art of Scientific Computing*, Cambridge University Press, NY, 2007.

[126] R. C. Gonzalez, and R. E. Woods, *Digital Image Processing*, Prentice Hall, Upper Saddle River, NJ, 2002.

[127] S. K. Mohideen, S. A. Perumal, and M. M. Sathik, "Image De-noising using Discrete Wavelet Transform," IJCSNS Intl. J. Comp. Sc. Net. Secu., **8** (1), pp. 213-216, 2008.

[128] J. Xie, D. Zhang, and W. Lu, "Spatially Adaptive Wavelet Denoising using the Minimum Description Length Principle," IEEE Trans. Img. Pros., 13 (2), pp. 179-187, 2004.

APPENDICES

Appendix A. Fourier Transform of the Fresnel Propagator

In Chapter 3 (see Section 3.4.2 and 3.4.3) it was shown that the phase contrast intensity distribution at the image plane, which is at a distance R from the object, can be obtained by convolving the object transmission function $q(x,y)$ with the Fresnel propagator at that distance. In order to perform the convolution operation Fourier transforms were used. Here derivation of the Fourier transform of the Fresnel propagator is being shown that was used in Section 3.4.3 to calculate the convolution and hence the phase contrast intensity distribution at the image plane.

The Fourier transform of a function $f(x,y)$ is given by

$$\mathcal{F}\left[f(x,y)\right] = F(\varsigma,\eta) = \int_{-\infty}^{\infty}\int_{-\infty}^{\infty} f(x,y)\exp\left\{2\pi i(\varsigma x+\eta y)\right\}dxdy\,, \tag{A.1}$$

where ς and η are spatial frequencies in x and y directions. The Fresnel propagator is given by

$$Fs(x,y,R,\lambda) = \frac{i\exp\{-ikR\}}{R\lambda}\exp\left\{\frac{-ik\left(x^2+y^2\right)}{2R}\right\}, \tag{A.2}$$

where R is the distance between the diffraction point and the observation point and λ is the wavelength of the neutron. The Fourier transform of the Fresnel propagator is given by

$$\mathcal{F}\left[Fs(x,y,R,\lambda)\right] = \mathcal{F}s(\varsigma,\eta) = \int_{-\infty}^{\infty}\int_{-\infty}^{\infty}\frac{i\exp\{-ikR\}}{R\lambda}\exp\left\{\frac{-ik\left(x^2+y^2\right)}{2R}\right\}\exp\left\{2\pi i(\varsigma x+\eta y)\right\}dxdy\,. \tag{A.3}$$

The integration in Eq. (A.3) can be separated as following

$$\mathcal{F}s(\varsigma,\eta) = \frac{i\exp(-ikR)}{R\lambda}\left\{\int_{-\infty}^{\infty}\exp\left(\frac{-ikx^2}{2R}\right)\exp(2\pi i\varsigma x)dx\right\}\left\{\int_{-\infty}^{\infty}\exp\left(\frac{-iky^2}{2R}\right)\exp(2\pi i\eta y)dy\right\}. \tag{A.4}$$

Both the integrals in Eq. (A.4) are similar and their solution will be similar. The solution of the Fourier integral in x will be presented here. In solving the above integration the following standard integral will be used.

$$\int_{-\infty}^{\infty} \exp\left(-a^2x^2\right) = \sqrt{\pi/a} \tag{A.5}$$

The Fourier integral in the x in Eq. (A.4) can be written as

$$\int_{-\infty}^{\infty} \exp\left\{-\frac{i\pi}{R\lambda}\left(x^2 - 2R\lambda\varsigma x\right)\right\}dx\,. \tag{A.6}$$

Performing completion of square the above integral can be written as

$$\exp\left(i\pi\lambda R\varsigma^2\right)\int_{-\infty}^{\infty} \exp\left\{-\frac{i\pi}{R\lambda}\left(x - R\lambda\varsigma\right)^2\right\}dx\,. \tag{A.7}$$

Standard integral in Eq. (A.5) is used to obtain

$$\int_{-\infty}^{\infty} \exp\left(\frac{-ikx^2}{2R}\right)\exp\left(2\pi i\varsigma x\right)dx = \sqrt{\frac{R\lambda}{i}}\exp\left(i\pi\lambda R\varsigma^2\right). \tag{A.8}$$

Using the above result Eq. (A.4) can be written as

$$\mathcal{F}s\left(\varsigma,\eta\right) = \frac{i\exp\left(-ikR\right)}{R\lambda}\left\{\sqrt{\frac{R\lambda}{i}}\exp\left(i\pi\lambda R\varsigma^2\right)\right\}\left\{\sqrt{\frac{R\lambda}{i}}\exp\left(i\pi\lambda R\eta^2\right)\right\}. \tag{A.9}$$

The above equation can be simplified to obtain the result shown in Eq. (3.13) as

$$\mathcal{F}s\left(\varsigma,\eta\right) = \exp\left(-ikR\right)\exp\left\{i\pi\lambda R\left(\varsigma^2 + \eta^2\right)\right\}. \tag{A.10}$$

Appendix B. Selected Properties of Fourier Transform

Here are listed few of the selected properties of the Fourier transforms that were used in Chapters 3 and 5.

If the Fourier transform of $f(x) = F(\varsigma)$ and $g(x) = G(\varsigma)$ then the Fourier transform of

1. $f(-x) = F(-\varsigma)$
2. $f(ax) = \frac{1}{a} F\left(\frac{\varsigma}{a}\right)$
3. $f(x-a) = \exp\{2\pi i a\varsigma\} F(\varsigma)$
4. $\frac{d^n}{dx^n} f(x) = (-2\pi i\varsigma)^n F(\varsigma)$
5. $f(x) * g(x) = F(\varsigma) \cdot G(\varsigma)$
6. $f(x) \cdot g(x) = F(\varsigma) * G(\varsigma)$

Appendix C. Conjugate Gradient Technique: A Brief Note

The Conjugate gradient (CG) iterative technique was used to solve the least and regularized least square problem in Chapter 5. CG method is an algorithm for the numerical solution of particular systems of linear equations, namely those whose matrix is symmetric and positive-definite. It is a iterative technique and can be applied to sparse linear systems that are too large to be handled by direct methods such as the Cholesky decomposition.

CG method is very much similar to the conjugate direction method but here the search directions after every step/iteration are constructed by conjugation of the residuals. In this case conjugacy refers to the orthogonality of the search direction with respect to a known matrix A. Mathematically, it can be written as

$$d_{(i)}^{T} A d_{(j)} = 0, \tag{A.1}$$

where $d_{(i)}$ and $d_{(j)}$ are the search directions. It is also referred to as A-orthogonality. More detail on the CG method can be found in [124]. The exact algorithm is not given here but can be found in any numerical analysis or optimization textbook [104], [125].

The CG method can be used to solve normal/least square equations. By definition the normal equation of $Ax = b$ is $A^T Ax = A^T b$. The matrix involved in the normal equation, $A^T A$ is always symmetric and positive definite for any matrix A. It is also know that if A is non-singular then the solution of $Ax = b$ is same as $A^T Ax = A^T b$. Moreover, if A is rectangular and $Ax = b$ is over-constrained then a solution may not exist but the norm $\|Ax - b\|^2$ can be always minimized. It is also important to know that the matrix $A^T A$ need not be stored explicitly. This becomes crucial because even if the matrix A is sparse the matrix $A^T A$ need not be sparse. On the other hand the convergence of the system of normal equations $A^T Ax = A^T b$ using CG method is slow because the condition number of $A^T A$ is square of that of matrix A.

Appendix D. Image De-noising Techniques: A Brief Note

Image de-noising techniques were used in Chapters 4 and 5 to de-noise the experimental images. Multiple image de-noising techniques can be found in the literature. The four techniques that have been used in the present work, namely median filtering, spike noise filtering, Wiener filtering, and thresholding of wavelet coefficients, will be discussed here in a little detail here.

Median Filtering

Median filtering is a nonlinear process useful in reducing impulsive or salt-and-pepper noise. It also has edge preserving characteristics while reducing the random noise. Impulsive or salt-and-pepper noise can occur in the image due to random pixel errors happening while taking the image. In the median filter, a window of selected size slides across the image and the median intensity value of the pixels within that window becomes the output intensity of the pixel being processed. For example, if the pixel value within a window are 9, 20, 30, 45, 50, 48 and 16, and the pixel being processed is the one with value 48, then it will be replaced by the value 30 (the median of the pixel given pixel values).

The median filter can preserve discontinuities in a step function and can smooth a few pixels whose values differ significantly from their surrounding without affecting the other pixels. This property of median filtering imparts it the edge preserving characteristics. If in the image the discontinuities are two-dimensional then it is better two apply separable median filter in order to preserve the discontinuity. Two dimensional separable median filters are basically composed of two one dimensional median filters that are in horizontal and vertical directions. Since median filtering is a nonlinear operation the order in which the separable filters are applied matters.

An important parameter in using a median filter is the size of the window. Depending on the size of the window selected the median filter can result into image de-noising or image distortion. Because it is difficult to select a window size in advance, it may be useful to try

different window sizes and choose the one which outputs the best de-noised image without image distortion.

Spike Noise Filtering

Spike noise filtering is a nonlinear operation on the image like median filtering, useful for reducing the salt-and-pepper noise. In this method, a window slides along the image, and average of the pixel values, excluding the pixel being processed, is obtained. If the value of the pixel being processed differs from the calculated average by more/less than some threshold, then the current pixel value is replaced by the average. Otherwise, the value of the pixel is not affected. Selection of the threshold determines the smoothing being performed by this filter. Because it is difficult to determine the best threshold value and the window size in advance, it may be useful to process an image using several different threshold values and window sizes and select the best result.

Wiener Filtering

Wiener filtering is based on the statistical concept of minimizing the mean squared error (MSE). In this case the noise is assumed to be additive and independent of the signal. Thus, the raw image $g(x,y)$ collected is assumed to be the sum of ideal image $f(x,y)$ and the noise $n(x,y)$. The Weiner filter is $w(x,y)$ is defined to be the filter such that if the estimated image $\hat{f}(x,y)$ is obtained by

$$\hat{f}(x,y) = g(x,y) * w(x,y), \tag{D.1}$$

then the MSE given by

$$MSE = E\left[\left|e(x,y)\right|^2\right], \tag{D.2a}$$

$$e(x,y) = f(x,y) - \hat{f}(x,y) \tag{D.2b}$$

is minimized. In Eq. (D.2) $E[\cdot]$ is the expected value of $[\cdot]$. Orthogonality principle is used to perform the minimization. The principle states that the MSE (given by Eq. (D.2)) is minimized by requiring $e(x,y)$ to be uncorrelated with any random variable in $g^*(x,y)$, where $g^*(x,y)$ denotes the complex conjugate of $g(x,y)$. Using this principle one can get

$$E\left[e(x,y)g^*(x',y')\right]=0, \text{ for all } (x,y) \text{ and } (x',y'). \tag{D.3}$$

Using Eq. (D.2b), Eq. (D.3) can be written as

$$E\left[f(x,y)g^*(x',y')\right]=E\left[\hat{f}(x,y)g^*(x',y')\right], \text{ for all } (x,y) \text{ and } (x',y'). \tag{D.4}$$

Using Eq. (D.1), Eq. (D.4) can be written as

$$\begin{aligned} E\left[\hat{f}(x,y)g^*(x',y')\right] &= E\left[g(x,y)*w(x,y)g^*(x',y')\right] \\ &= \sum_{n=-\infty}^{\infty}\sum_{m=-\infty}^{\infty} w(n,m)E\left[g(x-n,y-m)g^*(x',y')\right] \end{aligned}. \tag{D.5}$$

Re-writing Eq. (D.5) one can get

$$R_{fg}(x-x',y-y')=\sum_{n=-\infty}^{\infty}\sum_{m=-\infty}^{\infty} w(n,m)R_{gg}(x-n-x',y-m-y'), \tag{D.6}$$

where $R_{fg}(x,y)$ is the cross-correlation between $f(x,y)$ and $g(x,y)$ defined as $E\left[f(x,y)g^*(x',y')\right]$. From Eq. (D.6) it can be observed that

$$R_{fg}(x,y)=w(x,y)*R_{gg}(x,y) \tag{D.7}$$

and therefore using Property 5 from Appendix B,

$$W(\varsigma,\eta)=\frac{P_{fg}(\varsigma,\eta)}{P_{gg}(\varsigma,\eta)}, \tag{D.8}$$

where $W(\varsigma,\eta)$, $P_{fg}(\varsigma,\eta)$, and $P_{gg}(\varsigma,\eta)$ are the Fourier transforms of $w(x,y)$ $R_{fg}(x,y)$ and $R_{gg}(x,y)$ respectively. $P_{fg}(\varsigma,\eta)$ is also referred to as the *cross-power spectrum*. The filter $W(\varsigma,\eta)$ is called the *noncausal Wiener filter*.

Suppose, if it is further assumed that $f(x,y)$ and the noise $n(x,y)$ are uncorrelated then,

$$E\left[f(x,y)n^*(x',y')\right] = E\left[f(x,y)\right]E\left[n^*(x',y')\right]. \tag{D.9}$$

From Eq. (D.9) and assuming $f(x,y)$ and $n(x,y)$ are zero-mean processes (which can be achieved by shifting the mean), one can easily obtain

$$\begin{aligned} R_{fg}(x,y) &= R_{ff}(x,y) \\ R_{gg}(x,y) &= R_{ff}(x,y) + R_{nn}(x,y) \end{aligned}. \tag{D.10}$$

Taking the Fourier transform of Eq. (D.10)

$$\begin{aligned} P_{fg}(\varsigma,\eta) &= P_{ff}(\varsigma,\eta) \\ P_{gg}(\varsigma,\eta) &= P_{ff}(\varsigma,\eta) + P_{nn}(\varsigma,\eta) \end{aligned} \tag{D.11}$$

can be obtained. Using Eq. (D.11) the Wiener filter in Eq. (D.8) can be written as

$$W(\varsigma,\eta) = \frac{P_{ff}(\varsigma,\eta)}{P_{ff}(\varsigma,\eta) + P_{nn}(\varsigma,\eta)}. \tag{D.12}$$

If additional constraint that $f(x,y)$ and $n(x,y)$ are samples of Gaussian random processes is imposed then the Wiener filter in Eq. (D.12) is the optimal minimum MSE estimator of the signal among both the linear and nonlinear estimators. Since, minimizing MSE does not ensure if the processed image is judged by the human observer closer to the original, many ad hoc variations of Wiener filtering have been proposed in the literature.

One of the problems faced using the above Wiener filtering technique is significant blurring of the output image. This happens because the same filter is used on the entire image.

Above filter was developed with the assumption that characteristics of the signal and the noise do not change over different regions of the image. This assumption is not satisfied in general and therefore, degradation happens in the image that differs from one region to another. In order to tackle this problem adaptive Wiener filtering can be performed. The idea is to adapt the filter to the local characteristics of the image. Two approaches to adaptive processing has been developed, namely *pixel-by-pixel processing*, and *subimage-by-subimage processing*. In the pixel-by-pixel processing approach a neighborhood is taken around the pixel being processed and relevant local characteristics of the image is calculated using the neighborhood. These characteristics are used to adapt the processing filter. In the subimage-by-subimage processing approach the image is partitioned into different subimages and each subimage is processed separately and then combined with each other. Pixel-by-pixel approach performs better than the subimage-by-subimage approach but is also more computationally intensive. More detail on this can be found in [99], [126].

Thresholding of Wavelet Coefficients

Wavelet transforms fall under the broader field of multiresolution analysis. In the wavelet transform the basis functions that are used to expand the given function look like waves of different frequencies and are localized in space. This is unlike the Fourier transform where the basis functions are sine and cosine waves of different frequencies that reach up to infinity in space (no localization in space). The localization feature of wavelets in both frequency and spatial domain makes many functions and operations '*sparse*' (less data to store in wavelet domain) using wavelets. This sparseness, in turn, results in a number of useful applications such as data compression, detecting features in images, and signal and image de-noising. Moreover, unlike Fourier transforms, due to availability of varying size windows in time-frequency plane, wavelets are better in isolating discontinuities in the data, like edges in the image, while obtaining sufficiently detailed frequency spectrum of the object. Also, since wavelet transforms have multiple sets of basis functions, unlike Fourier transforms, selection of basis function set can be performed depending on the particular application.

The discrete wavelet transform of a function (here a 2-dimensional image) is represented by the *scaling* and *detail* coefficients in both x and y directions at different levels that have

different frequencies i.e. at different resolutions (levels). The two dimensional discrete time wavelet transform (DTWT) of an image can be obtained by expanding the image function using basis functions of four orthogonal vector spaces as indicated by

$$V_{k-1} = V_k \oplus W_{b,k} \oplus W_{c,k} \oplus W_{d,k}\,, \tag{D.13}$$

where V_{k-1} is the vector space consisting of the image at the (k-1)$^{\text{th}}$ resolution, $\oplus$ represents the linear sum of vector spaces, and $W_{i,k}\quad i=b,c,d$ represents the vector spaces consisting of the *detail* information of the image at the k^{th} resolution. Explicitly the expansion of the image function in the above four vector spaces can be written as

$$\begin{aligned} f_{k-1}(x,y) = &\sum_{n=-\infty}^{\infty}\sum_{p=-\infty}^{\infty} a_k(n,p)\, s_{\varphi\varphi}(x-n,y-p) + \sum_{n=-\infty}^{\infty}\sum_{p=-\infty}^{\infty} b_k(n,p)\, s_{\varphi\psi}(x-n,y-p) + \\ &\sum_{n=-\infty}^{\infty}\sum_{p=-\infty}^{\infty} c_k(n,p)\, s_{\psi\varphi}(x-n,y-p) + \sum_{n=-\infty}^{\infty}\sum_{p=-\infty}^{\infty} d_k(n,p)\, s_{\psi\psi}(x-n,y-p) \end{aligned}\,, \tag{D.14}$$

where, the expansion coefficients a_o, b_o, c_o and d_o are called 'Low-Low' (LL), 'Low-High' (LH), 'High-Low' (HL) and 'High-High' (HH) coefficients respectively and $s_{\phi\phi}$, $s_{\phi\psi}$, $s_{\psi\phi}$ and $s_{\psi\psi}$ are the basis functions in the space V_k and $W_{i,k}$, $i=b,c,d$ respectively. There are multiple different kinds of basis functions or wavelets that can be used e.g. Haar wavelets, Daubechies wavelet, symlets, ridglets, of different order. The choice of the wavelet depends upon the application.

The wavelets can be used for image de-noising using *thresholding* techniques. In the thresholding technique the measured values are compared against a threshold value (selected using some technique) and if the value is greater/less than the threshold (depending upon the application) then it is reset to the threshold. Thresholding is called *adaptive thresholding* when a different threshold is used for different regions in the image. This may also be known as *local* or *dynamic* thresholding

Thresholding is applied on the wavelet coefficients of the image to de-noise the image. The wavelet coefficients of the raw image (obtained using DTWT on it) go through a

thresholding process. The coefficients returned from the process are inverted back using the inverse DTWT to obtain the de-noised image. The de-noising performed on the image depends on the type of wavelet and the thresholding technique used.

In the present case symlets of order four were used to perform de-noising. The thresholding technique that was used tries to minimize the mean squared error subject to the condition that with high probability the de-noised image $\hat{f}(x,y)$ is as smooth as actual image $f(x,y)$ [111]. The technique assumes that the noise is white noise. The condition of smoothness is applied so that the noise induced structures like 'ripples', 'blips' and oscillations, that usually occur when only mean squared error is minimized, do not occur in the image. A soft thresholding technique has been proposed to achieve the minimized MSE along with the above smoothness constraint. Other schemes of thresholding can also be found in the literature in order to de-noise the image [126]-[128].